Fakultät für Medizin

Lehrstuhl für Biologische und Medizinische Bildgebung

Hybrid microscopy: A novel microscope integrating advanced optical and optoacoustic modalities for multi-modal examinations of biological specimens

Markus R. Seeger

Vollständiger Abdruck der von der Fakultät für Medizin der Technischen Universität München zur Erlangung des akademischen Grades eines

Doctor of Philosophy (Ph.D.)

genehmigten Dissertation.

Vorsitzender: Prof. Dr. Stefan Lichtenthaler

Betreuer: Prof. Dr. Vasilis Ntziachristos

Prüfer der Dissertation:

1. Prof. Dr. Simon Jacob

2. Prof. Dr. Gil G. Westmeyer

3. apl. Prof. Dr. Karl-Hans Englmeier

Die Dissertation wurde am 15.10.2019 bei der Fakultät für Medizin der Technischen Universität München eingereicht und durch die Fakultät für Medizin am 09.03.2020 angenommen.

Microscopes and Telescopes, in actual fact, confuse man's innate clarity of mind
Johann Wolfgang von Goethe, 1749-1832
in E. Lehrs *Man or Matter*

ZUSAMMENFASSUNG

Im Laufe der letzten Jahrzehnte entwickelte sich photonische (optische) Mikroskopie zu einem unverzichtbaren Werkzeug zur Untersuchung der strukturellen, molekularen und funktionellen Beschaffenheit von biologischen und biomedizinischen Proben im mikroskopischen Bereich. Mikroskopische Untersuchungen 'beleuchteten' in dem Sinne wie sich Leben unterhalb der Auflösungsgrenze menschlicher Augen manifestiert und revolutionierten so eine große Bandbreite an wissenschaftlichen Disziplinen angefangen bei biologischer Grundlagenforschung über translationale Medizin bis hin zur alltäglichen klinischen Praxis. Neueste Fortschritte in der photonischen Technologie erweiterten zusätzlich die Fähigkeiten modernster Mikroskope indem spezifische Licht-Materie-Wechselwirkungen als Kontrastmechanismus implementiert wurden. Dennoch ist jede Mikroskopie-Modalität limitiert bezüglich der erzielbaren Informationsfülle aufgrund einer vorbestimmten Auswahl an messbaren biologischen Komponenten, der Anwendbarkeit für *in vivo* Proben aufgrund toxischer Nebeneffekte der benutzten Markierungsstrategien und der Messtiefe aufgrund der geringen Eindringungstiefe von Licht in Gewebe. Diese Limitierungen beeinträchtigen sowohl eine allumfassende Untersuchung von lebenden Organismen als auch die Aussagekraft der erzielten Rückschlüsse auf deren Zustand.
Ein vielversprechender Ansatz diesen Einschränkungen der photonischen Mikroskopie entgegenzuwirken ist die Zusammenführung verschiedener kompatibler Bildgebungsverfahren zu einem einzigen Gerät, dem hybriden Mikroskop. Dieser Trend zur Hybridisierung gewinnt zunehmend an Beliebtheit, da er es erlaubt, präzise und passgenaue Modalitäten zu wählen, welche sich bestmöglich zur Adressierung der anvisierten wissenschaftlichen Fragestellung eignen. Von der Untersuchung von Einzelzellen über Gewebeschnitten bis hin zu ganzen Modellorganismen haben sich die Multiphotonen- sowie die optoakustische (photoakustische) Mikroskopie als vielversprechend herausgestellt. Erstere bedient sich nicht-linearer optischer Effekte, welche auftreten, wenn Licht hoher Intensität auf Materie trifft. Zweitere basiert auf der Detektion von akustischen Wellen, welche durch thermoelastische Expansion generiert werden, die von Molekül-spezifischer optischer Absorption bedingt wird. Aufgrund ihrer grundlegenden Funktionsweise und Kontrastmechanismus zeichnen sich diese beiden hochmodernen Mikroskopie-Technologien durch große Eindringtiefen, hohe räumliche Auflösung, gute Eignung für *in vivo* Anwendungen und potentiell markerfreien Einsatz aus, wodurch

sie bestens geeignet für die Untersuchung von kultivierten Zellen, Organoiden, Modellorganismen wie Zebrafischen und Mäusen und menschlichen Gewebeproben sind.
Diese Arbeit widmet sich der Aufgabe hybride Multiphotonen- und Optoakustik-Mikroskopie für die biologische und biomedizinische Forschung weiterzuentwickeln. Der Kern der Arbeit zielt auf den Schnittpunkt von Systementwicklung des optischen Aufbaus hinsichtlich Soft- und Hardware-Konfiguration, Nutzbarmachung des multimodalen Kontrastes von endogenen sowie speziell konzipierten Markern und Erforschung neuartiger Methoden für die mikroskopische Optoakustik ab.
Im ersten Teil wird das hybride Multiphotonen- und spektrale Optoakustik-Mikroskop mit optischer Auflösung (HyMPSOM) vorgestellt, welches sieben Mikroskopie-Modalitäten in einem einzigen optischen System vereint und sich durch hochsensitive, simultane und multimodale Messungen mit subzellulärer Auflösung in großer Eindringtiefe sowie schneller Bilderfassung auszeichnet. Dessen Funktionsweise wird detailliert ausgearbeitet, einschließlich des speziell entwickeltem Synchronisierungsverfahren basierend auf einem Global Trigger Signal zum zeitgleichen Betrieb der Modalitäten sowie des adaptiven Bildgebungsverfahren basierend auf einem Laser- und Proben-Abtastschema. Darüber hinaus wird eine neuartige Methodik zur Charakterisierung und Korrektur der optoakustischen Total Impulse Response dargelegt, welche durch die Anwendung eines Spatial Matched Filters auf der Signalebene sowohl das Signal-zu-Rausch Verhältnis als auch die axiale Auflösung maßgeblich verbessert, wodurch die optoakustische Leistungsfähigkeit verbessert wird um die Multiphotonen-Modalitäten von HyMPSOM zu komplementieren.
Der zweite Teil beschäftigt sich mit der Verwendung des multimodalen Kontrasts von HyMPSOM zur Untersuchung biologischer und biomedizinischer Proben sowie zur Erforschung neuartiger Kontrastmittel, die speziell für die multimodale Bildgebung entwickelt wurden. Zunächst wird HyMPSOM auf dessen Fähigkeit getestet, *in vitro*, *in vivo* und *ex situ* Proben zu messen wie etwa Einzelzellen, Organoide, Zebrafisch-Larven, Mäuse und histopathologische Gewebeschnitte. Darauf aufbauend wird HyMPSOM verwendet, um die mikrostrukturelle Komposition von menschlichen Carotis-Atherom-Präparaten zu studieren, was neue Einblicke in das Zusammenspiel der Schlüsselbausteine von Gewebe ermöglicht, wie beispielsweise der Mikrovaskulatur und des Bindegewebes, die zentrale Bedeutung im Krankheitsverlauf von Arteriosklerose besitzen. Der Transfer dieser Abbildungsfähigkeiten zu *in vivo* Proben erlaubt die Untersuchung des Wundheilungsprozesses in Mäuseohren mithilfe von HyMPSOM, wodurch räumlich-zeitliche Reaktionen des verletzten Gewebes aufgedeckt werden, die in engem Zusammenhang mit den verschiedenen Heilungsphasen stehen. Darüber hinaus werden neuartige Kontrastmittel, welche speziell für multimodale Mikroskopie entwickelt wurden, in Einzelzellexperimenten mit HyMPSOM getestet. Hierbei wird das Eisenspeicherprotein Ferritin zur Akkumulation in Lysosomen geleitet, was sowohl multimodalen Kontrast als auch Einzelzellinteraktion in Form von photothermischer Ablation ermöglicht. Des

Weiteren werden bio-konjugierte C_{70}-Fullerene als biokompatible, multimodale Kontrastmittel charakterisiert, welche eine vielversprechende Plattform für photodynamische Therapie-Ansätze darstellen. Schlussendlich wird HyMPSOM genutzt, um mit Hilfe von CaSPA, einem Calcium-Sensor für optoakustische Messungen, das intrinsische Schlagen von Herz-Organoiden abzubilden.
Der letzte Teil präsentiert technische Erweiterungen des HyMPSOM-Systems, die mikroskopische, optoakustische Messungen und Bildgebung jenseits der üblichen Funktionsweisen erlauben. So werden zwei Ansätze für die Durchführung optoakustischer Mikroskopie in der Frequenz-Domäne ausgearbeitet, welche einerseits sinuskurvenartig modulierte Dauerstrichlaser und andererseits zur Emission von Pulsfolgen übersteuerte Laserdioden verwenden. Beide Technologien ermöglichen simultane Multi-Wellenlängen-Optoakustik-Mikroskopie indem die einzelnen Anregungswellenlängen jeweils auf eine Trägerfrequenz geladen werden und dessen dazugehörige optoakustische Signale nachträglich im Frequenzraum separiert werden. Darüber hinaus wird die Integration einer rein-optischen Optoakustik-Detektion im HyMPSOM-System beschrieben, welche basierend auf einem π-FBG-Sensor zur Erfassung von akustischen Wellen es erlaubt, dicke Proben wie Mausabdomen zu messen. Abschließend wird eine optoakustische Durchflusszytometrie dargestellt, die darauf basiert detektierte optoakustische Signale mit gleichzeitig aufgezeichneter Lichtstreuung zu referenzieren und die es ermöglicht, zwischen verschiedenen in *E. coli* Zellen exprimierten Chromophor-Proteinen zu unterscheiden.
Zusammenfassend stellt das in dieser Arbeit konzipierte und weiterentwickelte hybride Mikroskop HyMPSOM eine vielseitig anwendbare Plattform dar, welche die Einsatzfähigkeit fortschrittlichster multimodaler Mikroskopie für biologische und biomedizinische Forschung aufzeigt. Durch die Fusion verschiedenster, leistungsstarker Mikroskopie-Modalitäten in einem einzelnen Gerät zeichnet sich HyMPSOM mit einem facettenreichen und einzigartigen Potential aus, biologische Proben von Einzelzellen bis hin zu Kleintieren umfassend zu studieren, die Entwicklung innovativer Kontrastmittel voranzutreiben und Pionierarbeit zur Weiterentwicklung optoakustischer Technologie im mikroskopischen Bereich zu leisten.

ABSTRACT

Over the past decades, photonic (optical) microscopy has emerged as an indispensable tool for investigating the structural, molecular, and functional composition of biological and biomedical specimens on the microscale. Microscopic examinations have 'enlightened' our understanding about how life manifests itself below the resolution limit of the human eye, and have revolutionized a wide range of scientific fields, from basic biological research over translational medicine to everyday clinical practice. Recent advancements of photonic technology further broadened the overall capabilities of photonic microscopy by exploiting specific types of light-matter-interactions as the underlying contrast mechanism. However, each microscopy modality is still limited in the wealth of extracted information due to a predetermined set of detectable biological moieties, in the applicability to *in vivo* specimen due to potentially toxic labeling strategies, and in the imaging depth due to a low penetration of light into tissue. These limitations thereby impede both a comprehensive examination of a living biological specimen as well as the extraction of information of value regarding the organism's condition.
An auspicious approach to overcome the current limitations of photonic microscopy is the integration of several compatible imaging modalities into a single hybrid microscope. The trend of hybridizing various microscopy technologies is increasingly popular, as it allows researchers to precisely select modalities with imaging performances well suited for the scientific task. In examinations of specimens that range from single-cells and tissue slices to small model organisms, multi-photon microscopy and optoacoustic (photoacoustic) microscopy have exhibited highly promising capabilities. The former utilizes reading of non-linear optical phenomena induced by distinct biological compounds when encountered with light of high intensity. The latter relies on detecting acoustic waves generated by thermoelastic expansion when exciting molecule-specific optical absorption. Due to their functioning principles, both of these advanced microscopy technologies feature deep imaging, high spatial resolution, *in vivo* applicability, and potentially label-free employment. Thus, they are well suited for the study of specimens that are well established in biological and biomedical research, such as plated cells, organoids, zebrafishs, mice, and human histopathology slices.
This work is dedicated to the further advancement of hybrid multi-photon and optical-resolution optoacoustic microscopy for biological and biomedical investigations at the junction between development of the optical setup in terms of hard- and software,

utilization of the multi-modal imaging to study endogenous or newly designed contrast agents, and exploration of novel approaches to perform optoacoustics on the microscale. The first part introduces the hybrid multi-photon and spectral optical-resolution optoacoustic microscope (HyMPSOM), an optical system that merges seven modalities into a single device and facilitates simultaneous multi-modal investigations with subcellular resolution, deep imaging, fast acquisition, and high sensitivity. Its functioning principle is elaborated in detail, including a devised synchronization method based on a global trigger signal for concurrent operation of the modalities, as well as an imaging procedure based on a combined laser- and sample-scanning schemes for fast image capturing. Moreover, a novel approach is presented to characterize the optoacoustic total impulse response and to correct for it on the signal level using a spatial matched filter algorithm, which improves the signal-to-noise ratio and the axial resolution of optoacoustic microscopy significantly and, thus, further strengthens the optoacoustic imaging capabilities to complement the multi-photon modalities of HyMPSOM.
The second part concerns the utilization of the multi-contrast imaging capability of HyMPSOM to investigate biological and biomedical specimen as well as to explore novel designed multi-modal contrast agents. HyMPSOM is first characterized towards its ability to image *in vitro*, *in vivo*, and *ex situ* samples ranging from single cells and organoids over zebrafish larvae and mice to histopathological tissue slices. Next, HyMPSOM is employed to study the microstructural composition of human carotid atheroma specimen giving new insights into the interplay of key tissue moieties, such as the microvasculature and the connective tissue, involved in the disease progression of atherosclerosis. Transferring these imaging capabilities to living specimens, HyMPSOM is used to investigate the process of wound healing in mouse ears on the microscale and precisely uncovers spatio-temporal tissue responses denoting specific healing phases. Moreover, specifically developed contrast agents for multi-modal microscopy are studied with HyMPSOM on the single-cell level. First, the iron-carrier protein ferritin is mediated to accumulate in lysosomes for generating multi-modal contrast and for facilitating the interaction of HyMPSOM with single-cells via photothermal ablation. Second, bioconjugated C_{70}-fullerenes are testified to be bio-compatible and to give rise to various imaging modalities. They therefore constitute a highly promising platform for photodynamic therapy. Third, CaSPA, a calcium sensor for optoacoustics, has been shown to undergo signal changes in the presence of calcium ions, which allowed HyMPSOM to depict the intrinsic beating of cardiac organoids.
The final part presents technical extensions of HyMPSOM for performing microscopic optoacoustic sensing and imaging beyond the standard mode of operation. Two approaches to conducting optoacoustic microscopy in the frequency domain are elaborated; in one case, the microscope was equipped with sinusoidal-modulated continuous wave lasers, and in the other case with laserdiodes overdriven to generate bursts of pulses. Both techniques allow for simultaneous multi-wavelength optoacoustic mi-

croscopy by loading the excitation sources onto specific frequencies, whose associated optoacoustic signals are subsequently separated in the frequency space. Furthermore, an all-optical optoacoustic sensing setup is integrated into HyMPSOM based on detecting acoustic waves via a π-FBG sensor, which enabled the imaging of thick samples, such as the mouse abdomen in epi-configuration. Lastly, an optoacoustic flow cytometer is conceptualized, which, based on referencing the received optoacoustic signals to simultaneously recorded light-scattering, achieves in-flow detection and distinguishing of chromoproteins expressed in *E. coli* cells.
Conclusively, the herein devised and further developed hybrid microscope HyMPSOM evolved to a versatile platform evincing the operational capability of advanced multimodal microscopy for biological and biomedical research. By fusing several powerful microscopy modalities into a single device, HyMPSOM is characterized by a multifaceted and unique potential to comprehensively study specimens from single-cells to small animals, to exploit multi-modal contrast to gain new insights into the microscopic properties of living species, to assist the development of novel contrast agents, and to advance the field of optoacoustic technologies on the microscale.

Content

Abstract iii

Content xi

Listings xiv

List of figures . . . xiv
List of tables . . . xvi
List of abbreviations . . . xvii

1 Introduction 1

1.1 Motivation of microscopy . . . 2
1.1.1 Understanding the macro from the micro . . . 2
1.1.2 Insights into the microscopic world . . . 2
1.1.3 Importance of microscopy in biomedical research . . . 3
1.2 Outline of the thesis . . . 5
1.2.1 Goals and objectives . . . 5
1.2.2 Approaches and relevance . . . 6

2 Principles of photonic microscopy 9

2.1 Introduction . . . 10
2.2 Interaction of light with matter . . . 10
2.2.1 Elastic and inelastic scattering . . . 13
2.2.2 Absorption and excitation . . . 15
2.2.3 Photoacoustic and photothermal phenomena . . . 19
2.2.4 Fluorescence and phosphorescence . . . 20
2.2.5 Energy transfer, photochemistry, and photobleaching . . . 22
2.3 Contrast mechanisms . . . 23
2.3.1 Microscopic modalities . . . 23
2.3.2 Spectral fingerprint . . . 26
2.3.3 Chromophores and labels . . . 28
2.4 Characteristics of photonic microscopy . . . 31
2.4.1 Diffraction limit and point spread function . . . 31
2.4.2 Light penetration and imaging depth . . . 34
2.4.3 Image formation and field of view . . . 36
2.5 Conclusion and Outlook . . . 37

3 Theoretical considerations of HyMPSOM **39**
3.1 Introduction . . . 40
3.2 Background on multi-photon microscopy . . . 40
3.2.1 Non-linear optical signal generation . . . 40
3.2.2 Second and third harmonic generation . . . 42
3.2.3 Two- and three photon excitation fluorescence . . . 46
3.2.4 Multi-photon signal acquisition and processing . . . 51
3.3 Background on optical-resolution optoacoustic microscopy . . . 52
3.3.1 Optoacoustic signal generation . . . 52
3.3.2 Optical-resolution optoacoustics . . . 56
3.3.3 Optoacoustic signal acquisition . . . 57
3.3.4 Total impulse response and correction . . . 58
3.4 Background on microscopy image processing . . . 62
3.4.1 Contrast processing . . . 63
3.4.2 Spatial processing . . . 65
3.4.3 Harmonized-color depiction . . . 67
3.5 Conclusion and Outlook . . . 71

4 Development of HyMPSOM **73**
4.1 Introduction . . . 74
4.2 Materials and methods . . . 74
4.2.1 Multi-photon modalities . . . 76
4.2.2 Optical-resolution optoacoustic modality . . . 78
4.2.3 Merged experimental setup . . . 79
4.2.4 Synchronization and data acquisition . . . 83
4.2.5 Scanning procedure and data processing . . . 87
4.3 General characterization of HyMPSOM . . . 91
4.3.1 Sensitivity and signal-to-noise ratio . . . 91
4.3.2 Spatial resolution . . . 93
4.3.3 Field of view and co-registration . . . 96
4.3.4 Imaging speed . . . 99
4.4 Optoacoustic total impulse response (TIR) of HyMPSOM . . . 100
4.4.1 Surrogate optoacoustic point sources . . . 101
4.4.2 Experimental determination of the optoacoustic TIR . . . 103
4.4.3 Simulation of the optoacoustic TIR . . . 107
4.4.4 Optoacoustic TIR correction by spatial matched filtering . . . 110
4.5 Conclusion and Outlook . . . 114

5 Application of HyMPSOM **117**
5.1 Introduction . . . 118
5.2 Samples and experimental settings . . . 118
5.2.1 Single cells and organoids *in vitro* . . . 118
5.2.2 Zebrafish and mice *in vivo* . . . 120
5.2.3 Histopathological tissue slices *ex situ* . . . 121
5.3 Key imaging projects of HyMPSOM . . . 123
5.3.1 Superparamagnetic Ferritin for multi-modal imaging . . . 123
5.3.2 Multi-modal imaging of bioconjugated Fullerenes . . . 129
5.3.3 Calcium sensing by imaging CaSPA . . . 135
5.3.4 Label-free imaging of wound healing sequences . . . 140
5.3.5 Hybrid microscopy of human carotid atheroma . . . 151
5.4 Technical extensions of HyMPSOM . . . 158
5.4.1 Frequency-domain optoacoustic microscopy . . . 158
5.4.2 High-speed and frequency-comb optoacoustic microscopy . . . 166
5.4.3 All-optical optoacoustic microscopy . . . 175
5.4.4 Optoacoustic flow cytometry . . . 181
5.5 Conclusion and Outlook . . . 189

6 Conclusion and Outlook **191**
6.1 Conclusive summary . . . 192
6.2 General outlook . . . 195

Appendices **199**
Photographs of the optical setup . . . 200
MATLAB^{TM} scripts . . . 202
Simultaneous multi-modal data acquisition and hybrid scanning . . . 202
Optoacoustic data processing and TIR correction . . . 215
Simulation of Total Impulse Response . . . 224

Attachments **i**
Acknowledgments . . . ii
Published material and reprint permissions . . . vi
List of publications . . . vii

References **x**

Index **xxxiv**

List of figures

2.1 Schematic depiction of possible interactions of light with matter . . . 11
2.2 Schematic depiction of the energetic landscape of a molecule. 13
2.3 Jablonski diagram of elastic and inelastic scattering processes 14
2.4 Jablonski diagram of electronic, vibrational, and rotational excitation processes 16
2.5 Jablonski diagram of optoacoustic signal generation upon electronic, vibrational, and rotational excitations 19
2.6 Jablonski diagram of photoluminescence processes 20
2.7 Jablonski diagram of energy transfer and photochemistry 22
2.8 Spectral fingerprint of water regarding its optical absorption and refractive index across the electromagnetic spectrum 28
2.9 Spectral fingerprints of the most abundant tissue chromophores . . . 29
3.1 Schematic depiction of the OR-OAM imaging function unraveled to the underlying relevant convolution steps 60
3.2 Image processing steps performed on HyMPSOM data 63
3.3 Schematic depiction of the chromaticity diagram in projected CIE-XY space and the extracted HSV color wheel 69
3.4 Schematic depiction of the harmonic color schemes 70
4.1 Schematic depiction of the scanning unit of HyMPSOM 75
4.2 Schematic depiction of the MP sub-system of HyMPSOM 76
4.3 Schematic depiction of the OR-OAM sub-system of HyMPSOM . . . 79
4.4 Merged HyMPSOM system integrating MPM and OR-OAM sub-system 80
4.5 Spectral merge of the MPM and OR-OAM excitation and detections . 81
4.6 Control systems for *in vivo* measurements 82
4.7 Synchronization of HyMPSOM based on a global trigger signal 84
4.8 Continuous multi-record (CMR) data acquisition 86
4.9 Scanning schemes of HyMPSOM 88
4.10 Exemplary results at applying different scanning schemes of HyMPSOM 89
4.11 Reference specimens for sensitivity and SNR characterization of HyMPSOM 92
4.12 Resolution determination of HyMPSOM by imaging microspheres . . 95
4.13 FOV size determination in HyMPSOM 96
4.14 FOV distortion determination in HyMPSOM 97
4.15 Co-registration of the modalities using a suture phantom 98
4.16 Comparison of a gold nanolayer and a 1 µm black polystyrene microsphere as optoacoustic point sources 102
4.17 3D scanning approach of distributing SOAPs throughout the sensitivity field of the transducer 103

4.18 Dependence of raw OA A-lines and frequency contents on axial and lateral offsets . . . 104
4.19 Comparison of ultrasound transducer characterized by optoacoustic and ultrasound pulse-echo . . . 105
4.20 Experimental characterization of a spherically focused transducer . . 106
4.21 Simulation scheme for characterizing a spherically focused transducer 108
4.22 Simulated characterization of a spherically focused 50-MHz transducer 110
4.23 TIR correction of optoacoustic microscopy by spatial matched filter . 111
4.24 Image improvement by TIR correction . . . 112
5.1 Multi-modal microscopy of single-cells and organoids . . . 119
5.2 Multi-modal microscopy of a 7-day-old medaka larva . . . 120
5.3 Multi-modal microscopy of an *in vivo* mouse ear . . . 121
5.4 Multi-modal microscopy of histopathological tissue slices . . . 122
5.5 Principle of genetically-controlled and lysosomal entrapment of ferritin variants . . . 124
5.6 Genetically-controlled ferritin uptake and lysosomal trafficking . . . 126
5.7 Cell-specific photoablation based on lysosomal entrapped hFTH-Mag in Tim-2 positive cells . . . 127
5.8 Cell-specific photoablation based on lysosomal entrapped eFTH+L in Tim-2 positive cells . . . 128
5.9 Principle of lysosomal uptake of the of C_{70}@lysozyme . . . 130
5.10 Multi-modal contrast of pure C_{70}@lysozyme . . . 132
5.11 C_{70}@lysozyme uptake and lysosomal accumulation . . . 133
5.12 Co-localization of C_{70}@lysozyme in lysosomes . . . 134
5.13 Principle of the cell-permeable calcium sensor for optoacoustic imaging 136
5.14 Imaging of CaSPA responses in HEK cells upon Ca^{2+} stimulation . . 138
5.15 Imaging of the CaSPA signature in a beating cardiac organoid . . . 139
5.16 Longitudinal imaging of the wound healing process in mouse ears *in vivo* 145
5.17 Separate depiction of microscopy modalities of wound healing imaging 146
5.18 Spatio-temporal assessment of the wound healing process . . . 148
5.19 Coarse assessment and ROI selection of a human carotid atheroma . . 153
5.20 Multi-modal microscopy of an unstained human carotid atheroma slice at the shoulder region . . . 154
5.21 Multi-modal microscopy of an unstained human carotid atheroma slice at the cap region . . . 155
5.22 Multi-modal microscopy of an unstained human carotid atheroma slice at the necrotic core . . . 155
5.23 Histopathological images of human carotid atheromas based on staining 156
5.24 Schematic depiction of the FDOM sub-system of HyMPSOM . . . 160

5.25 Characterization of the FDOM system by imaging a suture phantom and an zebrafish eye *ex vivo* 162
5.26 Dual-wavelength FDOM and MPM microscopy of an mouse ear *in vivo* 163
5.27 Optoacoustic microcirculatory blood flow imaging via µDoppler-FDOM 164
5.28 Schematic depiction of the CWLD sub-system of HyMPSOM 168
5.29 Optical characterization of the overdriven CWLD for ALEX and FComb optoacoustic microscopy 171
5.30 Characterization of the imaging performance of overdriven CWLDs for ALEX and FComb optoacoustic microscopy 172
5.31 *In vivo* multiwavelength microscopy of circulating melanocytes in mouse ears 173
5.32 Schematic depiction of the all-optical optoacoustic microscope 177
5.33 Characterization of the π-FBG sensor head 179
5.34 Mouse *in vivo* measurements using the π-FBG sensor head 180
5.35 Schematic depiction of the OAFC system 183
5.36 Validation of detecting single transit events in OAFC 185
5.37 Characterization of in-flow signals 186
5.38 Signal distribution of in-flow single transit events of *E. coli* cells expressing optoacoustic labels 187
A.1 Optical setup of the HyMPSOM system 200
A.2 Arrangement for *in vivo* mouse measurements 201
A.3 Arrangement for optoacoustic flow cytometry measurements 201

List of tables

1 Determined spatial resolutions of the modalities implemented in HyMPSOM 95
2 Imaging capabilities of HyMPSOM 114
3 Quantitative assessment of analyzed wound healing hallmarks 149

List of abbreviations

1D, 2D, 3D, 4D	1-, 2-, 3-, 4-dimensional
1PE, 2PE, 3PE	Two-, three-photon excitation
1PEF, 2PEF, 3PEF	Two-, three-photon excitation fluorescence
a.u.	Arbitrary units
AFM	Atomic force microscopy
ALEX	Alternating laser excitation
ANSI	American national standard institute
APD	Avalanche photodiode
AR-OAM	Acoustic-resolution optoacoustic microscopy
AWG	Arbitrary waveform function generator
BF	Brightfield
CARS	Coherent anti-Stokes Raman scattering
CaSPA	Calcium-sensitive photoacoustic agent
CCD	Charge-coupled device
CHO	Chinese hamster ovarian
CIE	Commission internal d l'Eclairage
CMR	Continuous multi-record
CNP	Carbon nanoparticle
CW	Continuous wave
CWLD	Continuous-wave laser diode
DAPI	4',6-diamidino-2-phenylindole
DAQ	Data acquisition
DMEM	Dulbecco's modified eagle medium
DMSO	Dimethyl sulfoxide
DPBS	Dulbecco's phosphate-buffered saline
dpf	Days post fertilization
E. coli	*Escherichia coli*
EIR	Electric impulse response
EMCCD	Electron multiplying charge-coupled device
ESF	Edge-spread-function
FACS	Fluorescence-activated cell sorting
FComb	Frequency comb
FCS	Fluorescence correlation spectroscopy
FD	Frequency domain
FDOM	Frequency-domain optoacoustic microscopy
FFT	Fast Fourier transform
FOV	Field of view
FSR	Frequency-space-representation

FWHM	Full width at half maximum
galvo	Galvanometric
GFP	Green fluorescent protein
GNL	Gold nanolayer
H&E	Hematoxylin & Eosin
HBSS	Hank's balanced salt solution
HEK	Human embryonic kidney
HeLa	Human cervical cancer
HOMO	Highest occupied molecular orbital
HSV	Hue-saturation-value
HyMPSOM	Hybrid multi-photon and spectral optoacoustic microscope
IR	Infrared
LD	Laser diode
LDL	Low-density lipoprotein
LED	Light emitting diode
LS	Light scattering
LSF	Line-spread-function
LUMO	Lowest unoccupied molecular orbital
µB	Microbeads
µDoppler	Micro-Doppler
MAP	Maximum amplitude projection
MFP	Mean free path
MIP	Maximum intensity projection
MP	Multi-photon
MPE	Maximum permitted exposure
MPM	Multi-photon microscopy
MRI	Magnetic resonance imaging
NA	Numerical aperture
NADP(H)	Nicotinamide adenine dinucleotide phosphate
NIR	Near-infrared
NLO	Non-linear-optical
NMR	Nuclear magnetic resonance
OA	Optoacoustic
OAFC	Optoacoustic flow cytometry
OAI	Optoacoustic imaging
OAM	Optoacoustic microscopy
OAT	Optoacoustic tomography
OCT	Optical coherence tomography
OR-OAM	Optical-resolution optoacoustic microscopy
π-FBG	π-phase-shifted fiber Bragg grating

PC	Personal computer
PCC	Pearson correlation coefficient
PE	Pulse-echo
PLD	Pulsed laser diode
PMT	Photomultiplier tube
PSF	Point spread function
PSR	Picro-Sirius Red
RBC	Red blood cell
RGB	Red-green-blue
ROC	Receiver-operator-characteristics
ROI	Region of interest
ROS	Reactive oxygen species
SHG	Second harmonic generation
SIR	Spatial impulse response
SMF	Spatial matched filter
SNR	Signal-to-noise-ratio
SOAP	Surrogate optoacoustic point sources
SRS	Stimulated Raman scattering
TBWP	Time-bandwidth product
TD	Time domain
TDOM	Time-domain optoacoustic microscopy
THG	Third harmonic generation
TIR	Total impulse response
TMFP	Transport mean free path
ToF	Time of flight
TSR	Time-space-representation
TTL	Transistor–transistor logic
UV	Ultraviolet
VIS	Visible
WD	Working distance
W.l.o.g.	Without loss of generality

1 | Introduction

This chapter provides a brief introduction into the field of microscopy and the associated inducement of conducting and improving microscopy technology for biological and biomedical research (see Section 1.1). Further, the objectives and approaches of this thesis are defined (see Section 1.2).

1.1 Motivation of microscopy

In the words of Edward O. Wilson, one of the grandfathers of biodiversity: *"Science, to put its warrant as concisely as possible, is the organized, systematic enterprise that gathers knowledge about the world and condenses the knowledge into testable laws and principles."* [1]. This universal description of science illustrates that it is of fundamental interest to understand man's surrounding, reveal its basic concepts of function, and contrive detailed explanatory approaches. The underlying curiosity is basis for the rise of a variety of flavors of science ranging from physics over chemistry towards biology and medicine. Once clearly separated, the scientific fields began to increasingly interact with each other, which led to a nowadays unified set of cross-disciplinary scientific approaches and tools to uncover the core of nature. Thus, methods that emerged from physics influenced the field of chemistry as well as biology and vice versa. [2–7]

1.1.1 Understanding the macro from the micro

To gather knowledge of a given issue scientifically, an essential approach is to divide the targeted problem into its building blocks, examine them on a much smaller scale, and subsequently draw conclusions for the problem on a bigger scale. This scale ladder is of special importance not only for the overall direction of the scientific concept, but also for the present thesis. The relevant scales for the problem of interest depend on the problem itself. Whereas e.g. astrophysics incorporates subatomic theories to unravel scale-wise massive phenomena such as the origin of the universe or the formation of black holes, chemistry makes use of calculation models derived from quantum-mechanical physics in order to explain the behavior of molecular reactions, and medicine is looking for clinical manifestations in studying the underlying biology down to the cellular or sub-cellular level. For the latter, it is of special importance to note that atoms or molecules do not constitute the smallest unit of life as they do not possess the basic abilities attributed to life. In other words, an atom or a molecule are per se neither diseased or healthy, although a molecule's concentration within a respective compartment of a bigger organisms is crucial for its pathological conditions. However, because the entirety of living organisms is composed of cells as the elementary building blocks, it is an ubiquitous approach to study them in detail in order to draw conclusions on the condition of the organism investigated. [5, 6, 8, 9]

1.1.2 Insights into the microscopic world

The cellular level of biology is in general defined as the world of single-cells, their behavior, and their interaction. As most of the relevant cells are on the scale of $\sim$10 µm and, thus, cannot be comprehensively grasped by the human eye, powerful tools for microscopic investigation are required. Robert Hooke, one of the founders

of microscopy, described his first look through a microscope as *"[...] a new visible world discovered to the understanding"* [10]. This world of cells is so vastly complex and rich of information, that in recent decades a huge variety of novel approaches have been developed in order to study life on the microscale. Starting with the first microscopes in the 17. century, the simple but profound idea of looking at life smaller than the human perception is even nowadays a common standard technique to explore the cellular regime. [7, 11–16]
The advancements of microscopic techniques enabled since then a flood of information about life below the resolution limit of human eyes. Today, we know that all cells can be assigned to either prokaryotic (without a nucleus) or eukaryotic cells (with a nucleus). Based on their sub-cellular characteristics, we can subdivide prokaryotes into bacteria or archaea, and eukaryotes into protists, fungi, plants, and animal cells. Furthermore, we know the basic sub-cellular components as well as their role for the cells such as the cell membrane, cytoskeleton, nucleus, endoplasmatic reticulum, ribosomes, vacuoles, flagella, and so on. Investigations of the area even one level below allowed to unravel the central molecular composition and their interplay. Although the complexity at this level overwhelms an all-embracing understanding, almost all molecules relevant to enabling life can be classified into proteins, nucleic acids, carbohydrates, and lipids. These smallest and most basic building blocks of life, which are suitably referred to as the *molecules of life*, design life by encoding genetic information, by modeling structural organization, and by performing essential functionalities. [7, 11–16]

1.1.3 Importance of microscopy in biomedical research

Understanding the functions and malfunctions on the cellular and sub-cellular level is key not only to get insights into the condition of the organism under investigation but also represents the most promising approach to provide solutions for enhancing the organism's life quality. In this regard, most pathological states of any living being can be assigned to a disturbed composition of the *molecules of life*. Precise exploration of such disturbances lays the ground for adapting accurately tailored and personalized treatments, which generally aims to target the culprit of the given ailment instead of merely treating the symptoms. To evaluate the attained therapeutic or medical effect, cutting-edge techniques operating on the microscale emerged in recent years. [6, 13, 14, 16]
In general, the field of microscopy is subdivided into three main sectors depending on their principle of function and their associated contrast mechanism. (1) Electron microscopy is based on reading the electron scattering properties thereby resolving the architecture of cells known as the ultrastructure. (2) Scanning probe microscopy rasters a physical probe across the specimen to sense its surface structure. (3) Photonic (optical) microscopy takes advantage of the interaction between light and matter, which is

unique for a given combination of electromagnetic radiation and molecular properties and, thus, awards optical imaging an intrinsic molecular contrast. Whereas the first two sectors require intensive sample treatment before imaging, preventing by that their application to living specimens, using light to generate contrast allows photonic microscopy to study biological material *in vivo* finally featuring it with topmost suitability for biomedical research. [14, 16]

The underlying ambition of photonic microscopy in biomedical research is its versatile application to living specimens ranging from single-cells over animal models up to humans covering by that the entire range known as translational medicine. Insight into the sub-cellular regime discovered *in vitro* or *ex situ* can then be used to design appropriate studies on *in vivo* model organisms, which finally facilitates to improve *in situ* measures in humans. Along that arc of linking laboratory experiments to clinical practice, optical microscopy strives to monitor the entire translational process as comprehensively as possible. The richness and complexity of information encoding the condition of each translational step renders the need to assess a large multitude of properties. In this regard, a microscopic technique can address a predetermined set of information, which might be specified by contrast agents to reduce the dimensionality of the assessment problem to certain preselected questions. Moreover, combining independent microscopy techniques represents a highly promising and emerging approach to investigate the respective specimens with more comprehensive ascertainments than their stand-alone counterparts. Since the desired specimens scale from single-cells up to small model organisms and potentially human tissue, optical microscopy modalities are of highest interested when they possess top-notch imaging capabilities regarding sensitivity and specificity, imaging depth and speed, unneccesity of labeling, and harmlessness to biological tissue. This concept of a multi-modal microscope ultimately constitutes an auspicious strategy to conquer limitations of current microscopy systems and potentially evolves to a versatile and indispensable tool for modern biomedical research. [13, 15, 17–20]

1.2 Outline of the thesis

1.2.1 Goals and objectives

This thesis concerns the further development of a hybrid multi-modal microscope for studies performed on specimens typical for basic biological research, translational medicine, as well as clinical practice. To conceptualize the design of a multi-modal imaging technique, such as a hybrid microscope, a thoughtful choice is required to select integratable modalities fulfilling certain criteria. These criteria can be in general classified in three categories, which thereby outline both the conducted work as well as this thesis: (1) Complementary and preferably label-free contrast mechanisms, (2) compatible optical components, and (3) similar imaging properties. [13, 17, 18]
Regarding **complementary contrast mechanisms**, a huge variety of microscopic techniques are in general compatible with each other. However, the contrasts should complement each other in terms of minimizing information redundancy as well as maximizing the similarity of the regime of information. In other words, the integrated microscopic modalities should have only marginal overlap in their extractable information of the tissue but should be able to present similar type of information. Further, molecular contrast is of greatest interest for studying biological tissue in the framework of basic research of developmental biology or translational medicine. Hence, the modalities of choice should be molecule-specific and give insights into the local concentration distribution of specific molecules.
In terms of the **optical components** required for equipping the corresponding microscopic modalities, a high compatibility is desired. As the modalities are ideally operated simultaneously, cross-influences or mutual restrictions should be avoided. The modalities of choice have therefore either to extract the information of the identical excitation source (i.e. the same laser) or have to be separated either spectrally (i.e. different wavelength ranges) or temporally (i.e. time- or frequency-wise distinction of operation).
Lastly, the **imaging properties** have to match regarding penetration depth, speed, and spatial resolution. In order to have a fully complementary hybrid microscope, all modalities should be able to extract their respective information throughout the identical volume imaged at a temporal and spatial resolution being on the same order of magnitude. In this regard, samples ranging from single-cells up to small animal models are of highest interest for biological research and translational medicine. Hence, the desired hybrid microscope should be characterized by a spatial resolution below the size of a single-cell, i.e. $\sim$10 µm, but able to study entire zebrafishs or mouse ears, which are in the range of $\sim$0.5 mm, and by imaging times adaptable to the targeted issue, which typically span from sub-seconds to minutes.

Essentially, the proposed hybrid microscope originates from a previous version as comprehensively described in [21–23]. However, the state of the system in its original form prevented an extensive application to biological and biomedical specimens as it was limited regarding the above mentioned criteria. The aim of the thesis presented here can therefore be formulated in five essential objectives:

1 Elaborate and equalize the imaging capabilities of the equipped microscopy modalities regarding speed, resolution, and sensitivity.

2 Achieve complementary multi-modal microscopy in terms of simultaneous and spatially co-registered imaging on the microscale.

3 Facilitate and evaluate the development of novel multi-modal contrast agents for multi-modal microscopy.

4 Explore the applicability and performance of multi-modal microscopy for biological and biomedical specimens within the scope of translational research.

5 Pioneer on advanced operating principles to conduct optoacoustic microscopy beyond its standard way of execution.

1.2.2 Approaches and relevance

Along the lines of the five above mentioned objectives, this thesis first explores microscopic imaging modalities starting from the basic principles of light-matter-interaction as the underlying contrast phenomena of optical imaging (see **Section 2**). Investigating the associated physical properties of such interaction outlines the expected imaging capabilities, which therefore facilitates a profound valuation of their integrability to a hybrid microscope.
Next, a comprehensive elaboration of compatible and complementary modalities is given, which evinced multi-photon and optoacoustic microscopy to be best suited for their integration into a single hybrid microscope to study biological and biomedical specimens (see **Section 3**). These modalities share similar characteristics based on the criteria of (1) complementary contrast mechanisms, (2) compatible optical components, and (3) similar imaging properties. Hence, they are ideally suited to operate in parallel and perfectly complement each other regarding their corresponding information content extracted.
Subsequently, this thesis will explain in detail the herein developed hybrid microscope, which integrates two custom-built sub-systems, namely a multi-photon modality part and an optical-resolution optoacoustic modality part, into a single optical setup (see **Section 4**). The overall aim of the hybrid multi-photon and spectral optical-resolution optoacoustic microscope (HyMPSOM) is the joint examination of biological samples in

a fully co-registered way. This means, all modalities are desired to operate in an aligned fashion, both temporally (i.e. simultaneous operation of the equipped modalities) and spatially (i.e. across the identical area or volume imaged). By that, HyMPSOM should enable the extraction of significantly more comprehensive information of the investigated sample compared to standard brightfield microscopy as well as their corresponding stand-alone versions of just applying one single modality. Further, the selected modalities should potentially be performed without administering contrast agents to the specimen which, thus, would facilitate a straight-forward translation from *in vitro* specimens to *in vivo* animal models and potentially to human applications.
Finally, this thesis will summarize selected projects conducted on HyMPSOM and showcase, how the system targets to address the bridging of basic biological research with clinical practice (see **Section 5**). In this regard, HyMPSOM opts to push the application boundaries of multi-modal microscopy techniques. HyMPSOM is therefore deployed to carry out single-cell observations using cell lines well established in the biological field, clinical research, small model organism studies being routine in the field of translational medicine, as well as investigations of tissue samples standard for clinical practice. Further, technical extensions of the HyMPSOM framework are elaborated to perform optoacoustic sensing and imaging on the microscale beyond the standard way of operation. In this regard, approaches for frequency-domain optoacoustic microscopy, for all-optical optoacoustic microscopy, and for optoacoustic flow cytometry are implemented and characterized.

2 Principles of photonic microscopy

This chapter considers the general background of photonic microscopy and elaborates the underlying physical processes taking place when light encounters matter (see Section 2.2). Such processes are the fundamental basis of all photonic microscopic modalities and can be roughly categorized based on the way of interaction in scattering phenomena (see Section 2.2.1) and optical absorption (see Section 2.2.2). As the light-matter-interaction can potentially deposit energy into the specimen, possible ways of subsequently releasing the energy enables further classification of the processes into radiationless de-excitations (see Section 2.2.3), radiative de-excitations (see Section 2.2.4), and optically induced chemical reactions and other forms of energy transfer (see Section 2.2.5). Next, the photonic processes are linked to their respective contrast mechanisms, especially at investigating biological specimens. In this regard it is outlined, how the processes are utilized as contrast mechanisms for microscopic modalities (see Section 2.3.1), how these modalities depend on the optical spectrum (see Section 2.3.2), and how in this way the modalities can specifically sense certain chromophores or contrast labels (see Section 2.3.3). Finally, the typical and modality-independent characteristics of photonic microscopy are described regarding the spatial resolution (see Section 2.4.1), the imagable volume (see Section 2.4.2), and possible ways of image formation (see Section 2.4.3).

2.1 Introduction

The basic principle of all photonic microscopy modalities is the illumination of a specimen under investigation with light and infer the thereby induced physical phenomena. To explore the achieved contrast as a microscopic modality, the basic working principle of the modality is crucial as it determines both the information extractable from the specimen as well as the imaging characteristics. The following chapters will concern the relevant steps from a more general point of view starting from the interaction of light with matter, over possibilities of energy deposition, and its subsequent release[1]. The associated theoretical physical considerations relevant for the equipped modalities in HyMPSOM is elaborated in detail in Section 3.

2.2 Interaction of light with matter

In general, when electromagnetic radiation, i.e. the fundamental description of light, encounters matter, the time-varying electromagnetic field interacts with the atoms of the matter. The respective interactions strongly depend on the properties of both the light in terms of energy, duration of illumination, and incident angle, and the structural and chemical composition of the matter. *W.l.o.g.*, possible interactions can be categorized in six essential physical phenomena based on their impact on the incident photon radiation (see Fig. 2.1).
First, the irradiated photons can transmit through the medium without any interaction. Second, the light can change its direction due to a variation of the refractive index of the surrounding. At more perpendicular angles of incidence, the light alters its way of propagation through the medium by refraction. Third, at more oblique angles, the light could possibly undergo total or partial reflection. Fourth, at encountering objects of sizes in the range of the wavelength, light can be bent by diffraction. Fifth, compounds like particles, molecules, or structural features of the medium can induce scattering of the light, which alters again the direction of light propagation. Such scattering processes can be either elastic, meaning the photon energy is conserved, or inelastic, meaning the photon energy is partially transferred to the medium[2]. Sixth, the entire photon energy is deposited to the medium by an absorption process, which thereby excites the absorbing entity in its energetic level.
The induced phenomena strongly depend on the properties of the incident light and the energetic landscape of the irradiated medium. *W.l.o.g.*, the former is typically described when viewed as waves by its wavelength λ (nm) or frequency ν (Hz) and speed c (m/s), and when viewed as photons by its carried energy $E = hc/\lambda$ (J) with h being

[1] The following chapters are based on [12, 16, 23–35].
[2] The phenomena of refraction, reflection, diffraction, and scattering share a similar principle of superimposing irradiated and eradiated electromagnetic waves in the close vicinity of the scatterers. Hence, the following theoretical considerations concern only scattering processes.

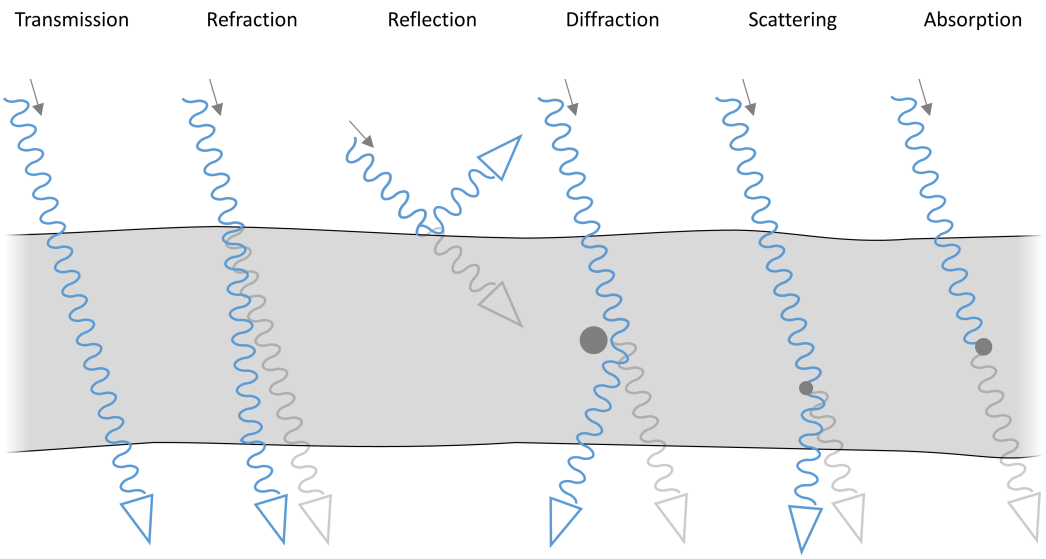

Figure 2.1: Schematic depiction of possible interactions of light with matter. (Adapted from [23])

the Planck's constant or $E = 1.24/\lambda(\mu m)$ (eV). The latter is defined on the atomic and molecular level by the molecular structure and its composition of nucleus and electrons and is quantized to discrete so-called energy levels or eigenstates. Such levels describe electronic, vibrational, and rotational states of the atom or molecule in distinct wave functions. The electronic states are determined by the orbital construction and its occupation with electrons and are characterized by energies in the range of ∼eV. A quantum-mechanical description leads in this regard the potential energy to follow an anharmonic oscillator, i.e. Morse potential (see Fig. 2.2a), being a function of the nuclear coordinate as:

$$V(r) = D_e \cdot (1 - e^{-\beta(r-r_e)})^2, \tag{2.1}$$

where V denotes the Morse potential energy, r and r_e the nuclear coordinate at presence and at equilibrium, respectively, and D_e the well depth between the ground vibrational mode ν_0 and the dissociation energy D_0. The width of the potential is defined by $\beta = \tilde{v_0}\sqrt{2\pi c\mu/D_e h}$ with $\tilde{v_0}$ as the wavenumber describing the ground state vibration, c as the speed of light, μ as the reduced mass, and h the Planck's constant. Vibrational and rotational states describe movements of the nucleus, the whole atom, chemical bonds, or even the entire molecule and exhibit distinct wavefunctions within the electronic states (see Fig. 2.2a). Vibrational states possess energies following:

$$E(\nu) = hv_0 \cdot (\nu + 1/2) - hv_0\chi_e(\nu + 1/2)^2, \tag{2.2}$$

with ν denoting the vibrational state and χ_e the anharmonicity constant. The vibrational modes are determined by the molecular structure of the absorber and include stretching and bending of the molecular backbone in a symmetric or asymmetric manner. By that, a molecule of n atoms possesses $3n-6$ vibrational modes[3], $3n-5$ in the case of a linear molecule. Furthermore, each vibrational state is compartmentalized to so-called rovibrational levels following:

$$E(J) = B \cdot J(J+1), \tag{2.3}$$

with B being the rotational constant, which is defined as $B = \hbar/4\pi c\mu r_v^2$, and J denoting the rotational state[4].
Transitions among these states are the quantum-mechanical basis of light-matter-interactions and are favored, when the involved wave functions exhibit significant overlap (see black arrow in Fig. 2.2a as $S_0;\nu_0 \rightarrow S_1;\nu_2$). As schematically depicted, this concept leads to selection rules of transitions being $\Delta\nu = \pm1, \pm2, \pm3...$, at which $\Delta\nu = \pm1$ is the ground tone and $\Delta\nu = \pm2, \pm3, ...$ are referred to as overtones. This fundamental concept is known as the Franck-Condon principle defining allowed and prohibited transitions, which thereby determines the absorption and emission spectrum of a molecule. The energetic landscape and facilitated transitions are typically represented in a simplified form, which is known as the Jablonski diagram (see Fig. 2.2b). In here, each column represents a specific spin multiplicity, i.e. singlet ($S_{0,1,2,...}$) or triplet ($T_{1,2,..}$). Horizontal lines constitute energetic levels which can be either electronic (bold, solid), vibrational (thin, solid), rotational (dashed), or virtual (dotted). The energy difference and, thus, the required energy to be deposited or released for the corresponding transition is in the range of ∼eV for electronic transitions, ∼meV for vibrational transitions, and ∼µeV for rotational transitions (see Fig. 2.2a). Whereas electronic, vibrational, and rotational states constitute stable states with lifetimes larger than $\sim10^{-9}$s, virtual states typically are located in between stable states and possess lifetimes in the range of $\sim10^{-15}$s (see Fig. 2.2b). Arrows depict possible ways of energy transfers between the levels, which can involve radiative processes, such as absorption, fluorescence, and phosphorescence, or non-radiative processes, such as vibrational relaxations, spin conversions, or photochemical reactions.

[3] A n-atom molecule has $3n$ degrees of freedom, 6 of which are rotations and translations and, thus, do not constitute a vibrational mode.
[4] r_v denotes the average nuclear distance for a given vibrational mode.

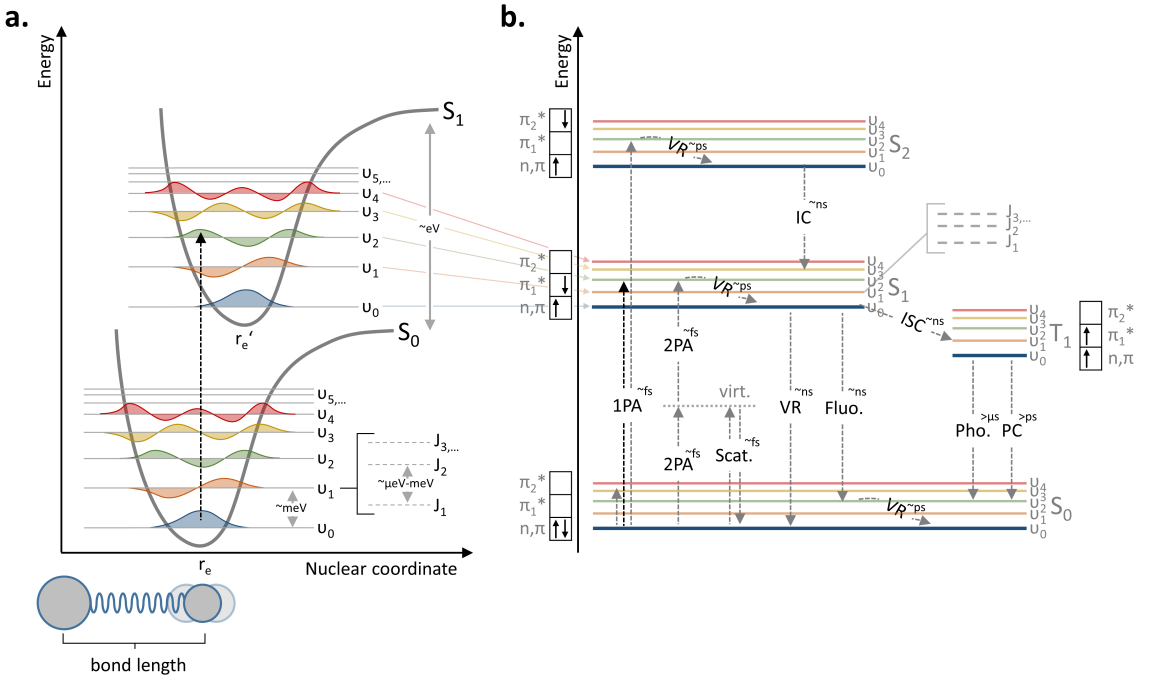

Figure 2.2: Schematic depiction of the energetic landscape of a molecule. **(a)** The quantum mechanical Morse potential as a function of the nuclear coordinate includes distinct waveforms of intrinsic energetic states of a di-atomic bond or molecule. Typically, energy differences between electronic (S_i), vibrational (ν_i), or rotational (J_i) states are indicated. **(b)** Simplified depiction of (a) as a Jablonski diagram with possible mechanisms of energy transitions between the states, typically associated durations, and corresponding settings of spin configuration. An exemplary selected allowed transition (1PA: $S_0; \nu_0 \rightarrow S_1; \nu_2$) is indicated as a black arrow in (a) and (b). Abbreviations: 1PA: one-photon absorption; 2PA: two-photon absorption; Fluo.: fluorescence; IC: internal conversion; ISC: intersystem crossing; n&π: molecular orbitals ($*$ indicates excited states); PC: photochemistry; Pho.: phosphorescence; r: rotational level; r^e: nuclear distance at equilibrium; S: Singlet; Scat.: scattering; T: Triplet; VR: vibrational relaxation

2.2.1 Elastic and inelastic scattering

One apparent phenomenon occurring by exposing matter to light is scattering. Scattering can be either elastic, by which the entire energy of the photon is conserved, or inelastic, by which the energy of the photon is increased or decreased. Scattering processes involve the elevation of an electron to a virtual state and its subsequent reversion (see Fig. 2.3). In here, the virtual states do not constitute stationary solutions of the time-dependent Schrödinger equation and, thus, are not specified by a distinct energy. Further, their lifetime is determined by the uncertainty principle.

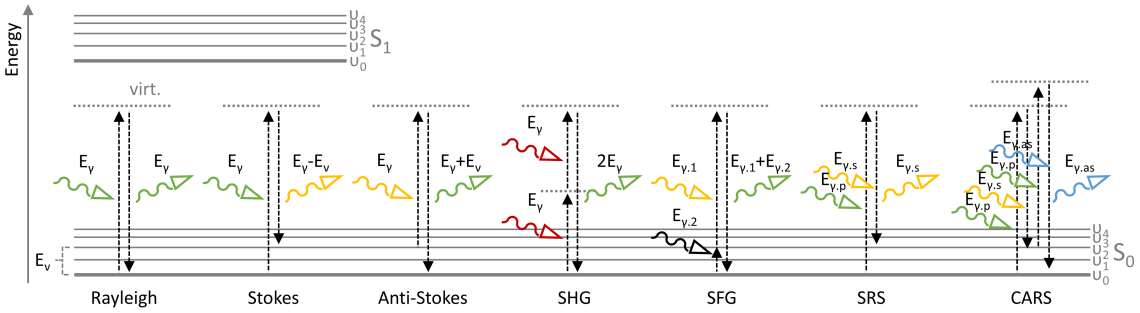

Figure 2.3: Jablonski diagram of elastic and inelastic scattering processes.

Single-photon scattering

Scattering processes which start and end at the identical energy level, i.e. conserving the irradiated photon energy E_γ^{in} or also referred to as elastic, are termed Rayleigh scattering (see Fig. 2.3). Rayleigh scattering typically occurs at objects much smaller than the wavelength and is oriented isotropically in all directions. The associated cross section $\sigma_{Rayleigh}$ strongly depends on the wavelength λ of the incident light:

$$\sigma_{Rayleigh} \propto \frac{1}{\lambda^4}. \tag{2.4}$$

Processes ending at a higher energy level are termed Stokes scattering (see Fig. 2.3), which thereby excites vibrational modes at energies E_ν of the molecule corresponding to the energy difference between the irradiated and eradiated photon $\Delta E_\gamma^{in/out} = E_\nu$. The reversed situation of ending at a lower energy level is termed anti-Stokes scattering (see Fig. 2.3), which in simple words de-excites vibrational modes. These two inelastic scattering processes are collectively known as Raman transitions, which are characterized by a cross section several orders of magnitude weaker than the one of Rayleigh scattering. Furthermore, Raman transitions require the vibrational mode to change the polarizability of the molecule.

Multi-photon scattering

Furthermore, scattering can involve more than one photon of identical or different energy. On the one hand, harmonic generations (e.g. second or third harmonic generation (SHG or THG)) constitute energy conserving and, thus, elastic transitions with $E_\gamma^{out} = x \cdot E_\gamma^{in}$ with x denoting the integer harmonic number (see Fig. 2.3). Harmonic generations require phase-matching and, depending on the number of involved photons, birefringence to induce double refraction. On the other hand, sum-/difference-

frequency generation (SFG or DFG) combine, similar to harmonic generation, several photons (typically two) in an energy conserving process. Their energies differ so that one is adjusted to a vibrational mode of the molecule, which leads to $E_\gamma^{out} = E_\gamma^{in} + E_\nu$ (see Fig. 2.3). Furthermore, stimulated and coherent Raman processes (e.g. SRS or CARS), utilize two or three irradiated photons to induce the Raman scattering process (see Fig. 2.3). Due to the involved vibrational state, the energy ratio $\Delta E_\gamma^{in1/in2} = E_\nu$ of the irradiated wavelengths change after scattering[5].

In addition to scattering in the Rayleigh regime induced by diminutive objects, light can also interact in form of Mie scattering at objects of size similar or significantly larger than the wavelength. In this case, the cross section depends only marginally on the wavelength and the scattering occurs predominantly in the forward direction. Regarding biological tissue, the most abundant scattering entities are cells and subcellular compartments such as nuclei or organelles. Due to their size, Mie scattering is the dominating scattering mechanism by applying visible illumination. However, biological tissue also contains scatterers of much smaller size such as collagen fibers or cell membranes, which thereby induce various forms of Rayleigh scattering. Such phenomena of specific Rayleigh scattering can be utilized in dedicated microscopic modalities. Relevant principles of employing energy conserving multi-photon scattering processes in HyMPSOM are explained in detail in Section 3.2.2 .

2.2.2 Absorption and excitation

Another prominent process happening upon illuminating matter with light is absorption, which is for most of the optical techniques the underlying principle of contrast generation (see Fig. 2.4 for energies below few eV). In this context, absorption represents the uptake of the energy of incident photons. Depending on the properties of the matter as well as the irradiated light, different absorption processes can be distinguished, each of which is characteristic for a distinct spectral or energetic range.

γ, X-ray, and UV-C/B spectral range[6]

Incident photons of energies beyond $\sim$1 MeV, which is approximately twice the resting energy of the electron ($2 \cdot m_e \cdot c^2 \approx 1022$ keV), can potentially convert into an electron-positron pair emitted under 180° via pair production. The associated cross section of this process can be expressed as:

[5] SRS is based on two irradiated photons (i.e. pump- and Stokes-beam) and stimulates Stokes scattering. CARS uses three irradiated photons (i.e. pump-, Stokes-, and anti-Stokes-beam) and stimulates a Stokes-anti-Stokes scattering process, which is based on elevating the electron twice to a virtual state.

[6] These processes typically interact with electrons other than in the valence band and are therefore not depicted in Fig. 2.4.

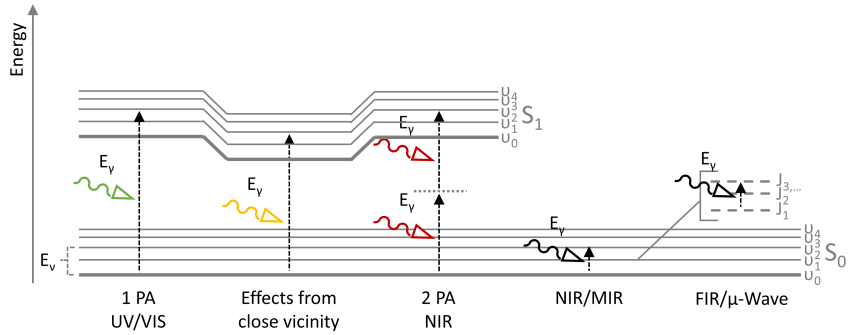

Figure 2.4: Jablonski diagram of electronic, vibrational, and rotational excitation processes.

$$\sigma_{pair} \propto Z^2 \cdot ln(E_\gamma), \tag{2.5}$$

with Z as the atomic number, $E_\gamma = h \cdot \nu$ as the photon energy, h the Planck's constant, and ν the frequency. At energies between ∼1 MeV and ∼100 keV, irradiated photons can release weakly bound particles via Compton scattering being an inelastic scattering process[7]. Compton scattering leads to a modification of the propagation direction and wavelength of the incident photon as well as the ionization of the targeted atom with a corresponding cross section of:

$$\sigma_{compt} \propto \frac{1}{E_\gamma}. \tag{2.6}$$

The absorption mechanism occurring between ∼100 keV and ∼10 eV of photon energy is primarily via the photoelectric effect. Similar to Compton scattering, this process induces the ejection of a bound electron by depositing the full photon energy. The photoelectric effect requires thereby photon energies higher than the binding energy of the electron and is described by a cross section of:

$$\sigma_{photoel.} \propto \frac{Z^2}{E_\gamma^3}. \tag{2.7}$$

[7] This process does not constitute an actual absorption process. However, it is conventionally mentioned along with pair production due to the shared or similar range of photon energy.

UV-A and VIS spectral range

In the range between few eV and ∼1 eV of photon energy, the predominant photon absorption mechanism is the elevation of an electron to an electronic excited state (see Fig. 2.4). As mentioned previously, in this case the energetic levels are quantized and predetermined by the orbital construction of the atom or molecule. In the case of molecules as the primary addressed targets in imaging, the transition typically occurs from the highest occupied molecular orbital (HOMO) in the ground singlet state S_0 to the lowest unoccupied molecular orbital (LUMO) of the first excited singlet state S_1(see spin configuration in Fig. 2.2b)[8]. The required energy to induce the elevation of the electron depends on the energetic properties of the absorbing molecule. In general, the more the electron is de-localized within the molecule in form of e.g. elongated π-electron conjugations, the lower the energy difference between HOMO and LUMO. Furthermore, the vicinity of the targeted molecular bond occupied by the electron can impact the energy of the bond itself (see Fig. 2.4). Such influences can be achieved by neighboring functional groups of the molecule in form of the mesomeric effect (i.e. ±M-effect: electron-releasing or -withdrawing impact of an unsaturated functional group elongating the de-localized electron conjugation) or the inductive effect (i.e. ±I-effect: electron-pushing or -pulling impact of the involved atoms due to their electronegativity), or the solvent in form of the solvatochromatic effect (i.e. batho-/hypsochromic shift: de- or stabilization of the electronic excited state; and hyper-/hypochromic shift: increasing/decreasing the intensity of the transition).
To induce the transfer of an electron from one state to another, the delivered energy carried by the incident photon has to exactly match the energy difference between the states, i.e. the energetic difference between HOMO and LUMO. In here, the Franck-Condon principle asserts the selection rules of possible transitions based on the overlap of the underlying wave functions of these states. Based on that, the elevation of the electron does hardly ever occurs to the lowest vibrational level of the excited state but targets higher vibrational levels (see Fig. 2.2a). As molecules typically occupy the electronic ground state S_0 at room temperature, the above mentioned considerations explain favored transitions to a vibrational level ν_i higher than the vibrational ground level at $i = 0$ within the electronic excited state S_1. Special cases such as excited state absorptions (i.e. $S_1 \rightarrow S_2$) or higher-state absorptions (i.e. $S_0 \rightarrow S_2$) are disregarding here due to their rare occurrences, especially for biological imaging techniques as they require high photon energy potentially harming living tissue. The corresponding cross section of such one-photon excitation (1PE) can be expressed as:

[8] Special cases of optical absorption to higher electronic excited states (e.g. Soret-band of hemoglobin) are disregarded in this context due to their rare occasions.

$$\sigma_{1PE} \propto \mu_a \cdot E_\gamma, \tag{2.8}$$

which proportionally depends on the underlying absorption coefficient μ_a. In analogy to multi-photon scattering, the required energy for elevating an electron among electronic states can be delivered by more than one photon impinging simultaneously (see Fig. 2.4). Such multi-photon absorption processes, typically up to maximum three involved photons, are also based on virtual states, which requires the arrival of the involved photons to happen within the lifetime of the virtual state (typically in the range of $\sim 10^{-15}$s). In first approximation, the surmountable energy difference and, thus, the achievable transition by multi-photon absorption requires n photons of energies at the n-th fraction of the corresponding one-photon absorption and, by that, twice the wavelength[9]. However, the associated cross section is defined by a dedicated n-photon absorption coefficient as[10]:

$$\sigma_{nPE} \propto \mu_a^{nPE} \cdot E_\gamma^n, \tag{2.9}$$

Near- and mid-IR spectral range

Photon energies below ∼1 eV are not sufficient to elevate an electron into electronic excited states. However, they can be absorbed by molecules and induce vibrational movements (see Fig. 2.4). In contrast to Raman transitions as explained above, these vibrational modes are directly excited by infrared light. Although the vibrational spectrum of a molecule examined with IR or Raman techniques are highly similar, IR-induced transitions need the vibrational mode to change the dipole moment of the molecule. The involved energetic levels still follow the Franck-Condon principle, require significant overlap of their associated wave functions, and allow transitions (e.g. $\nu_i \rightarrow \nu_j; \forall\, \mathrm{j} > \mathrm{i}$) within electronic states (e.g. S_0 or S_1). For such a transitions, energies in the range of hundreds of meV are required. The corresponding cross section follows Equation 2.8. Furthermore, vibrational transitions can be separated into three branches depending on the associated change in rotational state $\Delta J = J_{before} - J_{after}$, which finally leads to a mirrored spectrum: ΔJ = -1 P-branch; $\Delta J = 0$ Q-branch[11]; $\Delta J =$

[9] Typical multi-photon excitations employ incident light at wavelengths in the near infrared range between 800-1200 nm, but are conventionally mentioned alongside one-photon absorption.

[10] A detailed derivation of the multi-photon absorption cross section is given in Section 3.2.

[11] $\Delta J = 0$ represents vibrational transitions without a associated change in rotational mode. However, due to the angular momentum of the absorbed photon, such a transition is classically forbidden albeit existing for specific molecules.

+1 R-branch[12]. Besides exciting the main vibrational mode, their higher harmonics can also be excited with photon energies above ∼500 meV. Such higher vibrations are typically called overtones and can be excited in first approximation with a-times the photon energy of the original vibrational mode for the a's overtone.

Far-IR and μ-wave spectral range

Beyond the infrared spectral range at energies below ∼meV, rotational modes of molecules or functional groups can be excited by incident photons (see Fig. 2.4). Similarly to vibrational modes, rotations are quantized and underlie specific selection rules. In this case, molecules have to exhibit a permanent dipole moment which changes by rotational modes. In analogy to vibrational modes, rotational modes follow Equation 2.8 regarding their excitation and have overtones.

2.2.3 Photoacoustic and photothermal phenomena

As explained in the previous chapter, incident light at energies ranging from ∼meV to eV can induce the excitation of electronic, vibrational, or rotational states. In all cases, the absorbed energy can be dissipated by non-radiative processes, in which no photon is re-emitted by the absorber (see Fig. 2.5). Such processes are based on vibrational and/or rotational relaxations and require, in analogy to the Franck-Condon principle, overlap of the energetic levels forming thereby an energetic ladder to descend.

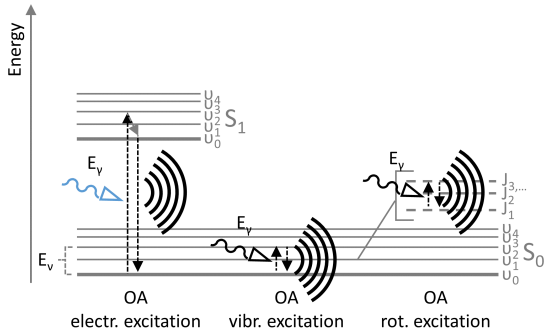

Figure 2.5: Jablonski diagram of optoacoustic signal generation upon electronic, vibrational, and rotational excitations.

Vibrations and rotations transform the once absorbed photon energy into molecular friction with the vicinity of the absorber, which subsequently leads to a co-localized

[12] Each transition $\nu_i \rightarrow \nu_j$ can undergo changes in their rotational state such as e.g. $J_2 \rightarrow J_3$ and $J_3 \rightarrow J_2$. As the energetic level follow an anharmonic oscillator and, thus, are not equidistant, the R-branch exhibits smaller energetic differences than the P-branch.

temperature increase. This phenomena is typically referred to as the photothermal effect describing the heat generation upon optical absorption. The temperature increase further initiates a thermoelastic expansion of the medium, finally leading to an increase of the local pressure. This second step is called photoacoustic or optoacoustic effect. In both cases, the initially deposited optical energy carried by photons is finally translated to another domain being either a thermal wave or a pressure wave propagating through the medium (see Fig. 2.5). For generating transient thermal or acoustic waves, the optical illumination intensity has to vary in a time-dependent manner. This can be achieved by pulsed excitation, which is then called time-domain, or periodically modulated excitation, which is then called frequency-domain. Regarding the photothermal effect, induced temperature changes are usually in the range of ∼µK-mK. These temperature variations induce a change in the local temperature-dependent refractive and reflective index of the medium, which can thus be utilized for certain imaging or spectroscopic techniques. Regarding the photoacoustic effect, generated initial pressures typically lie in the range of ∼100-1000 Pa, which can be detected by acoustic sensors. The detailed derivation of the photothermal and photoacoustic equations relevant for its implementation in HyMPSOM is elaborated in Section 3.3.

2.2.4 Fluorescence and phosphorescence

Besides radiationless de-excitations, molecules in an electronic excited state can release the absorbed energy via re-emission of a photon, which is in general termed photoluminescence (see Fig. 2.6).

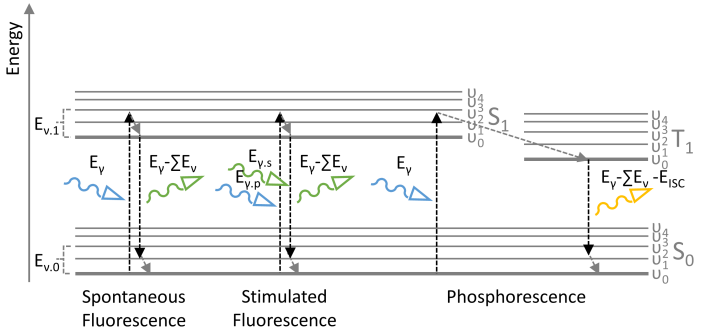

Figure 2.6: Jablonski diagram of photoluminescence processes.

The emission of a photon from a higher electronic excited singlet state typically occurs from the vibrational ground state $S_1;\nu_0$, to which the excited molecule gets via vibrational relaxation mechanisms[13]. The transition back to vibrational levels within electronic ground singlet state S_0 occurs, similarly to the absorption process, based on a significant overlap of the wave functions, which do typically not represent the vibrational ground state $S_0;\nu_0$. Hence, the re-emitted photon is of smaller energy compared to the absorbed photon due to lost energy in vibrational relaxations. This phenomenon is known as the Stokes-shift[14]. Whereas the optical absorption takes place on the femtosecond scale, vibrational relaxations last for picoseconds, and the lifetime of the vibrational ground level of the first electronic state is in the range of nanoseconds, thereby dominating the overall duration of the process. This incoherent process is referred to as fluorescence (see Fig. 2.6) and is characterized by the molecule's specific quantum yield determining the proportion of re-emitted compared to absorbed photons. A detailed derivation of fluorescence yielded upon multi-photon excitation is elaborated in Section 3.2.3 in the scope relevant for HyMPSOM. Furthermore, besides the above described spontaneous emission of a photon, fluorescence can also be stimulated by irradiating light with an energy matching the expected fluorescence wavelength (see Fig. 2.6).
In contrast to the above described fluorescence process happening in the singlet state, excited molecules in S_1 of spin $s = 0$ can potentially undergo intersystem crossing, which leads to a spin conversion to the triplet state T_1 of spin $s = 1$. In analogy to fluorescence, a photon can be re-emitted from the triplet state T_1 by a transition back to the singlet ground state S_0[15]. This process is termed phosphorescence (see Fig. 2.6). Although, classical quantum mechanical principles generally impede this process by forbidding to undergo spin-conversion (i.e. $s_0 \rightarrow s_1$), it happens eventually which leads to a long lifetime typically above milliseconds. Similarly to fluorescence, the re-emitted photon is of lower energy compared to the absorbed photon and even the fluorescence counterpart. The latter is explained by the Hund's rules, which state that a given electron configuration exhibits the lowest energy when possessing the maximum multiplicity.

[13] Special cases of emitted photons by transitions of higher electronic excited states (e.g. $S_2 \rightarrow S_1$) are extremely rare due to the decreasing energy differences between high vibrational states of S_1 and the ground vibrational mode of S_2. Hence, vibrational relaxations are energetically favorable.
[14] The Stokes-shift also holds for multi-photon excitations. However, the re-emitted photon consequentially is of lower energy than the sum of all simultaneously absorbed photons.
[15] For most molecular absorbers, especially organic biomolecules, a triplet ground state T_0 does not exist. Exceptions are $^3O_2$ or free CH_2.

2.2.5 Energy transfer, photochemistry, and photobleaching

Generally, the absorbed photon energy can potentially induce interactions with molecules in close proximity of the excited molecule itself (see Fig. 2.7).

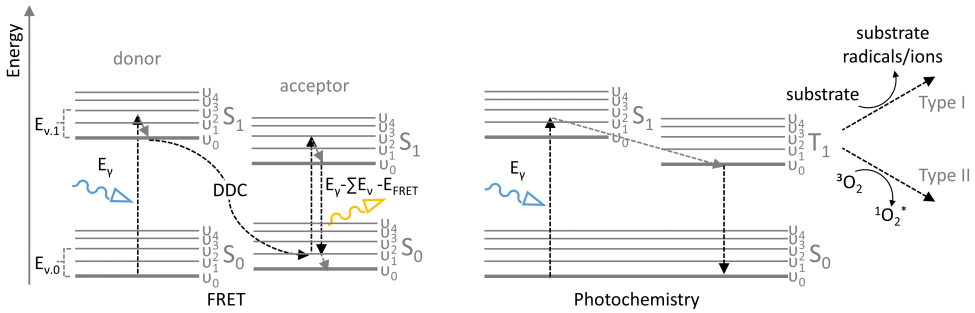

Figure 2.7: Jablonski diagram of energy transfer and photochemistry.

One way molecules can interact upon excitation is the forwarding of the uptaken energy from an energy-donating molecule, i.e. the donor, to another energy-accepting molecule, i.e. the acceptor. In simple words, the photoinduced electronically excited donor molecule is transferring its energy via non-radiative dipole-dipole coupling (DDC) to a neighboring acceptor molecule rather than emitting a fluorescence photon. The efficiency E of this process, which is referred to as Förster resonance energy transfer (FRET; see Fig. 2.7), depends on the donor-to-acceptor distance r as:

$$E = \frac{1}{1 + (r/R_0)^6}, \tag{2.10}$$

with R_0 being the specific Förster distance at which the efficiency is 50%. R_0, typically in the range of a few nanometer, is determined by both the overlap integral of the emission spectrum of the donor and the absorption spectrum of the acceptor as well as their molecular orientations during energy transfer. In case the acceptor molecule is not re-emitting a photon, this process is termed quenching and describes the suppression of a molecule to execute fluorescence. Both variants of energy transfer are typically reversible.

Additionally, excited molecules can dissipate the absorbed energy by inducing chemical reactions, which is then called photochemistry (see Fig. 2.7). In here, the absorbing molecule can either be the reactant, i.e. the absorber itself undergoes the chemical reaction (Type I), or a photosensitizer, i.e. the absorber interacts with a secondary molecule (Type II). Typical examples are the entire process of photosynthesis or the production of reactive oxygen species (ROS). The former utilizes the absorbed light energy to transfer an electron over an electron transport chain to reduce the co-factor $NADP^+$ to NADPH, which then induces a proton gradient activating the synthesis

of ATP being the biological 'energy currency'. The latter transmits an electron to an oxygen-containing molecule to form superoxide $^1O^{\cdot}{}_2$ as the precursor of other ROS products (e.g. $OH^{\cdot}$). Whereas ROS appear naturally during metabolism of oxygen and serve in processes like cell signaling, dramatically increased ROS levels are potentially harmful for cells as they can permanently destroy biomolecules such as DNA.
In contrast to the above mentioned forwarding of the absorbed light energy, excited molecules can be permanently destroyed by molecular reorientation, restructuring, or formation of new chemical bonds with surrounding molecules. Such processes are typically termed photobleaching and state the expiration of a molecule to emit fluorescence or phosphorescence[16]. In here, the number of photoinduced excitations and de-excitations usually determines when a light absorber gets photobleached. As the bleaching rate of a certain light absorbing molecule is in first approximation constant, the life span of the absorber proportionally depends on the applied light intensity. Furthermore, the occurrences of intersystem crossing to the triplet state are assumed to reinforce photobleaching based on the long lifetime of the chemically reactive T_1-state.

2.3 Contrast mechanisms

The following chapters regard the use of the above mentioned light-matter-interactions as contrast mechanisms for implementing different imaging modalities. In the context of HyMPSOM, this elaboration is limited to the spectral range from UV to IR as the corresponding energy range is applicable without harming biological tissue[17]. Further, the discussion will focus on the relevant aspects for utilizing the physical processes for microscopic methodologies in Section 2.3.1 followed by outlining the concept of a molecule-specific spectral fingerprint Section 2.3.2. Finally, the most abundant chromophores or labels typically measured with photonic microscopy are summarized in Section 2.3.3.

2.3.1 Microscopic modalities

As described in Section 2.2, the interaction of light with matter induces a variety of physical processes, which can, in general, be used as a contrast mechanisms for implementing microscopic imaging modalities to study various specimens. In here, the light is typically provided by optical lasers, which deliver highly stable and controllable illumination optimized to induce the aimed physical process with high efficiency.

[16] Due to various mechanisms to chemically alter the chromophoric group of a molecule, photobleaching can potentially also just diminish the quantum yield but restore the absorbing properties of the chromophore.

[17] Spectral ranges of energies higher than ∼10 eV potentially harm the tissue by eliminating bound electrons. However, such radiation is also applied on biological tissue on a daily basis in form of e.g. X-ray computer tomography (XCT) scans.

Optical coherence

Imaging techniques based on reading optical coherence retrieve information out of the backscattered and backreflected light, analogous to ultrasound using scattered and reflected sound waves. Depending on the optical system configuration and image reconstruction, these techniques are called optical coherence tomography (OCT) or microscopy (OCM). Both approaches sense local changes in the optical properties of the sample, especially differences in the refractive index, and the light scattering characteristics. Such optical properties are predetermined by the underlying microstructure and morphological subcompartments of the examined specimen. For sensing alterations of optical properties, the backscattered/backreflected light from the sample is brought to interfere with the initially applied light via interferometric approaches (e.g. Michaelson or Mach-Zehnder interferometer). Subsequent image generation uses frequency analysis and demodulation of the detected interference signals. In general, OCT imaging systems are characterized by resolutions in the range 10-15 µm for an imaging depth of up to 3 mm and typical imaging speed of several Hz.

Harmonic Generation

Similar to methods based on optical coherence, imaging modalities using optical harmonic generations extract local optical properties of the specimen under investigation. For inducing significant harmonic generations upon illumination, a high photon flux is required, thereby limiting their realization as imaging modalities to microscopic approaches. Depending on the number of involved photons, the generated harmonic signals exhibit strong directionality, typically dominated to the forward or transmission direction. Signals are usually detected by highly sensitive optical detectors equipped with spectral filters to selectively pick up the harmonic signals. Microscopic imaging with harmonic generation signals typically achieves spatial resolutions of $\sim$1 µm at depth of up to $\sim$500 µm and imaging speeds beyond 1 kHz.

Raman

Methods based on Raman scattering utilize inelastic light scattering, by which energy is partially deposited in the sample. The two most popular approaches to excite vibrational modes by Raman processes are stimulated Raman scattering (SRS) and coherent anti-Stokes Raman scattering (CARS). In both cases, the molecule under investigation is first brought to a virtual state by a so-called pump beam. In SRS, an inelastic scattered beam, i.e. Stokes beam, and in CARS a combination of two beams, i.e. Stokes and anti-Stokes beam, actively de-excites the molecule, which reinforces the modality's sensitivity. Although the finally excited vibrational state of the molecule corresponds to energies provided by IR light, illuminations typically in the VIS range are used.

Light at the wavelength of the inelastic scattered beams (SRS: Stokes; CARS: anti-Stokes) varies by the induced Raman transitions in its intensity, which can be sensed by optical detectors, and thereby carries information about the excited vibrational mode of the molecule. Raman imaging achieves resolutions based on the optical diffraction limit of about 1 µm to a depth of 200 µm and imaging speeds of up to several kHz.

NIRS

Near-infrared spectroscopy (NIRS) measures the molecule-specific absorption in the near-infrared region (800 - 2500 nm). In this region, molecules interact with the excitation light by vibrational overtones being characteristic for certain molecular bonds. The most prominent detectable vibration overtones in the NIR region belong to CH, NH, and OH groups. These vibrational modes are further altered by molecular groups in close vicinity via intramolecular interactions, which, thereby, leads to a molecule specific absorption pattern. Regarding possible imaging systems, spatially resolved NIRS can be applied in either transmission or reflection mode. Thus, NIRS allows to examine arbitrarily thick samples up to an imaging depth of few cm and a resolution of $\sim$1 cm at an imaging rate of sub-Hz.

Optoacoustic

Optoacoustic imaging (OAI) relies on sensing ultrasonic waves generated by thermoelastic expansion upon transient light excitation of molecules via the previously mentioned photoacoustic effect. Hence, OAI enables label-free imaging of biomolecules due to not relying on significant quantum yield of the targeted molecules. By tuning the optical excitation throughout the entire electromagnetic spectrum, the OAI contrast mechanism can be based on absorption induced electronic transitions (UV-VIS) to sense tissue-intrinsic chromophores such as hemoglobin and melanin, or vibrational transitions (IR) to sense tissue constituents such as water, lipids, and carbohydrates. In OAI, the uncoupled excitation (i.e. pulsed or modulated optical laser) from the detection (e.g. ultrasound transducer) enables OAI to work in three main configurations allowing to utilize OAI contrast over a wide range of size scales: (1) In OA tomography, the sample is illuminated entirely or at least broadly and an array of ultrasound detectors is used for acoustic signal detection, from which the absorbed optical energy is subsequently reconstructed to retrieve the distribution of excited absorbers in the sample. OA tomography typically yields resolutions of hundreds of µm at depths up to several cm with imaging speeds of tens of Hz; (2) OA mesoscopy, also called acoustic-resolution OA microscopy, is based on a broad sample excitation, raster-scanning a single-element detector across the region of interest, and acoustic reconstruction of the signals. OA mesoscopy achieves resolutions of tens of µm at depth of several mm and imaging speeds of hundreds of Hz; (3) The microscopic version of OA operates with

diffraction-limited focusing the optical excitation into the sample within the sensitivity field of an ultrasound detector. OA microscopy is characterized by resolutions below 1 µm, can image as deep as several hundreds of µm with speeds up to the kHz-range. Recent advances in detecting the acoustic signals by optical sensing techniques (e.g. interferometry) further boosts the application scope of OAI towards catheter integration.

Fluorescence

From a methodological point of view, imaging systems based on fluorescence can be differentiated into tomographic and microscopic approaches. In fluorescence molecular tomography (FMT), 3D reconstruction algorithms are used to deduce the position of fluorophores by reading diffusive photons and by accounting for light propagation in tissue. By that, wavelength dependent imaging depths between several mm (VIS) to a few cm (NIR) can be achieved. In fluorescence microscopy, either the optical excitation or the detection is focused by objective lenses to a diffraction-limited spot. In here, the utilized wavelength defines the spatial resolution, which is typically around 0.5 µm in the VIS range. In order to further enhance the spatial resolution, advanced approaches aim to overcome the diffraction limit of the equipped wavelength: (1) multi-photon excitation (multi-photon microscopy (MPM)) narrows the excited volume to only the focal region in which the fluence is high enough for the previously mentioned two- or three-photon excitation process; (2) systems equipping a spatial pinhole (confocal laser scanning microscopy (CLSM)) or a spinning disk (spinning disk microscopy (SDM)) confine the detectable volume by blocking out-of-focus light; (3) super-resolution techniques utilize either time-wise separable de-excitations (photoactivated localization microscopy (PALM), stochastic optical reconstruction microscopy (STORM)) or induced spatial de-excitation patterns (stimulated emission depletion microscopy (STED)). With such advanced fluorescence microscopy systems, spatial resolutions down to several tens of nm can be achieved allowing to resolve single molecules.

2.3.2 Spectral fingerprint

The previously elaborated utilization of light-matter-interactions as contrast mechanism for microscopic modalities rely on the underlying physical processes induced upon irradiation.
On the one hand, methods based on optical coherence or harmonic generation as a special form of elastic scattering read optical properties of the sample. Such contrast mechanisms are in first approximation wavelength independent and, thus, can be implemented over a relatively large spectral range. However, to induce non-linear processes (e.g. SHG), the size of the scatterer has to resemble the wavelength and, thereby, determines the size of the optical focus of the irradiated light. Hence, for sensing spe-

cific tissue moieties such as collagen fibrils of typical diameters of ∼300-1000 nm in biological tissue with SHG, wavelengths between ∼600 and 2000 nm are favored.
On the other hand, methods exciting a molecule depend on the underlying energetic properties of the absorbing chemical group. As elaborated in Section 2.2, such properties are determined by the chemical construction of the molecule, from which the energetic states can be deduced. First, electronic states are *w.l.o.g.* defined by the degree of de-localizations of electrons and, thus, depend on the length of the conjugated π-electron system of a molecule. In other words, if p-orbitals of adjacent chemical bonds overlap and align, they allow the contained electrons to de-localize across all involved atoms. Consequently, the larger such a conjugated π-electron system is, the lower the corresponding electronic states and their energetic difference are and, thus, the lower the energies required to excite a transition are. Second, vibrational states depend on the motility of the addressed chemical groups. The close vicinity within the molecule can therefore influence the vibrational motion of a functional group, which is typically referred to as vibrational coupling. Besides spatial enclosures restricting vibrations, functional groups of the molecules can affect the vibration. Vibrational coupling is in this aspect significant, when a secondary functional group is of equal energy in its vibrational states, is closer than two chemical bonds, shares a common atom or a common bond, and constitutes a modification of the vibrational motion[18].
Analogous considerations hold for rotational states as well as their previously described combination into rovibrational modes (see Section 2.2.2). Next to these intrinsic effects, the energetic states of a molecule experience influences from their environment (see Section 2.2). Hence, each molecule is associated with a characteristic spectral fingerprint being distinct for a given situation, which can be specifically addressed by optical excitation and/or de-excitation.
In summary, the energetic states of a molecule are predefined by the underlying chemical composition and construction that eventually shape a molecule-specific spectral fingerprint, which is exemplarily shown for the spectrum of water in Fig. 2.8. This approach constitutes the basis of spectroscopic techniques that increasingly emerge towards spectromicroscopy. The specific spectral fingerprints of molecules allow in this regard for their differentiation inside specimens on the microscale. Finally, the exploration of the unique interactions between molecules and irradiated light facilitates the development of molecular imaging and, subsequently, molecular microscopy techniques.

[18] A stretching vibration can be influenced by a bending vibration of an adjacent bond, if the stretching bond constitutes one arm of the bending motion.

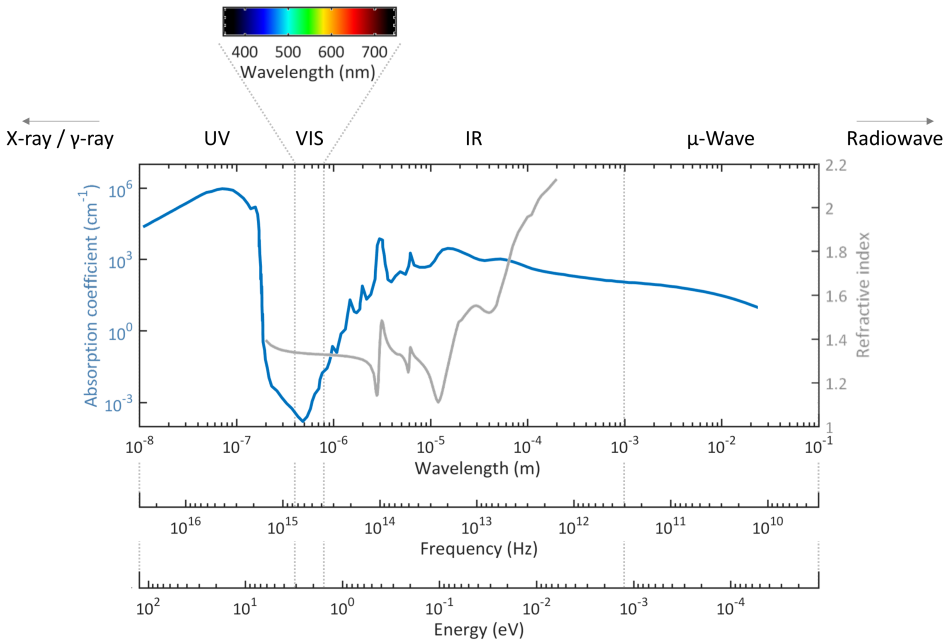

Figure 2.8: Spectral fingerprint of water regarding its optical absorption and refractive index across the electromagnetic spectrum. Data extracted from [23, 36]

2.3.3 Chromophores and labels

Based on the above mentioned spectral fingerprint, photonic microscopy modalities can sense specific chromophores or contrast agents. For each modality, compounds possess detectable contrast when they fulfill the associated prerequisites. Whereas for scattering-based modalities the compounds solely have to present the required optical properties, for absorption-based modalities the compounds have to exhibit significant optical absorption and either a high quantum yield for fluorescence detection or a low quantum yield for optoacoustic readings. In case of a high optical absorption, the quantum yield value can potentially allow for only fluorescence, only optoacoustic, or both detection approaches of the identical optical excitation process. Furthermore, the sensitivity of the microscopic modalities determines the required abundance of the compound to be detectable, which can be viewed as the local concentration or local density within the focus of the microscope[19]. Moreover, each photonic microscopic modality can in general be operated label-free, i.e. detecting endogenous compounds of the specimen, or by administering dedicated labels, i.e. detecting exogenous compounds addressing a specific target within the specimen.

[19] When considering a homogeneously distributed compound (e.g. dissolved molecules), the concentration equals the local density. For a spatially structured compound (e.g. fibrillar components), the spatial density on a hierarchical higher level is decisive.

Endogenous

Endogenous compounds of biological specimens are of highest interest as they (1) do not require additional steps of sample preparation, which subsequently would constitute a time- and cost-expensive procedure; (2) are harmless to the organism under investigation due to their natural occurrence; and (3) facilitate a straight forward translation of the associated imaging approach to humans without the need of approving a contrast agent for human applications. Hence, imaging modalities carried out in a label-free manner by means of detecting endogenous and naturally presented compounds are of highest interest, especially for translational medicine bridging basic biology research with clinical practices.

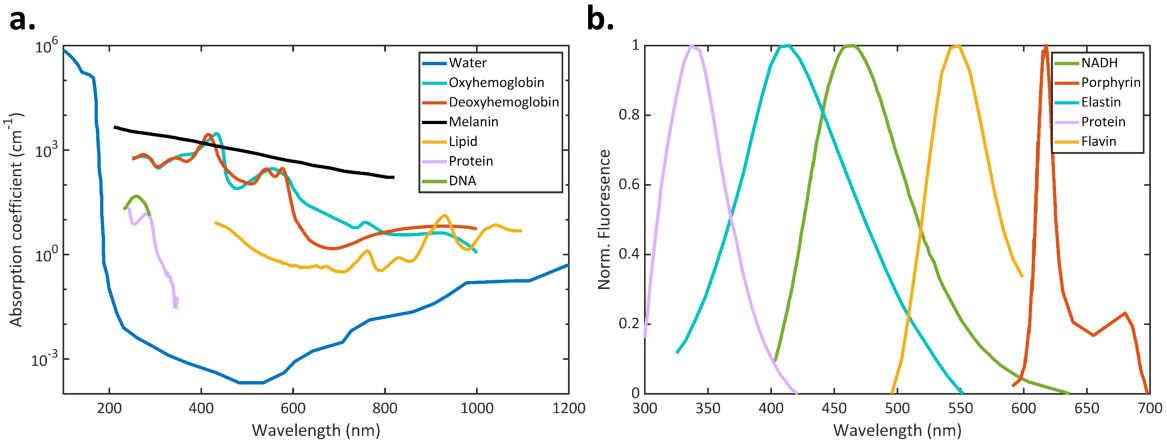

Figure 2.9: Spectral fingerprints of the most abundant tissue chromophores regarding **(a)** intrinsic absorption and **(b)** autofluorescence. Data extracted from [23, 37–42].

Fig. 2.9a compiles the most abundant optical absorbers in biological tissue in the spectral range from 100 to 1200 nm. Whereas the spectrum of water exhibits a low optical absorption from ∼200 - 1000 nm, thereby constituting a so-called 'optical window', the visible range is dominated by melanin and hemoglobin being the strongest optical absorbers. Furthermore, as both these compounds posses a negligible quantum yield of <1%, they constitute a well-suited contrast source for optoacoustic imaging. Fig. 2.9b depicts various relevant tissue chromophores[20] with significant quantum yield, which thereby yield an autofluorescence nature of biological tissue. In here, proteins and nucleic acids (e.g. DNA or RNA) show fluorescence in the range of ∼250-380 nm, metabolic messenger molecules such as NADH or FAD as well as components of the connective tissue like collagen and elastin can autofluoresce in ∼300-580 nm, vitamins and flavins dominate the range of ∼500-650 nm, and, finally, porphyrins[21] can exhibit

[20] The following list should not be seen as complete but rather as exemplary.

[21] Porphyrins are large heterocyclic groups which often complex with metal ions. One example is heme as the co-factor of hemoglobin.

fluorescence at wavelengths above ∼600 nm. As described in Section 2.2.1, non-linear scattering processes such as SHG or THG do in first approximation not depend on the irradiated wavelength but on the size ratio between the optical focus and the compound. More importantly, the strength of harmonic generation signals strongly depends on the optical properties determined by the microstructure, which vary considerably in biological tissue. However, the strongest endogenous SHG signal is generated by collagen (type I, II, and IV), myosin, and bone. As THG in general could potentially sense all optical interfaces between two media of different refractive index, especially water-lipid boundaries (e.g. lipid droplets in adipocytes or cell membranes as lipid-bilayers) yield strong THG contrast.

Exogenous

Exogenous contrast agents are heavily used to generate contrast for basic biological research, translational medicine, and in everyday clinical practice because they (1) enable highly specified targeting of certain biological moieties; (2) facilitate imaging of components lacking intrinsic contrast; (3) enlarge the usable spectral range to further unburden differentiation tasks; and (4) allow for the development of contrast agents exhibiting e.g. multi-modal contrast or interplay with the specimen. The latter is of central importance towards theranostic approaches, in which the dedicated addressing of certain biological components for diagnostic imaging could potentially also be utilized to apply therapeutic measures to the targeted component.
In general, exogenous contrast agents can be classified to be either externally administered and genetically encoded. Externally administered agents include on the one hand staining techniques, which are mostly performed on histopathological tissue or fixed single-cells to stain e.g. nuclei, extracellular matrices, and cytoplasms based on chromophoric colorants complexing with the target structure such as DNA, proteins, or lipids. As an extension, the colorants can be linked to a specified antibody to target e.g. a protein specifically, which is then termed immunostaining. On the other hand, vital contrast agents could be administered to living specimen via multiple mechanisms such as injections (e.g. intravenously, subcutaneously, intracranially) for small model organisms and humans, or via induced or spontaneous uptake into cells (e.g. endocytotic, transporter-based, phagocytotic). Typically used administered contrast agents include hematoxylin & eosin (H&E), 4',6-diamidino-2-phenylindole (DAPI), Nile red, and Immunoglobulin G-based reporters (IgG). Genetically encoded contrast typically describes the genetic modification of specimens to induce expression of chromophore-proteins such as the green fluorescent protein (GFP). In this case, the targeted cell or class of cells generates and regulates the desired exogenous contrast. Additionally, as this processes is controlled by the cell metabolism, the level of expression can potentially be both induced by an external stimulus as well as monitored to enhance the

amount of extracted information. In summary, the most widely spread exogenous fluorescent probes are Alexa Fluor and ATTO dyes as organic molecules (e.g. Alexa647, ATTO488), fluorescent quantum dots as nanomaterials, Cyanine- or indocyanine-dyes as synthetic fluorophores (e.g. Cy5, ICG), and fluorescent proteins (e.g. GFP, YFP, GCaMP[22]). Furthermore, Dextran is typically used as an exogenous THG agent.

2.4 Characteristics of photonic microscopy

This chapter deals with the general characteristics and principles being relevant for exploiting the previously elaborated imaging mechanisms as microscopic modalities. Despite essential differences in the associated contrast phenomena, the following considerations are modality-independent and constitute rather basic concepts of photonic microscopy. In this regard, the spatial resolution determined in form of the diffraction-limited point spread function will be outlined in Section 2.4.1. Next, the propagation of light in tissue will be elaborated in Section 2.4.2, from which the penetration depth and, thus, the imagable volume can be deduced. Finally, an overview of commonly used image formation approaches is given in Section 2.4.3.

2.4.1 Diffraction limit and point spread function

The achievable spatial resolution of photonic microscopy describes the minimum distance at which two objects can be distinguished, i.e. individually resolved. In general, the resolution depends on the light focusing abilities of the equipped optical system, which concerns either the optical excitation or the signal detection. In both cases, focusing light can be described using the formulation as waves: light of a wavelength λ originating from a single spatial point in the object plane constitutes a spherical wave centered at this point in space. By assuming a series of perfect optical lenses, this spherical wave is transformed into another spherical wave finally being focused onto a single point in the imaging plane. In this regard, Huygen's principle states that a spherical wavefront consists of adjacent single point sources as emanation origins of spherical waves with identical wavelength λ. These waves exhibit an identical phase origin and subsequently interfere with each other, which finally results in a diffraction pattern in the imaging plane, termed the Airy pattern. This lateral pattern consists of a central bright region (i.e. diffraction disk), which is referred to as the zero-th order diffraction spot, surrounded by concentric rings called first-, second-, third-, ... order diffraction rings with intensities I_{lat} along the lateral direction following:

$$I_{lat} = I_0 \cdot \left| \frac{2 \cdot J_1(\zeta)}{\zeta} \right|^2, \tag{2.11}$$

[22] GCaMP is a derivative of GFP and constitutes a genetically encoded sensor for calcium ions.

where I_0 is the peak intensity of the central diffraction disk, J_1 is the Bessel function of first order, and ζ denotes the dependence on the radial distance as $\zeta = 2\pi d_r NA/\lambda$. In here, d_r denotes the radial distance to the central intensity peak and NA the numerical aperture of the objective lens defined as $NA = n \cdot sin(\theta)$ with n as the refractive index of the immersion medium and θ the aperture angle of the objective[23]. From this intensity profile, the lateral resolution limit can be derived by assuming a perfect lens-based optical system. Furthermore, the considerations hold for approaches of either focusing the optical excitation, focusing the signal detection, or both. The theoretically achievable lateral resolution for a given optical system can be correspondingly deduced as the minimum distance at which two point like objects can be distinguished. Different interpretations of the required level of distinguishing between two objects leads to three commonly used definitions for the lateral (lat) resolution:

$$r_{lat}^{Rayleigh} = 0.61 \cdot \lambda/NA, \tag{2.12}$$

$$r_{lat}^{Abbe} = 0.50 \cdot \lambda/NA, \tag{2.13}$$

$$r_{lat}^{Sparrow} = 0.47 \cdot \lambda/NA. \tag{2.14}$$

In here, the Rayleigh criterion $r_{lat}^{Rayleigh}$ defines readily spatial distinction of two point sources, when the center of the diffraction pattern of one point source gets superimposed by the first minimum of the secondary diffraction pattern of the other point source[24]. To fulfill the Abbe criterion r_{lat}^{Abbe}, the two objects under investigation have to be separated at least by the full width at half maximum (FWHM) of their diffraction disk of zero-th order. In contrast, the Sparrow criterion $r_{lat}^{Sparrow}$, which is mostly used in astronomy, is satisfied when two objects are so close so that the summed Airy patterns lead to a flat intensity profile without a recognizable dip.
Analogously, the intensity profile of an optical focus in the axial direction I_{ax} can be expressed as:

$$I_{ax} = I_0 \cdot sinc^2\Big(\frac{\xi}{4\pi}\Big), \tag{2.15}$$

with $sinc(x) = sin(\pi x)/\pi x$ and $\xi = 2\pi NA^2 d_a/n\lambda$, in which d_a is the axial distance from the central peak intensity. The corresponding axial resolutions based on the above mentioned criteria are defined as:

[23] The aperture angle θ is half of the opening or collection angle of the objective.
[24] The factor 0.61 results from the description of an optical focus as a Bessel function with its first minima at 1.22 a.u. from its center.

$$r_{ax}^{Rayleigh} = 2 \cdot n\lambda/NA^2, \tag{2.16}$$
$$r_{ax}^{Abbe} = 1.67 \cdot n\lambda/NA^2, \tag{2.17}$$
$$r_{ax}^{Sparrow} = 1.4 \cdot n\lambda/NA^2. \tag{2.18}$$

Besides the diffraction-induced intensity pattern, the optical system further induces blurring effects caused by imperfections in/on the lenses, misalignments of the optical beam path, and chromatic and spherical aberrations, as well as by the collection technology in form of background noise and alterations in signal digitization. Eventually, the so-called point spread function (PSF) characterizes the actual response of an imaging system to a point source and constitutes the associated spatial imaging function [43–45]. As the higher-order diffraction rings of the Airy pattern possess relatively small intensities, the PSF is typically approximated by a Gaussian function having a standard derivation of $\sigma_{Gauss} \approx 0.21 \cdot \lambda/NA$. In practice the resolution of an imaging system is therefore usually defined by the FWHM of the Gaussian PSF.
The PSF of an imaging system is typically determined by measuring objects being much smaller than the theoretically estimated resolution. Finally, the PSF can be, in general, utilized for spatial deconvolution approaches to further enhance the resolution of the recorded images (see Section 3.4.2) and is standardly performed in all kinds of photonic microscopy [43–57]. In contrast to pure optical microscopy modalities, the PSF and, thus, the achieved spatial resolution of optical-resolution optoacoustic microscopy experiences additional influences of the optoacoustic signal generation process and acoustic detection technology. This is of high importance for applying analogous PSF-correction algorithms and is elaborated theoretically in Section 4.4.4 as well as practically in Section 4.4.
Furthermore, the above described physical limitations of spatially focusing or resolving light can be overcome by particular approaches for super-resolution microscopy. In here, the limitation of diffraction is conquered either by transferring the resolving issue to a time-varying process or by redefining the PSF. The former includes concepts such as photoactivated localization microscopy (PALM) or stochastic optical reconstruction microscopy (STORM), which *w.l.o.g.* are based on separating the signal from different point sources in time, measuring them as diffraction-limited PSF's, localizing their PSF's center, and then assembling the found locations together to form the final image. The latter comprises techniques such as stimulated emission depletion (STED) or structured illumination microscopy (SIM), which refine the acting excitation either by superimposing a depletion beam of higher laser mode or by illuminating the specimen with a spatial pattern thereby resolving spatial information in frequency space. In this regard, STED uses a secondary beam to induce stimulated fluorescence (see Fig. 2.6) in a doughnut-shaped rim co-localized with the primary excitation beam, which

thereby minimizes the fluorescence-active illumination area. SIM is based on investigating specimens in reciprocal space, i.e. exciting the sample with an illumination pattern of distinct spatial frequency, reading information in Fourier space, repeating the process with modified illumination patterns, superimposing all recorded information, and reconstructing the final image via Fourier transformation.

2.4.2 Light penetration and imaging depth

To explore how light propagates through a medium and limits by that the maximum imaging depth, the light-matter-interactions (see Section 2.2) are assumed to occur suddenly within an infinitely short duration[25]. In this assumption, light only reduces in intensity while propagating through a medium, but does not change in its energy spectrum. This is in contrast to charged particles continuously loosing their energy while propagating. In this regard, the two most dominating ways of light interacting with matter are absorption and scattering[26]. The thereby yielded attenuation of light traveling in a medium can be expressed by the exponential Beer-Lambert law as:

$$I(x) = I_0 \cdot e^{-\mu_e x}, \tag{2.19}$$

where $I(x)$ denotes the light intensity at a given propagation distance x of light with an initial intensity I_0. In here, the extinction coefficient μ_e (cm^{-1}) combines the phenomena of absorption and scattering, both leading to a removal of light intensity from its original propagation path, and can be expressed as:

$$\mu_e = \mu_a + \mu_s = \sum_i N_i \cdot \sigma_i, \tag{2.20}$$

in which μ_a and μ_s are the absorption and scattering coefficients, respectively, N_i is the number of entities inducing absorption or scattering (cm^{-3}), and σ_i is the corresponding cross section (cm^2) of the interaction phenomenon[27] i. Further, the average propagation distance a photon can travel before undergoing one of the above mentioned phenomena is typically captured as the mean free path (MFP) expressed as:

[25] The previously mentioned ways of light-matter-interactions typically occur on a time-scale of $\sim 10^{-15}$-10^{-8} s.

[26] Secondary effects such as re-absorbed fluorescence light, self-excitations, and photochemical reactions can be in first approximation neglected as their contribution to the light propagation is not decisive.

[27] Here, equation 2.20 can be extended by all possible processes of light-matter-interaction to refine the description of light propagation.

$$MFP \approx \frac{1}{\mu_s}. \tag{2.21}$$

The effective MFP in biological tissue is typically defined by only considering scattering phenomena because of its dominance over absorption processes. In here, the MFP assesses predominantly anisotropic scattering and measures the extent of the ballistic regime of photon propagation. Beyond one MFP, photons propagate quasi-ballistically, meaning they undergo multiple scattering events. Although the photon's propagation directions get randomized in this regime, predominantly Mie scattering conserves a general directivity.
Additionally, the transport mean free path (TMFP), deduced as the extension of the MFP, marks the boundary after which photons have lost such a general directivity on average and propagate randomly. The TMFP includes isotropic scattering, marks the entrance into the diffuse regime, and can be expressed as:

$$TMFP \approx \frac{1}{\mu_s \cdot (1-g)}, \tag{2.22}$$

in which g is the anisotropy factor capturing the proportion of forward-directed scattering events. In biological materials, the MFP is typically assumed at ∼0.1 mm and, due to g being in the range of 0.8 - 0.99, the TMFP at ∼1.0 mm.
Concludingly, the MFP determines the achievable imaging depth for pure optical microscopy such as brightfield, single-photon excitation fluorescence, or Raman scattering. These methods mostly rely on detecting ballistic photons and localize their origin spatially. Due to that, their imaging depth is typically limited to ∼100 µm. This limitation can be overcome by techniques applying optical sectioning. On the one hand, special illumination techniques, such as multi-photon excitations, use longer excitation wavelengths, which are associated with weaker scattering coefficient and subsequently facilitate a larger MFP. On the other hand, techniques restricting the detected volume, such as confocal microscopy, diminish the detection of scattered photons from origins other than the intended location in the specimen. In contrast to pure optical microscopy, optoacoustic imaging techniques are applicable to depth in the order of one TMFP based on the detection of ultrasound, which scatters orders of magnitude weaker in biological tissue. Hence, the propagation directivity of the irradiated optical excitation is of no relevance whilst ensuring sufficient optical excitation. Even though optical-resolution optoacoustic microscopy still relies on a diffraction-limited focus, the light has to propagate only once through the tissue, which therefore allows deeper imaging than the pure optical microscopy counterpart.

2.4.3 Image formation and field of view

The maximum area covered by photonic microscopy is typically referred to as the field of view (FOV), the size of which predominantly depends on the performed method of image formation. For that, three commonly used approaches can be distinguished, each of which is also implemented in HyMPSOM as described Section 4.2.5:
First, in widefield microscopy, a 2D areal detector is equipped to simultaneously capture the information across the entire FOV placed in the specimen. In here, each pixel of the final image is in first approximation acquired at the same time[28], which limits the acquisition rate to the internal processing speed of the sensor. Second, in laser-scanning microscopy, a diffraction-limited optical excitation is raster-scanned across the specimen using high-speed scanning units such as galvanometric (galvo) mirrors or micro-electro-mechanical systems (MEMS). The image formation is typically performed in a serpentine-like scheme, which leads to the successive acquisitions of pixels. The maximum scanning speed, also termed the small angle response, of the scanning unit determines in this regard the acquisition rate. In both concepts of widefield or laser-scanning microscopy, the magnification of the equipped objective lens sets the maximum FOV, which is typically in the range of several hundreds of µm. The illumination cone is broader and, analogously, the outer scanning angles are more perpendicular at lower magnifications, which leads to a larger FOV, and vice versa. Third, in sample-scanning microscopy, the images are formed by mechanically raster-scanning the specimen through a stationary interrogation area. Similarly to laser-scanning techniques, the raster scheme follows in most cases a serpentine-like procedure using e.g. sample-holding stages, the acceleration and translation speed of which limits the acquisition time. In this case, the maximum FOV is only limited by the travel range of the exploited stages, typically up to several cm. Combination of these image formation methods can potentially take advantage of large FOVs and high-speed acquisition by e.g. continuously translating the specimen while using high-speed laser-scanning to form a stripe-like image at highest acquisition speed and beyond the maximum FOV associated to the current magnification (see Section 4.2.5).
In all cases, the concept of spatial sampling is of high importance to properly measure a specimen. The Nyquist–Shannon sampling theorem states in this regard a spatial sampling step of maximum half the expected spatial resolution. Typical ratios between FOV-dimension and spatial resolution of ∼1000 therefore lead to the acquisition of images with several megapixels[29]. Furthermore, to achieve 3D imaging, the specimen

[28] 2D optical sensors are based either on a global shutter ensuring identical time points of acquisition for all sensor pixels, or on a rolling shutter, in which the data is acquired either pixel-by-pixel or line-by-line across the sensor.
[29] Standard objective lenses for visible light used in biomedical research are characterized by a magnification of 10x-100x and by a NA of 0.2-1.4. Hence, achieved FOVs are ∼1.000-100 µm and resolutions are ∼2.000-200 nm.

is in most cases translated axially by using a stationary imaging plane. The 3D volume is by that optically sectioned, at which 2D images are successively scanned as stacked layers. Besides that, techniques such as single-plane illumination microscopy (SPIM) combine the use of a 2D areal sensor with laser-scanning approaches of rastering a 2D plane of optical excitation throughout the specimen.

2.5 Conclusion and Outlook

In conclusion, illuminating matter with light induces a huge variety of physical phenomena, in which the specific combination of the incident light and the irradiated specimen determines the dominating optical interaction. Such induced interactions can subsequently be exploited as contrast mechanisms for imaging modalities, which generally possess a molecular-specific contrast when adapting the optical excitation to the spectral characteristics of the targeted moiety. In this regard, optical imaging techniques allow not only to sense a wide range of endogenous or exogenous labels but also to differentiate among them based on their distinct optical properties. Furthermore, the usage of light as the utilized energy source enables the development of imaging techniques operating on different size scales ranging from single-molecule approaches over cellular microscopy to small model organisms and beyond. The associated physical principles determine here the achievable imaging capabilities regarding spatial resolution, penetration depth, imaging speed, and sensitivity, which can however be overcome by augmenting the way of signal generation and detection. In the scope of photonic microscopy, advanced modalities like multi-photon and optoacoustic microscopy present advantageous characteristics over standard brightfield microscopy as they achieve better resolution, deeper imaging, higher sensitivity, and greater molecular-specific contrast, especially regarding label-free applications.
Whereas each microscopy modality is generally associated with a distinct wealth of extractable information of biological tissue, a combination of compatible microscopy techniques implemented in a single device is of vast potential by acquiring complementary signals. Hence, hybrid microscopy attains more comprehensive insights into the investigated specimens and, thus, enables more extensive conclusions. To implement a hybrid microscope, all integrated modalities should be characterized by similar properties regarding spatial resolution, imagable volume, compatible contrast, acquisition speed, and the associated optical system. In this regard, multi-photon and optical-resolution optoacoustic microscopy constitute an exceptionally well-suited combination of modalities as they allow for investigation with sub-cellular resolution, deep and fast imaging, and application to *in vitro* and *in vivo* specimens, can extract information label-free or from specific contrast agents, and require similar optical components. Finally, merging multi-photon and optoacoustic modalities into a single microscope features unique imaging capabilities overcoming their stand-alone counterparts and, thus, describes a novel powerful approach to conduct hybrid imaging on the microscale.

3 Theoretical considerations of HyMPSOM

This chapter elaborates in detail the theoretical consideration relevant for the microscopy modalities implemented into HyMPSOM. Whereas the previous chapter gives a general overview of basic principles of photonic microscopy based on light-matter-interaction and subsequent induced physical processes, this chapter will focus exclusively on the modalities employed in HyMPSOM, being multi-photon (see Section 3.2) and optical-resolution optoacoustic microscopy (see Section 3.3). In there, the associated signal generations are formulated in their respective physical equations. Finally, an overview is given regarding the practical realization of microscopy image processing steps (see Section 3.4).

3.1 Introduction

Based on the principles of photonic microscopy as generally elaborated in Section 2 by means of exploring possible ways of light-matter-interaction, this chapter elucidates their subsequent use as contrast mechanisms for the implementation as a microscopy imaging modality. As mentioned previously, HyMPSOM equips multi-photon and optoacoustic microscopy modalities due to shared imaging properties such as resolution, imaging volume and speed, complementary contrast, label-free imaging capabilities, and *in vivo* applicability. The associated physical processes are in the following formulated as derived from the underlying light-matter-interactions.

3.2 Background on multi-photon microscopy

Multi-photon microscopy collectively describes optical modalities based on non-linear-optical (NLO) processes, which take place when light of high intensity interacts with matter. Such NLO processes, as generally elaborated already in Section 2.2.1 and Section 2.2.2, involve more than one photon, i.e. typically up to four, and can be subdivided into multi-photon scattering[30], harmonic generation, and multi-photon excitation[31].

W.l.o.g., all multi-photon microscopy modalities are based on a high laser intensity or rather a high photon flux, typically achieved in ultra-short laser pulses with durations <200 fs. These temporally focused optical radiations lead to the induction of NLO processes, which underlying theory is elaborated in Section 3.2.1. In HyMPSOM, such are utilized for implementing microscopy modalities of two kinds: First, NLO processes leading to energy conserving phenomena are exploited in HyMPSOM in the form of second and third harmonic generation modalities as elucidated in Section 3.2.2; Second, NLO processes exciting chromophores, which subsequently de-excite via emission of fluorescence signals, are exploited in the form of two- and three-photon excitation fluorescence as described in Section 3.2.3.

3.2.1 Non-linear optical signal generation

NLO processes emerge in general as electromagnetic phenomena described by the macroscopic Maxwell equations. NLO processes are mostly formulated in dependency of the polarization $\tilde{P}(t)$, i.e. the dipole moment per unit volume, on the applied electric field $\tilde{E}(t)$, because a time-varying $\tilde{P}(t)$ potentially can generate additional components of $\tilde{E}(t)$. The wave equation in NLO-active media is in generally given by[32]:

[30] Although a huge variety of multi-photon modalities are based on inelastic or Raman scattering, e.g. CARS and SRS, the associated modalities are not integrated in HyMPSOM and, thus, are disregarded in the following.

[31] The following chapters are based on [16, 23, 24, 26, 28, 32–34, 58–68].

[32] In here, $\sim$ indicates the associated quantity to vary rapidly in time, whereas quantities without $\sim$ constitute constant or slowly varying values [63, 64].

$$\nabla^2 \tilde{E} - \frac{n^2}{c^2} \cdot \frac{\partial^2 \tilde{E}}{\partial t^2} = \frac{1}{\epsilon_0 c^2} \cdot \frac{\partial^2 \tilde{P}^{NL}}{\partial t^2}, \tag{3.1}$$

where n denotes the linear refractive index, c the speed of light, ϵ_0 the permittivity of free space (i.e. vacuum), and $\tilde{P}^{NL}$ the non-linear polarization[33]. Equation 3.1 can be interpreted as an inhomogenous wave equation, in which $\tilde{E}$ gets driven by $\tilde{P}^{NL}$. *W.l.o.g.*, the Maxwell equations define in this regard the light-matter-processes based on the associated polarization or, more precise, the susceptibility[34] $\chi^{(N)}$, induced by applying electromagnetic radiation with an electric field $\tilde{E}(t)$. Preluding, the induced polarization by linear optical processes can be expressed by:

$$\tilde{P}(t) = \chi^{(1)} \cdot \epsilon_0 \cdot \tilde{E}(t), \tag{3.2}$$

where $\chi^{(1)}$ is the linear first-order susceptibility and constitutes by that the constant of proportionality. Equation 3.2 holds for low-intensity light propagating through a dielectric medium. Considering monochromatic light, the time-varying electric field is given by:

$$\tilde{E}(t) = E_0 \cdot sin(\omega t) = E_0 \cdot e^{-i\omega t} + c.c., \tag{3.3}$$

with the magnitude of the oscillating field E_0 and the angular frequency $\omega = 2\pi c/\lambda$, and *c.c.* donating the complex conjugates. By increasing the irradiated light intensity to approximate the electric fields of atomic field strengths, the linear proportionality of Equation 3.2 becomes invalid as the induced polarization saturates. The atomic field strength is given by $E_{at} = e/(4\pi\epsilon_0 a_0^2)$, where $-e$ is the electron charge and $a_0 = 4\pi\epsilon_0\hbar^2/m_e e^2$ is the Bohr radius with $\hbar$ being the reduced Planck's constant and m_e being the mass of the electron. In such cases, the NLO response of Equation 3.2 can be expressed by Taylor-expanding the polarization as a power series in the field strength as:

$$\begin{aligned} \tilde{P}(t) &= \epsilon_0 \Big[\chi^{(1)} \tilde{E}(t) + \chi^{(2)} \tilde{E}^2(t) + \chi^{(3)} \tilde{E}^3(t) + ... \Big] \\ &= \tilde{P}^{(1)}(t) + \tilde{P}^{(2)}(t) + \tilde{P}^{(3)}(t) + ... \\ &= \tilde{P}^{(1)}(t) + \tilde{P}^{NL}(t) \end{aligned} \tag{3.4}$$

[33] This interpretation is in agreement with Larmor's theorem, according to which $\partial^2 \tilde{P}^{NL}/\partial t^2$ describes the acceleration of charges that generate electromagnetic radiation.

[34] The susceptibility $\chi^{(N)}$ take in general the form of a tensor of order N, but is reduced to a scalar value for an isotropic dielectric material.

or in matrix-notation:

$$\begin{aligned}\tilde{P}_i(t) = {} & \epsilon_0\chi_{ij}^{(1)}\Big[E_j e^{-i\omega t} + E_j^* e^{i\omega t}\Big] \\ & + \epsilon_0\chi_{ijk}^{(2)}\Big[E_j e^{-i\omega t} + E_j^* e^{i\omega t}\Big]\Big[E_k e^{-i\omega t} + E_k^* e^{i\omega t}\Big] \\ & + \epsilon_0\chi_{ijkl}^{(3)}\Big[E_j e^{-i\omega t} + E_j^* e^{i\omega t}\Big]\Big[E_k e^{-i\omega t} + E_k^* e^{i\omega t}\Big]\Big[E_l e^{-i\omega t} + E_l^* e^{i\omega t}\Big] \\ & + ... \quad .\end{aligned} \tag{3.5}$$

Substituting Equation 3.3 leads to:

$$\begin{aligned}\tilde{P}(t) = {} & \chi^{(1)} \cdot \epsilon_0 \cdot E_0 \cdot sin(\omega t) \\ & + \chi^{(2)} \cdot \frac{\epsilon_0 \cdot E_0^2}{2} \cdot [1 - cos(2\omega t)] \\ & + \chi^{(3)} \cdot \frac{\epsilon_0 \cdot E_0^3}{4} \cdot [3sin(\omega t) - sin(3\omega t)], \\ & + ... \quad ,\end{aligned} \tag{3.6}$$

where $\chi^{(1)}$, $\chi^{(2)}$, and $\chi^{(3)}$ denote the susceptibility tensors of first-, second-, and third-order, respectively, and are typically given in [(m/V)$^{\text{N-1}}$]. In general, $\chi^{(1)}$ can be rigorously described as the product of the atomic number density of condensed matter of $\rho_A \approx 1/a_0^3$ and the non-resonant atomic polarizability of a_0^3. Higher order susceptibilities can be analogously deduced as $\chi^{(2)} \simeq (4\pi\epsilon_0)^3\hbar^4/m^2e^5$ and $\chi^{(3)} \simeq (4\pi\epsilon_0)^6\hbar^8/m^4e^{10}$. Thus, $\chi^{(1)}$ exhibits values of $\sim$1 whereas the higher-order susceptibilities $\chi^{(2)}$ and $\chi^{(3)}$ are in the range of $\sim 10^{-12}$ and $\sim 10^{-22}$, respectively, which evinces the negligible contribution of NLO processes under low-intensity irradiation. Further, the first term of Equation 3.4 incorporates the linear polarization response as defined by Equation 3.2, which describes optical phenomena like reflection and refraction. Here, $\tilde{P}(t)$ and $\tilde{E}(t)$ are considered as scalar values for simplicity reasons. In this regard, the Kramers-Kronig relation[35] postulates an instantaneous response of the matter, i.e. $\tilde{P}(t)$ at a timepoint t depends exclusively on the current value of $\tilde{E}(t)$, which subsequently implies the irradiated matter to be lossless and dispersionless.

3.2.2 Second and third harmonic generation

As described in Section 2.2.1, incident light can undergo energy conserving and coherent scattering by means of parametric harmonic generation processes, meaning a time-invariant population of the quantum mechanical states. In simple words, multi-

[35] *W.l.o.g.*, the non-linear susceptibilities $\chi^{(N\geq 2)}$ are approximated as constants although they depend on the frequencies of the applied electromagnetic fields.

ple photons of identical energy with matching phases get fused into a single photon carrying the summed energy by a single quantum-mechanical process. The following elaboration only concerns all incident photons being of identical energy, i.e. identical wavelength and frequency[36]. The harmonic processes are termed based on the number of the incident photons, i.e. second and third harmonic generation (SHG and THG), are associated with the respective susceptibility tensor of identical order, and differ in their underlying physical requirements. Higher harmonic generations involving more than three photons and, thus, requiring intense optical radiation are extremely rare as they possess a susceptibility tensor too diminutive to lead to a significant contribution. Hence, only SHG and THG are typically employed as microscopy modalities, especially for investigating biological specimens, because of which only their theoretical considerations are in following elaborated. Furthermore, the hereinafter derived theoretical considerations hold for both a plane-wave radiation as well as a Gaussian-like diffraction-limited focused radiation.
For the Nth-harmonic generation process, the electric field strength of frequency ω_N along the propagation direction z can be in general expressed by:

$$\tilde{E}_{\omega_N}(z,t) = A_{\omega_N}(z) \cdot e^{i(k_{\omega_N} z - \omega_N t)} + c.c. \quad , \tag{3.7}$$

where $A_{\omega_N}(z)$ denotes the spatially slowly varying amplitude field envelope. Substituting Equation 3.7 into Equation 3.5 leads finally to:

$$\begin{aligned}\Big[\frac{\partial^2 A_{\omega_N}(z)}{\partial z^2} + 2ik_{\omega_N}\frac{\partial A_{\omega_N}(z)}{\partial z} - k_{\omega_N}^2 A_{\omega_N}(z) + \frac{n_{\omega_N}^2\omega_N^2}{c^2}A_{\omega_N}(z)\Big] \cdot e^{i(k_{\omega_N} z - \omega_N t)} + c.c. \\ = -\epsilon_0\mu_0\chi^{(N)}[A_{\omega_1}(z)]^N\omega_N^2 e^{i(Nk_{\omega_1} z - \omega_N t)} + c.c. \quad .\end{aligned} \tag{3.8}$$

Under the assumption of a slowly varying amplitude approximation as defined by:

$$\Big|\frac{\partial^2 A_{\omega_N}(z)}{\partial z^2}\Big| \ll \Big|k_{\omega_N}\frac{\partial A_{\omega_N}(z)}{\partial z}\Big|, \tag{3.9}$$

and substituting $k_{\omega_N} = n_{\omega_N}\omega_N/c$ as well as $c^2 = 1/\epsilon_0\mu_0$, and defining the wavevector mismatch $\Delta k = Nk_{\omega_1} - k_{\omega_N}$, Equation 3.8 simplifies to:

$$\frac{\partial A_{\omega_N}(z)}{\partial z} = \frac{i\chi^{(N)}\omega_N^2}{2c^2 k_{\omega_N}} \cdot \Big[A_{\omega_1}(z)\Big]^N e^{i\Delta k z}. \tag{3.10}$$

[36] Processes such as sum- or difference-frequency generation (SFG or DFG) are disregarded as they are not implemented in HyMPSOM.

Further assuming the incident field amplitude $A_{\omega_1}(z)$ to be unaffected by the NLO processes, a solution of Equation 3.10 can be obtained via integration from zero to a propagation distance L:

$$A_{\omega_N}(L) = \frac{i\chi^{(N)}\omega_N^2[A_{\omega_1}]^N}{2c^2k_{\omega_N}} \int_0^L e^{i\Delta kz}dz = \frac{i\chi^{(N)}\omega_N^2[A_{\omega_1}]^N}{2c^2k_{\omega_N}} \cdot \frac{e^{i\Delta kL}-1}{i\Delta k}. \tag{3.11}$$

The thereby yielded light intensity of the Nth-harmonic generation can be derived via the magnitude of a time-averaged Poynting vector defined by $I_{\omega_N} = 2n_{\omega_N}\epsilon_0 c|A_{\omega_N}|^2$ using the identity $sinc^2(x) = sin^2(x)/x^2$ as:

$$I_{\omega_N} = \frac{n_{\omega_N}\epsilon_0[\chi^{(N)}]^2\omega_N^4|A_{\omega_1}|^{2N}}{2k_{\omega_N}^2c^3} \cdot \left|\frac{e^{i\Delta kL}-1}{\Delta k}\right|^2 \tag{3.12}$$

$$= \frac{N^2\omega_1^2[\chi^{(N)}]^2{I_{\omega_1}}^N L^2}{2^{N+1}n_{\omega_1}^N n_{\omega_N}\epsilon_0^{N-1}c^{N+1}} sinc^2\Big(\frac{\Delta kL}{2}\Big). \tag{3.13}$$

Second harmonic generation (SHG)

The NLO process based on the second term of Equation 3.5 or Equation 3.6 is typically referred to as second harmonic generation (SHG) in the case of two incident photons of identical energy. SHG is by that a polarization response proportional to $cos(2\omega t)$ and describes the fusion of two incident photons into one photon of twice the incident frequency, i.e. twice the energy and half the wavelength. Assuming a non-vanishing second-order susceptibility tensor $\chi^{(2)}$ and substituting Equation 3.3 into Equation 3.5 leads to a non-linear polarization of:

$$\tilde{P}(t)^{(2)} = 2 \cdot \chi^{(2)} \cdot \epsilon_0 \cdot E \cdot E^* + \Big(\chi^{(2)} \cdot \epsilon_0 \cdot E^2 \cdot e^{2i\omega t} + c.c.\Big). \tag{3.14}$$

The first term of Equation 3.14 describes the contribution at zero frequency, which does not generate any electromagnetic radiation as its second time derivative vanishes and constitutes by that optical rectification. The second term is the contribution at frequency $\omega_2 = 2\omega_1$, which, based on Equation 3.1, leads to a generation of radiation at the second harmonic frequency. In a simplified form, the second-order susceptibility tensor is given by $\chi^{(2)} = \rho_A < \beta_h >$ with ρ_A as the atomic number density and $< \beta_h >$ as the orientally-averaged molecular hyperpolarizability, which finally leads to a proportionality of the SHG-intensity I_{SHG} of:

$$I_{SHG} \quad \propto \quad \chi^{(2)} \cdot I_{\omega_1}^2 \cdot sinc^2\Big(\frac{\Delta kL}{2}\Big). \tag{3.15}$$

In Equation 3.15 it becomes apparent that SHG signals require on the one hand a non-vanishing second-order susceptibility tensor $\chi^{(2)}$, which typically only exists in media of non-centrosymmetry, i.e. media without a structural inversion center which would decrease $< \beta >$. On the other hand, I_{SHG} is maximized for perfect phase matching $\Delta k = (n_{\omega_2} 2\omega_2/c) - 2(n_{\omega_1}\omega_1/c)$ which requires $n_{\omega_2} = n_{\omega_1}$. As in media with normal dispersion, the refractive index n is non-constant and typically increases with the light frequency ω, only materials exhibiting optical birefringences can induce SHG processes by possessing a polarization-dependent optical anisotropy. Thus, incident light being polarized along the orientation of higher refractive index of the medium compensates for the dispersion of the SHG-light polarized along the other orientation. In other words, a net degree of orientation of atomic dipoles, typically presented by highly organized and elongated structures, is required for SHG-light to interfere constructively and coherently with itself as well as the incident light. [23, 63–65]

Third harmonic generation (THG)

Analogously to SHG, third harmonic generation (THG) refers to the NLO process induced by the third term of Equation 3.5 or Equation 3.6 in the case of three incident photons of identical energy. Likewise, THG is proportional to $3sin(\omega t) - sin(3\omega t)$ and describes a process, in which three incident photons are eliminated under the generation of a single photon carrying the summed energy, i.e. thrice the frequency or a third of the initial wavelength. Using $\tilde{E}(t) = \mathcal{E}cos(\omega t)$ and the identity $cos^3(\omega t) = 1/4 \cdot cos(3\omega t) + 3/4 \cdot cos(\omega t)$, the corresponding non-linear polarization is given by:

$$\tilde{P}(t)^{(3)} = \frac{1}{4}\epsilon_0 \chi^{(3)} \mathcal{E}^3 cos(3\omega t) + \frac{3}{4}\epsilon_0 \chi^{(3)} \mathcal{E}^3 cos(\omega t). \tag{3.16}$$

In here, the first term represents the non-linear response at frequency $\omega_3 = 3\omega_1$, which therefore denotes for the THG. The second term regards the effect of the non-linear polarization to the incident field at frequency ω_1, which thereby leads to a non-linear property of the refractive index at frequency ω_1 as:

$$\begin{aligned} n &= n_0 + n_2 \cdot I \\ &= n_0 + \frac{3}{2n_0^2\epsilon_0 c}\chi^{(3)} \cdot I \\ &= n_0 + \frac{3}{2n_0^2\epsilon_0 c}\chi^{(3)} \cdot \frac{1}{2} n_0 \epsilon_0 c \mathcal{E}^2. \end{aligned} \tag{3.17}$$

In a simplified form, the third-order susceptibility tensor is defined as $\chi^{(3)} \propto (2\Delta n_0^2 c\gamma)$ $/(3\pi\omega_1)$ with Δn_0 being the difference in refractive index and γ the non-linear coefficient. Finally, the intensity of THG for focused Gaussian beams can be expressed as:

$$I_{THG} \propto \chi^{(3)} \cdot I \cdot {\omega_1}^3 \cdot \int_{z_1}^{z_2} \frac{e^{i\Delta kz}}{(1+2iz/b)^2} dz. \tag{3.18}$$

Equation 3.18 illustrates that THG is sensitive to refractive index inhomogeneities, dispersion, and $\chi^{(3)}$ variations within the focal volume of the beam. Assuming a diffraction-limited optical focus at frequency ω_1, thereby defining the axial extent (i.e. z_1 to z_2) over which THG signals are generated, THG is maximized for an optical boundary located within the optical focus. Furthermore, THG requires a non-vanishing phase mismatch but, in contrast to SHG, no optical anisotropy inducing birefringing.

3.2.3 Two- and three photon excitation fluorescence

Besides energy conserving harmonic generation, highly intense optical irradiation can lead to non-parametric multi-photon excitation processes (see Section 2.2.2), meaning a time-dependent population of the quantum mechanical states. In simple words, multi-photon excitation can be seen as the simultaneous absorption of several photons of identical energy[37]. In analogy to Section 3.2.2, the following elaboration only concerns multi-photon excitation processes involving two (2PE) and three photons (3PE), as higher numbers of simultaneously absorbed photons would require highly-intense radiation, are therefore extremely rare, and are not applicable on biological specimens[38]. Furthermore, in the following, only de-excitation processes via the emission of fluorescence photons are considered, whereas intersystem crossing, radiationless de-excitation, and photochemical energy transfer mechanisms are disregarded (see Section 2.2.4 and Section 2.2.5).

[37] The excitation of a molecule can however be also induced by the simultaneous absorption of photons of different energy, which is disregarded in this context due to the rare usage.

[38] For simplicity reasons, the absorption processes are abbreviated as 2PE and 3PE as they are directly associated with the excitation. This only holds under the assumption of the absorbed energy exciting the chromophore and neglecting other photophysical phenomena.

W.l.o.g., for fluorescence processes a three-state level can be considered (see Section 2.2 and Fig. 2.2) by defining the populations Ψ_1 of the ground state $(S_0;\nu_0)$, Ψ_2 of the targeted vibrational state in the first electronic excited state before internal conversion $(S_1;\nu_{i>0})$, and Ψ_3 of the vibrational ground state in the first electronic excited state $(S_1;\nu_0)$ from which the chromophore de-excites $(S_1;\nu_0 \rightarrow S_0;\nu_0)$ via the emission of a fluorescence photon[39]. The population rate of Ψ_2 is given by:

$$\frac{d\Psi_2}{dt} = \beta^{(N)}(t) \cdot \Psi_1 - \frac{1}{\tau} \cdot \Psi_2, \tag{3.19}$$

with:

$$\beta^{(N)}(t) = \sigma^{(N)} \cdot \frac{I(t)^N \xi^{(N)}}{(h\nu)^N}, \tag{3.20}$$

where $\sigma^{(N)}$ denotes the absorption cross section of the Nth-photon excitation, $I(t)$ the temporal profile of the incident laser pulse, and $\xi^{(N)}$ characterizes the spatial component[40] of the absorption process by:

$$\xi^{(N)} = \frac{1}{V} \cdot \int_V S^N(\vec{r}) d^3r. \tag{3.21}$$

In here, $S(\vec{r})$ describes the spatial profile of the laser pulse by $I(\vec{r},t) = I(t)S(\vec{r})$. Further, τ is the effective relaxation time defined as $\tau^{-1} = \tau_{21}^{-1} + \tau_{23}^{-1}$ (τ_{21} is the spontaneous de-excitation $\Psi_2 \rightarrow \Psi_1$ and τ_{23} is the time for internal conversion $\Psi_2 \rightarrow \Psi_3$). The population of the fluorescence state Ψ_3 is then defined as:

$$\frac{d\Psi_3}{dt} = \frac{\Psi_2}{\tau_{23}} - \frac{\Psi_3}{\tau_{31}}, \tag{3.22}$$

where τ_{31} represents the fluorescence lifetime with $\tau_{31} > \tau_{21} > \tau_{23}$ (see Section 2.2). Postulating $\Psi_1 + \Psi_2 + \Psi_3 = \Psi_0 = const.$ and assuming a rapid internal conversion with negligible accumulation of Ψ_2, a steady state can be approximated, which leads to[41]:

[39] The actual de-excitation via fluorescence reaches a vibrational mode of $\nu_{i>0}$ within S_0 based on the Franck-Condon principle (see Section 2.2.2 and Section 2.2.4).

[40] $\xi^{(N)} = 1$ for plane waves and $\xi^{(N)} < 1$ for the actual diffraction-limited Gaussian-like excitation spot.

[41] $B^{(N)}(t) \cdot \Psi_3$ describes saturation of the fluorescent state and can be neglected for $\Psi_3 \ll \Psi_0$.

$$\frac{d\Psi_3}{dt} + B^{(N)}(t) \cdot \Psi_3 = \beta^{(N)}(t) \cdot \Psi_0, \tag{3.23}$$

with $B^{(N)}(t) = \beta^{(N)}(t) + \tau_{31}^{-1}$. The time-dependent population of the fluorescent level Ψ_3 after optical absorption can be obtained as:

$$\Psi_3(t) = \Psi_0 \cdot \int_0^t \beta^{(N)}(t_1) e^{-\int_{t_1}^{t} B(t')dt'} dt_1. \tag{3.24}$$

Multi-photon excitation fluorescence

Next, the emitted fluorescence signal $F^{(N)}(\Delta t)$ upon Nth-photon excitation is expressed as:

$$F^{(N)}(\Delta t) = \Phi \cdot \int_0^{\Delta t} \Psi_3(t) f(t, \Delta t) dt, \tag{3.25}$$

where Δt represents the laser pulse duration, Φ the fluorescence quantum efficiency, i.e. quantum yield, and $f(t, \Delta t)$ the envelop of the laser excitation pulse. Under the assumptions of a square laser pulse with an average intensity I over the duration of the pulse and $\Delta t / \tau_{31} \ll 1$, Equation 3.25 can be rewritten as the Nth-photon excitation fluorescence intensity:

$$F^{(N)} \simeq \Phi \cdot \Psi_0 \cdot \left[1 + \frac{1}{I^N / I_s^{(N)}} \cdot (e^{I^N / I_s^{(N)}} - 1)\right], \tag{3.26}$$

with:

$$I_s^{(N)} = \xi^{(N)} \cdot \frac{(h\nu)^N}{\sigma^{(N)} \Delta t}. \tag{3.27}$$

Finally, assuming the incident laser excitation intensity to be significantly smaller than the saturation intensity ($I < [I_s^{(N)}]^{1/2}$), Equation 3.26 can be approximated to:

$$F^{(N)} \simeq \Phi \cdot \Psi_0 \cdot \frac{I_0^N}{I_s^{(N)}} \tag{3.28}$$

for the detected Nth-photon fluorescence intensity. Substituting Equation 3.27 into Equation 3.28, a dependency of:

$$F^{(N)} \propto I_0^N \cdot \sigma^{(N)} \tag{3.29}$$

can be observed, which illustrates that the yielded Nth-photon fluorescence intensity is directly proportional to the Nth-power of the incident excitation and to the Nth-photon excitation cross section $\sigma^{(N)}$. In here, the former points out that excitation processes above three photons would require extremely intense optical excitation, which potentially harms the specimen. The latter defines the actual light-matter-interaction including chromophore-specific properties such as the optical absorption characteristics as well as the non-linear response to the applied field.

Multi-photon excitation cross section

Using Equation 3.7 as the general description of electromagnetic waves propagating through a medium, dissipative losses like optical absorption relate to the imaginary part of the susceptibility $\Im[\chi^{(N)}]$. Further, as absorption processes alter the population of the underlying states in time-dependent excitation transitions, the even terms of the non-linear polarization extensions in Equation 3.4 can be neglected as they would vanish by time-wise averaging. Consequently, only the following contributions to the non-linear polarization are relevant for absorption processes[42]:

$$\tilde{P}_i^{(1)}(t) = \chi_{ij}^{(1)} \cdot \epsilon_0 \cdot E_j e^{-i\omega t} + c.c. + ... \tag{3.30}$$

$$\tilde{P}_i^{(3)}(t) = 3 \cdot \chi_{ijkl}^{(3)} \cdot \epsilon_0 \cdot E_j e^{-i\omega t} \cdot E_k^* e^{i\omega t} \cdot E_l e^{-i\omega t} + c.c. + ... \tag{3.31}$$

$$\tilde{P}_i^{(5)}(t) = 10 \cdot \chi_{ijklmn}^{(5)} \cdot \epsilon_0 \cdot E_j e^{-i\omega t} \cdot E_k^* e^{i\omega t} \cdot E_l e^{-i\omega t} \cdot E_m^* e^{i\omega t} \cdot E_n e^{-i\omega t} + c.c. + ... \tag{3.32}$$

By that, the absorbed light energy ΔE per volume V can be expressed as:

$$\left\langle \frac{d}{dt}\left(\frac{\Delta E}{V}\right)\right\rangle_{time} = \left\langle \frac{\partial \tilde{P}^{(1)}}{\partial t} \cdot E \right\rangle + \left\langle \frac{\partial \tilde{P}^{(3)}}{\partial t} \cdot E \right\rangle + \left\langle \frac{\partial \tilde{P}^{(5)}}{\partial t} \cdot E \right\rangle + ... \quad . \tag{3.33}$$

The first term corresponds to one-photon absorption processes with:

$$\begin{aligned} \left\langle \frac{\partial \tilde{P}^{(1)}}{\partial t} \cdot E \right\rangle &= 2 \cdot \epsilon_0 \cdot \omega \cdot \Im[\chi_{ij}^{(1)}] E_j E_j^* \\ &= \frac{4\pi\hbar\omega}{nc} \cdot \Im[\chi^{(1)}] I, \end{aligned} \tag{3.34}$$

[42] The notation in here is adapted to the matrix-form as conventionally used in multi-photon excitation fluorescence.

in which $I = \frac{nc}{2\pi}E^2$ is defined as the intensity and $\Im$ denotes the imaginary part. Analogously, two-photon absorption is given by:

$$\left\langle \frac{\partial \tilde{P}^{(3)}}{\partial t} \cdot E \right\rangle = \frac{24\pi^2\hbar^2\omega}{n^2c^2} \cdot \Im[\chi^{(3)}]I^2, \tag{3.35}$$

and three-photon absorption by:

$$\left\langle \frac{\partial \tilde{P}^{(5)}}{\partial t} \cdot E \right\rangle = \frac{160\pi^3\hbar^3\omega}{n^3c^3} \cdot \Im[\chi^{(5)}]I^3. \tag{3.36}$$

By that, the associated absorption coefficients $\mu_{a,\alpha}$, $\mu_{a,\beta}$, and $\mu_{a,\gamma}$ corresponding respectively to one-, two-, and three-photon absorption can be obtained as:

$$\mu_{a,\alpha} = \frac{4\pi\hbar\omega}{nc} \cdot \Im[\chi^{(1)}], \tag{3.37}$$

$$\mu_{a,\beta} = \frac{24\pi^2\hbar^2\omega}{n^2c^2} \cdot \Im[\chi^{(3)}], \tag{3.38}$$

$$\mu_{a,\gamma} = \frac{160\pi^3\hbar^3\omega}{n^3c^3} \cdot \Im[\chi^{(5)}], \tag{3.39}$$

using $dI/dz = -\mu_{a,\beta}I - \mu_{a,\gamma}I^2 - \mu_{a,\gamma}I^3$. Finally, the absorption cross sections can be derived as:

$$\sigma^{(1PA)} = \frac{\mu_{a,\alpha}}{\rho_A}, \tag{3.40}$$

$$\sigma^{(2PA)} = \frac{\hbar\omega\mu_{a,\beta}}{\rho_A}, \tag{3.41}$$

$$\sigma^{(3PA)} = \frac{\hbar^2\omega^2\mu_{a,\gamma}}{\rho_A}, \tag{3.42}$$

with ρ_A being the atomic number density. As the absorption coefficients depend directly proportional to the susceptibility tensors of first-, third-, and fifth-order, respectively, high-number optical absorption is typically limited to regions with highly intense optical excitation.

3.2.4 Multi-photon signal acquisition and processing

As the previously derived physical considerations of NLO processes require highly intense photon fluxes, multi-photon microscopy is associated with an intrinsic optical sectioning as the underlying NLO process are only induced within the optical focal volume according to Equation 2.15 as explained in Section 2.4.1. This is due to the dependency on higher powers of the applied optical irradiation as well as the process-corresponding susceptibility tensor. In general, such optical irradiation is typically achieved by lasers emitting ultra-short pulses of durations <200 fs at repetition rates of tens of MHz, which are focused in a diffraction-limited manner into the specimen. Whereas the latter spatial confinement is achieved by microscopic objective lenses, the former temporal confinement is enabled by mode-locked lasers, such as solid state lasers based on Ti:Sapphire, Nd:YAG, or Nd:YLF, with emission wavelengths in the near-infrared range. This spectral range is, as explained in Section 2.2, assigned with lower tissue absorption and lower Rayleigh scattering, which therefore allows for deeper penetration. Furthermore, the time-bandwidth product (TBWP), i.e. the product of pulse duration and spectral bandwidth, relates the minimum achievable pulse duration to the carried spectral bandwidth for so-called transform-limited Gaussian pulses by $\tau_\lambda = 0.44\lambda_0^2/c\lambda_{FWHM}$.
Commonly, multi-photon microscopy is performed using 2D laser-scanning approaches (see Section 2.4.3) due to the high repetition rates of the lasers. For 3D imaging, typically referred to as 'Z'-scan, axially stacked 2D-scanned images are recorded by either axially moving the optical focus via translating the objective lens, by modifying the optical dispersion through implementing special optical elements, or by mechanically translating the specimen. In contrast to the time-wise instantaneous harmonic generations, multi-photon excitation fluorescence is characterized by the lifetime of the fluorescent state of up to tens of nanoseconds, which thereby limits the applicable scanning speed. Furthermore, whereas multi-photon excitation fluorescence signals are assumed to be emitted isotropically in all directions, harmonic generation signals possess an anisotropic and predominant forward direction. In this regard, the forward-to-backward ratio of SHG is ∼5/1 and of THG ∼20/1.
Multi-photon signal acquisition is typically achieved by highly-sensitive single-element non-descanned photodetectors[43], such as avalanche photodiodes (APD) and photomultiplier tubes (PMT), or by 2D detectors such as electron multiplying charge-coupled devices (EMCCD). In order to specifically dedicate the equipped detectors to a multi-photon signal, optical elements such as dichroic mirrors or bandpass filters are installed to select the respective spectral range (e.g. $\lambda_{in}/2$ for SHG), prevent crosstalk among the signals, and block the excitation light from reaching the detector. The optical detec-

[43] Non-descanned detection describes the unneccesity of spatially confining the detection via e.g. pinholes as used in confocal microscopy.

tion itself is typically performed by collecting the respective photons over a time period referred to as pixel dwell or bin time. With sensitivities of down to a few photons, such detectors enable pixel dwell times of <1 µs. Besides integration of collected photons, approaches like time-correlated single-photon counting (TCSPC) assign arrival times to individually detected photons. Such approaches allow on the one hand for temporal differentiation among NLO processes (e.g. instantaneous harmonic generation vs. lifetime-defined fluorescence), and on the other hand for studying the temporal profiles of the processes themselves, which then facilitates fluorescence lifetime microscopy (FLIM) or fluorescence correlation spectroscopy (FCS). Furthermore, the photon collection ability strongly depends on the position of the detector. Whereas most of the multi-photon signals can be recorded in backward- or epi-direction, i.e. through the equipped focusing objective, harmonic generations are best captured in forward direction as explained earlier. In both arrangements, the 2D sensitivity of the detector can however be approximated to follow a 2D Gaussian shape covering the scanned FOV of the imaging plane, which therefore lowers the contrast at outer regions of the area and subsequently favors 2D sensitivity field corrections to achieve homogeneous contrast.

3.3 Background on optical-resolution optoacoustic microscopy

As generally elaborated in Section 2.2.3, the radiationless de-excitation upon optical absorption leads to a temperature rise and subsequently to an increase of the local pressure known as the optoacoustic effect. In contrast to optoacoustic mesoscopy (i.e. acoustic-resolution optoacoustic microscopy (AR-OAM)) and optoacoustic tomography (OAT), optical-resolution optoacoustic microscopy (OR-OAM) is based on a diffraction-limited optical excitation volume. The following chapter will therefore first formulate generally the theoretical considerations for optoacoustic signal generations (see Section 3.3.1) and then elaborate on the adaption to OR-OAM (see Section 3.3.2). Furthermore, relevant concepts for its practical realization are described regarding the signal acquisition and processing (see Section 3.3.3) as well as the total impulse response of a given OR-OAM system (see Section 3.3.4)[44].

3.3.1 Optoacoustic signal generation

As described in Section 2.2.3, non-radiative de-excitation of absorbed optical energy induces photoacoustic (optoacoustic) processes. The underlying light-matter-interaction is in the following simplified in order to derive the corresponding optoacoustic signal generation theoretically.

[44] The following chapters are based on [23, 24, 35, 42, 69–74].

Initial optoacoustic pressure

Regarding the initial optoacoustic pressure generation, the thermal relaxation time τ_{th} and the stress relaxation time τ_{st} define the typical time scale of the optoacoustic effect:

$$\tau_{th} = \frac{d_{th}^2}{\alpha_{th}} \tag{3.43}$$

$$\tau_{st} = \frac{d_{th}}{c}, \tag{3.44}$$

with d_{th} measuring the dimension of the heated area upon laser radiation[45], α_{th} denoting the thermal diffusivity (m^2/s), and c being the speed of sound in the heated medium (m/s), i.e. $\sim$1500 m/s for water. In a regime termed thermal confinement, the laser pulse duration is significantly shorter than τ_{th} leading to a negligible heat conduction during the laser pulse. Analogously, within the regime of so-called stress confinement, the laser pulse is shorter than τ_{st}, which means a negligible stress propagation during the laser pulse. Based on that, the laser-irradiation-induced fractional volume expansion is given by:

$$\frac{dV}{V} = -\kappa p(\vec{r}) + \beta T(\vec{r}), \tag{3.45}$$

where κ is the isothermal compressibility (Pa^{-1}), β is the thermal coefficient for volume expansion (K^{-1}), and $p(\vec{r})$ and $T(\vec{r})$ are the locally induced changes in pressure (Pa) and temperature (K), respectively. Further, κ is defined as:

$$\kappa = \frac{C_p}{\rho c^2 C_V}, \tag{3.46}$$

in which ρ denotes the mass destiny of the irradiated matter (kg/m^3) and C_p and C_V describe the specific heat capacity at constant pressure and volume (J/kg K), respectively. The initial pressure $p_0(\vec{r})$ generated optoacoustically upon laser excitation with a sufficiently short pulse to fulfill heat and stress confinement can be expressed as:

$$p_0(\vec{r}) = \frac{\beta T(\vec{r})}{\kappa} = \Gamma \cdot \eta_{th} \cdot \mu_a(\vec{r}) \cdot \Phi(\vec{r}). \tag{3.47}$$

[45] d_{th} is the smaller instance of either the dimension of the targeted object or the decay constant of the optical energy deposition.

where μ_a is the optical absorption coefficient (cm^{-1}) and Φ the optical fluence (W/cm^2). In here, Γ is defined as the dimensionless Grüneisen parameter as:

$$\Gamma = \frac{\beta}{\kappa \rho C_V} = \frac{\beta c^2}{C_P}, \tag{3.48}$$

which can be empirically approximated for aqueous matter with $\Gamma_{aq}(T_0) = 5.3 \cdot 10^{-3} \cdot T_0 + 4.3 \cdot 10^{-3}$ with T_0 as the current temperature in °C.

Optoacoustic pressure wave propagation

At fulfilling the thermal confinement condition, the propagation of an optoacoustically induced pressure wave can be formulated as:

$$\left(\nabla^2 - \frac{1}{c^2}\frac{\partial^2}{\partial t^2}\right) p(\vec{r}, t) = -\frac{\Gamma}{c^2}\frac{\partial}{\partial t} H(\vec{r}, t). \tag{3.49}$$

with $p(\vec{r}, t)$ denoting the acoustic pressure at a given location $\vec{r}$ and time t, and $T(\vec{r}, t)$ denoting analogously the rise in temperature. Here, the right side represents the source term with the heating function $H(\vec{r}, t)$:

$$H(\vec{r}, t) = \eta_{th} \cdot \mu_a(\vec{r}) \cdot \frac{\partial}{\partial t}\Phi(\vec{r}, t), \tag{3.50}$$

defined as the converted thermal energy per unit volume and time. Thus, the source term contains the time derivative of the heating function H, which evinces that only time-variant heating or rather laser radiation leads to the generation of a pressure wave. As the time derivative of the optical fluence equals the irradiated light intensity $I(\vec{r}, t)$ by $\frac{\partial}{\partial t}\Phi(\vec{r}, t) = I(\vec{r}, t)$, pulsed or time-wise modulated illumination are required to generate optoacoustic pressure waves. The forward solution of Equation 3.49 can be obtained by the Green's function approach[46]. For that, the Green's function $G(\vec{r}, t)$ is defined as the response to a delta impulse in time and space of the differential equation:

$$\left(\nabla^2 - \frac{1}{c^2}\frac{\partial^2}{\partial t^2}\right) G(\vec{r}, t) = \delta^3(\vec{r})\delta(t), \tag{3.51}$$

[46] In the context of optoacoustics, the usage of the Green's function leads to an interpretation of the spatial δ-function as a point source and of the time δ-function as a step heating function. The latter is due to the proportional dependence of the source term to the second derivative of the temperature.

in which the free-space Green's function $G(\vec{r},t)$ follows:

$$G(\vec{r}-\vec{r}',t-t') = \frac{\delta\left((t-t') - \frac{|\vec{r}-\vec{r}'|}{c}\right)}{4\pi|\vec{r}-\vec{r}'|} \tag{3.52}$$

and constitutes a spherical wave originating at a speed c from a position $\vec{r}'$ at a time t' with an amplitude linearly decreasing with distance $|\vec{r}-\vec{r}'|$. By that, the forward solution of Equation 3.49 can be expressed as:

$$\begin{aligned} p(\vec{r},t) &= \frac{\Gamma}{4\pi c^2}\iiint_V \int_t \frac{\delta\left((t-t') - \frac{|\vec{r}-\vec{r}'|}{c}\right)}{|\vec{r}-\vec{r}'|}\frac{\partial}{\partial t'}H(\vec{r}',t')d^3\vec{r}'dt' \\ &= \frac{\Gamma}{4\pi c^2}\frac{\partial}{\partial t}\iiint_V \frac{d^3\vec{r}'}{|\vec{r}-\vec{r}'|}H(\vec{r}',t')\Big|_{t'=t-|\vec{r}-\vec{r}'|/c} \end{aligned} \tag{3.53}$$

In this regard, Equation 3.53 leads to the interpretation of the pressure $p(\vec{r},t)$ at a given position $\vec{r}$ and time t as the time derivative of summed and heating-function-weighted spherical waves each originating from a point source. It therefore can be seen as the optoacoustic analogy of Huygens' principle. Finally, the light propagation can be assumed as infinitely fast within a spatially limited sample size, which allows to separate the heating function into a spatial and a temporal term. Further assuming an ultra short pulse, the temporal term can be substituted with a delta function, which finally leads to $H(\vec{r},t) = H_r(\vec{r})\cdot H_t(t) = H_r(\vec{r})\cdot\delta(t)$. Inserting this expression in Equation 3.47 allows to simplify Equation 3.53 to:

$$p_{\delta t}(\vec{r},t) = \frac{\partial}{\partial t}\left[\frac{t}{c}\iint_S p_0(\vec{r}')d\Omega\right]\Big|_{|\vec{r}-\vec{r}'|=ct} \tag{3.54}$$

In here, the time derivative accounts for the bipolar nature of the pressure signal, which is typically referred to as the N-shape signal and can be explained physically by the combination of a diverging and converging compression wave. Assuming a spherical and finite absorber, the converging spherical wave transforms into a diverging rarefraction wave upon passing through the center of the absorber and, thus, accounts for the negative part of the bipolar signal. By that, the absorber determines the duration of the optoacoustic bipolar signal and, thus, the carried frequency content. Hence, the frequency spectrum of the optoacoustic signal is inversely proportional to the size of the absorber and typically reaches up to several hundreds of MHz for absorbing entities in biological tissue.

3.3.2 Optical-resolution optoacoustics

Optical-resolution optoacoustic microscopy (OR-OAM) is based on exciting the specimen with a diffraction-limited optical focus. The induced optoacoustic effect therefore generates pressure waves exclusively originating from the optical focal cone. Assuming that the optical focus is generally smaller than the optoacoustically-active moieties in biological specimens[47], OR-OAM obtains in all situations signals that emanated from objects of identical size, i.e. the optical focal volume. In this regard, the optical fluence $\Phi(\vec{r})$ of an optical focus can be expressed as a Gaussian beam depending on the distance $\vec{r} = (r_x, r_y, r_z)$ from the central focal point at $\vec{r} = 0$ by:

$$\Phi(\vec{r}) = \Phi_0 \cdot (\omega_0/\omega(r_z))^2 \cdot e^{-2(r_x^2+r_y^2)/\omega(r_z)^2} \tag{3.55}$$

with Φ_0 denoting the maximum fluence at the central focal point, ω_0 the waist radius, and $\omega(r_z)$ the beam spot size at axial position r_z. In here, effects of absorption and scattering processes are neglected on the beam propagation and focal shape. In reality, such effects induce a so-called optical shadowing, which describes decreased visibility of objects aligned axially within the focal volume. For a given microscopic objective with a numerical aperture NA at an optical excitation wavelength λ, Eq. 3.55 can be adapted to:

$$\Phi(\vec{r}) \approx \frac{\Phi_0 \lambda^2}{\lambda^2 + r_z^2 \pi^2 NA^4} \cdot e^{-\frac{-2(r_x^2+r_y^2)\pi^2 NA^2}{\lambda^2 + r_z^2 \pi^2 NA^4}}. \tag{3.56}$$

Inserting Equation 3.56 into Equation 3.47 leads to formulating OR-OAM signals as:

$$p_0(\vec{r}) \approx \frac{\Gamma \eta_{th} \mu_a(\vec{r}) \cdot \Phi_0 \lambda^2}{\lambda^2 + r_z^2 \pi^2 NA^4} \cdot e^{-\frac{-2(r_x^2+r_y^2)\pi^2 NA^2}{\lambda^2 + r_z^2 \pi^2 NA^4}}. \tag{3.57}$$

Here, the initial pressure is predominantly determined by the excitation wavelength λ, the local absorption coefficient $\mu_a(\vec{r})$ as well as the numerical aperture NA of the exploited objective lens [69]. Assuming a constant excitation wavelength (e.g. 532 nm) and a homogeneously distributed absorption coefficient (e.g. hemoglobin in RBCs and, thus, in blood in microvasculature), the initial pressure is determined predominantly by the microscope objective's NA. By further assuming absorbing moieties being larger than the optical focal volume, the initial pressure is according to Eq. 3.57 constant for a given type of absorber.

[47] This holds in most cases of e.g. microvasculature, red blood cells (RBCs), or melanocytes.

To assess the expected frequency content of generated OR-OAM signals, the optical focal volume can be roughly approximated to be a sphere[48] with a diameter of <2 µm. Using $f_{peak} \approx 0.66 c_\alpha / d_\alpha$ with c_α and d_α being the speed of sound and diameter of the optoacoustic-active object, respectively (in this consideration the entire optical focus of $d_\alpha \approx 2$ µm), the frequency content of initial OR-OAM signals peak at frequencies beyond $f_{peak} > 500$ MHz. During propagation through a medium, acoustic pressure waves experience acoustic attenuation, which is caused on the one hand by internal frictional losses and on the other hand by heat diffusion among areas of different temperature inducing non-isothermal and non-adiabatic pressure changes. Furthermore, the acoustic attenuation is frequency-dependent, so that higher frequencies are affected stronger, and is empirically found as:

$$p(|\vec{r}|, f) = p_0 \cdot e^{-\alpha(f)\cdot|\vec{r}|} = p_0 \cdot e^{-5ln10\cdot(10^{-6})^n \alpha_0 \cdot |f|^n \cdot |\vec{r}|}, \tag{3.58}$$

with $|\vec{r}|$ being the propagation distance and f the respective optoacoustic frequency, $\alpha(f)$ describes the frequency dependent attenuation coefficient, α_0 is the attenuation constant[49] in $[\alpha_0] = dB$, and n is a medium dependent constant. Water exhibits values of $\alpha_0 = 0.002$ dB/MHz^2 and n ≈ 2; soft tissue of $\alpha_0 \approx 0.5$ dB/MHz^2 and n ≈ 1. As typical focal distances of ultrasound transducers used for OR-OAM are in the range of 1-4 mm, the highest detectable frequency of OR-OAM signals propagating through water as a coupling medium is in the range of ∼300 MHz, which therefore determines both the appropriate properties of the ultrasound sensor for a given propagation distance and the acoustically-limited maximum imaging depth of OR-OAM.

3.3.3 Optoacoustic signal acquisition

In order to sense the optoacoustic signals carrying a broadband frequency content over tens to hundreds of MHz, a detection characterized by a matching frequency range, by a high dynamic range, and by high sensitivity is required. For that, piezo-electric ultrasound transducers are typically equipped. The actual sensing component of the transducer, i.e. the active element, transforms incoming pressures waves into voltage signals via the piezo-electric effect. This effect is based on the fact that incoming pressure waves lead to a mechanical deformation of the piezo-electric material, which induces a re-orientation of molecular dipole moments and finally ends in a voltage difference directly proportional to the degree of deformation, i.e. the amplitude of the

[48] The actual focal volume is defined by the optical PSF according to Eq. 2.14 and Eq. 2.18 in Section 2.4.1 and possesses typical values of 500 nm laterally and 4 µm axially at λ= 500 nm and NA=0.5, respectively.

[49] α_0 is typically given in $[\alpha_0] = Np$, which can be transformed to decibels by $\alpha_{0,Np} = 5ln10 \cdot (10^{-6})^n \alpha_{0,dB}$.

pressure wave. Standard piezoelectric materials are piezoceramics (i.e. ferroelectric materials in crystalline structures; e.g. lead zirconate titanate (PZT) or lithium niobate (LiNbO3)), composite materials (i.e. polymer-embedded piezoceramics), or polymer-films (e.g. polyvinylidene fluoride (PVDF)). In here, the thickness of the active element determines the central frequency of detection, which, based on the considerations in Section 3.3.2, is optimized for transducers used for OR-OAM to have a central frequency in the range of ∼50-100 MHz and a bandwidth of ∼70-200%. For sensitivity enhancement, most widespread transducers used in OR-OAM facilitate acoustic focusing by either a curved piezo-electric element or a plan-concave glass lens (e.g. SiO_2). The focusing leads thereby either to a flat plane-like sensitivity field for cylindrical 2D focusing or a double-conical sensitivity field for spherical focusing. In both cases, a focused transducer exhibits a spatially-dependent acoustic sensitivity, which is highest in the acoustic focus or focal volume and decreases at increasing lateral and axial distance. Furthermore, a backing material is typically placed behind the active element, which compensates for reverberations and, thus, influences sensitivity and bandwidth of the entire transducer.
Besides piezo-electric ultrasound transducers, optoacoustic or ultrasound waves in general can be sensed by pure optical techniques. Although such methods are not a central key aspect of this thesis, an approach for optically sensing OR-OAM signals was conducted on HyMPSOM. This project is elaborated in Section 5.4.3, which also contains a brief overview of all-optical optoacoustic methods.

3.3.4 Total impulse response and correction

As described in Section 2.4.1, the imaging capabilities or, in other words, the imaging function of a given photonic microscope is typically characterized by the PSF. In analogy to pure optical microscopy (e.g. fluorescence microscopy), OR-OAM is also associated with a PSF, which, however, differs from the optical PSF in various key aspects. On the one hand, OR-OAM signals are inherently three-dimensional as they are time-dependent readings, whereas optical signals are typically time-independent single-plane signals. On the other hand, the PSF of OR-OAM depends on both optical and acoustic properties. In here, the former defines the OR-OAM PSF laterally and the latter axially. In contrast, pure optical PSFs are exclusively determined by optical parameters. Additionally, OR-OAM signals are detected by an inhomogeneously-shaped sensitivity field of the equipped ultrasound detector and, thus, depend stronger on the signals origin compared to the detection of optical signals, which is typically based on a homogeneous capturing by optical detectors throughout the imaged volume. In this regard, the PSF is best treated as the spatial representation of signals originating from a point source. For an appropriate description of the OR-OAM PSF, the entire imaging function can be unraveled into four central and mostly independent factors

each describing a process step of OR-OAM from the optical excitation to the signal digitization:
First, an optical excitation pulse $I_\gamma(t)$ excites the specimen within the optical focus. Typical optical excitation pulses used for OR-OAM are in the range of ∼1 ns and can be approximated by a δ-impulse in time. **Second**, the laser pulse gets transformed into the initial pressure $p_0(\vec{r}, t)$ following the typical N-shape. As elaborated in Section 3.3.2, $p_0(\vec{r}, t)$ can, in first approximation, be assumed to be spatially independent by implying the absorbing moiety being always larger than the optical focal volume. **Third**, depending on the image formation procedure, e.g. laser-scanning (see Section 2.4.3), OR-OAM potentially receives signals with lateral and/or axial offset with respect to the focus of the acoustic sensitivity field. In contrast to signals originating from the acoustic focus of the equipped transducer, which encounter the active element in parallel[50], signals from lateral and/or axial offset positions encounter the active element in a bent, tilted, and modified way depending on their respective origin. Furthermore, at equipping an acoustic focusing lens, optoacoustic signals generated at offset positions can potentially reflect and interfere within the glass lens. By assuming that each optoacoustically generated initial pressure wave $p_0(t)$ is independent of the spatial location, the above mentioned ways of spatially dependent modifications are referred to as spatial impulse response $SIR(\vec{r}, t)$. The $SIR(\vec{r}, t)$ is in general defined as the spatial dependence of a system to capture impulse signals, i.e. δ-signals, in time and space, and compiles thereby the modification of detected pressure waves as a function of their origin. **Fourth**, detected OR-OAM signals are additionally altered by the electrical properties of the acquisition chain including the ultrasound detector, signal amplifiers, cables, and the utilized data acquisition card and signal processing. The corresponding response of the entire electric acquisition system to a δ-signal is termed electric impulse response $EIR(t)$, which is a spatially invariant characteristic of a given system [12, 23, 75–78].
All of the four above mentioned factors of the OR-OAM imaging function, i.e. the laser excitation pulse $I_\gamma(t)$, the initial pressure $p_0(\vec{r}, t)$, the spatial impulse response $SIR(\vec{r}, t)$, and the electric impulse response $EIR(t)$, constitute in this regard signal convolutions, which are typically collectively described as the total impulse response $TIR(\vec{r}, t)$ of a system. The $TIR(\vec{r}, t)$ constitutes a 4D array (r_x, r_y, r_z, t) containing time-dependent impulse responses at all detectable positions throughout a 3D volume [75–78]. In this regard, detected OR-OAM pressure signals can be expressed as:

[50] Transducers equipping an acoustic focusing glass lens usually contain a flat active element, due to which the acoustic focus is defined as the signal origin at which the pressure wave hits the active element as a plane wave. Transducers using a bent active element for focusing have an acoustic focus at a spatial location, at which the spherical wavefront matches the bending radius of the active element.

$$\begin{aligned} p_{det}(\vec{r},t) &= I_\gamma(t) * p_0(\vec{r},t) * SIR(\vec{r},t) * EIR(\vec{r},t) \\ &= p_0(\vec{r},t) * TIR(\vec{r},t), \end{aligned} \tag{3.59}$$

where $*$ denotes the mathematical convolution operation. Analogously, the influences of the captured frequencies f can be described by the Fourier transformed ($\mathcal{F}$) counterpart as:

$$TFR(\vec{r},f) \;=\; SFR(\vec{r},f) * EFR(\vec{r},f) = \mathcal{F}\Big\{TIR(\vec{r},t)\Big\}, \tag{3.60}$$

where $TFR(\vec{r},f)$, $SFR(\vec{r},f)$, and $EFR(\vec{r},f)$ are the total, spatial, and electric frequency response, respectively. As the $TIR(\vec{r},t)$ is in general a system characteristic, precise knowledge would potentially facilitate the application of signal correction algorithms by:

$$p_{corr}(\vec{r},t) \;=\; p_{det}(\vec{r},t) * TIR^{-1}(\vec{r},t) \cong p_0(\vec{r},t), \tag{3.61}$$

where $p_{corr}(\vec{r},t)$ is the $TIR(\vec{r},t)$-corrected version of the detected pressure $p_{det}(\vec{r},t)$ and, thus, approximates the initially generated pressure $p_0(\vec{r},t)$.

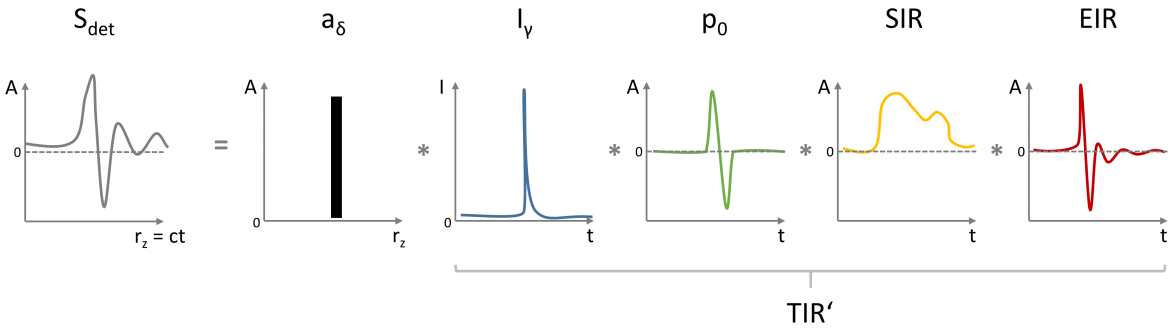

Figure 3.1: Schematic depiction of the OR-OAM imaging function unraveled to the underlying relevant convolution steps. The detected signal $S_{det}(a_\delta(\vec{r}),r_z)$ in OR-OAM results from the excitation of spatial point-like absorber a_δ with a laser pulse $I_\gamma(t)$, which generates an initial pressure $p_0(\vec{r},t)$ that gets sensed by the transducer according to its spatial impulse response $SIR(\vec{r},t)$ and modified during digitization by the electric impulse response $EIR(t)$.

Regarding the final imaging conducted on an OR-OAM system under the assumption of a constant and spatially-independent initial pressure $p_0(\vec{r},t)$, $S(a_\delta(\vec{r}),r_z)$ can be

defined as the detected and spatially backprojected signal[51] of a point-like absorber $a_\delta(\vec{r})$ (see Fig. 3.1):

$$\begin{aligned} S_{det}(a_\delta(\vec{r}), r_z) &= a_\delta(\vec{r}) * I_\gamma(t) * p_0(\vec{r}, t) * SIR(\vec{r}, t) * EIR(\vec{r}, t) \\ &= a_\delta(\vec{r}) * TIR'(\vec{r}, t), \end{aligned} \tag{3.62}$$

where $TIR'(\vec{r}, t) = p_0(\vec{r}, t) * TIR(\vec{r}, t)$ includes the initial OR-OAM pressure response as an additional convolution. Accordingly, corrections based on:

$$S_{corr}(a_\delta(\vec{r}), r_z) \quad = \quad S_{det}(a_\delta(\vec{r}), r_z) * TIR'^{-1}(\vec{r}, t) \cong a_\delta(\vec{r}), \tag{3.63}$$

where $S_{corr}(a_\delta(\vec{r}), r_z)$ denotes the corrected spatial projection of the δ-absorber $a_\delta(\vec{r})$ and integrates the entire physical process from signal generation to digitization in form of an imaging function of the OR-OAM system. In other words, corrections performed using $TIR'(\vec{r}, t)$ compensate for all steps of imaging an object with OR-OAM and lead directly to a correct spatial representation.
These considerations demonstrate, that OR-OAM data should be corrected on the signal level rather than on the level of the final reconstructed image. Furthermore, such a signal correction has to be carried out in a 3D spatially-dependent fashion as the $TIR'(\vec{r}, t)$ highly depends on the signal origin $\vec{r}$. For that, a high-precision determination of the $TIR'(\vec{r}, t)$ is necessary, which requires identical δ-absorbers, i.e. point sources, located at all observable positions in space. Previous attempts were based on utilizing absorbing microspheres, which was shown to be time-consuming, prone to positioning errors, and impeded by sensitivity issues and microsphere destruction [79–82]. Thus, these approaches could only be used to characterize the focal impulse response, i.e. $a_\delta * I_\gamma(t) * p_0(t) * EIR(\vec{r}, t)$, but dismissed spatial dependencies of signal acquisition. Other approaches used an optical focused excitation of an absorber plane of finite thickness [79–83], which therefore did not constitute a δ-absorber and led subsequently to a characterization of $a_{non-\delta}(\vec{r}) * I_\gamma(t) * p_0(\vec{r}, t) * SIR(\vec{r}, t) * EIR(\vec{r}, t)$. In addition to that, using an active ultrasound device was used to generate acoustic signals within the sensitivity field [79, 80], which also constitutes the standard way of ultrasound transducer characterization performed by the respective manufacturer. For that, either the ultrasound sensor itself is used for both acoustic signal emission and sensing, i.e. pulse-echo mode, or a secondary ultrasound device is equipped as the acoustic source. In both cases, the characterization leads to $TIR(\vec{r}, t) = TIR_1(\vec{r}, t) * TIR_2(\vec{r}, t)$, in which the determined total impulse response contains the properties of both ultrasound devices, i.e. 1 and 2, in an inseparable manner [77, 79, 80]. Finally, numerical simulations

[51] In $S(a_\delta(\vec{r}), r_z)$, $\vec{r}$ denotes the spatial position of the absorber a_δ and r_z denotes the distance of backprojection along the z-axis with $r_z = c \cdot t$ based on the speed of sound c.

have been proposed for the characterization of an OR-OAM system. [77]. However, computational approaches do neither reveal the electric properties of the acquisition change accurately as well as incorporate the actual laser pulse shape and, thus, lead to a determination of $p_0(\vec{r},t) * SIR(\vec{r},t)$.
To address this lack of a high-precision $TIR'(\vec{r},t)$-determination for OR-OAM, we devised a novel method based on spatially-dependent surrogate optoacoustic point sources, which are generated by 3D-raster-scanning an optical focus across an ultra-thin absorbing plane. This approach facilitated not only complete analysis of the imaging properties of the OR-OAM modality of HyMPSOM but also allowed for appropriate correction algorithms to be applied on the signal level. The practical realization is elaborated in detail in Section 4.4.

3.4 Background on microscopy image processing

Regardless of the modality used for capturing microscopy images, image processing is widely used due to two reasons: First, image processing aims for improving the depiction of captured information for the human eye. In this regard, an image constitutes a 2D matrix carrying spatially encoded information retrieved from the investigated specimen. The information itself is hierarchically organized from single-pixel values over local structures up to image-wide signal patterns. Second, image processing facilitates the application of several quantitative and qualitative analysis approaches to explore the investigated specimen in more detail. In here, image processing opts for enabling automated perceptions of applied analysis algorithms by purifying the contained information[52].
This chapter discusses exclusively the image processing applied typically on microscopy images recorded using HyMPSOM. For that, the input images constitute 2D matrices $f(x,y)$ carrying raw signal values of the respective imaging modality stored at pixel position (x,y). An image processing operation can thus defined as:

$$g(x,y) = T\Big[f(x,y)\Big], \tag{3.64}$$

where $g(x,y)$ is the processed output image yielded by applying a processing operator T on the image. The operator T represents by that all applied processing steps, which could target in general each location (x,y) of the image either individually, i.e. the neighborhood size 1 x 1, or in 2D patches of size i x i, where i takes values between 2 and the dimension of the image.
Fig. 3.2 illustrates exemplary image processing steps typically carried out on HyMPSOM data including contrast adjustments (e.g. Gamma correction and histogram

[52] The following chapters are based on [43, 84–92].

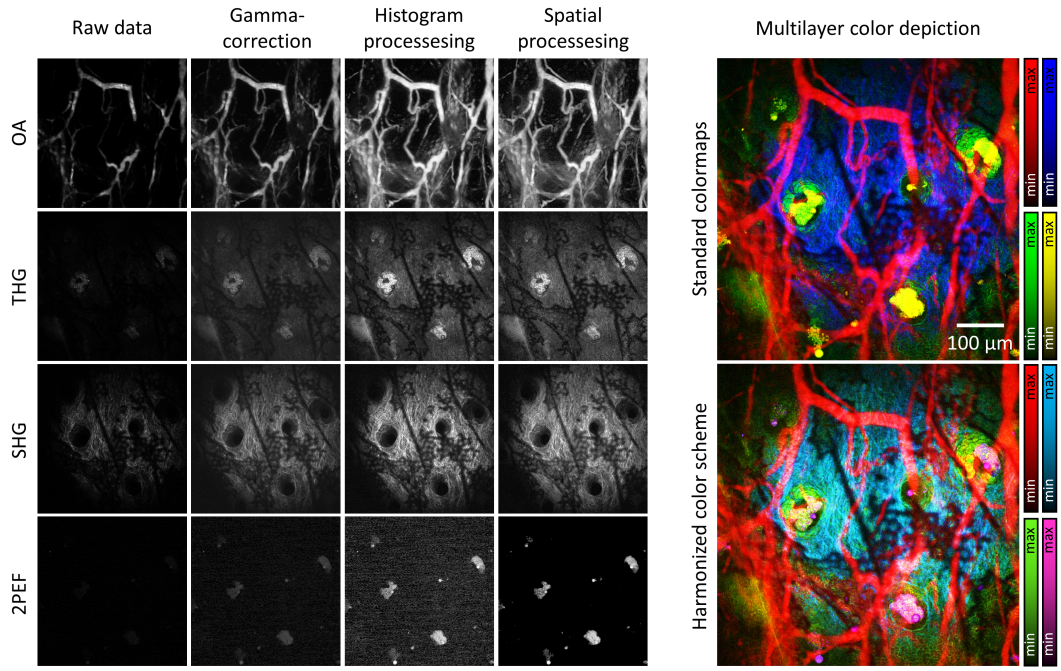

Figure 3.2: Image processing steps performed on HyMPSOM data exemplary shown for label-free imaging on an *in vivo* mouse ear. Processing steps include contrast adjustment like gamma- and histogram-processing, spatial filtering, and multilayer overlay using harmonized color schemes.

processing), spatial processing (e.g. spatial filtering and deblurring), and multicolor overlay (e.g. application of harmonized color schemes). Whereas the raw data features low visibility, the final processed and overlayed image reveals the extracted information in high detail precision while unimportant information (i.e. background noise) is suppressed.

3.4.1 Contrast processing

One step of image processing concerns enhancing the appearance of the recorded image. This step aims therefore to highlight features, boost the visibility of obscured information, and equalize the contrast throughout the image. Hence, techniques for enhancing the contrast of an image target the individual pixel values. Contrast is mostly defined as the Weber fraction $\frac{I_f - I_b}{I_b}$, with I_f and I_b denoting the luminance of the feature and the background, respectively. All of the following contrast processing steps can potentially be also applied on successively-shifted sub-regions of the image, which therefore attempts to equalize the contrast for signals captured inhomogeneously throughout the image[53].

[53] E.g. contrast limited adaptive histogram equalization (CLAHE) adjusts the local contrast to a preset target value within a predefined area that is successively shifted across the entire image.

Dynamic range

The human eye typically can adapt to a range of light intensities covering up to ten orders of magnitude, i.e. brightness values from the so-called scotopic threshold to the glare limit. Considering the perception of colors, i.e. the photopic vision, the range reduces to $\sim 10^6$. However, for a given situation, the human eye is not able to capture such enormous intensity ranges but rather adapts to a certain sub-range within it. Hence, e.g. at looking at an image, the so-called brightness adaption allows for a rather small fraction of intensity levels to be discriminated, which is typically in the order of $\sim 10^2$ to $\sim 10^3$. Hence, although the microscopy signals are typically acquired at dynamic ranges covering up to 24-bit, i.e. $2^{24} \approx 1.7 \cdot 10^7$ entries, the final images are typically depicted in 8-bit, i.e. $2^8 = 256$ entries, or 16-bit, i.e. $2^{16} \approx 6.5 \cdot 10^4$ entries.

Histogram adjustment

The histogram of an image depicts the incidence of certain intensity values, i.e. how often they occur in the image. Considering raw data being recorded with a dynamic range larger than the one of the aimed processed image, the entries $f(x, y)$ are compressed by a step-transformation to the final dynamic range. As an example, by considering the mapping of 24-bit data on an 8-bit scale, $f(x, y)$ values being slightly smaller than the mean between two 8-bit entries $(m_2 + m_1)/2$ are set to m_1, whereas values slightly higher are mapped to m_2. This process, known as contrast stretching, separates by that entries based on a thresholding-function at $(m_2 + m_1)/2$. Furthermore, similar approaches can be used to cut the boundary values of the original set of intensity values. This process, typically referred to as windowing, maps the highest and lowest values to either 0 or 1 (or 255 for an 8-bit scale) at a boundary conventionally selected at twice the standard deviation to cover 95% of the data[54]. By doing so, the intensity values of an image get spread to span the entire dynamic range, which thereby increase the image contrast.

Gamma correction

Gamma correction refers to a power transformation based on:

$$g(x, y) = f(x, y)^{\gamma}, \tag{3.65}$$

[54] In many cases, the boundaries of windowing are chosen subjectively to enhance the visibility of certain features of an image and, thus, depend on the underlying research questions.

in which γ is a positive constant[55]. For $\gamma < 1$, small values spread over a narrow band of the histogram are mapped to high values covering a wider band, and vice versa for $\gamma > 1$. Further, at $\gamma = 1$, the values remain unchanged. Gamma correction, as a non-linear transformation, is typically used to reinforce dim features of the image which are concealed by dominant features of high intensities by using γ-values below one. In this regard, small intensity entries get stronger amplified compared to high intensity entries, which therefore increase their visibility. Furthermore, gamma correction is an essential step for displaying images on a monitor or a projector, which typically tend to show images too dark.

Histogram processing

Subsequent to mapping the recorded pixel intensities to a chosen dynamic range and applying gamma correction, transformations targeting the entire histogram of an image can be applied. Considering the histogram $h(g_k)$ of an image covering the range of $k = [0, L-1]$ with L being the maximum of the chosen dynamic range (i.e. 256 for 8-bit or 65.536 for 16-bit) as a discrete function $h(g_k) = n_{g_k}$, where g_k denotes the kth-intensity value which is possessed by n_{g_k} pixels. One commonly applied technique to process the histogram of an image is histogram normalization, by which each intensity value is divided by the total number of pixels. A normalized histogram is thus given by $h_{norm}(g_k) = n_{g_k}/n_{tot.}$. Hence, $h_{norm}(g_k)$ denotes the probability of the intensity value g_k, and follows $\sum_{k=0}^{L-1} h_{norm}(g_k) = 1$. Histogram normalization counteracts by that against a bias of the recorded data and yields a high contrast over the entire dynamic range. Another typically performed transformation is histogram equalization, which attempts to equalize the frequency of all contained intensity values. Thus, histogram equalization flattens the histogram by adjusting the intensity values g_k so that the number of pixels n_{g_k} carrying that intensity are independent on the value itself, or in other words the probability $h_{eq}(g_k)$ is constant for all g_k. Histogram equalization is in this regard a non-linear transformation restricted by the underlying dynamic range as well as by preserving monotonicity conditions in intensity mapping.

3.4.2 Spatial processing

Another step of image processing aims to improve the visibility of investigated information of the specimen. As mentioned earlier, such information is mostly stored in 2D signal patterns across the scanned FOV. Hence, spatial processing steps are also termed neighborhood operations as they take into account the proximity of a targeted pixel, which is typically termed kernel or mask. Furthermore, as spatial filtering regards 2D processing concepts, they alter the contained spatial frequencies of the respective image

[55] In certain cases, an offset is introduced by $f'(x, y) = f(x, y) + \epsilon$ to account for zero-values within the image.

and, thus, operate in the frequency domain as a convolution. In all following spatial processing methods, the filter kernel $w(x, y)$ of size $2i$ is successively-shifted across the entire image[56], which can be generally expressed by[57]:

$$g(x, y) = \sum_{x'=x-i}^{x+i} \sum_{y'=y-i}^{y+i} w(x', y') f(x', y'), \tag{3.66}$$

where i refers to the maximum distance the applied kernel covers with respect to the central pixel (e.g. a 3 x 3 kernel has $i = 1$ and covers by that all directly adjacent pixels from the targeted one).

Smoothing and denoising

Linear smoothing filters aim to blur the image in order to compensate for small unattempted details in images in form of random noise, such as intensity gaps or peaks resulting from inhomogenous data acquisition (e.g. laser instabilities or mechanical vibrations). The most simple smoothing process is by applying an average filter, in which each coefficient of the kernel weights the respective pixel identically, i.e. $w(x, y) = 1/i$. Besides that, a weighted average filter contains different coefficients to assign levels of importance to the pixels covered within the kernel. Typically, the coefficients in such weighted average filters decrease with increasing distance to the kernel center. A commonly applied form of a weighted average filter follows a 2D Gaussian distribution of coefficients, which are then termed Gaussian kernels or Gaussian blurs.

Despeckling and outlier removal

Non-linear spatial filters, which are also referred to as order-statistic filters, are based on a histogram-like ranking of the pixels within the applied kernel. The respective pixel is then replaced by a predefined rank of the analyzed pixel intensities, which is most cases chosen as the median. In that case, a median kernel corrects for single-pixel noise, which does not match the close neighborhood. Such single pixels possessing a much greater or much lower value than its close proximity are typically called outliers or salt-and-pepper noise, due to which median filtering is termed despeckling or outlier removal. In contrast to the previously described linear smoothing filters, order-statistic filters affect the global histogram of the image as they subtract or add intensity values.

[56] For an odd-sized kernel, the filter accounts for the central pixel $2i = 2a - 1$, whereas even-sized kernels place the filtered value in between the original pixels by $i = 2a$. In the following, an odd-sized kernel is assumed.

[57] For simplicity reasons, a square kernel is assumed, which is also the conventional shape of filters used in image processing.

PSF correction

Another form of spatial filtering concerns the correction of the intrinsic resolution limit of the used imaging system. As explained in Section 2.4.1, optical microscopy is characterized by the PSF, which constitutes the physical resolution limit. Considering a properly sampled image, i.e. according to the Nyquist–Shannon theorem, the captured image is blurred inherently by a convolution with the PSF. Similar to linear smoothing kernels, spatial deconvolutions can potentially correct for this blurring effect. Whereas in most optical microscopy the PSF can be in first approximation assumed to follow a 2D Gaussian shape, precise knowledge of the actual PSF (e.g. by imaging a point source), leads to more accurate corrections. Spatial PSF deconvolutions attempt in this regard to find an estimated image (i.e. the desired filtered image), which convolved with the system's PSF resembles the raw input image. Most commonly, such correction is performed by applying inverse filters, e.g. Wiener deconvolutions, regularized least squares, linear least squares, or Tikhonov-Miller regularization. *W.l.o.g.*, inverse filters Fourier-transform the original image and divide it by the Fourier-transformed PSF to yield the estimate, which mathematically constitutes deconvolutions in the real space. Mostly, this process is carried out iteratively with constrains to prevent the induction of artifacts known as ringing. Commonly used constrains in the iterative process compute the similarity between the original image and the PSF-convolved estimate. A preset error criterion (i.e. figure of merit) stops the process eventually[58]. Another approach attempting to correct for the PSF is e.g. a deblurring algorithm, in which out-of-focus planes of a 3D image are blurred and subtracted, but it requires a 3D-imaged volume.

3.4.3 Harmonized-color depiction

The depiction of microscopy images plays a crucial role for proper presenting and highlighting features and information of the recorded data. Whereas the previous chapters concern the basic processing of microscopy images, their representation is typically realized in assigning certain colormaps to fit the range of the values. A critical factor in here is to achieve an eye-pleasing visualization of the data, which is essential to address the perception of the human eye, especially for multilayer images of a specimen recorded with multiple modalities. In simple words, the selected colormaps for an j-layer image aim for a pleasant composition of colors yet possessing high distinctiveness among the colors[59]. In this regard, j denotes the number of spatial information

[58] A typical error criterion is to proceed deconvolving until the difference between the input image and the PSF-convolved estimate is minimized. Further deconvolution steps would induce noise artifacts, which would subsequently increase this difference. Other used error criteria are maximum likelihood estimation or expectation maximization.

[59] In here, only 1D colormaps containing one RGB-code (i.e. red, green, blue) are regarded. More-dimensional colormaps, such as e.g. rainbow- or jet-maps, are typically not suited for multilayer depictions.

within an image. For multi-modal microscopy, j typically equals the number of modalities. However, j could potentially get enlarged by the application of further analysis methods[60]. Besides conventionally predetermined colors to show certain moieties (e.g. yellow for lipids), they can in general be selected freely and subjectively or be deduced by a more strategical approach.

Color perception of the human eye

In all cases, the selection of the colormap of an image or an image-layer targets to effectively deliver the contained information to the human eye[61]. The color-sensitive receptors in the human retina can be classified into S-, M-, and L-cones depending on their wavelength-dependent sensitivity[62]. This uneven color perception carries therefore an intrinsic property of highlighting image features depicted in color regions of high sensitivity. In principle, image features with low presence in the image should be assigned to colors at which the eye is highly sensitive and vice versa. By doing so, the image is prevented to appear overloaded and glaring. The overall color perception of the human eye, originally defined as the CIE-XYZ space[63], typically stretches from ∼400 nm to ∼700 nm, thereby determining the visible spectral range (see Fig. 2.8), and follows an almost symmetric Gaussian curve peaking at ∼520 nm (i.e. green).
Fig. 3.3 depicts the chromaticity diagram in CIE-XYZ space projected in 2D. x and y denote the color coordinates and account in here for the color perception of the human eye. The white point marks the point of monochromacity, from which straight lines towards the curve of chromaticity possess equal hue[64]. Centered at the white point, the so-called color wheel can be extracted.

Palette-based framework

In order to illustrate the concept of combinations of colors, each color can be described as the hue (i.e. the tone of the color), the saturation (i.e. the colorfulness), and the value (i.e. the brightness of the color), which is then referred to as the HSV model[65]. Whereas the latter typically is used to present the underlying intensity of the pixel,

[60] As an example, optoacoustic microscopy can potentially be carried out in a spectral manner, which, depending either on the number of imaged wavelengths or on the number of spectrally separated chromophores, leads to several image layers to be depicted.
[61] In here, color-based mathematical analyses, such as e.g. image clustering, are disregarded.
[62] The other receptors are rods being sensitive to brightness values and, thus, account for black-and-white vision.
[63] This perceptual space was first proposed by the commission international de l'Eclairage (CIE).
[64] As illustrated, the colors in the magenta range are not assigned to a wavelength within the electromagnetic spectrum and, thus, are not considered as natural colors.
[65] The HSV model assigns maximum values to maximum color tint, whereas the associated HSL model (L = luminance) assigns a white representation.

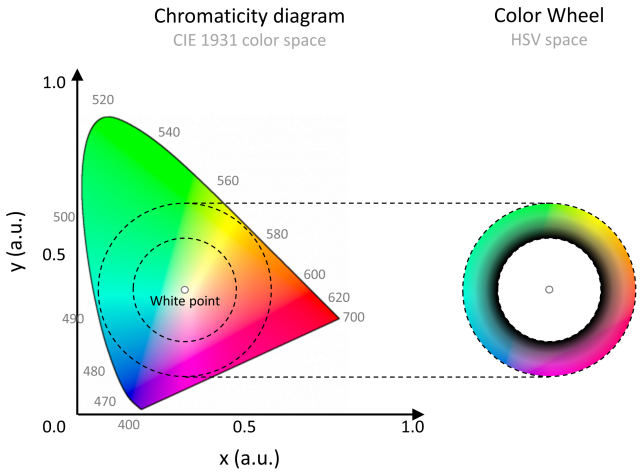

Figure 3.3: Schematic depiction of the chromaticity diagram in projected CIE-XY space and the extracted HSV color wheel. The white point marks the coordinates of monochromacity (∼[0.3, 0.3]). Gray values mark the wavelengths (nm) along the curve of chromaticity. Data extracted from [93].

the first two are determined by the selected colormap or color combination. In order to illustrate the concept of combinations of colors, a color wheel is commonly used in which the hue is parameterized by the angle and the saturation by the radius. The entire HSV model describes the mapping of the CIE-defined color perception onto cylindrical coordinates, but as the parameter along the length of the cylinder represents in images the underlying intensity of the pixel, it can be disregarded for colormap selections. Applying certain palette-based color schemes onto the HSV model determine subsequently the colors (e.g. RGB code) for each layer of the image. Whereas the hue-value selection determines the color composition, the saturation-value ensures no over-saturation at congruent color patterns within the image. In other words, the determined RBG-codes for x layers of the image should sum up to an identical value c_{max} so that $\sum_x [max(R_x), max(B_x), max(G_x)] = [c_{max}, c_{max}, c_{max}]$, in which c_{max} subsequently defines the range of the image[66]. The saturation adjustment is crucial for congruent signal patterns, whereas for complementary signal patterns it can be disregarded as at each position within the image, e.g. at each pixel, only one color is present.

Harmonic schemes

In order to find good matching colormaps for a multilayer image, several schemes are proposed based on three aspects: First, the perceptional distinctiveness among

[66] Assuming e.g. three channels in a 8-bit being red [255,0,0], green [0,255,0], and blue [0,0,255], the maximum summed value is white [255,255,255], Likewise for 3 mixed-channel colors, i.e. $[r_1,g_1,b_1]$, $[r_2,g_2,b_2]$, and $[r_3,g_3,b_3]$, their coefficients should be selected as $\sum_i r_i = \sum_i g_i = \sum_i b_i = 255$.

colors should be maximized to illustrate the contrast among the layers. For that, a perceptional color-distance between two colors can be defined being proportional to their separation angle on the color wheel. Second, the use of computing iso-luminance curves, typically incorporated when extracting the color wheel, ensures equal color perception and, thus, facilitates direct comparability among the layers. Third, the symmetry among all selected colors defines the aesthetic harmony, i.e. how eye-pleasing the color combination appears. In general, the more symmetric the scheme, the more pleasant the combination and the more equal the display. Acute yet symmetric schemes of colors induce the emphasis of the more isolated layer and the suppression of other layers. Depending on the number of layers, following harmonic schemes are typically proposed and used for multilayer image depictions:

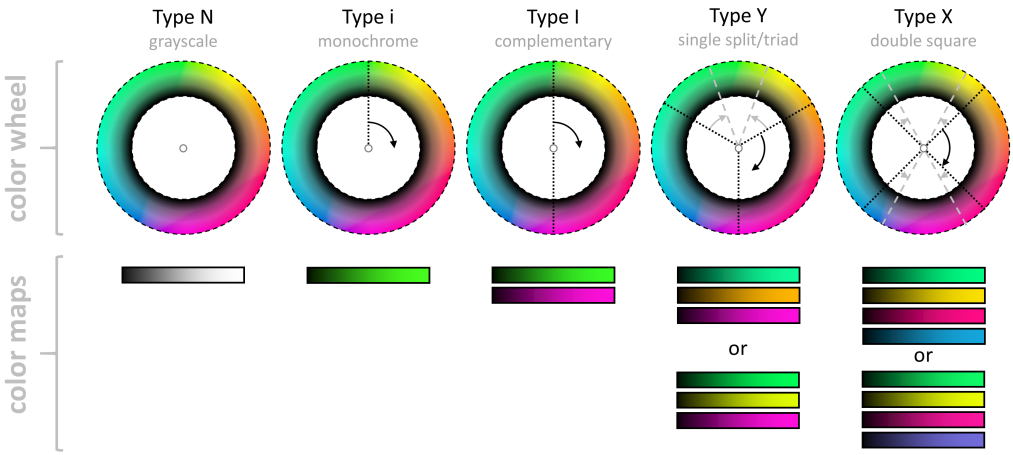

Figure 3.4: Schematic depiction of the harmonic color schemes illustrated as combinations in the HSV color wheel and the thereby determined colormaps. Black arrows denote the freedom of rotation of the entire harmonic scheme, gray arrows and lines denote possible degrees of symmetric stretching and compressing of the scheme.

In here, the type N describes a gray-scale image (i.e. the hue coordinates equal the white point) and type i a monochrome colormap, which therefore equals the colormap of each individual layer of the finally composed image. Type I constitutes the highest contrast among two colors in a complementary scheme. Type Y and X illustrate harmonic schemes for three and four channels, respectively, which can either distribute the colors in identical angles between all channels for equal appearance and distinctiveness of the layers (black lines), or stretch/compress the angle for highlighting selected layers (gray lines). In a special form of the acute-shaped type Y, more than two channels can be located opposed to the highlighted one. In all cases, the chosen harmonic scheme can be freely rotated within the color wheel (black arrow) while preserving the condition of equal or weighted appearance. The final selection of colors based on harmonic schemes is however still subjective, project-dependent, and potentially predefined by convention for the specific layers (e.g. lipids in yellow; blood in red).

3.5 Conclusion and Outlook

In summary, precisely deriving the physical background of microscopy modalities allows to understand their fundamental functionality as imaging techniques. The detailed assessment of the underlying principles subsequently facilitates to comprehend the respective imaging properties as well as their interpretation. In this regard, the initial signal generation of each microscopy modality can be explained as the associated specific light-matter-interaction, which deduces the expected contrast. Elaborating such contrast with respect to the optical properties of the investigated specimen like its refractive indices, scattering characteristics, absorption spectrum, and spatial composition enables a detailed grasp of the extracted information. Furthermore, in order to gather the desired information, an extensive elaboration of the contrast principles facilitates to adapt the optical system correspondingly regarding signal generation and detection as well as image formation. This is of high importance not only for recording the data adequately but also for applying data and image processing tools appropriately. Whereas the former determines the assembling of the required optical system, the latter designates the visual representation of the extracted information of the investigated specimen and, thus, specifies the legibility of the findings. Finally, comprehensive knowledge of the theoretical considerations from signal generation up to image depiction of microscopic modalities allows for developing and refining both the operation mode as well as their multi-modal display. That enabled the development of HyMP-SOM for simultaneous multi-modal imaging of biological specimen with advanced data recording and image scanning procedures as well as appropriate ways of data depiction.

4 | Development of HyMPSOM

This chapter summarizes the development and design of the hybrid multi-photon and spectral optoacoustic microscope (HyMPSOM). The system originated from a previous version as described in [21–23], but constitutes an entire newly designed optical setup overcoming previous limitations and is based on a novel operating principle. For simplicity reasons, only the final state of HyMPSOM is described in this chapter. This chapter will explain in detail the integration of multi-photon modalities (see Section 4.2.1) and optical-resolution optoacoustics (see Section 4.2.2), as well as describe the merger of the modalities into the final experimental setup (see Section 4.2.3), the mode of operation (see Section 4.2.4), and the image formation procedure (see Section 4.2.5). Subsequently, this chapter contains a comprehensive characterization of HyMPSOM regarding the achieved sensitivity (see Section 4.3.1), spatial resolution (see Section 4.3.2), imagable field-of-view (see Section 4.3.3), imaging speed (see Section 4.3.4), and, finally, the optoacoustic total impulse response (see Section 4.4).

4.1 Introduction

Previously, the basic role of optical microscopy has been discussed regarding its importance in nature science, its fundamental way of operating, as well as its theoretical considerations. As elucidated, the combination of complementary microscopic modalities into a hybrid microscope is significantly more powerful than the corresponding stand-alone modalities. The main reason for this is the ability to extract complementary information of the sample under investigation. This is of special interest for studies performed regarding both developmental biology and translational medicine. The merger of various microscopy techniques requires however precise adaption of both the optical system as well as the data recording. This is of high importance to prevent mutual influence while preserving the imaging capabilities, especially for simultaneous data acquisition.

4.2 Materials and methods

HyMPSOM is a laser-scanning microscope based on a set of high-precision galvanometric (galvo) mirrors (6215H Galvanometer Scanners, Cambridge Technologies) in combination with an inverted microscope stand (AxioObserver.D1, Zeiss) as the shared central scanning unit of the microscope (see Fig. 4.1 and Appendices: Photographs of the optical setup). All equipped laser excitation beams for the previously mentioned microscopic modalities were guided over this set of galvo mirrors. The beams were subsequently enlarged 6-fold by a telescopic arrangement of achromatic doublet lenses (AC254-050-B-ML and AC254-300-B-ML, Thorlabs) in a 4f-configuration to fill the back apertures of the employed objective lenses which were of ∼20 mm in diameter. Achromatic doublet lenses enabled minimal spatial distortions and chromatic aberrations at large scanning angles as characterized in Section 4.3.3 and Fig. 4.14. The galvo-mirror-based scanning system of HyMPSOM was thus designed for accepting incoming laser beams with a diameter of ∼3 mm at the point of entering the scanning unit. The 4f-configured telescope additionally contained an interchangeable guidance optic, which could be a silver mirror, a shortpass dichroic, or a multinotch dichroic depending on the modality used[67] (see Section 4.2.3 and Fig. 4.1). The scanning scheme, i.e. the voltage waveforms determining the angular movement of the galvos, was sent to the galvo controller by a 16-bit DAQ card (PCIe 6363, National Instruments; max. sampling rate: 1MS/s), its theoretical background is comprehensively described in Section 2.4.3 and its practical realization in Section 4.2.5 as part of the available scanning procedures enabled.

[67] The two sub-systems could be operated sequentially as well as simultaneously. Latter uses the multinotch dichroic, which led to slight performance reduction compared to the individual operation modes using the silver mirror (for optoacoustic only) or the shortpass filter (for multi-photon only).

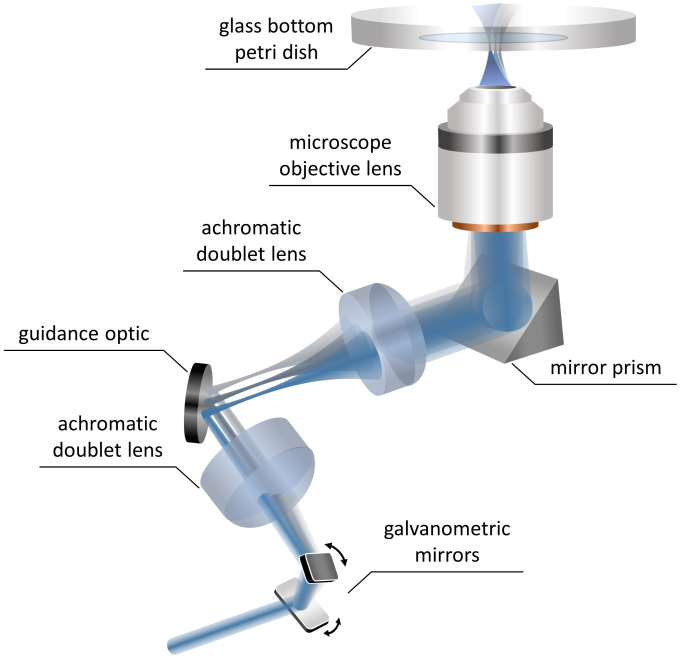

Figure 4.1: Schematic depiction of the scanning unit of HyMPSOM. The scanning unit accepts incoming beams of ∼3 mm diameter and scans the beams using a two-mirror galvo-system. The beams are enlarged by a 4f-configuration of achromatic doublets, are directed by a guidance optic adapted to the modality performed, and are coupled into an inverted microscope holding the microscope objective lens.

Subsequent to the beam expansion, the excitation beams were coupled into the inverted microscopic stand and were focused by infinity corrected microscopic objective lenses (Plan-Apochromat 10x/0.45 and W Plan-Apochromat 20x/1.0, Zeiss). The chosen objective lens was dictating hereby the achievable field of view (FOV) as a function of the magnification and the achieved spatial resolution as a function of the numerical aperture (NA) (see Section 2.4.1 and Section 4.3.3). All utilized microscopic objective lenses were corrected for a sample-holding glass substrate of 170 µm thickness, because of which glass bottom petri dishes (D60-30-1.5-N, IBL and 81158 #1.5H D 263 M, ibidi), thin cover slides (107242 No. 1.5H, Marienfeld), or glass bottom multi-well plates (80826 #1.5H D 263 M, ibidi) were used for holding the examined specimen (see Fig. 4.1 exemplary for the glass bottom petri dish). In order to provide best optical focusing and automated system control, a high-precision endless rotational stage (DT-34, Physik Instrumente) was attached to the fine drive of the microscope stand achieving a precision of axial displacement of the objective lens and, thus, the optical focus of ∼2 µm. The sample was positioned by set of motorized xy-stages (MLS203-2, Thorlabs) together with a piezoelectric z-stage (MZS500-E, Thorlabs) adapted to the microscope stand.
Sensors positioned in transmission-mode, i.e. above the sample, such as optical detectors for THG readings (see Section 4.2.1) or an ultrasound transducer for OA readings

(see Section 4.2.2) were attached to another set of high-precision motorized xyz-stages (M-683.2, M-501.1, Physik Instrumente). These stages were used to align the installed sensors appropriately to the scanned area within the specimen (see Section 2.4.3). The entire system was controlled by self-written MATLAB^{TM} scripts (see Appendices: MATLAB^{TM} scripts) for controlling the stages, the movement of the galvo mirrors, the triggering and synchronization, as well as the data acquisition (see Section 4.2.4).

4.2.1 Multi-photon modalities

The multi-photon microscopy (MPM) sub-system equipped an Yb-based solid state femtosecond laser emitting near-infrared light at a wavelength of 1043 nm as the excitation source (YBIX, Time-Bandwidth; pulse width: 170 fs, average power: 2.8 W, repetition frequency: 84.4 MHz) as schematically depicted in Fig. 4.2 and shown in Appendices: Photographs of the optical setup. The laser beam was first reduced in diameter by a telescopic arrangement of plan-convex lenses to match the required diameter for entering the galvo scanning system as mentioned above.

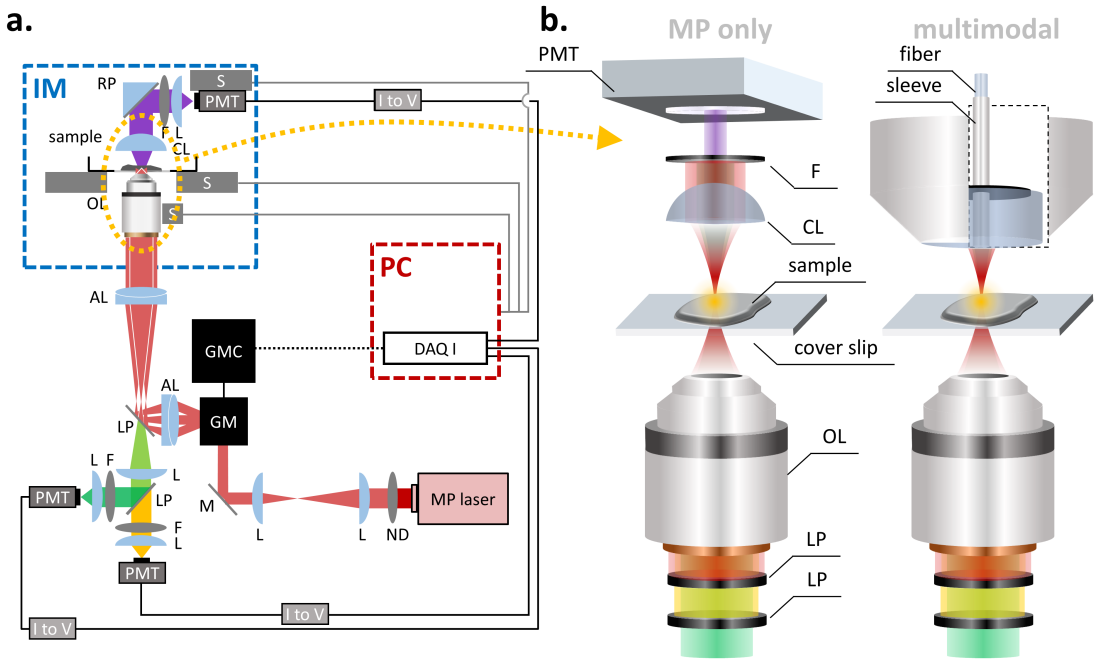

Figure 4.2: Schematic depiction of the MPM sub-system of HyMPSOM. (a) The MPM system is based on raster-scanning an optically focused laser excitation across a sample placed in an inverted microscope using galvanometric mirrors and acquires multi-photon signals in transmission- as well as epi-mode. **(b)** Close-up depiction of the arrangement of either a PMT or a fiber-coupled-PMT in transmission-mode. Abbreviations: AL: achromatic doublet lens; CL: condenser lens; DAQ: data acquisition card; F: optical filter; GM: galvanometric mirror scanner; GMC: GM controller; IM: inverted microscope; L: plan-convex lens; LP: longpass dichroic; M: dielectric mirror; ND: neutral density filter; OL: microscope objective lens; PMT: photomultiplier tube; S: high-precision motorized stage.

The excitation of biological tissue with this laser generated a variety of multi-photon signals, namely second and third harmonic generation (SHG and THG) as well as two- and three-photon excitation fluorescence (2PEF and 3PEF) as theoretically elaborated in Section 3.2. Based on the laser wavelength of 1043 nm, SHG and the excitation of 2PEF was at 521.5 nm, THG and the excitation of 3PEF at 347.7 nm. Whereas both fluorescence signals are emitted isotropically (see Section 3.2.3), harmonic generations are highly orientated towards the forward direction (see Section 3.2.2). However, sufficient SHG signal could be also detected in the backward direction. Hence, SHG, 2PEF, and 3PEF signals were guided back through the equipped objective lens and were separated from the excitation beam path spectrally by a shortpass filter for only multi-photon imaging (DMSP805R, Thorlabs) or by a multinotch dichroic mirror for multi-modal imaging (ZT488/532/633/830/1064rpc, Chroma) before encountering the galvo mirrors. The multinotch optic, as schematically depicted in Fig. 4.5, allowed the transmission of expected multi-photon signals of SHG at 521.5 nm, of 2PEF at 550-615 nm, and of 3PEF at 440-480 nm, as well as the reflection of the excitation at 1043 nm. In contrast, THG signals were sensed in a transmission-configuration either using an aspheric condenser lens (ACL25416U-A, Thorlabs) with a NA of 0.79 in combination with a right-angle prism mirror (MRA25-F01, Thorlabs) or through a multimode fiber (FP1000URT, Thorlabs) with a NA of 0.5 to direct the light onto the PMT. The latter was essential for simultaneous recordings of THG along with optoacoustic signals by utilizing a hole-through ultrasound transducer (see Section 4.2.2 and Section 4.2.3) due to space limitations above the sample in transmission-configuration. All multi-photon signals were detected by ultra-sensitive photomultiplier tubes (PMT) (H9305-03, Hamamatsu), which were further amplified (C7319, Hamamatsu) and gain-controlled by a linear DC voltage output supply (GPD-4303S, GW Instek). Two of the PMTs were installed in an epi-configuration in combination with a motorized filter wheel (FW102C, Thorlabs) for sensing SHG, 2PEF, and 3PEF, and another PMT in transmission-configuration for sensing THG. In order to assign the PMTs specifically to these multi-photon modalities, appropriate optical filters were installed (SHG: FB520/10, Thorlabs; THG: FGUV11, Thorlabs; 2PEF: FGS900, Thorlabs; 3PEF: D470/38, Chroma). Further, a longpass dichroic mirror (DMLP550, Thorlabs) was separating SHG/3PEF and 2PEF signals in epi-configuration. For simultaneous optoacoustic microscopy at 532 nm, each PMT was additionally equipped with notch filters (NF533-17, Thorlabs) to prevent crosstalk and potential damage of the optical sensor by the optoacoustic laser. The entire spectral setting was described in Section 4.2.3 and depicted in Fig. 4.5. The multi-photon readings were digitized by a 16-bit DAQ card (PCIe 6363, National Instruments; max. sampling rate: 1 MS/s), binned, and sampled at the global triggering frequency (see Section 4.2.4).

4.2.2 Optical-resolution optoacoustic modality

The optical-resolution optoacoustic microscopy (OR-OAM) sub-system operating in time-domain used a variety of different laser excitation sources depending on the imaging project. The used laser sources were a diode-pumped solid state laser (SPOT-10-200-532, Elforlight Ltd; pulse width: 1.4 ns, actively Q- switched, average power: 2 W, repetition rate: up to 50 kHz, emitted wavelength: 532 nm), a fiber-based supercontinuum laser (SC-Pro 7, YSL Photonics; pulse width: 108 ps, seeded Q-switch, average power: 20 W, repetition rate: up to 200 MHz, emission spectrum: 400-2400 nm) in combination with variable linear filters (VLF 400-840, YSL Photonics; spectral bandwidth: 10 nm - full transmission; and VLF 900-1700, YSL Photonics; spectral bandwidth: 23 nm), and multimode diodelaser modules (PD-01236, PD-01289, PD-01229, Lasertack; emitted wavelengths: 445 nm, 520 nm, 638 nm). The latter were controlled by a self-designed electrical circuit in order to achieve a pulsed operation mode, which is described in detail in Section 5.4.2. All used laser sources for OR-OAM followed the identical optical setup consisting first of a set of plan-convex lenses[68] in a pinhole-equipped telescopic arrangement to both scale the beam to the above mentioned required diameter of $\sim$3 mm and spatially clean the beam to a Gaussian profile. Interchange between the excitation sources was realized by mirrors installed on flip mounts (FM90/M, Thorlabs). However, all beam paths were attenuated by selecting appropriate neutral density filters (FW1AND, Thorlabs) and were guided over the galvo mirrors as described in Section 4.2. The OR-OAM arrangement is schematically depicted in Fig. 4.3 and shown in Appendices: Photographs of the optical setup.
For sensing the generated optoacoustic signals, spherically-focused single-element ultrasound transducers (HFM23; central frequency: 54.5 MHz, -6 dB bandwidth: 29.5 - 79.6 MHz (92%), focal distance: 3 mm; HFM27; central frequency: 96 MHz, -6 dB bandwidth: 42 - 149 MHz (111%), focal distance: 2.85 mm; HFM31; central frequency: 53.4 MHz, -6 dB bandwidth: 29.5 - 77.3 MHz (90%), focal distance: 4 mm, central hole: 1 mm diameter; Sonaxis) were positioned in transmission-mode by the previously mentioned xyz-stages. The ultrasound transducers achieved acoustic focusing by a concave glass lens attached to the active element constituting the actual acoustic sensor. Whereas the HFM23 and HFM27 transducer differed only in their lens geometries and active elements, the HFM31 transducer constituted another kind of ultrasound transducer comprising a central hollow metal sleeve for fiber guidance (see Fig. 4.3). The transducers were acoustically coupled to the samples by either a droplet of deionized water, the used sample buffer (e.g. for single-cell measurements), or a combination of centrifuged ultrasound gel squeezed onto the sample by a thin polyethylene foil and a droplet of deionized water (e.g. for small animal imaging) to provide best acoustic

[68] The near infrared part of provided by the supercontinuum laser utilizes analogously silver-coated parabolic mirrors with identical focal lengths.

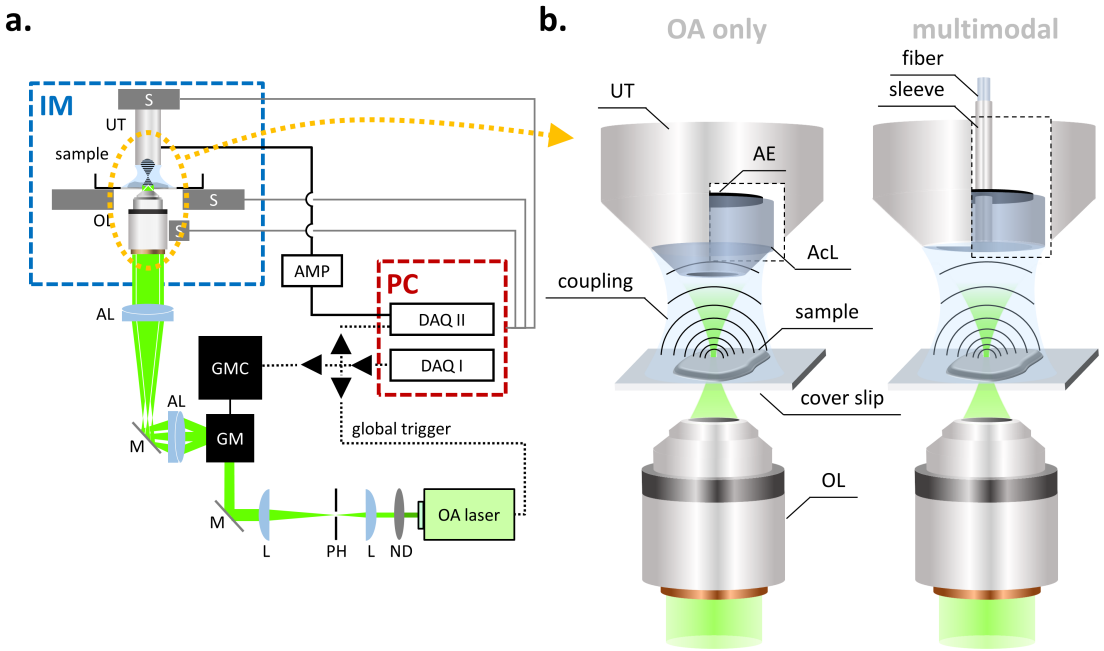

Figure 4.3: Schematic depiction of the OR-OAM sub-system of HyMPSOM exemplary for one laser source. **(a)** The OR-OAM system is based on raster-scanning an optically focused laser excitation across a sample placed in an inverted microscope using galvanometric mirrors, uses a global trigger signal, and acquires optoacoustic signals in transmission-mode. **(b)** Close-up depiction of the arrangement of the two equipped ultrasound transducer types. Abbreviations: AcL: acoustic lens; AE: active element; AL: achromatic doublet lens; AMP: low noise amplifier; DAQ: data acquisition card; GM: galvanometric mirror scanner; GMC: GM controller; IM: inverted microscope; L: plan-convex lens; M: dielectric mirror; ND: neutral density filter; OL: microscope objective lens; PH: pinhole; S: high-precision motorized stage; UT: Ultrasound transducer.

transmission from the sample to the sensor. In order to match the sensitivity field with the entire scanned area, the used transducer was positioned in positive defocus as explained theoretically in Section 3.3.4 and practically in Section 4.4. The detected signals were further amplified by a low-noise 63 dB amplifier (AU-1291, Miteq) and digitized by a high-speed 12-bit DAQ card (ADQ412, SP Devices; max. sampling rate: 3.6 GS/s) in a streaming-like acquisition mode described in detail in Section 4.2.4.

4.2.3 Merged experimental setup

The two sub-systems of HyMPSOM, namely the multi-photon part (see Section 4.2.1) and the optoacoustic part (see Section 4.2.2), were merged into a single optical setup. The combined system, as schematically depicted in Fig. 4.4 and shown in Appendices: Photographs of the optical setup, integrated the above mentioned modalities in a way in which that they could operate spatially and temporally aligned, meaning at the same time and at the same position. For this alignment, all equipped beam paths were merged along their way towards the galvo mirrors being the common scanning unit of

HyMPSOM. Optical long- and shortpass filters as well as exchangeable mirrors were installed for this purpose.

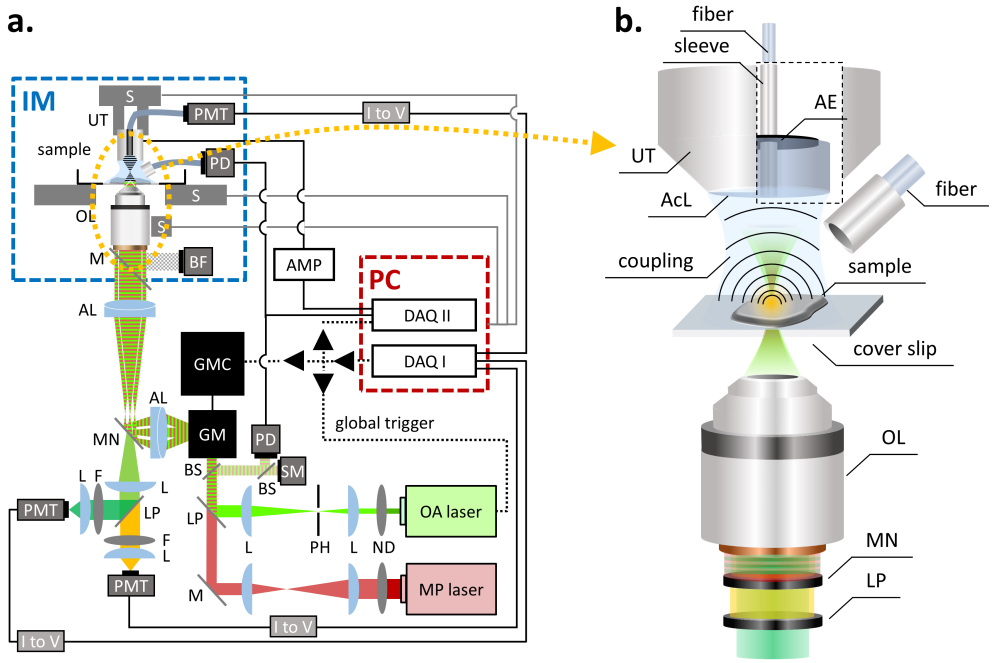

Figure 4.4: Merged HyMPSOM system integrating MPM and OR-OAM sub-systems. **(a)** HyMPSOM integrates the two previously described sub-systems as well as some additional devices (i.e. spectrometer, photodiodes, brightfield camera) for referencing purposes. **(b)** Close-up depiction of the interrogation area for multi-modal acquisition. Abbreviations: AcL: acoustic lens; AE: active element; AL: achromatic doublet lens; AMP: low noise amplifier; BF: brightfield camera; BS: beamsplitter; DAQ: data acquisition card; F: optical filter; GM: galvanometric mirror scanner; GMC: GM controller; IM: inverted microscope; L: plan-convex lens; LP: longpass dichroic; M: dielectric mirror; MN: multinotch dichroic; ND: neutral density filter; OL: microscope objective lens; PD: photodiode; PH: pinhole; PMT: photomultiplier tube; S: high-precision motorized stage; SM: spectrometer; UT: ultrasound transducer.

Due to the spectral locations or covered spectral ranges colliding with the MP signals, the supercontinuum source and the high-speed diodes were only able to operate alone whereas the solid state laser at 532 nm could be combined with the previously described multi-photon sub-system. Hence, simultaneous OR-OAM and MPM imaging was exclusively possible for an optoacoustic excitation wavelength of 532 nm. To merge the 532 nm laser for OR-OAM with the 1043 nm laser for MPM, a longpass dichroic mirror was installed (DMLP650, Thorlabs). As the laser equipped for the multi-photon modalities emitted at 1043 nm excitation wavelength, the SHG signal occurred at 521.5 nm, whereas utilized laser for optoacoustic emitted light at 532 nm. This difference of ∼10 nm was sufficient to install high-precision optical filters for spectral separation, which was of crucial importance for recording the SHG signals in backward-direction and was achieved by the above mentioned multinotch dichroic

mirror (ZT488/532/633/830/1064rpc, Chroma). Furthermore, this slight wavelength difference allowed to utilize notch filters to suppress back-reflected 532 nm light (NF533-17, Thorlabs) in order to protect the PMT assigned for SHG recordings. The combinations of optical filters for simultaneous multi-modal microscopy are schematically depicted in Fig. 4.5 divided in groups relevant for the respective modality.

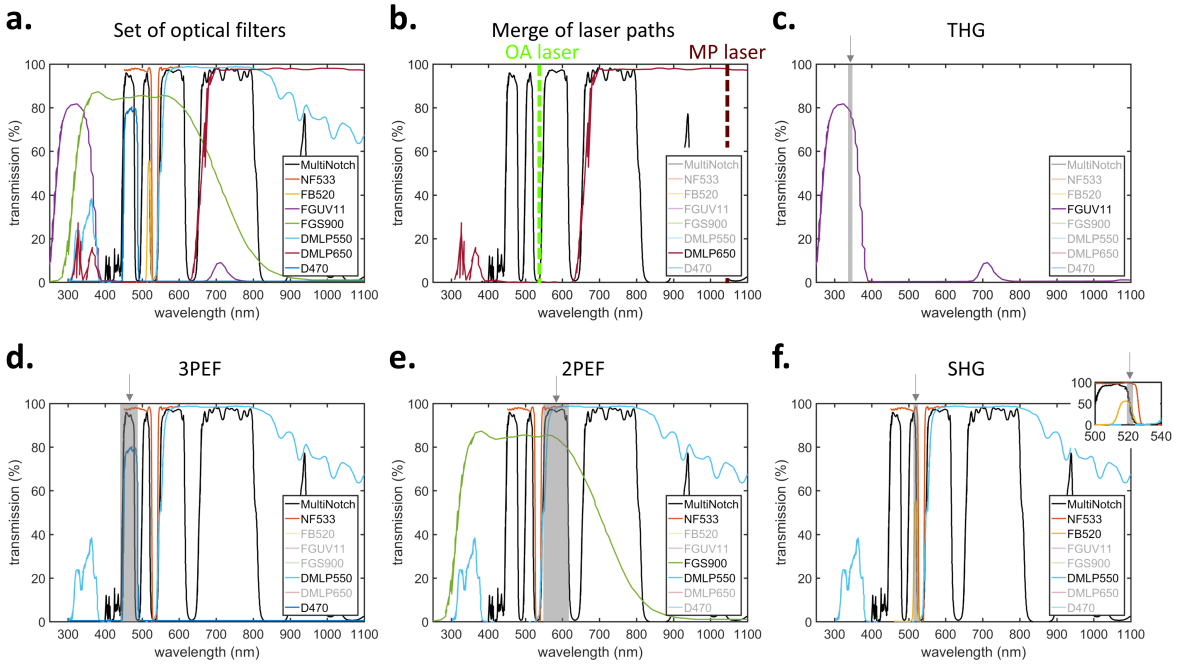

Figure 4.5: Spectral merge of the MPM and OR-OAM excitation and detections. **(a)** The combined set of optical filters installed for simultaneous multi-modal microscopy. **(b)** Spectral merge of the optoacoustic laser at 532 nm and the multi-photon laser at 1043 nm. Relevant optical filters for detecting **(c)** THG, **(d)** 3PEF, **(e)** 2PEF, and **(f)** SHG. Arrows indicate spectral position of the respective MP signals; Transmission plots are extracted from the respective data sheets.

The system further contained several replaceable mounts to quickly interchange between the different laser excitation sources or approaches of signal recording. Thus, for instance, all sensors positioned above the sample in transmission-mode were hooked on magnetic mounts (SB1/M, Thorlabs). In combination with the high-precision sensor-holding stage, these magnetic mounts enabled a quick return to previous alignment settings, which was crucial for time-critical experiments, such as mouse *in vivo* measurements. The interchange between the different laser excitation sources for optoacoustics was analogously achieved by either flip mounts (FM90/M, Thorlabs) or magnetic mirror mounts (KS1R, Thorlabs).

Further, an ultra-fast metal-semiconductor-metal photodetector (G4176-03, Hamamatsu; response time: 30 ps) was installed to characterize all equipped laser excitation sources for pulse shapes, pulse-to-pulse variations, and power stability. The diode was connected to a Bias Tee and finally terminated to 50 Ω to match the connector

termination of the data acquisition cards. Additionally, a fiber-coupled (M15L01, Thorlabs) high-speed photodetector (DET10A, Thorlabs) could be mounted in transmission-mode to read scattering signals (see Section 5.4.4). Both photodiodes were read out by the identical high-speed 12-bit data acquisition card used for optoacoustic signals (ADQ412, SP Devices; max. sampling rate: 3.6 GS/s). A compact USB spectrometer (QWave, rgb photonics; spectral resolution: 0.5 nm, spectral range: 350-800 nm) linked to an optical multi-mode fiber (M15L01, Thorlabs) was integrated to monitor the spectral characteristics of the excitation source. As a standard reference modality, HyMPSOM contained a brightfield microscopic imaging capability by using a CCD camera (AxioCam ICc 1, Zeiss). The brightfield illumination was provided by a white light LED either in transmission- or in reflection-mode, depending on the sample under investigation.

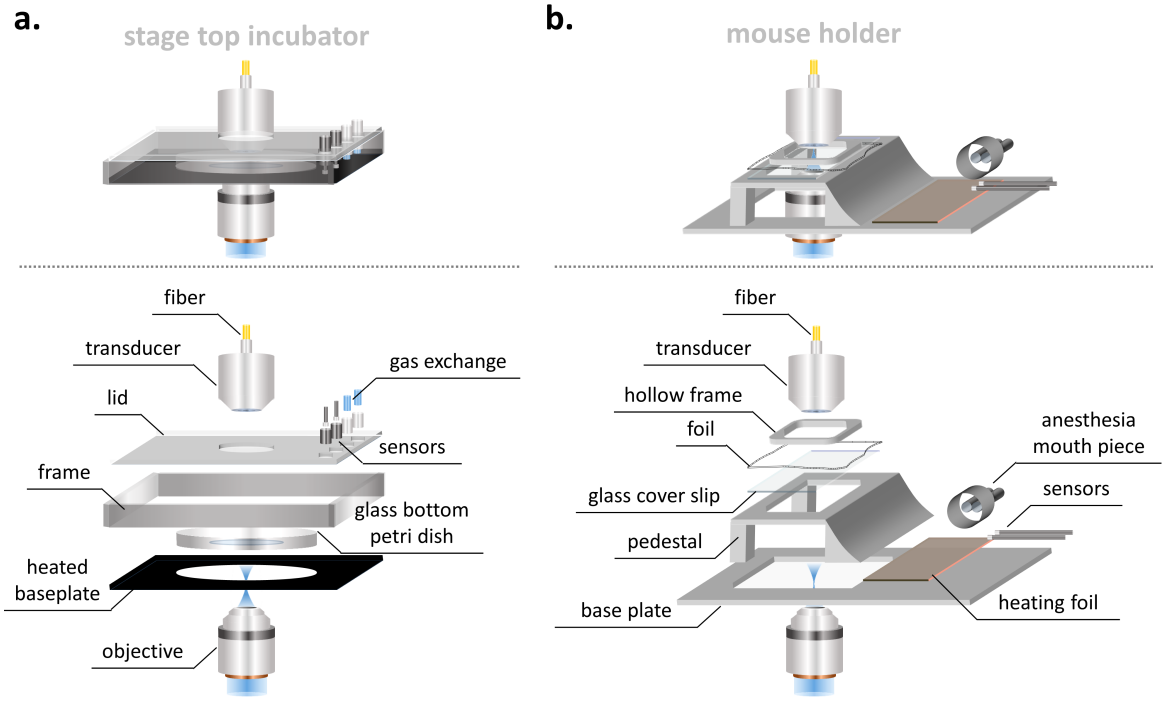

Figure 4.6: Control systems for *in vivo* measurements. **(a)** Stage top incubator for alive cell culture measurements controlling the environmental condition (i.e. CO_2, N_2, O_2, and humidity) and the temperature of the petri dish. **(b)** Custom-designed holder for mouse ear *in vivo* measurements containing the anesthesia mouth piece, an automated feedback-system for temperature control of the mice, and sensors for heart- and breathing-rate and blood oxygenation monitoring.

Measurements of *in vivo* specimens, e.g. alive single-cell cultures, paralyzed zebrafish larvae, and anesthetized mice, required precise control of their environmental conditions for maintaining their physiological state (see Fig. 4.6 and Appendices: Photographs of

the optical setup). For that, the system was equipped with a stage top incubator system (10722 Stage Top Incubator, ibidi) as drawn in Fig. 4.6a for samples being placed in glass bottom petri dishes (81158 #1.5H D 263 M, ibidi) or multiwell-plates (80826 #1.5H D 263 M, ibidi). The incubator lid was customized to allow lowering of the equipped ultrasound transducer through a hole to contact the sample buffer for acoustic coupling. This system ensured the required environmental conditions by controlling the sample temperature, humidity, CO_2, N_2, and O_2 levels, as well as the gas perfusion rate. Such control was essential for long time measurements. Analogously, an automated physiological monitoring system was installed for mouse *in vivo* measurements (PhysioSuite, Kent Scientific). This system monitored heart- and breathing-rate, blood oxygenation, and body temperature of the mice. The latter was controlled in a fully automated feedback scheme using heating foils (thermo polyester heating foils, Conrad) being placed beneath the mice. Furthermore, a small animal anesthesia unit (Tabletop Veterinary Anesthesia Machine, Keebovet) was used for mouse *in vivo* measurements. The end pieces of both, the monitoring and the anesthesia system for mouse *in vivo* measurements, were fixed to a custom-designed mouse holder (see Fig. 4.6b) fitting on the sample-holding stages. This holder contained an elevated pedestal comprising a central hole across which an 170 µm cover slip is placed. On top of the cover slip, the mouse ear was placed and fixated. A drop of ultrasound gel could be squished on top of the ear with a thin polyethylene foil wrapped around a hollow frame, which was finally screwed to the mentioned pedestal. In this condition, the mouse ear was sandwiched between the glass cover slip from below and the ultrasound-gel-pressing foil from above. By that, the ear could be accessed optically from below by elevating the equipped microscopic objective lens and acoustically from above by lowering the ultrasound transducer into the hollow frame filled with water. The holder had been iteratively optimized using a 3D printer (RF1000, Renkforce) and finally fabricated of aluminum to enhance stability.

4.2.4 Synchronization and data acquisition

Synchronization and simultaneous data acquisition of HyMPSOM was facilitated by the use of two data acquisition cards, hereinafter called DAQ1 and DAQ2 (DAQ1: PCIe 6363, National Instruments; max. sampling rate: 1 MS/s; and DAQ2: ADQ412, SP Devices; max. sampling rate: 3.6 GS/s). The entire multi-modal scanning procedure was programmed in a self-developed MATLAB^{TM} script (see Appendices: MATLAB^{TM} scripts). These two DAQs were required to specifically carry out different tasks as schematically depicted in Fig. 4.7.

DAQ1, which was connected to a BNC connector block (BNC-2110, National Instruments; 16 analog input/output connections, 2 digital input/output connections, range: ±10 V), sends out a trigger signal; hereafter called global trigger signal. This

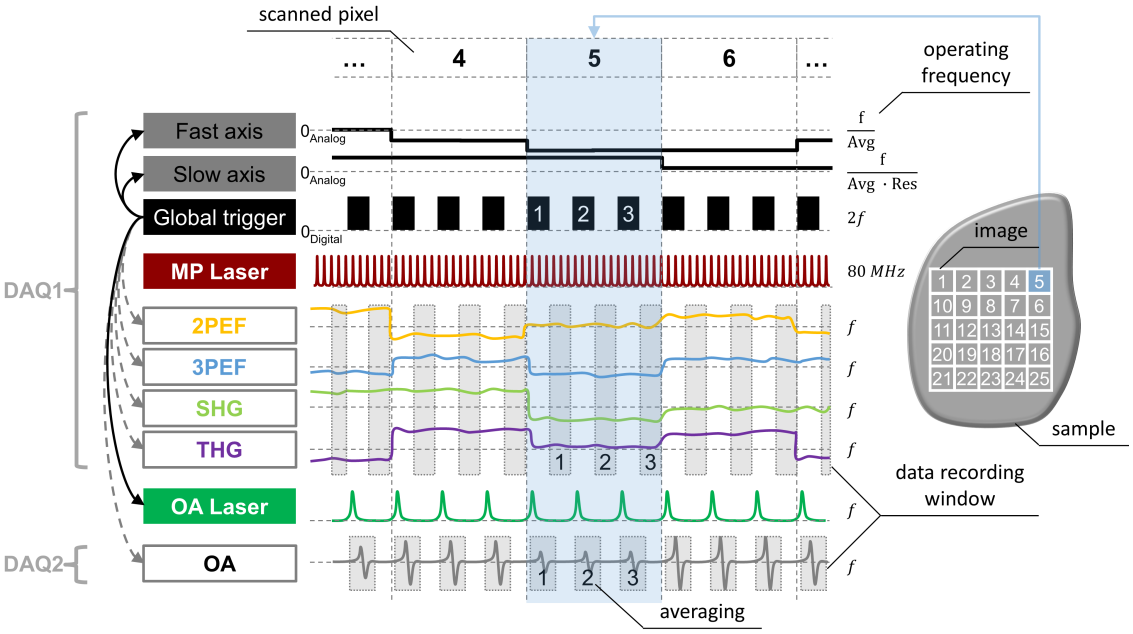

Figure 4.7: Synchronization of HyMPSOM based on a global trigger signal. Shown is a synchronized multi-modal triggering for a $5 \cdot 5$ pixel image with a pixel-averaging of 3, highlighted for the fifth pixel in blue. DAQ1 is controlling the movement of the fast and slow scanning axis, sends out a global trigger and records the multi-photon signals excited by the MP laser in free-run in the off-times of the global trigger signal. The OA laser as well as the DAQ2 for OA detection are actively triggered by the global trigger.

global trigger signal determined the scanning frequency, the acquisition frequency, as well as the repetition rate of actively triggered lasers for optoacoustic microscopy (see Section 4.2.2). The global trigger signal constituted a 0-5 V TTL signal as a digital waveform and was specified actively before starting the measurement. For generating a trigger TTL signal at a repetition rate of f, the underlying control frequency of DAQ1 operated at $2f$ to code digitally for the On and Off states, i.e. 1 and 0, of the TTL. DAQ1 further sent out two analog waveforms ranging across ± 2 V as the slow-axis and fast-axis scanning curves for the galvo mirrors (see Section 4.2). In addition to that, DAQ1 digitized the multi-photon signals as detected by the three PMTs (see Section 4.2.1) on a ± 10 V range. These analog signals were binned according to the underlying control frequency $2f$. As the optoacoustic laser was actively triggered by the sent-out On-states of the global trigger signal at frequency f, only the Off-states were used for recording the multi-photon signals to prevent cross-talk or sensing optical signals excited by the optoacoustic laser.

DAQ2 was used for reading the high-speed data such as the optoacoustic and photodiode signals. For synchronization purposes, the global trigger signal provided by DAQ1 was also fed into the trigger input of DAQ2. As DAQ2 ran at a very high sampling frequency and accepted incoming signals in the range of ± 750 mV, electri-

cal attenuators and a high-pass filter (EF515, Thorlabs) were installed to shape the incoming TTL signal of 50% duty cycle appropriately to a sharp trigger peak. Hence, both data acquisition cards were electrically synchronized. Based on ∼200 MHz being the highest frequency expected to be sensed by the equipped ultrasound transducers, the sampling rate[69] of DAQ2 was set to a minimum of 450 MS/s in order to fulfill the Nyquist–Shannon sampling theorem[70]. As the optoacoustic signals were traveling at ∼1500 m/s through water-like media, DAQ2 actively recorded data after a properly adjusted trigger delay matching the expected duration of the sound wave traveling to the transducer. In this trigger delay, optional defocused positions of the transducer were taken into account (see Section 4.2.2). Due to that, noise signals generated by the laser directly hitting the active element in the transducer and, thus, occurring directly after the laser excitation pulse, were temporally removed. The recorded sample length per trigger signal and, thus, per laser pulse was chosen to cover the detectable axial extension of the acoustic sensitivity field of the equipped transducer of ∼500 µm.
Running the system at high scanning frequencies of more than 50 kHz at a sufficient sampling rate for optoacoustics led to acquiring several tens to hundreds of megabytes of raw data per second. As the internal storage of data acquisition cards are limited in capacity, in case of DAQ2 to ∼60 MB/channel, standard acquisition modes were insufficient to record such huge amount of data. Hence, a streaming-like acquisition mode was implemented being only restricted by the data transfer rate of the PCIe-connection of DAQ2 to the computer (i.e. 3.2 GB/s) and the memory capacity of the used computer (i.e. 64 GB in case of the used PC). The streaming-like acquisition mode was based on assigning temporary data buffers internally on the DAQ2 memory, in which the recorded data could be continuously filled. This approach was therefore called continuous multi-record (CMR) and is schematically presented in Fig. 4.8. (see Appendices: MATLAB™ scripts).
The basic principle of CMR was the definition of temporary buffers which were read-out during data recording. In detail, the internal storage of DAQ2 was subdivided into shorter data buffers of data point[71] length 4096. By starting the data acquisition, the first buffer would be filled with signals until the internal loop coded in the acquisition algorithm (see Appendices: MATLAB™ scripts) returned to start. The duration of the

[69] The DAQ2 (ADQ412, SP Devices) only allowed to set the sampling frequency as integer divisions by 2 of its maximum sampling rate of 3.6 GS/s. Hence, the following sampling frequencies were possible: 3.6 GS/s, 1.8 GS/s, 900 MS/s, 450 MS/s, 225 MS/s, 112.5 MS/s, etc.

[70] The Nyquist–Shannon sampling theorem claims a minimum sampling frequency of twice the expected signal frequency for proper discretizing the signal. However, as discussed in Section 3.3, arbitrarily shaped signals require more than twice their highest frequency for appropriate sampling without loss of information.

[71] Data point means here the number of trigger signals and, thus, the number laser pulses. A buffer length of 4096 has therefore the capacity of storing 4096 optoacoustic signals sampled in an appropriate sampling window of e.g. 512, in which case the actual size of these buffers would be $4096 \cdot 512$.

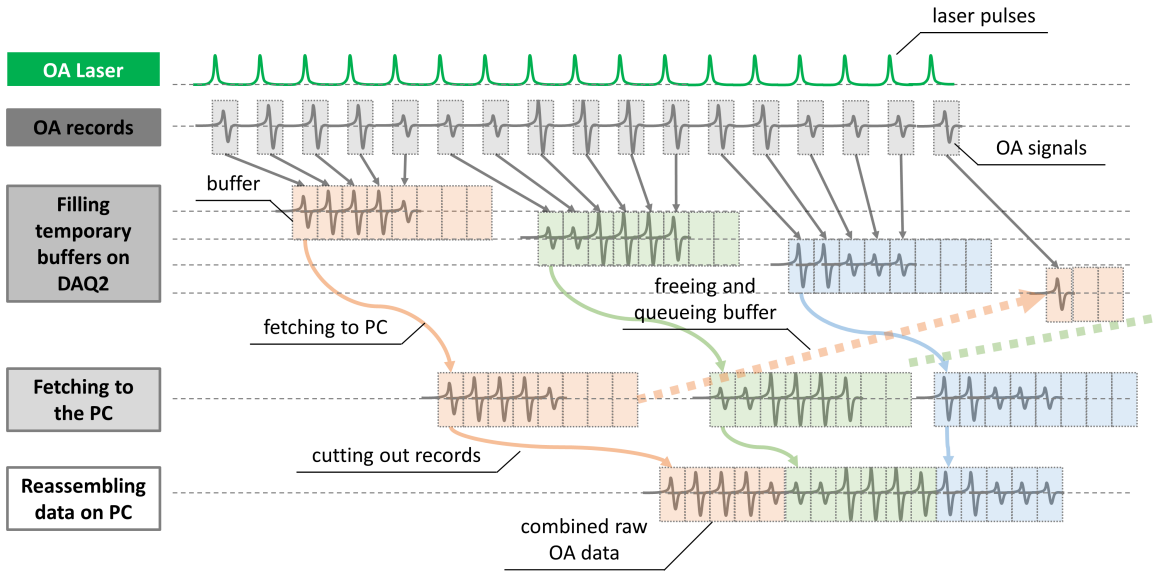

Figure 4.8: Continuous multi-record (CMR) data acquisition is based on temporary buffers defined on the internal storage of DAQ2 and is shown for an exemplary buffer length of 8 entries. After subsequently filling a buffer, the buffered data is fetched to the computer, meanwhile remaining data is recorded and assigned to the following buffer. After a complete fetch, buffers are freed and queued again to the buffer chain on DAQ2.

first loop of records depended on the underlying scanning frequency, the record length per data point, as well as background operations of the computer itself. As the latter varied over time, the number of data points per loop was not constant. The size of the temporary buffers was hence selected to be sufficiently large. As exemplary depicted in Fig. 4.8, the first loop of records received e.g. N data points which were stored in the first N entries of the first temporary buffer. As the data recording continued, the second loop assigned the recorded data to the second buffer, and so on and forth. Meanwhile, in order to record the remaining data in such a continuous manner, the first buffer partly filled with data was fetched to the computer memory, freed after complete data transfer, and was queued to the end of the buffer chain again. In this way, the data was transferred simultaneously to the recording, required minimal extra time after recording the last data points, constituted the fastest acquisition mode of large data sets, and was not limited by the internal storage capacity of DAQ2. Besides that, CMR data acquisition was independent of the scanning procedure and averaging method (see Section 4.2.5).

At the same time as DAQ2 performed the CMR for recording the high speed data, DAQ1 was recording the multi-photon signals. As the optical signals digitized from the three PMTs were binned to the scanning frequency and, thus, only represented a one-value data point per trigger signal, the multi-photon modalities led to a significantly smaller data size. It was therefore possible to collect one-dimensional data vectors during the CMR in so-called background mode. This means, that the entire data of

DAQ1 was acquired in a secondary MATLAB™ script and, subsequent to finishing the CMR acquisition on DAQ2, was transferred back to the main script using a global variable (see Appendices: MATLAB™ scripts).

4.2.5 Scanning procedure and data processing

The image formation and scanning procedure took advantage of the synchronized and simultaneous acquisition of all modalities equipped in the HyMPSOM system as described in the previous chapters. HyMPSOM offered high spatial controllability and automation of all relevant parts required for the image scanning: movement of the optical focus in x, y, and z; movement of the sample in x, y, and z; and movement of the detector in x, y, and z. Although HyMPSOM featured by that nine translational degrees of freedom in spatial directions, the positions of the sensors could be assumed as pre-aligned before the actual measurement. Further postulating that the sensors were able to pick up signals across the entire scanned area led to an equal effect of either moving the optical focal plane axially or displacing the sample axially. Finally, the relevant movements for 3D imaging in HyMPSOM were the sample translation in x, y, and z using the sample-holding stages (MLS203-2 and MZS500-E, Thorlabs) and the translation of the optical focus in x and y using the galvo mirrors (6215H Galvanometer Scanners, Cambridge Technologies). HyMPSOM achieved by that a precision of 250 nm to position the sample both laterally and axially, and 60 nm · 2 µm precision to place the optical focus laterally and axially, receptively. The full control of the remaining five degrees of freedom enabled HyMPSOM to conduct several scanning operations, which are described in the following and schematically depicted in Fig. 4.9, and which were performed either separately or in successively depending on the imaging project (see Section 5.3). All available scanning procedures were based on a serpentine-like acquisition, in which a fast axis was scanning line-wise bi-directionally and a slow axis was scanning step-wise perpendicularly in a uni-directional manner. As a convention, the reference coordinate system in the following is set to the global orientation of the microscope stand defining x, y, and z related to the stand itself pointing to the right, the back, and up, respectively, from the point of view of the binocular.
First, HyMPSOM could operate in a **sample-scanning** mode (see Fig. 4.9a), in which the sample was translated whereas the optical focus and, thus, the actual interrogation area stayed stationary. This scanning operation constituted the slowest procedure, because the movement of the sample-holding stages carrying bulky loads of e.g. the incubator system or an *in vivo* mouse could not accelerate arbitrarily fast. However, the maximum scanable FOV was rather unlimited and only restricted by either the travel range of the stages, i.e. 110 · 75 mm^2, or by the dimension of the sample itself, e.g. ±1.5 cm for the petri dishes. This scanning procedure was mainly used for a coarse assessment of large samples of sizes bigger than 1 cm.

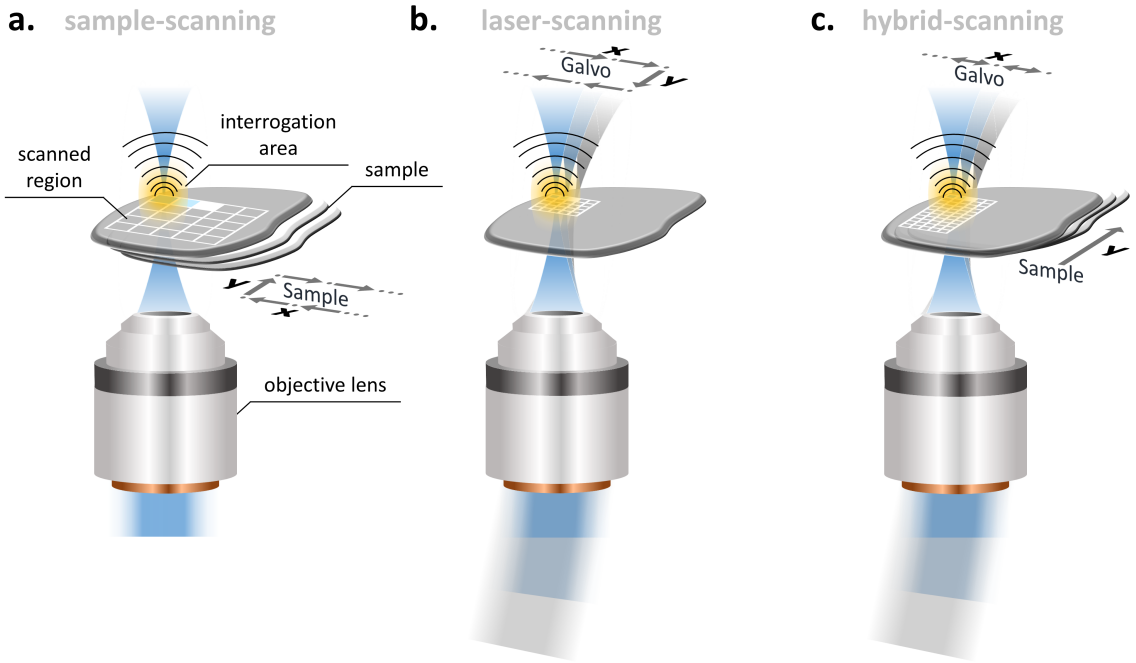

Figure 4.9: Scanning schemes of HyMPSOM. (a) Sample-scanning translates the sample in a step-wise manner through a stationary interrogation area and can image arbitrarily large FOVs for a coarse assessment of the specimens. **(b)** Laser-scanning raster-scans the optical focus across an area of max. ∼630 µm edge length and is used for high-resolution-high-speed imaging. **(c)** Hybrid-scanning continuously moves the sample and perpendicularly scans the optical focus bi-directionally along a line. Hybrid-scanning covers the specimen in stripes of width ∼630 µm and arbitrary length, and can be used for imaging large regions with high resolution. Arrows indicate movement direction of the respective parts.

Second, HyMPSOM could apply **laser-scanning** (see Fig. 4.9b) by the galvo mirrors to scan the optical excitation focii across an area determined by the equipped microscope objective lens. For the two used objective lenses[72], the maximum FOVs obtained were $638 \cdot 638$ µm^2 and $318 \cdot 318$ µm^2, respectively. The previously mentioned achromatic doublet lenses were ensuring herein minimum field distortions and chromatic aberrations at large deflection angels and, thus, at the edges of the images (see FOV characterization in Section 4.3.3). This scanning procedure represented the fastest scanning scheme and allowed to zoom into smaller FOVs such as a single-cell. It was therefore used for studying samples or ROIs smaller than 500 µm or fast processes. Third, HyMPSOM could take advantage of the fully automated control to combine the above mentioned scanning procedures in a hereinafter called **hybrid-scanning** mode (see Fig. 4.9c). In this scanning procedure, the sample-holding stage was moving in one direction continuously, whereas the galvo mirrors were scanning the optical focii

[72] The maximum applicable deflection angle of the galvos is 4° without shifting the beam out of the back apertures of the objective lenses. The two microscope objective lenses are characterized by magnifications of 10x and 20x, respectively (see Section 2.4.3).

along a straight line back and forth perpendicularly to the sample movement. For this procedure, the translation speed of the sample, the deflection of the optical focus, and the number of pixels placed was fully automated and coded into a MATLAB^{TM} script (see Appendices: MATLAB^{TM} scripts). Hybrid-scanning enabled the acquisition of stripes of 638 µm maximum width and nearly unlimited length with maximum spatial precision. The combination of the fast bi-directional scanning of the galvos with a continuous translation of the sample represented the fastest and most elaborated scanning procedure of HyMPSOM for ROIs larger than the maximum FOV achieved by laser-scanning only. Hence, it was used for studying large ROIs at which maximum spatial resolution is required. Fig. 4.10 compiles exemplary optoacoustic images of black sutures at performing different scanning schemes.

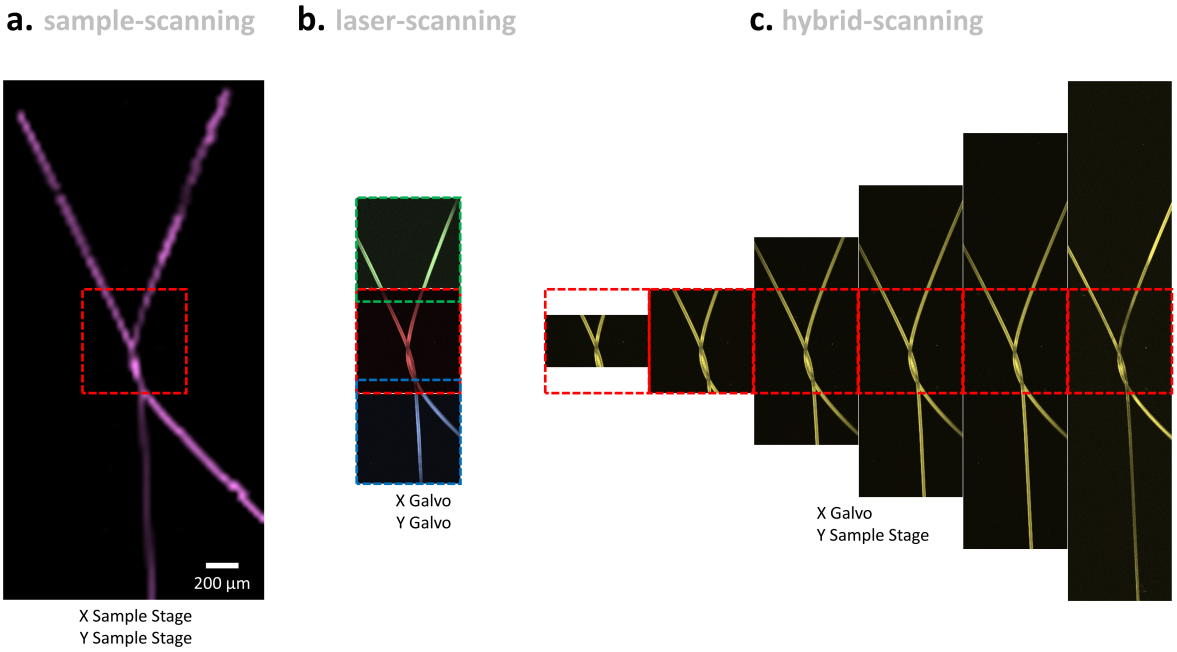

Figure 4.10: Exemplary results at applying different scanning schemes of HyMPSOM by imaging black sutures with OR-OAM. **(a)** Sample-scanning allows for a coarse assessment, **(b)** laser-scanning achieves high-resolution and high-speed but requires FOV stitching (see adjacent colored FOVs), and **(c)** hybrid-scanning enables stripe-like scanning of high-resolution and arbitrary length. The central FOV of maximum size using laser-scanning, i.e. $\sim 630 \cdot 630$ µm^2, is indicated as a red dashed box.

Furthermore, HyMPSOM allowed for both pixel-averaging as well as image-averaging. This means, that the desired number of averages could be either carried out on a per-pixel- or per-image-basis. The latter required a pixel-scanning frequency being equal to the global trigger frequency and, thus, the repetition rate of the optoacoustic laser and acquisition. The former reduced the pixel-scanning frequency by the factor of the

applied averaging. The small-angle step response[73] of the galvo mirrors of 130 µs limited the maximum pixel-scanning frequency to ∼7.7 kHz for non-resonant scanning, but was found to perform well up to scanning frequencies of up to ∼20 kHz. Regarding the timepoints of data sampling, pixel-averaging led to the biggest time difference between the first and the last pixel, whereas image-averaging led to the shortest. However, most scans were performed using averaging on the per-pixel-basis in order to facilitate higher global trigger frequencies. For imaging fast dynamics, a minimal averaging was performed to best approximate a simultaneous pixel acquisition (see Section 2.4.3). The imaging speed achieved in HyMPSOM is characterized in Section 4.3.4.
As the data acquisition cards sampled on a 16-bit (DAQ1) and 12-bit (DAQ2) scale, the corresponding data was recorded as 16-bit single-precision in MATLAB™. The raw recorded data of the multi-photon channels was initially stored in a 1D vector of a length being the number of trigger signals. The raw optoacoustic data was compiled analogously in a 2D matrix, where the first axis equals the number of trigger signals and the second axis equaled the recorded time window per laser pulse. Based on the measurement settings, the code was performing the desired averaging of the raw data on either the per-pixel- or per-image-basis by averaging the respective entries of the raw data. Whereas the multi-photon signals only underwent dark-noise subtraction[74] before image formation, the optoacoustic signal underwent several data processing steps (see Section 3.3.1, Section 3.3.4, and Appendices: MATLAB™ scripts). First, the OA data was frequency-filtered with an asymmetric bandpass filter matching the expected bandwidth of the transducer with:

$$H_f = e^{-(f/f_{hi})^{n_o}} \cdot (1 - e^{-(f/f_{lo})^{n_o}}), \tag{4.1}$$

where f_{hi} and f_{lo} denote the high and low cutoff frequencies and n_o the filter order, which was typically set to 6. Depending on the imaging project, the code further allowed for time-of-flight correction, Hilbert transformation, and total impulse correction. The former estimated the difference of the arrival time based on the scanned FOV and shifted the data accordingly in time, the second was used for projecting the data in 3D, and the latter was correlating the frequency-filtered data with the corresponding spatially assigned impulse responses as described in detail in Section 4.4.4. Next, the code reshaped the signals, both the multi-photon data as well as the optoacoustic data, to a 2D or 3D matrix, respectively. For 2D representations of the optoacoustic data, the maximum amplitude was projected per matrix entry. Finally, all modalities were combined by exporting a 16-bit tiff-stack for further image processing either

[73] This response is defined as the tilt of 0.1° with a precision of 99%, which equals 15.95 µm when using the 10x objective or 7.875 µm when using the 20x objective lens.
[74] The dark-count rate of photomultiplier tubes is the dark noise background signal. In the case of the equipped photomultiplier tubes, the dark-noise level is at ∼60 mV.

in 2D or 3D. The stacks comprised four channels corresponding to the four recorded modalities (i.e. OA, THG, SHG, 2PEF/3PEF) and potentially had a fourth dimension representing these modalities over time for a multi-frame acquisition. The generated tiff-stacks were further processed in Fiji (ImageJ, Wayne Rasband, NIH; latest used version 1.52o) according to Section 3.4, applying gamma correction, contrast enhancements, histogram adjustments, noise reduction by despeckling or outlier-removal, and bi-cubic interpolation. For final representation, multi-modal recordings were depicted based on harmonized color schemes as described in Section 3.4.3.

4.3 General characterization of HyMPSOM

The following chapters concern a general characterization of HyMPSOM. Although the optical-resolution optoacoustic modality is realized in HyMPSOM by a variety of laser sources for excitation, the following characterization is carried out for the finally merged system as described in Section 4.2.3. This is due to exciting optoacoustic signals at 532 nm and multi-photon signals at 1043 nm for simultaneous multi-modal microscopy being the main focus of this work. The investigation of other laser sources are presented in subsequent chapters of their respective projects (see Section 5). Furthermore, reading light scattering and recording brightfield microscopy images is not considered herein a main microscope modality of HyMPSOM and are exclusively used as reference readouts.

4.3.1 Sensitivity and signal-to-noise ratio

The sensitivity and signal-to-noise ratio (SNR) was characterized for each modality as a function of the applied pulse energy in the focus of the respective laser. The characterization was performed on reference specimens such as red blood cells (RBC) in a blood smear, purified elastin and NADH, and starch granules, as well as an *in vivo* mouse ear tissue as shown in Fig. 4.11.

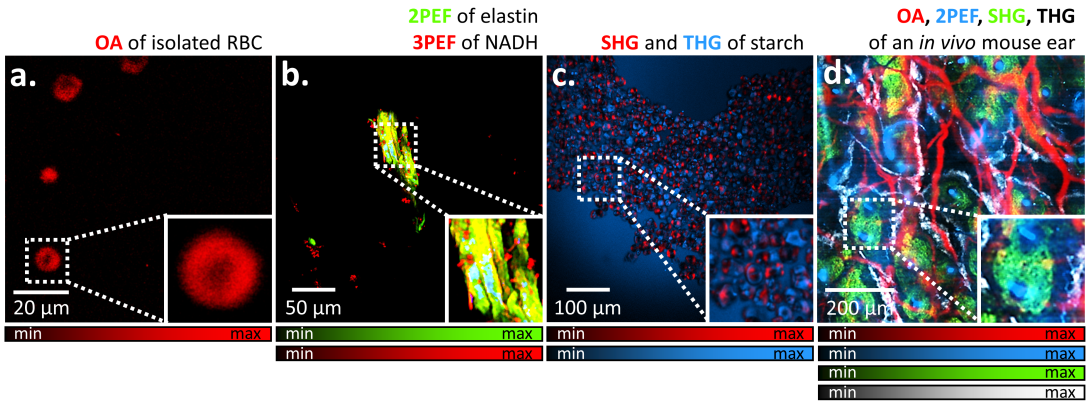

Figure 4.11: Reference specimens for sensitivity and SNR characterization of HyMPSOM. **(a)** Isolated RBCs in a mouse blood smear imaged by OA; **(b)** Pure elastin and NADH imaged by 2PEF and 3PEF, respectively; **(c)** Starch granules imaged by SHG and THG.

Optoacoustic

Fig. 4.11a shows the measurement of an isolated single red blood cell (RBC) in a fresh mouse blood smear at 532 nm laser excitation and ultrasound detection using the 50 MHz transducer HFM23 as the most sensitive detector. The scan was carried out using an energy of 4.35 nJ/pulse at the sample, 20 averages, a FOV of ∼100 · 100 µm^2, and a sampling rate of 900 MS/s. The averaged amplitude was measured to be 31.7 mV thresholded above a background noise level of 7.9 mV, which leads to an associated SNR of 9.6 dB using $SNR = 20 \cdot log(Signal/Noise)$.

2PEF and 3PEF

The sensitivities of 2PEF and 3PEF were determined by measuring pure elastin (CAS Number 9007-58-3, Elastin, Sigma-Aldrich) and pure NADH (CAS Number 606-68-8, NADH, Sigma-Aldrich), respectively (see Fig. 4.11b). The measurement was performed using an energy of 1.1 nJ/pulse at the sample, 20 averages, a FOV of ∼315 · 315 µm^2, and a scanning rate of 300 kHz. The averaged intensities of 177 mV for elastin sensed by 2PEF and 35 mV for NADH sensed by 3PEF both at a background noise of 0.7 mV led to SNRs of 48.0 dB and 33.8 dB, respectively.

SHG and THG

The achieved sensitivities of SHG and THG were obtained by imaging starch granules as a reference sample (see Fig. 4.11c). In here, amylopectin constituted the main source for SHG signals [94]. THG was characterized alongside the glass-air interface

(Difference in refractive index: Δn_0=0.53). The entire measurement was carried out using 1.1 nJ/pulse and 20 averages across a FOV of ∼630 · 630 µm^2. Obtained averaged intensities were 30.1 mV for SHG at a background noise of 0.7 mV and 127.3 mV for THG at a background noise of 7.2 mV, leading to SNRs of 32.5 dB and 24.4 dB, respectively.

Multi-modal imaging

For characterizing the sensitivity of HyMPSOM when performing simultaneous multimodal microscopy, an *in vivo* mouse ear scan was analyzed as shown in Fig. 4.11d. The image was acquired at pulse energies of ∼53 nJ (OA) and 3.6 nJ (MP), 50 averages, stitched to form a total FOV of ∼0.8 · 0.8 mm^2 and a scanning rate of 50 kHz. Analogous analysis led to SNRs of 33.4 dB (OA), 36.4 dB (2PEF), 44.8 dB (SHG), and 27.2 dB (THG).

4.3.2 Spatial resolution

The spatial resolution of the equipped OR-OAM and MPM modalities in HyMPSOM was determined by imaging polystyrene microspheres using the following preparation protocol: (1) The microsphere-stock-suspensions were diluted ∼1/200 times, mixed with ∼1%$^{\text{vol.}}$ TWEEN^{TM} 20 (Sigma-Aldrich), and sonicated by ultrasonic baths to prevent agglomerations; (2) Low-melting agar (Sigma-Aldrich) was dissolved in a ratio of 1g/100 mL into deionized water, heated to ∼70 °C until a transparent gel-like substance was obtained, and cooled down again to room temperature; (3) During cool-down at temperatures lower than ∼35 °C, at which the agar gel is still fluid, the microspheres were added; (4) The agar-sphere-gel was gently panned for mixing and placed into a heated ultrasound bath for ∼30 s to eliminate air bubbles; (5) Finally, the mixed agar-sphere-gel was poured into glass bottom petri dishes (D60-30-1.5-N, IBL). The dish contained a 170 µm glass plate for which the used objectives are corrected for to ensure optimum focusing. The resolutions were determined for laser-scanning as described previously (see Section 2.4.3), as it offers the finest rastering of the optical focii and is used for high-resolution imaging. In addition to that, the resolution was characterized for both objectives of 0.45 NA (Plan-Apochromat 10x/0.45, Zeiss) and 1.0 NA (W Plan-Apochromat 20x/1.0, Zeiss). For each measurement, a FOV of >5 · 5 µm^2 was scanned with 100 · 100 pixels. The dimensions were determined by stepwise translating the spheres in 1 µm steps as explained in Section 4.3.3.
The spatial resolution of the OR-OAM modality was based on imaging a black polystyrene microspheres of 200 nm diameter (Polybead® Black Dyed Microspheres, 0.20 µm, Polysciences). In here, the lateral resolution is independent of the properties of the ultrasound detector as it is purely determined by the focusing abilities of the objective.

In contrast, the axial resolution depends on the frequency bandwidth of the transducer and, thus, on the highest frequency captured. The optoacoustic sampling rate was set to 900 MS/s to ensure proper capturing of the highest expected frequency sensed by the transducer[75]. For the 10x 0.45 NA objective, a FOV of $8.512 \cdot 8.512$ µm^2 was scanned with a resolution of $100 \cdot 100$ pixels, a per-pixel averaging of 100, and a pulse energy of ∼613 pJ at the sample; for the 20x 1.0 NA objective, a FOV of $5.645 \cdot 5.645$ µm^2 was scanned with a resolution of $100 \cdot 100$ pixels, a pixel averaging of 100, and a pulse energy of ∼573 pJ at the sample.
The MPM modalities were characterized regarding their spatial resolution by assuming that the effective optical PSF of each modality is proportionally to the power N of the energy distribution $\propto I^N$ required to induce the corresponding multi-photon processes (see Section 3.2). Hence, at recording two- and three-photon processes (two-photon (N=2): 2PEF and SHG; three-photon (N=3): 3PEF and THG), the effective PSF and subsequently the expected spatial resolution of 2PEF and SHG could thus be assumed to be identical, analogously to 3PEF and THG. The multi-photon modalities were therefore categorized by the number of involved photons and characterized by the fluorescent modality in each group (i.e. 2PEF and 3PEF). For that, fluorescent nanobeads were used, absorbing at 521.5 nm (two-photon excitation; Fluoresbrite® YO Carboxylate Microspheres, 0.10µm, Polyscience Inc.) and at 347.6 nm (three-photon excitation; Fluoresbrite® BB Carboxylate Microspheres, 0.10µm). For the 10x 0.45 NA objective, a 3D volume of $8.478 \cdot 8.478 \cdot 30$ µm^3 was scanned with $200 \cdot 200$ pixels and an axial slice distance of 0.75 µm, an per-image averaging of 5, and a pulse energy of 542 pJ at the sample; for the 20x 1.0 NA objective, a FOV of $5.631 \cdot 5.631 \cdot 21$ µm^3 was scanned with $200 \cdot 200$ pixels and an axial slice distance of 0.75 µm, an per-image averaging of 5, and a pulse energy of 473 pJ at the sample.
Fig. 4.12 depicts all carried out spatial resolution characterizations by imaging microspheres. The shown images constitute spatial projections onto the xy- and xz-planes of the raw signals as recorded by the HyMPSOM system without image-post-processing steps, except normalization for enhancing the visibility. For comparable depiction, each FOV was cropped to $5 \cdot 5$ µm^2. Each lateral or axial projection was analyzed by measuring the FWHM of a Gaussian curve fitted to the respective lateral and axial data profile, which was extracted from the unprocessed image.
For direct measurement of the spatial resolution, i.e. the PSF of the modalities, proper signal point sources would be required. As the size of the used bead sizes were in the range of the expected resolution of the system, their diameters could not be neglected. To receive the actual spatial resolution R, each measured FWHM of the fitted data was assumed to follow a Gaussian shaped PSF (either optically or acoustically) convolved with the sphere diameter, which was in this regard also assumed Gaussian shaped with

[75] The highest expected frequency to be sensed by the 50-MHz transducer is ∼120 MHz. According to the Nyquist–Shannon sampling theorem, the sampling rate should be at least twice that frequency.

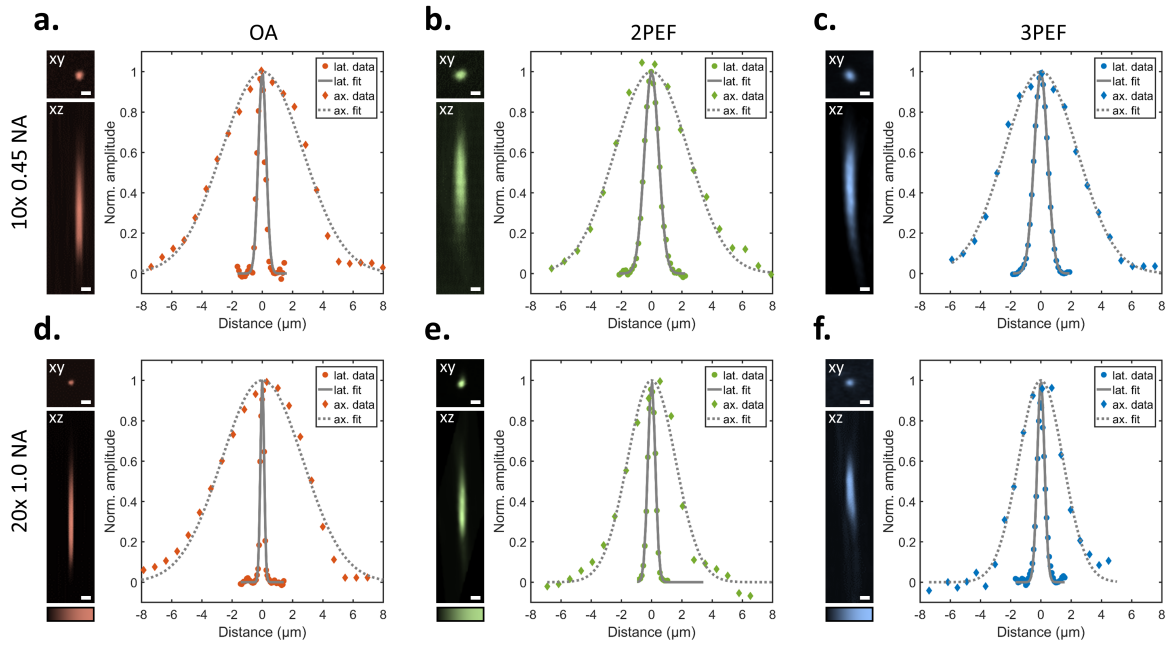

Figure 4.12: Resolution determination of HyMPSOM by imaging microspheres. The achieved spatial resolution is characterized by imaging 200 nm black microspheres for OR-OAM and 100 nm fluorescent microspheres for 2PEF and 3PEF. **(a)** *xy*- and *xz*-MAP images for OR-OAM using the 10x 0.45 NA objective; lateral (dots) and axial (diamonds) data profiles and lateral (line) and axial (dashes) Gaussian fits. Analogous depiction of **(b)** 2PEF and **(c)** 3PEF for the 10x 0.45 NA objective; and of **(d)** OA, **(e)** 2PEF, and **(f)** 3PEF for the 20x 1.0 NA objective. Scale bar is 1 µm, images are scaled isotropically.

a nominal diameter of $\pm 3\sigma$ [23]. Under these assumptions, the actual resolutions could be analytically derived by:

$$R = \sqrt{d_{exp}^2 - \left(\frac{1}{3} \cdot \sqrt{2 \cdot \ln(2)} \cdot d_{nom}\right)^2}, \tag{4.2}$$

where d_{exp} is the experimentally determined FWHM of the Gaussian fit. Gaussian fits corrected according to Equation 4.2 obtained following spatial resolutions:

Modality	OA		2PEF/SHG		3PEF/THG	
Objective	10x 0.45 NA	20x 1.0 NA	10x 0.45 NA	20x 1.0 NA	10x 0.45 NA	20x 1.0 NA
Lateral resolution	604.3 nm (R^2=0.988)	279.9 nm (R^2=0.985)	1104.0 nm (R^2=0.997)	574.6 nm (R^2=0.996)	1072.3 nm (R^2=0.999)	563.6 nm (R^2=0.997)
Axial resolution	6.324 µm (R^2=0.984)	6.302 µm (R^2=0.976)	5.710 µm (R^2=0.989)	3.739 µm (R^2=0.976)	5.667 µm (R^2=0.992)	3.714 µm (R^2=0.992)

Table 1: Determined spatial resolutions of the modalities implemented in HyMPSOM.

Tab. 1 compiles the fitted data profiles, both axially and laterally, for the OA, 2PEF, and 3PEF modality at imaging with the 10x 0.45 NA as well as with the 20x 1.0 NA objective.
In summary, all modalities operate at similar spatial resolutions in both lateral and axial direction. Whereas the formed images of each modality can apply spatial corrections of the corresponding PSF by e.g. Wiener deconvolution, the optoacoustic signals can be corrected on the signal level. For that, each optoacoustic signal is corrected for its spatially assigned impulse response as described in Section 4.4.

4.3.3 Field of view and co-registration

The maximum FOV that can be imaged in HyMPSOM strongly depends on both the scanning technique (see Section 4.2.5) and the equipped objective lens (Plan-Apochromat 10x/0.45 and W Plan-Apochromat 20x/1.0, Zeiss). For the former, only the maximum FOV enabled by laser-scanning needs to be determined, as sample-scanning achieves arbitrarily large FOV and hybrid-scanning arbitrarily long stripes, the widths of which are determined by the maximum FOV of the laser-scanning. For the latter, the maximum displacement of the optical focus is defined by the objective's magnification. As described in Section 2.4.3, laser-scanning microscopy opts for objectives offering high-resolution by a high numerical aperture combined with a large FOV by low magnification. The maximum FOVs were thus determined for both objective lenses as well as for the optoacoustic and multi-photon modality. To obtain the FOV size, suture phantoms placed in glass bottom petri dishes (D60-30-1.5-N, IBL) were used due to strong OA and THG contrast. The suture phantom was translated laterally in a step-wise manner by using the sample-holding stage (MLS203-2, Thorlabs) after appropriate focusing.

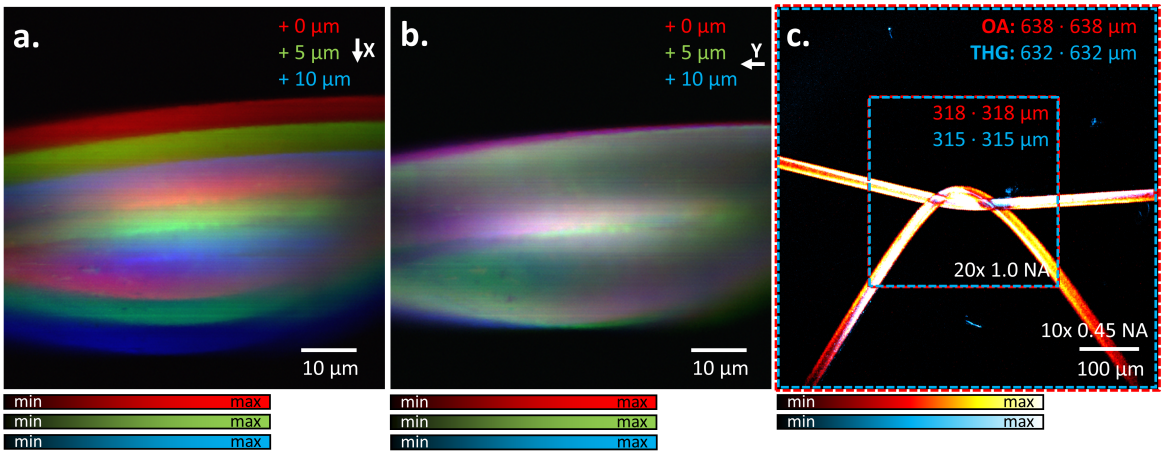

Figure 4.13: FOV size determination in HyMPSOM. The scanned FOV determined by step-wise translating 18 µm sutures along the **(a)** x- and **(b)** y-axis as exemplary shown in a zoom-in. **(c)** The achieved FOVs indicated on a scan performed with the 10x objective.

Fig. 4.13a and b show exemplarily the lateral displacement of two 18 µm intertwined sutures translated in 5 µm steps in the x-direction (see Fig. 4.13a) and y-direction (see Fig. 4.13b) measured with OR-OAM. The achieved FOV sizes as shown in Fig. 4.13c for the 10x objective were determined to be $638 \cdot 638$ µm^2 for the OR-OAM modality operated at 532 nm excitation wavelength and $632 \cdot 632$ µm^2 for the MPM modalities. The FOV using the 20x objective were determined to be $318 \cdot 318$ µm^2 for OR-OAM and $315 \cdot 315$ µm^2 for MPM using an identical approach (Data not shown; FOV size indicated in Fig. 4.13c).
The FOV linearity was characterized via imaging a grid resolution test target (R1L3S3P, Thorlabs) to rule out FOV distortions due to non-linear displacements of the optical focii. In this regard, achromatic doublet lenses were installed as mentioned in Section 4.2 and schematically shown in Fig. 4.1 to minimize such FOV distortions.

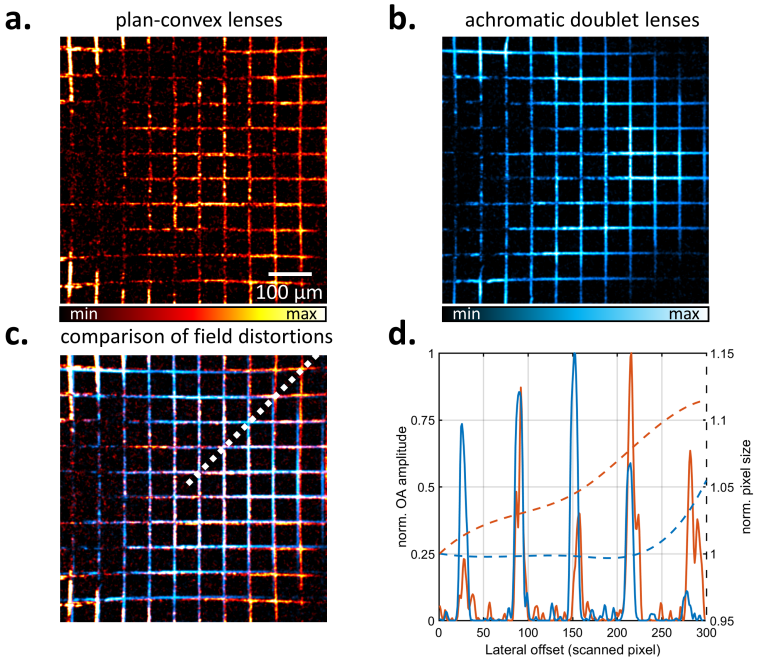

Figure 4.14: FOV distortion determination in HyMPSOM. FOV distortions due to non-linear scanning of the optical focii determined by a grid resolution test target for **(a)** plan-convex lenses and **(b)** achromatic doublet lenses as the scan lens pairs. **(c)** The comparison indicates significant reduction in FOV distortion using achromatic doublet lenses. **(d)** Non-linear pixel positions of the grid lines and derived pixel sizes along the line shown in (c) for plan-convex lenses (red) and achromatic doublet lenses (blue).

Fig. 4.14 depicts the measurements of the grid resolution test target in OR-OAM. Fig. 4.14a shows the test target imaged with the 10x objective using conventional plan-convex lenses as the scan lenses. Fig. 4.14b depicts the analogous measurement using achromatic doublet lenses. The overlay in Fig. 4.14c indicates a reduction of FOV distortions by using achromatic doublet lenses as compared to plan-convex lenses, especially at the most outer grid lines. Analogous measurements with the 20x objective (Data not shown) had similar findings. Analysis of the grid line positions for both lens

pairs along the line in Fig. 4.14c is shown in Fig. 4.14d. Although the grid lines coincided for small lateral offsets, they deviated at outer regions of the FOV. Deriving the corresponding pixel size indicated an almost linear increase as the lateral offset gets larger for the plan-convex lenses (dashed red line), whereas the pixel sizes stayed constant over the first 220 pixels (corresponding to ∼75% lateral size of the FOV) for the achromatic doublet lenses.

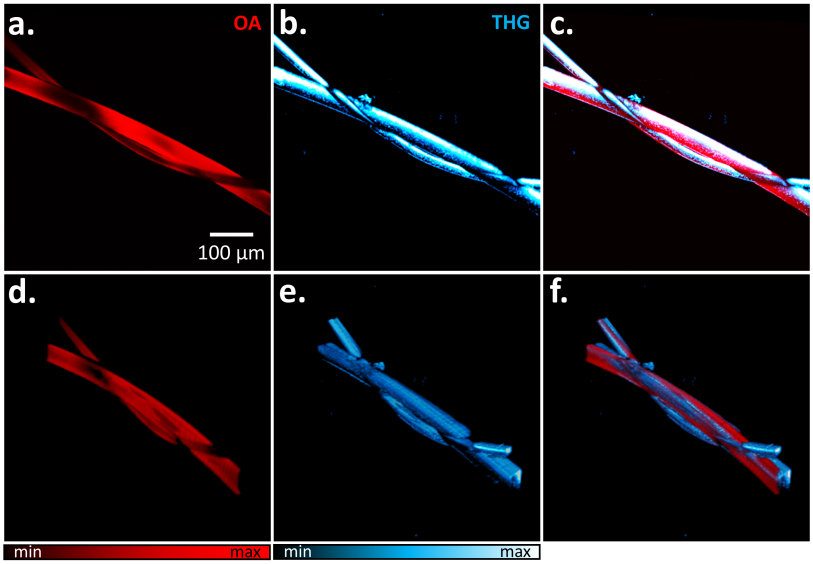

Figure 4.15: Co-registration of the modalities using a suture phantom. Co-alignment of the modalities using a suture phantom giving rise to OA and THG signals. 2D projections of the **(a)** OA and **(b)** THG measurement. **(c)** The overlay indicates negligible lateral offset among the modalities. **(d-e)** Analogous 3D projections of the signals. **(f)** 3D overlay after correction of the chromatic aberration induced focal shift between the excitation wavelengths and time-of-flight differences in OA signals originating from lateral offset positions.

Subsequent to the FOV determination, a suture phantom was used to minimize the spatial offset between the modalities. Fig. 4.15 shows the suture phantom consisting of two intertwined sutures (18 µm and 30 µm nominal diameter) imaged with OR-OAM (see Fig. 4.15a) and THG (see Fig. 4.15b), respectively, after co-aligning the laser beam paths. The overlay of OR-OAM and THG (see Fig. 4.15c) indicated a lateral offset among the modalities referenced to OR-OAM of 1.4 µm in $+x$ and 1.2 µm in $+y$ at measuring the suture boundaries in the center of the FOV with the 10x objective and 0.7 µm in $+x$ and $+y$ with the 20x objective. Fig. 4.15d and e depict 3D projections of the suture phantom data. The axial offset was analogously measured in the center of the FOV[76] by translating the suture phantom axially and was determined to -34.8 µm with

[76] As the recorded OA images are bent in 3D due to differences in the arrival times of signals coming from a lateral offset, this offset only holds for a central position. The axially bent FOV in OA can be corrected by subtracting the expected time-of-flight differences or by correcting for the total impulse response (see Section 4.4).

the 10x objective and -7.0 µm with the 20x objective. These offsets could be explained by chromatic aberrations of microscope objective lenses at focusing wavelengths of 532 nm (OR-OAM) and 1043 nm (MPM). The yielded offsets resembled the expected values according to the datasheets of the two objectives being -31.11 µm focal shift between the two wavelengths for the 10x objective and -6.1 µm for the 20x objective and, thus, confirmed a proper collimation of the two laser beams before entering the objectives. After correcting the axial offset and the time-of-flight difference in OR-OAM of signals originating from lateral offset positions, the 3D overlay shown in Fig. 4.15f revealed a good spatial co-registration among the modalities. Although the axial offset at using the 10x objective was relatively large, it was of benefit at measuring mouse *in vivo* tissue as the vasculature sensed by optoacoustic lays significantly deeper than the moieties of the epidermis sensed by multi-photon modalities (see Section 5.2).

4.3.4 Imaging speed

Fast imaging is a crucial factor in microscopy, especially in order to enable measurements of *in vivo* samples such as cells, zebrafishs, and mice. The conditions for cell- and zebrafish-imaging can in this regard be controlled using the previously mentioned stage top incubator (see Section 4.2.3), which therefore allows for long-time measurements. Imaging *in vivo* mice is however limited in their duration by the granted animal protocol restricting the allowed time of anesthesia to a maximum of 1.5 h. This includes sample preparation, i.e. fixation of the mouse to the mouse holder (see Fig. 4.6), as well as optical focusing, leaving a pure measurement time of ∼50 min. This further decreases to ∼40 min due to the time required for saving the acquired data. On the other hand, imaging of dynamic processes, e.g. calcium responses in cells and cardiac organoids as described in Section 5.3.3, requires imaging framerates fast enough to obtain such dynamics. Hence, imaging at maximum framerate is in general of high interest to facilitate a broad range of applications for HyMPSOM.
For that, HyMPSOM implements multi-modal microscopy by a simultaneous data acquisition based on a global trigger technique (see Section 4.2.4). This data acquisition enabled to sense and record all global trigger pulses thereby defining the imaging speed. To perform such multi-modal imaging, the 532 nm laser dedicated for generating optoacoustic signals restrained the maximum trigger frequency by its maximum repetition rate of 50 kHz. Due to the need of signal averaging Avg times, the pixel-scanning frequency could thus be expressed as $f_{pixel} = 50/Avg$ kHz, which led subsequently to a framerate of $f_{frame} = 50/(Pix \cdot Avg)$ kHz of images containing Pix number of pixels. Standard values for a laser-scanning imaging placing $400 \cdot 400$ pixels in a FOV of $\sim 630 \cdot 630$ µm^2 at a pixel-averaging of 20 resulted in a framerate of 0.015 Hz or 64 s. FOVs covering a single-cell, i.e. $\sim 20 \cdot 20$ pixels across $10 \cdot 10$ µm^2 averaged 20 times, could be acquired at 6.25 Hz or in 160 ms. For mouse *in vivo* imaging of maximum 40 min acquisition time, the maximum amount of scanned pixels was ∼120 million.

Due to 50 averages required for imaging deep *in vivo* tissues, a maximum of 2.5 million pixels could be scanned finally leading to a maximum applicable FOV of ∼1500 ·1500 pixels placed across $3 \cdot 3$ mm^2 at a pixel size of 2 µm as applied typically for mouse measurements.
Besides simultaneous multi-modal imaging, the modalities equipped in HyMPSOM can operate individually. Multi-photon microscopy based on a laser running at ∼80 MHz was limited by the required time for collecting the optical signals in binning times and was ascertained to be optimized at a pixel scanning frequency[77] $f_{pixel} = 300$ kHz. Furthermore, alternative laser sources for optoacoustic microscopy, namely high-speed laser diodes and a supercontinuum laser, enabled significant faster repetition rates of up to several MHz. However, the duration of generated ultrasound waves traveling from the sample to the transducer was herein the time-limiting factor. At a sample-transducer distance[78] of ∼3.5 mm and taking into account the built-in delay-line of the transducers[79], ultrasound waves arrived at ∼3 µs after the excitation pulse by using water as the coupling medium (speed of sound: ∼1500 m/s). Hence, the maximum repetition rate to allow complete travel and sensing of the ultrasound waves was ∼300 kHz. However, optoacoustic microscopy could also operate in the frequency domain at using modulated CW lasers as described in Section 5.4.1 or laser diodes running in burst mode as described in Section 5.4.2. In here, the optoacoustic signals were generated and sensed at a MHz repetition rate and, thus, facilitated faster scanning. However, the maximum applicable scanning speed of the equipped galvanometric mirrors of ∼300 kHz limited the pixel scanning speed likewise to $f_{pixel} = 300$ kHz.

4.4 Optoacoustic total impulse response (TIR) of HyMPSOM

The theoretical foundation of a systems total impulse response (TIR), its concept of characterization, and possible ways of correction are comprehensively elaborated in Section 3.3.4, whereas this chapter focuses on its realization within the HyMPSOM system[80].
In short, optoacoustic microscopy based on laser-scanning image formation acquires signals originating from lateral and axial offset positions with respect to the acoustic focus as described theoretically in Section 3.3 and practically in Section 4.2.2 regarding its realization in HyMPSOM. As acoustic waves enter the focusing element of the equipped ultrasound detector from positions outside of the acoustic focal volume, the waves do not impinge the ultrasound sensing element as plane waves. Such spatial

[77] This scanning rate can be interpreted as the resonant movement of the galvo mirrors.
[78] The equipped transducers have a focal distance of ∼3 mm. Furthermore, the transducers were placed in ∼500 µm positive defocus.
[79] The delayline depends on the thickness of the ultrasound focusing glass lens. For the equipped transducers, the delayline was 0.65 µs.
[80] The subsequent chapters are part of an article in revision [78] during the time of writing this thesis.

offsets lead subsequently to distortions and interferences of the signals. Further, the use of an electric acquisition chain, i.e. all electrical components from the detector to the data acquisition card, leads to the recording of signals that are additionally modified electrically compared to their original shape, which alters their representation within the images (see Section 3.3.1). The combined effect of these modifications is typically termed the total impulse response (TIR) of the optoacoustic microscope being a system specific characterization describing how optoacoustic signals are sensed by the system.

4.4.1 Surrogate optoacoustic point sources

Precise TIR characterization requires proper optoacoustic point sources distributed throughout the detectable volume or, in other words, the transducers sensitivity field. For that, an optical excitation was focused onto a super-flat and ultra-thin 2D absorbing plane realized by a gold nanolayer (GNL). The GNL constituted in this approach an emanation basis of optoacoustic signals upon optical excitation with a laser source. The GNL, as depicted in Fig. 4.16a, consisted of a 250 nm thick layer of gold (>99.99% purity; Agosi AG, Pforzheim, Germany) evaporated on top of a 4 nm thick titanium adhesion layer (>99.995% purity; HMW Hauner, Röttenbach, Germany and >99.98% purity; Material Research S.A.) deposited onto a 170 µm cover slip (107242 No. 1.5H, Marienfeld). Both layers were coated under high vacuum of $<10^{-7}$ mbar by electron beam assisted deposition (Metal Evaporator L560, Leybold, Köln, Germany) at 0.2 Å/s to ensure high crystalline quality required for high homogeneity of the gold layer. Calculations of the reflectivity and transmission of these two layer using Fresnel equations [95,96] of excitation light at 532 nm wavelength at normal incidence revealed ∼13% transmission through the titanium layer followed by ∼29% absorption within the gold layer.

The combination of a diffraction-limited optical excitation of ∼600 nm diameter with a light penetration at the used wavelength of ∼40 nm defined the extent of the excited volume being significantly smaller than the acoustic resolution in both lateral and axial directions (see Fig. 4.16a). Hence, the generated signal originated from a volume constituting an acoustic point source which is hereafter called surrogate optoacoustic point source (SOAP). In this view, the excitation with an optical focus led the GNL to act effectively as an infinite plane, in which optoacoustic point sources can be generated at desired locations.

First, a validation of the SOAP approach was carried out to prove the generation of proper optoacoustic point sources required for TIR characterization (see 4.16b-e). For that, the OR-OAM signals received from exciting the GNL were compared to the ones from a 1 µm black polystyrene microsphere (Polybead® Black Dyed Microspheres, 1.00 µm, Polysciences) embedded in agar as a standard optoacoustic point source. Both samples were measured with identical acquisition parameters and processing steps (i.e. pulse energy, lateral and axial position, number of averages, sampling rate, frequency filtering, and projection).

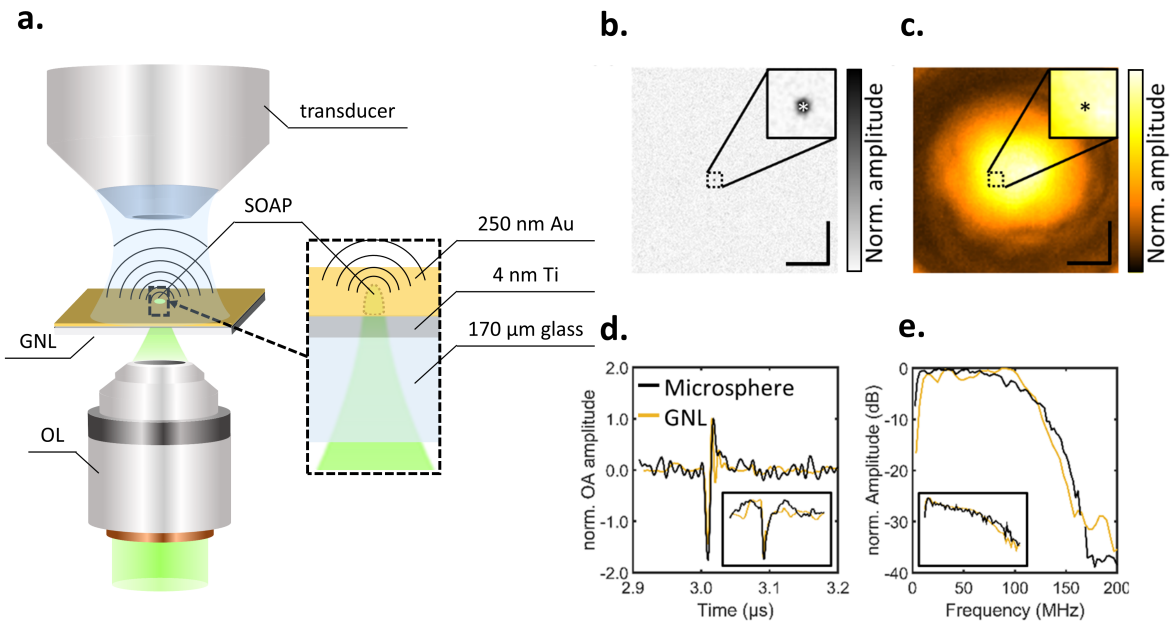

Figure 4.16: Comparison of a gold nanolayer and a 1 µm black polystyrene microsphere as optoacoustic point sources. **(a)** Experimental setting for generating SOAPs by exciting the GNL with a diffraction-limited focus. Close up of the cross-section of the GNL and the generated SOAP. Yielded OR-OAM MAP onto the xy-plane of a **(b)** black polystyrene microsphere and the **(c)** GNL at the same axial position. **(d)** Raw OR-OAM signals and corresponding impulse responses (inset) of the positions in panels (b) and (c) marked with asterisks. **(e)** Frequency content of the microsphere (black) and the gold nanolayer (gold), and their corresponding frequency responses (inset). Scale bars, 100 µm. (Adapted from [78])

Fig. 4.16b and c show the maximum amplitude projections (MAP) onto the xy-plane of the scan of the microsphere and the GNL, respectively. Whereas in Fig. 4.16b, the microsphere was the only optoacoustic point source in the scanned area, the scan of the GNL covering an identical area (see Fig. 4.16c) was composed of adjacent SOAPs and, thus, constituted optoacoustic point sources at each pixel. Hence, each areal 2D scan of the GNL contained several orders of magnitude more point sources, depending on the number of pixels placed in the FOV. Due to identical measurement parameters, analysis on the raw signal level was enabled. The raw time-resolved signals of both samples (see Fig. 4.16d) resembled each other regarding the arrival time and amplitude relation of the bipolar signal shape. Similar finding was yielded for the associated frequency contents shown in Fig. 4.16e as well as the corresponding impulse responses (see Fig. 4.16d, inset) and frequency responses (see Fig. 4.16e, inset), latter were still convolved with the electric impulse response and electric frequency response, respectively. Moreover, the GNL signal was featured with significantly higher SNR (28.3 dB) than the microsphere signal (20.7 dB).

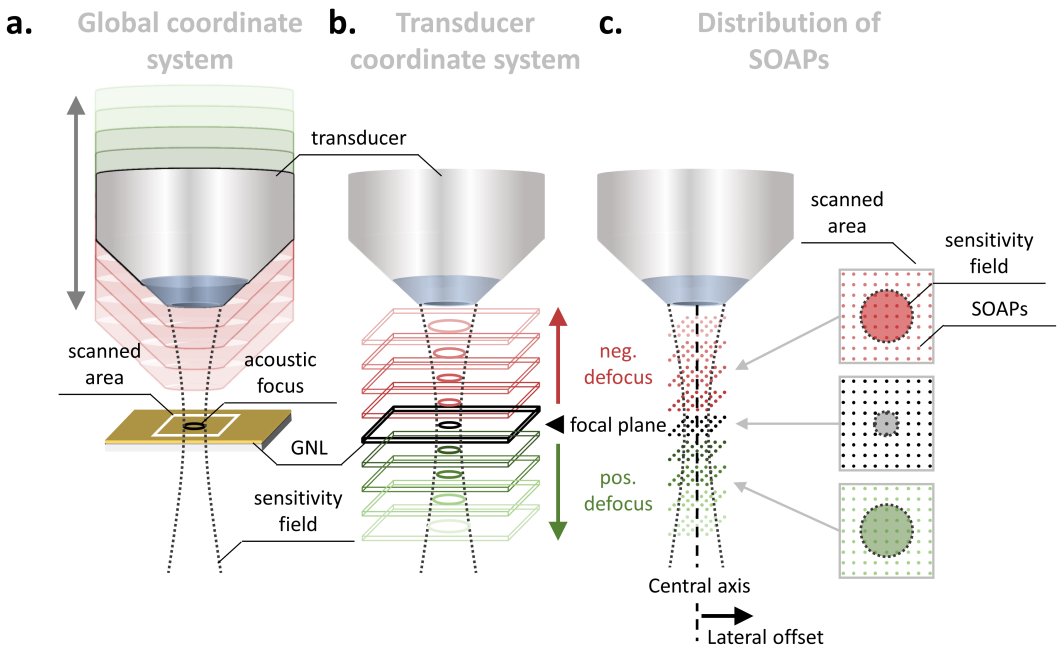

Figure 4.17: 3D scanning approach of distributing SOAPs throughout the sensitivity field of the transducer. Scanning scheme for distributing SOAPs throughout a 3D volume in **(a)** the global coordinate system of the microscope and **(b)** relative to the transducer position. **(c)** Step-wise distributing SOAPs throughout a 3D volume axial adjacing 2D lateral scans exemplary shown in **(d)**.

4.4.2 Experimental determination of the optoacoustic TIR

The resemblances of the raw signals and the frequency contents between a microsphere and the GNL suggested that by axially translating the transducer with respect to the GNL, 2D scans of the GNL in a laser-scanning approach (see Section 4.2.5 and Fig. 4.17a) would generate SOAPs for patterning a 3D volume. As described previously, HyMPSOM can precisely control the spatial position of the transducer, the sample, and the optical focus each in 3D (see Section 4.2) and, thus, facilitated such a 3D scanning approach as required for experimental TIR characterization. Hence, the high controllability of HyMPSOM in combination with the GNL approach for generating SOAPs allowed to characterize the entire sensitivity field of the transducer by distributing identical point sources throughout a 3D volume of choice. For that, the transducer was moved perpendicularly to the GNL whereas the optical focal plane and GNL position were kept constant throughout this procedure. Referenced to the coordinate system of the transducer, it seemed that the GNL and, thus, the layer of SOAPs generated in a 2D scan were moving axially (see Fig. 4.17b). By that, a 3D volume of $630 \cdot 630 \cdot 2300$ µm^3 was characterized covering lateral offsets up to 445 µm and axial offsets of up to $\pm$ 1150 µm with respect to the acoustic focus (see Fig. 4.17c).
The entire sensitivity field was characterized in this manner covering the acoustic near field (i.e. negative defocus) and the acoustic far field (i.e. positive defocus) (see Fig.

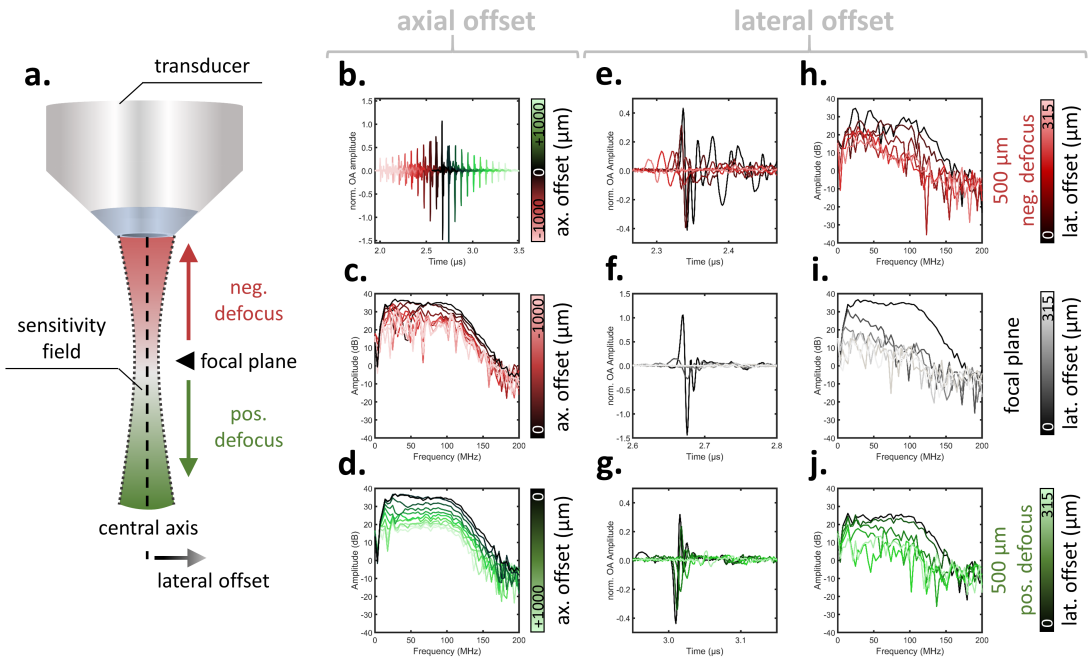

Figure 4.18: Dependence of raw OA A-lines and frequency contents on axial and lateral offsets. (a) Schematic depiction of the characterized sensitivity field of the transducer. **(b)** Raw OA A-lines of synthetic OA point sources co-axially to the transducer from -1000 µm (red) to the focal plane (black) and +1000 µm defocus in 100 µm steps. **(c-d)** Frequency content of co-axial OA point sources in panel (b) in the direction of (c) negative or (d) positive defocus. **(e-g)** Lateral offset dependence of raw OA A-lines from 0 to 315 µm measured at (e) 500 µm negative defocus, (f) the focal plane and (g) 500 µm positive defocus. **(h-j)** Frequency content of the A-lines shown in panels (e-g). Abbreviations: ax., axial; lat., lateral, neg., negative; norm., normalized; pos., positive. (Adapted from [78])

4.18a). At each axial position, the signals were gradually analyzed from the co-axial offset (i.e. centered beneath the transducer along the central axis) to lateral offset (away from the central axis). Fig. 4.18 depicts the dependence of raw optoacoustic A-lines as well as their corresponding frequency contents on both axial and lateral offsets with respect to the acoustic focus. Fig. 4.18b revealed a double-sided parabolic optoacoustic amplitude profile of the raw optoacoustic signals along the axial direction of SOAPs placed along the central axis. This profile peaked at the focal plane (black line) which pinpointed the area of highest sensitivity. Fig. 4.18c and d depict the frequency content of central SOAPs towards the negative and positive defocus, respectively. The captured frequencies deviated from the detectable bandwidth and sensitivity at the acoustic focus (black lines in both plots). In negative defocus (see Fig. 4.18c), significant spatial dependent variation in frequency sensitivity were observed, whereas in positive defocus the frequencies were collected similarly homogeneous to the acoustic focus but with lower sensitivity. Fig. 4.18e-j depict analogous analysis of lateral offset dependencies from 0 to 315 µm of the raw optoacoustic signals (see Fig. 4.18e-g) and the corresponding frequencies (see Fig. 4.18h-j) for three axial positions. The raw

optoacoustic signals received at 500 µm negative defocus (see Fig. 4.18e) indicated several signal repetitions. At the focal plane (see Fig. 4.18f), the signals followed the typical N-shape (see Section 3.3.1). At 500 µm positive defocus (see Fig. 4.18g), the signal flipped in their polarity leading to the time-wise first peak being negative. Overall, the acoustic near field, i.e. negative defocus, was found more affected by signal alterations and repetitions than the acoustic far field. The associated frequency contents showed multiple disordered frequency sensitivity losses for a negative defocus of 500 µm (see Fig. 4.18h), homogeneously covered frequencies at the focal plane (see Fig. 4.18i), as well as a frequency coverage at 500 µm positive defocus (see Fig. 4.18j) similar to the focal plane. Although the sensitivity of raw optoacoustic signals and their contained frequencies was generally higher in the acoustic near field, the far field was characterized by fewer alterations compared to the signals and frequencies. Hence, the acoustic far field was found more suitable for laser-scanning optoacoustic microscopy and, thus, was also utilized for all measurements carried out in HyMPSOM.

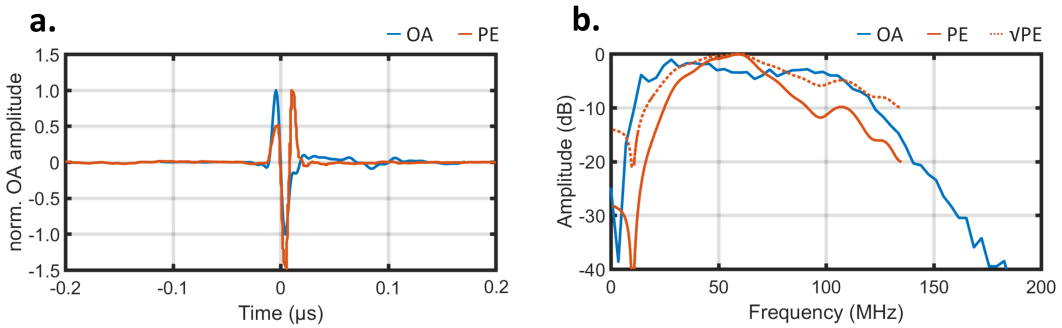

Figure 4.19: Comparison of ultrasound transducer characterized by optoacoustic and ultrasound pulse-echo. **(a)** Raw signals received from the acoustic focus by the optoacoustic approach using the GNL and pulse-echo ultrasound extracted from the manufacturer datasheet on a centered time-axis. **(b)** Corresponding frequency content of both characterization techniques. Abbreviations: OA, optoacoustic; PE, pulse-echo.

Furthermore, such comprehensive TIR characterization allowed to compare the results with the datasheet provided by the manufacturer. Whereas the GNL approach by generating SOAPs is a receive-only method, transducers are typically characterized by the manufacturer by pulse-echo (PE) techniques. The latter is based on utilizing the transducer actively for emitting an ultrasound wave upon a delta-voltage pulse, which is echoed back from a flat ultrasound-reflective surface positioned in the acoustic focal plane. As shown in Fig. 4.20a, the time-wise centered raw signals resembled each other regarding the first and the second peak as well as their shape. However, the PE technique comprised a third peak not being visible in the OA technique, which most probably resulted from the acoustic wave generated being already a bi-polar signal upon a delta-voltage pulse and being reflected at a surface. The frequency content as shown in Fig. 4.20b reveals, that an OA characterization led to a wider bandwidth especially

regarding the upper frequency cut-off. Whereas in PE, a -10 dB cut-off covered a frequencies from ∼25 MHz to ∼90 MHz, the optoacoustic counterpart stretched from ∼10 MHz to ∼120 MHz. This might reflect both the EIR of the transducer acting twice on the ultrasound wave and the ultrasound wave passes twice through the focal length in PE characterization, whereas in OA both occurred only once. To demonstrate this, the square-root of the PE-sensed frequencies is shown in Fig. 4.20b as a dotted line approximating better the OA bandwidth.

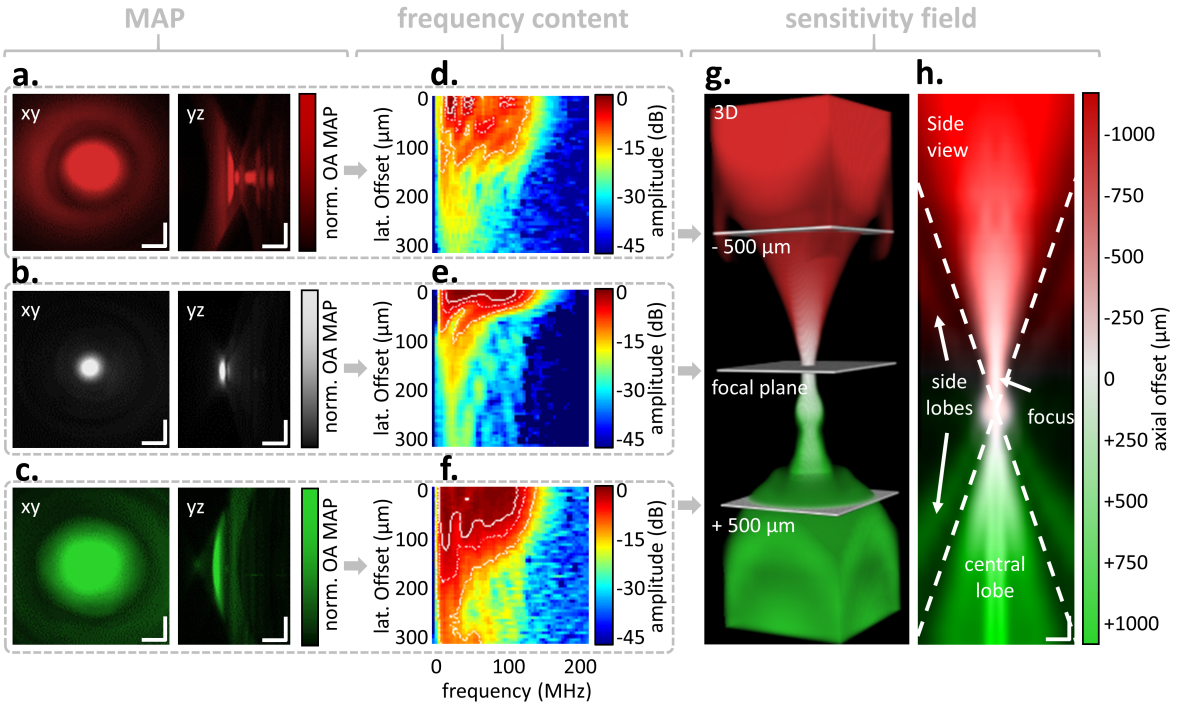

Figure 4.20: Experimental characterization of a spherically focused 50-MHz transducer by raster-scanning the optical excitation across a GNL. **(a)** Raw OR-optoacoustic microscopy MAP onto the *xy*- (left panel) and *yz*-plane (right panel) when the transducer was (a) 500 µm negatively defocused (red); (b) in-focus (gray), and (c) 500 µm positively defocused (green).**(d-f)** Frequency contents for the three cases. Dashed lines show boundaries of -3 dB, -6 dB, and -12 dB. **(g)** Joined 3D sensitivity field of the transducer. **(h)** Side view of the central plane of the 3D sensitivity field. Scale bars, 100 µm. Abbreviations: lat., lateral; MAP, maximum amplitude projection; norm. normalized; OA optoacoustic. (Adapted from [78])

Given these capabilities of the GNL approach, the entire detectable volume of the transducer was examined with respect to influences on the imaging formation. In this regard, the GNL was projected onto the *xy*- or *yz*-plane as shown in Fig. 4.20 representative for the GNL located located 500 µm above the acoustic focal plane (red; see Fig. 4.20a), at the focal plane (gray; see Fig. 4.20b), and 500 µm below the focal plane in positive defocus (green; see Fig. 4.20c). Although the GNL constituted an ultraflat absorbing plane, the MAPs in the *xy*- and *yz*-planes, calculated after frequency

filtering and Hilbert transformation of the optoacoustic signal, showed deviations from a planar representation. In negative defocus, the xy-MAP showed spatial side lobes of the sensitivity field as concentric rings around a central lobe. The associated yz-MAP contained multiple axial artifacts. In the focal plane, both the xy- and yz-MAP illustrated the GNL homogeneous and flat without spatial side lobes or axial artifacts. Measurement of the full-width-at-half-maximum in here indicated an acoustic resolution of 35 µm laterally and 6.3 µm axially of the transducer. At positive defocus, spatial side lobes, axial artifacts, and a curved surface of the GNL were observable. However, the MAPs in positive defocus were less affected than the negative defocus counterpart. The associated frequency content to these three exemplary positions were analyzed depending on the lateral offset as spatial-frequency plots depicted in Fig. 4.20d-f. For the negative defocus, Fig. 4.20d reveal destructive and constructive frequency interference patterns varying with lateral offset. At the focal plane shown in Fig. 4.20e, frequencies were captured homogeneously in the central region. In positive defocus shown in 4.20f, the spatial-frequency presentation contained less interferences than at the negative defocus. Furthermore, high frequencies at minimal lateral offset were lost compared to the focal plane and they decreased as the lateral offset gets larger. By axially joining and interpolating xy-MAPs of the GNL scanned with an axial distance of 100 µm, the total sensitivity field over a volume of $630 \cdot 630 \cdot 2300$ µm^3 of the transducer could be formed as depicted in Fig. 4.20g. The sensitivity field followed an asymmetric shape including spatial side lobes as seen in the individual xy-MAPs of defocused GNL. Furthermore, the sensitivity field featured a knob-like bulge at positive defocus of ∼150 µm. This bulge might result from the overlap of spatial side lobes of the sensitivity field as illustrated in the side view of the central plane in Fig. 4.20h. Due to signal and frequency sensitivity being significant more homogeneous in the acoustic far field and the asymmetry of the sensitivity field stretching to a diameter of ∼600 µm at ∼500 µm positive defocus, this axial defocus position was chosen for carrying out laser-scanning imaging in OR-OAM as part of HyMPSOM.
The approach of generating SOAPs by raster-scanning an optical focus across an arbitrary thin gold layer constituted thereby the first fully experimental way of characterizing the TIR of a high-frequency transducer (see Section 3.3.4). It overcame alternative methods by placing proper and identical optoacoustic point sources throughout a 3D volume of interest. As the TIR is a static property of an ultrasound detector, this approach could potentially be used as a standard technique for characterizing high-frequency transducers in 3D independent on the targeted application.

4.4.3 Simulation of the optoacoustic TIR

Next, the k-wave package [97] in MATLAB^{TM} was used to explore reasons for the findings of the experimental characterization by simulating the experiment. For com-

parable results, a discrete simulation was designed covering a volume of 800 · 800 · 2300 µm^3 resembling the experiment (see Fig. 4.21a).

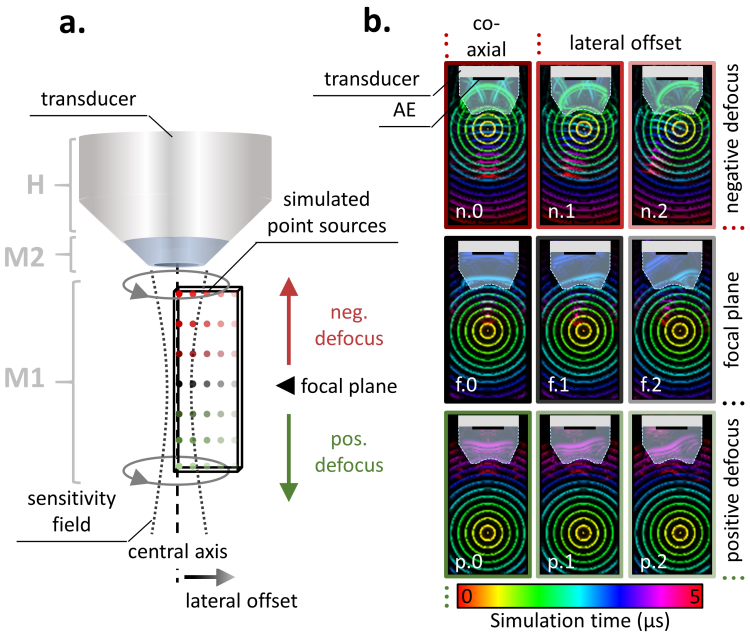

Figure 4.21: Simulation scheme for characterizing a spherically focused 50 MHz transducer. (a) The simulation grid of acoustic point sources using two materials M1 and M2 representing the actual setting and geometry of OR-OAM utilizing a water-coupled spherically focused transducer by means of a conical-shaped plan-concave glass lens attached to the sensor. Abbreviations: AE: single active element; M1, medium 1 (water); M2, medium 2 (glass); H: housing. **(b)** Representative visualization of TIR color-coded simulation time points for arrangements in axial focus (f.0-2), negative defocus (n.0-2), or positive defocus (p.0-2) at co-axial (*.0) and with lateral offsets (*.1-2). Only in the co-axial and axial focused case (f.0) a plane wave reached the active element, whereas in axial and lateral offsets (all other panels), interference and wavefront distortion patterns could be observed. (Adapted from [78])

The simulated transducer was shaped according to the datasheet provided by the manufacturer. It therefore contained a 3 mm disc constituting the active ultrasound sensing element over which simulated incoming sound waves were integrated. Adjacing the active element, a cylinder of 5 mm diameter and 4 mm thickness was positioned as the acoustic focusing glass lens (speed of sound, 5200 m/s; density, 2500 kg/m^3). The lens further comprised a conical bevel with an angle of 45° over the lower 1.3 mm. As the actual acoustic focusing, the glass lens contained an inward-bend concave surface of 1.1 mm radius and 0.5 mm depth, finally leading to a rim of ∼0.3 mm. Surrounding the simulated transducer, the simulation grid was specified with acoustic properties of deionized water to match the experiment (speed of sound, 1500 m/s; density, 1000 kg/m^3). The actual simulations positioned initial acoustic point sources successively within a vertical standing 2D plane of 400 · 2300 µm^3 adjacent to the central

axis of the transducer. Each simulation was carried out with a maximum supported frequency of 100 MHz and a simulation duration dynamically adjusted to ensure that the acoustic waves reach the active element after propagating through the coupling medium and the glass lens. To cover a 3D volume, the results from the point sources placed in the vertical plane were circularly projected and interpolated finally covering a characterized volume identical to the experimental one. Fig. 4.21b depicts exemplary simulation time points for positions analogous to Fig. 4.20 at ±500 µm axial defocus and 0 - 300 µm lateral offset. When the acoustic point source was positioned at the axial and lateral focus (see Fig. 4.21b, f.0), a plane wave encountered the active element. At lateral offset positions within the axial focal plane (see Fig. 4.21b, f.1 and f.2), the wavefront in the glass lens appeared bent and contains interferences, which could be explained by different arrival times of the wave at the surface of the glass lens. At negative defocus (see Fig. 4.21b, n.0-n.2), the wavefronts were strongly curved. This resulted from a non-planar wave entering the surface of the glass lens, which further induced numerous interferences and reflections of the wave. A similar finding could be observed at positive defocus (see Fig. 4.21b, p.0-p.1), but with opposite bending and fewer interferences.

For a final comparison, the simulation results were projected and analyzed analogously to the experimental results shown previously. Fig. 4.22 depicts the MAPs, 2D frequency plots, and the 3D sensitivity field of the simulation. In general, a good agreement was observed between the simulation and the experiment (see Fig. 4.20). Similar dependence of spatial side lobes and axial artifacts were contained in the simulated MAPs in negative defocus (see Fig. 4.22a), at the focal plane (see Fig. 4.22b), and in positive defocus (see Fig. 4.22c). The FWHM at the focal plane indicated a simulated acoustic focus of 42 µm · 13 µm size. Further, the spatial-frequency plots showed analogous interference patterns for the negative defocus (see Fig. 4.22d), at the focal plane (see Fig. 4.22e), and the positive defocus (see Fig. 4.22f). The frequency bandwidth at the focal plane (see Fig. 4.22e) ranged at -3 dB from 15 to 85 MHz. Final 3D joining of the 2D xy-MAPs over the entire simulated volume (see Fig. 4.22g) as well as the side view of the central plane (see Fig. 4.22h) revealed an asymmetric sensitivity field along the central axis.

This convergence of simulation and experiment (compare Fig. 4.20 and Fig. 4.22) suggested that observed optoacoustic signal alterations and distortions could be attributed to internal reflections and interferences in the glass lens due to axial and lateral offset of the signal origin. Nevertheless, the simulated results differed from the experimental characterization regarding the prominence and shape of spatial, frequency artifacts, and the knob-like bulge of the sensitivity field. Furthermore, the simulation disregarded all signal alterations induced by the electric acquisition chain. Such differences renders, that for precise TIR characterization, exclusively experimental approaches are meaningful.

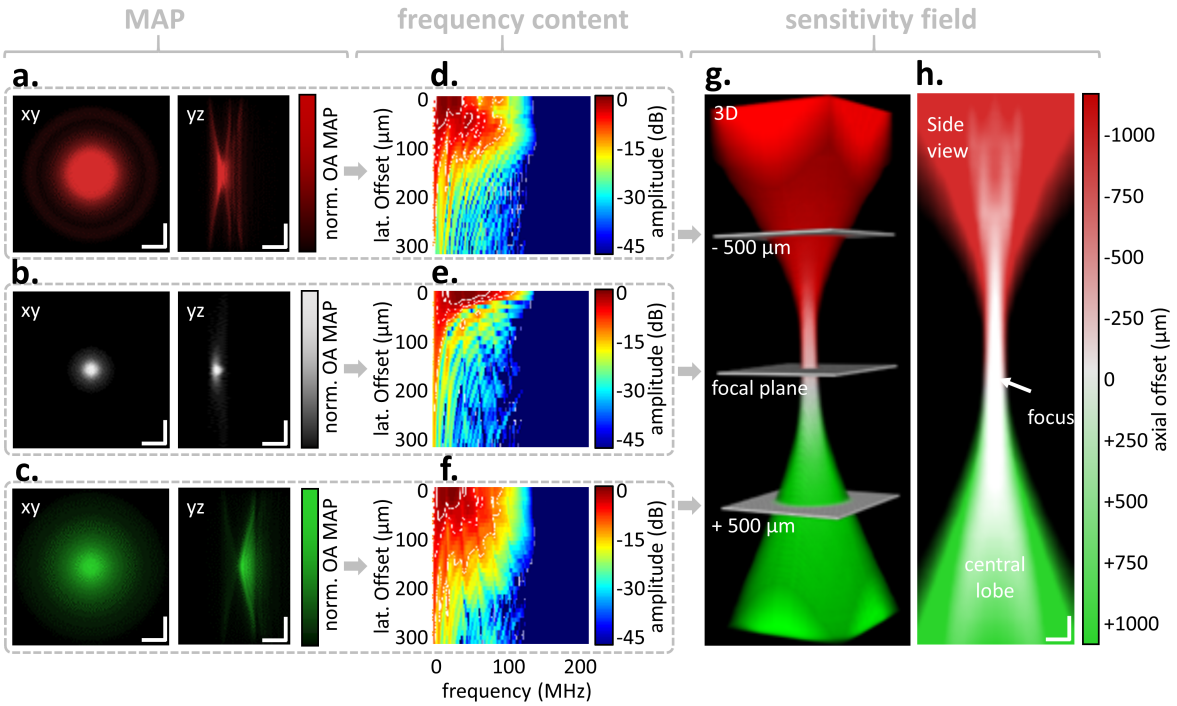

Figure 4.22: Simulation of a spherically focused 50-MHz transducer by successively simulating acoustic point sources. **(a)** Raw simulated MAP onto the *xy*- (left panel) and *yz*-plane (right panel) when the transducer was (a) 500 µm negatively defocused (red); (b) in-focus (gray), and (c) 500 µm positively defocused (green).**(d-f)** Frequency contents for the three cases. Dashed lines show boundaries of -3 dB, -6 dB, and -12 dB. **(g)** Joined 3D sensitivity field of the transducer. **(h)** Side view of the central plane of the 3D sensitivity field. Scale bars, 100 µm. Abbreviations: lat., lateral; MAP, maximum amplitude projection; norm. normalized; OA optoacoustic. (Adapted from [78])

4.4.4 Optoacoustic TIR correction by spatial matched filtering

The detailed characterization of spatial-depended modifications of ultrasound detection as described in Section 4.4.2 facilitated the development and application of correction algorithms. As elaborated theoretically in Section 3.3.4, optoacoustic signal should in general be corrected on the signal level before projecting them into images due to their time-encoded information and bi-polar shape. Possible signal correction approaches could be realized by deconvolution or correlation techniques processing the recorded signals from a sample with their spatially associated impulse response. Latter were used in this study in form of a spatial matched filter (SMF) due to reasons of being a mathematical linear method, of correcting time-of-flight differences, of transferring the recorded signals into the correlation domain, and of being implemented straight forwardly [72, 98, 99] (see Section 3.3.4).

The developed SMF algorithm is schematically depicted in Fig. 4.23 and was based on cross-correlating the averaged and frequency-filtered signals with their spatially corresponding impulse response yielded from the experimental characterization of the transducer by the SOAP approach. After cross-correlation, the signals were transferred

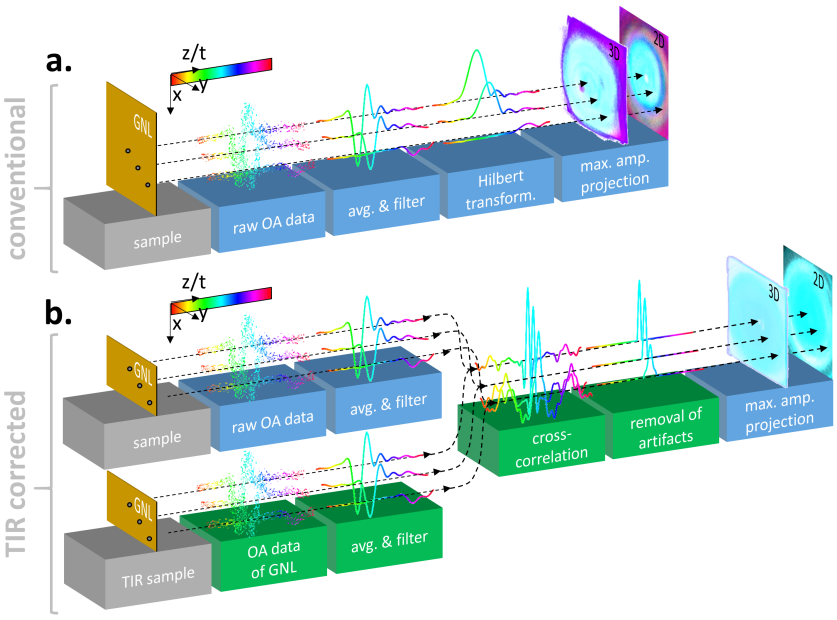

Figure 4.23: TIR correction of optoacoustic microscopy by spatial matched filter. Schematic depiction of the data processing steps for **(a)** conventional sequence of signal collection, averaging, frequency filtering, Hilbert transformation, and projection; and **(b)** the developed spatial matched filter approach, in which recorded, averaged, and filtered signals are cross-correlated with the signals of SOAPs of identical spatial position followed by artifact removal and projection. (Adapted from [78])

into correlation curves containing a main correlation peak framed by several correlation side-lobes. Next, the main correlation peak was cut out and negative correlation values, i.e. anti-correlation, were removed by thresholding before projecting the correlation curves in 2D or 3D. For comparison, the identical dataset was processed using the conventional technique of applying Hilbert transformation before projection.

The TIR-SMF correction algorithm was tested on samples placed in 500 µm positive defocus in order to have the sensitivity field covering the entire scanned area of ~630 · 630 µm^2 as explained previously. In Fig. 4.24a-b, the GNL served as both the investigated sample as well as the sample for TIR characterization[81]. Whereas the conventional way led to a curved representation of the GNL containing several axial artifacts (see Fig. 4.24a), the TIR-SMF corrected counterpart (see Fig. 4.24a) led to a flat, thin, and single-layer depiction of the GNL by correcting field curvatures and signal repetition artifacts. The achieved axial resolution was determined by measuring the axial extent of the projection of the GNL, constituting a layer of optoacoustically negligible thickness, i.e. an axial point source. The FWHM values were 6.85 µm at a centered position in the FOV and 10.69 µm at an lateral offset of 200 µm for the conventional approach and 5.32 µm and 7.37 µm for the TIR-SMF correction, respectively.

[81] The GNL was in here measured twice successively to avoid data redundancy.

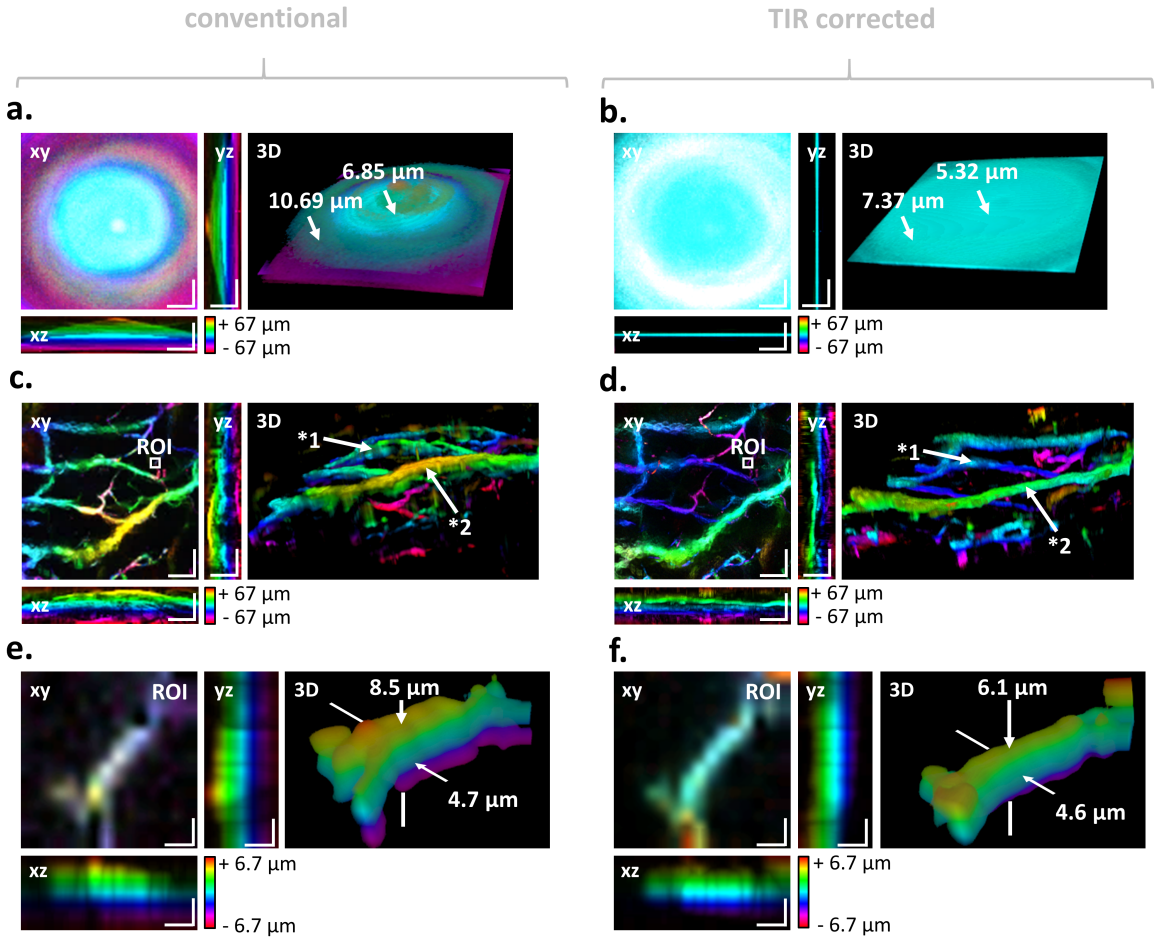

Figure 4.24: Image improvement by TIR correction. Comparison between MAP projections onto the xy-, yz-, and xz-plane, as well as 3D renderings of optoacoustic microscopy data between the conventional approach and TIR correction. Reconstructions were performed using conventional Hilbert transformation and TIR correction and projected in a depth-color code. **(a-b)** Imaging of a gold nanolayer (GNL); (a) Conventional reconstruction revealed strong field curvature and decreased axial resolution, especially at outer parts of the imaged FOV; (b) TIR-correction eliminated field curvature and significantly improved and equalized the axial resolution throughout the FOV. **(c-d)** Imaging of a mouse ear vasculature *in vivo*; (c) Conventional reconstruction showed vessels multiple times in z (see vessel *1) as well as strongly bend in z (see vessel *2); (d) TIR-correction let vessel appear smooth and once only (*1) and leveled (*2). **(e-f)** Zoomed-in view of the indicated ROI in panels (c-d), showing a microcapillary. (e) Conventional reconstruction yielded an elongated microcapillary in z, whereas (b) TIR-correction approximated a presumably circular microcapillary more accurate. Scale bars, 100 µm (a-d) or 5 µm (e-f). (Adapted from [78])

Hence, the TIR-SMF correction led to an axial resolution improvement of 22.4% (at the center) and 31.1% (at 200 µm offset). The field curvature estimated between the center and a 200 µm lateral offset was 7.1 µm for the conventional approach and <1.66 µm for the TIR-SMF approach. Thus, the TIR-SMF eliminated entirely field curvatures induced by different time-of-flight values at lateral offset positions[82]. Similar findings could be observed for OR-OAM images of mouse ear vasculature *in vivo* shown in Fig. 4.24c and d. The vasculature in this experiment was ∼100 µm deep in the tissue. The conventional way of processing and projecting data (see Fig. 4.24c) led to a bent vasculature layer in which individual vessels appear multiple times stacked axially on top of each other. The TIR-SMF correction eliminated bending and vessel-repetition (see Fig. 4.24d). The entire vasculature seemed to be placed in a more homogeneous flat layer with removed multiple appearances of the vessels. In the zoom-in into a microcapillary shown in Fig. 4.24e and f, the improvement by applying TIR-SMF correction became even more evident. After correction, the microcapillary appeared significant more homogeneous regarding axial and lateral extent and, thus, constituted a more faithful image of presumably circular microvasculature. Measurements of this microvessel gave an ellipsoid ratio of 1:1.81 (lateral diameter, 4.7 µm; axial diameter, 8.5 µm) for the conventional projection and 1:1.32 (lateral diameter, 4.6 µm; axial diameter, 6.1 µm) for the TIR-SMF version. Furthermore, the image-SNR improvement ΔSNR was calculated using:

$$\Delta SNR = 10 \cdot \log_{10}\left[\frac{\sum_0^{n_x-1}\sum_0^{n_y-1}[a_r(x,y)^2]}{\sum_0^{n_x-1}\sum_0^{n_y-1}[a_r(x,y)-a_c(x,y)]^2}\right], \tag{4.3}$$

where a_r and a_c denote the amplitude values for respectively the raw and corrected images at the pixel positions x and y for all pixel n_x and n_y [100]. Using this analysis, the SNR improvement achieved by applying TIR-SMF correction enabled by the SOAP approach was 10 dB for the xy-MAP, 7.2 dB for the xz-MAP, and 5.1 dB for the yz-MAP.

In summary, the application of the experimentally characterized TIR of the transducer in a spatial matched filter constituted a new powerful way of correcting optoacoustic data on the signal level. The achieved improvements in SNR and axial resolution strengthened the imaging capabilities of optoacoustic microscopy in a laser-scanning approach, especially in a hybrid microscopy in combination with advanced optical microscopy modalities. The correction finally led to a more credible projection of the optoacoustic data, in particular by making use of the inherent 3D information gathered

[82] The sampling rate of 900 MS/s at an assumed speed of sound in water of 1500 m/s leads to a sampling-point spatial extent of 1.66 µm. A lateral offset of 200 µm at a sample-transducer-distance of ∼3.5 µm including a axial defocus of 500 µm leads theoretically to an field curvature of 5.7 µm at 200 µm lateral offset.

in optoacoustic readings. OR-OAM becomes thereby better compatible and complementary with other existing advanced microscopy techniques. Furthermore, as the characterized TIR constitutes an application independent property of the transducer, similar correction can be applied to not only microscopic data but also on mesoscopic or tomographic measurements carried out with the identical sensor.

4.5 Conclusion and Outlook

In summary, HyMPSOM constitutes a new kind of microscope by combining several complementary imaging modalities. The developed system offers simultaneous multi-modal examination of biological tissue at high spatial and temporal resolutions. The concurrent read-out of different microscopy modalities is achieved by implementing a complex excitation and signal acquisition technique. As listed in Tab. 2, all equipped key-modalities[83] share similar imaging properties regarding resolution, depth, speed, and sensitivity.

	Modality	Contrast	Bio. moities	Resolution	Depth	Speed	SNR	Principle
OA	OR-OA	optical absorption	hemoglobin, melanin	XY: ~ 0.6 µm Z: ~ 6.3 µm	< 600 µm	Pixel: 50 kHz FOV: < 10 Hz	~ 34 dB	
NLO	2PEF	(intrinsic) fluoresence	elastin, lysosomes, hair follicle	XY: ~ 1.1 µm Z: ~ 5.7 µm	< 450 µm	Pixel: 300 kHz FOV: < 20 Hz	~ 36 dB	
NLO	3PEF	(intrinsic) fluoresence	NADH, FAD	XY: ~ 1.1 µm Z: ~ 5.7 µm	< 200 µm	Pixel: 300 kHz FOV: < 20 Hz	n.a.	
NLO	SHG	non-centro-symmetry; birefringes	collagen, myosin, bone	XY: ~ 1.1 µm Z: ~ 5.7 µm	< 450 µm	Pixel: 300 kHz FOV: < 20 Hz	~ 45 dB	
NLO	THG	optical interfaces	membranes, lipid droplets	XY: ~ 1.1 µm Z: ~ 5.7 µm	< 450 µm	Pixel: 300 kHz FOV: < 20 Hz	~ 27 dB	
OP	LS	optical scattering	particles, cells, surfaces	XY: ~ 0.6 µm	< 100 µm	Pixel: 50 kHz FOV: < 10 Hz	n.a.	
OP	BF	optical attenuation	absorbing constituents	XY: ~ 1.5 µm	< 50 µm	FOV: < 1 Hz	n.a.	

Table 2: Imaging capabilities of HyMPSOM. Overview of the integrated modalities and their imaging properties in HyMPSOM. Values are listed exemplary for simultaneous multi-modal microscopy of *in vivo* mouse tissue.

The yielded capabilities of HyMPSOM were shown to be best suitable for investigations of specimens ranging from single-cells to small model organisms. Comprehensive characterization of these capabilities, especially for optoacoustic microscopy, and subsequent correction enabled concepts for equalizing the individual performances of the

[83] Light-Scattering (LS) and Brightfield (BF) are listed as reference imaging modalities.

different modalities. It therefore suggested its application in studies for developmental biology as well as translational medicine. The great potential for comprehensive and, if desired, label-free extraction of information allowed HyMPSOM to conduct a huge variety of imaging projects, which are described in detail in the following Section 5.
At the current state, HyMPSOM lacks in label-free molecular contrast. As described in Section 2.3.2, biomolecules possess an intrinsic absorption profile, which in general could be sensed label-free. For that, a spectral excitation source is required, the implementation of which is currently carried out by integrating a supercontinuum laser. With such an excitation source, optoacoustic microscopy could read out vibrational overtones (i.e. molecule specific absorption bands in the near-infrared range) and, thus, facilitate label-free molecular contrast. Furthermore, the underlying imaging speed could be enhanced by faster excitation sources. As the optoacoustic readout is currently the time-limiting factor, alternative laser and/or acquisition approaches are preferred. For that, optoacoustic microscopy could be either performed in the frequency domain (see Section 5.4.1) or by using high-speed laser diodes (see Section 5.4.2). Both ideas are currently tested in the HyMPSOM framework. Next, the maximum thickness[84] of specimens investigated by HyMPSOM is up to now limited to ∼2 mm. This is mainly due to reading at least two modalities in transmission-mode. To overcome this limitation, an all-optical optoacoustic signal sensing technique was developed and tested on the HyMPSOM system (see Section 5.4.3). Finally, HyMPSOM constitutes up to now a complex and user unfriendly microscope. Personnel has to be trained precisely in order to be able to operate the system. On the one hand, the complex and modular construction and control allows to integrate in future additional complementary microscopic modalities such as Raman-based scattering (i.e. SRS or CARS) or optical coherence readouts (i.e. OCT) completing the label-free imaging capabilities. On the other hand, complicated usage and control of the system prevents its application for high-throughput imaging projects. As most of the relevant components of HyMPSOM are controllable, an automated computer algorithm could be developed in general to perform tedious and non-intuitive tasks such as system alignment and focusing.

[84] The maximum imaging penetration depth is ∼500 µm. The samples, however, could be significantly thicker.

5 | Application of HyMPSOM

This chapter compiles representative projects conducted with HyMPSOM. First, the system was characterized towards its ability of imaging specimens ranging from single-cells and organoids over small model organisms like mice or zebrafish up to histopathological tissue slices (see Section 5.2). Based on that, HyMPSOM was used to study biological and biomedical samples as well as to investigate novel contrast agents developed for multi-modal imaging (see Section 5.3). Further, the microscopy framework of HyMPSOM was used to explore innovative technical approaches for performing optoacoustic signal generation, sensing, and imaging on the microscale (see Section 5.4).

5.1 Introduction

The unique capabilities of HyMPSOM for multi-modal and potentially label-free signal acquisition, high resolution, deep penetration, fast and simultaneous recording, and technical flexibility allowed to conduct a huge variety of projects concerning both imaging biological specimens and exploring novel approaches to conduct microscopic optoacoustic readings. The herein described projects are selected to demonstrate and highlight the achieved performance of HyMPSOM rather than giving a complete list of all conducted studies.

5.2 Samples and experimental settings

HyMPSOM was tested towards its imaging capabilities to investigate specimens of sizes ranging from sub-micrometer to few-millimeter as well as from artificial materials to living organisms. The following chapters demonstrate exemplary imaging results from single-cells and organoids *in vitro* (see Section 5.2.1), biological models *in vivo* such as zebrafish larvae and mice (see Section 5.2.2), and histopathological tissue slices *ex situ* of excised human specimens (see Section 5.2.3).

5.2.1 Single cells and organoids *in vitro*

As explained in Section 4.2.3, HyMPSOM enables studies performed on single-cell monolayers cultured in glass bottom petri dishes. This allows to study cell types being standard for biological research such as Human Embryonic Kidney (HEK) cells, Human cervical cancer (HeLa) cells, differentiated 3T3-L1 adipocytes, *Escherichia coli* (*E. coli*), and Chinese Hamster Ovary (CHO) cells. During most of such measurements, the cells were kept in physiological conditions regarding their environmental parameters of a temperature of 37 °C, a humidity of 80%, a CO_2 concentration of 5%, an O_2 concentration of 20%, at a gas perfusion flow rate of 10 mL/h. Further, all cells were suspended in standardly used cell media such as Dulbecco's modified eagle medium (DMEM), Dulbecco's phosphate-buffered saline (DPBS), or Hank's balanced salt solution (HBSS) (Thermo Fisher Scientific, USA). 3D cell cultures mimicking organ functions, such as cardiac organoids, were treated and handled analogously.
Fig. 5.1 shows exemplarily, how HyMPSOM was able to resolve single-cells and organoids. Fig. 5.1a-c depict multi-photon microscopy of differentiated 3T3-L1 adipocytes stained with Nile Red for lipid droplets[85]. The lipid droplets are detected as drastic changes of the refractive local index (THG; see Fig. 5.1b) and as fluorescent signals based on the Nile Red staining (2PEF; see Fig. 5.1c). Fig. 5.1d-f show HeLa

[85] These results are part of a project headed by Miguel Pleitez regarding mid-infrared optoacoustic microscopy for label-free chemical contrast. The corresponding publication is in revision during writing of this thesis [101]. The associated pre-print is available on [102].

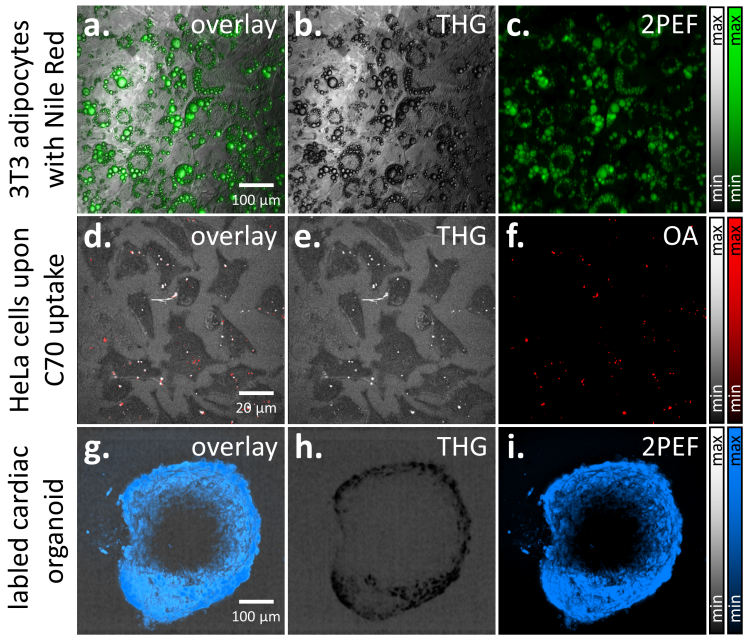

Figure 5.1: Multi-modal microscopy of single-cells and organoids. **(a-c)** Imaging of 3T3 adipocytes stained with Nile Red for lipid droplets; **(a)** Overlay and separate depiction of **(b)** THG and **(c)** 2PEF. **(d-f)** Imaging of HeLa cells incubated with C70; **(d)** Overlay and separate depiction of **(e)** THG and **(f)** OA. **(g-i)** Imaging of a cardiac organoid incubated with a fluorescent label; **(g)** Overlay and separate depiction of **(h)** THG and **(i)** 2PEF.

cells incubated with the fullerene C_{70} as part of a project described in more detail in Section 5.3.2. Whereas the cell membranes can be observed as an intrinsic optical boundary regarding the refractive index due to the lipid-bilayer (THG; see Fig. 5.1e), sub-resolution agglomerations of the fullerenes can be seen due to their optical absorption (OA; see Fig. 5.1f). Fig. 5.1d-f display a single imaging plane of a cardiac organoid incubated with a fluorescent label as part of the project described in Section 5.3.3. In analogy, the outer shell of cells of the organoid can be seen as an optical interface (THG; see Fig. 5.1h), whereas the intracellular label emits fluorescent signal (2PEF; see Fig. 5.1i).
These exemplary results from imaging single-cells and organoids showcase that HyMP-SOM facilitates extraction of multi-modal contrast on the sub-micrometer scale and, thus, can be used for performing studies on cell monolayers cultured in petri dishes as typically done in biological research.

5.2.2 Zebrafish and mice *in vivo*

The fast, deep, volumetric, and potentially label-free imaging capabilities of HyMPSOM open the possibility of its application on small model organisms *in vivo* such as zebrafish larvae and mouse ears. For the former, larvae of zebrafish and descendants like medaka or casper breeds of maximum 7 days post fertilization (dpf) were paralyzed with 1%$^{\text{vol.}}$ of the muscle relaxant Flexeril (cyclobenzaprine hydrochloride, Sigma Aldrich) and embedded in low melting agar prepared with eggwater to prevent movements. For the latter, athymic nude Hsd foxn1 mice were anesthetized with ∼2% isofluorane. The physiological condition of the mice was monitored and controlled by the mouse monitoring system as explained in Section 4.2.3. The mice were imaged with a custom-designed 3D holder as depicted in Fig. 4.6 and shown in Appendices: Photographs of the optical setup.

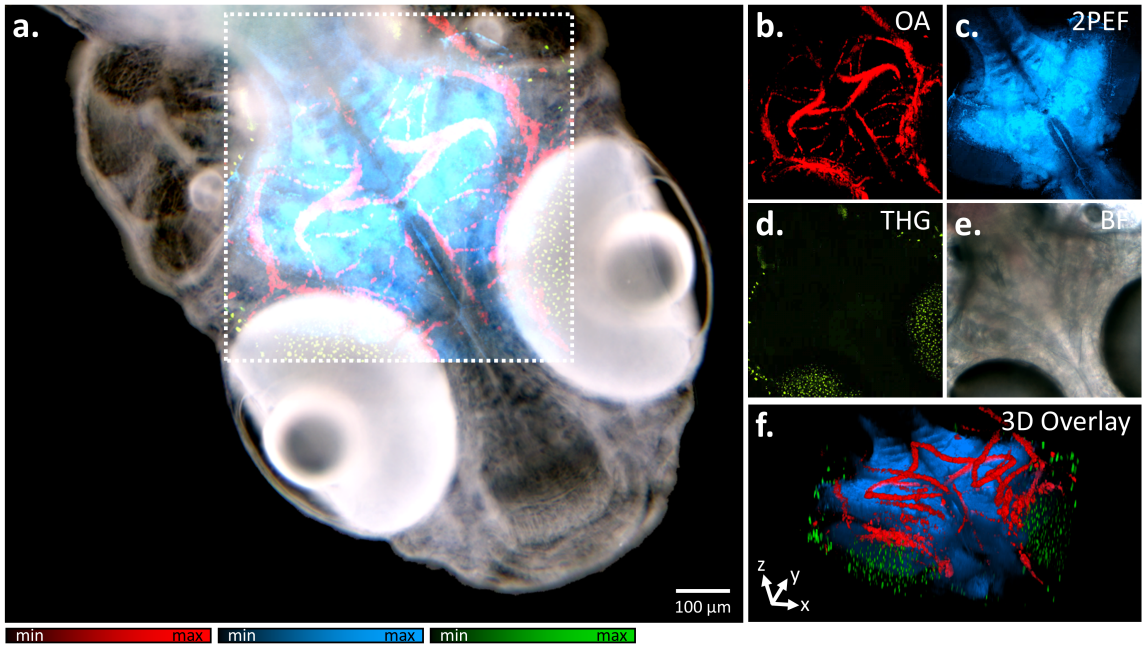

Figure 5.2: Multi-modal microscopy of a 7-day-old medaka larvae. Imaging of a paralyzed medaka fish with labeled neurons. **(a)** Multi-modal microscopy images blended on top of the inverted brightfield image; separate depiction of **(b)** OA, **(c)** 2PEF, **(d)** THG, and **(e)** BF. **(f)** 3D rendering of the entire medaka fish brain. (Adapted from [103])

Fig. 5.2a depicts the multi-modal images acquired from a 7-dpf medaka larva with fluorescence-labeled neurons via intraventricular injection (label: CaSPA-550, see Section 5.3.3) blended on top of an inverted brightfield image. The multi-modal contrast of HyMPSOM allows for vastly more detailed investigation of the brain vasculature (OA; see Fig. 5.2b), of the entire neuronal network (2PEF; see Fig. 5.2c), and of lipid droplets behind the eyes (THG; see Fig. 5.2d) as compared to their brightfield impression (BF; see Fig. 5.2e). A 3D rendering of the data is depicted in Fig. 5.2f and reveals high spatial complement of the vasculature embedded in brain furrows.

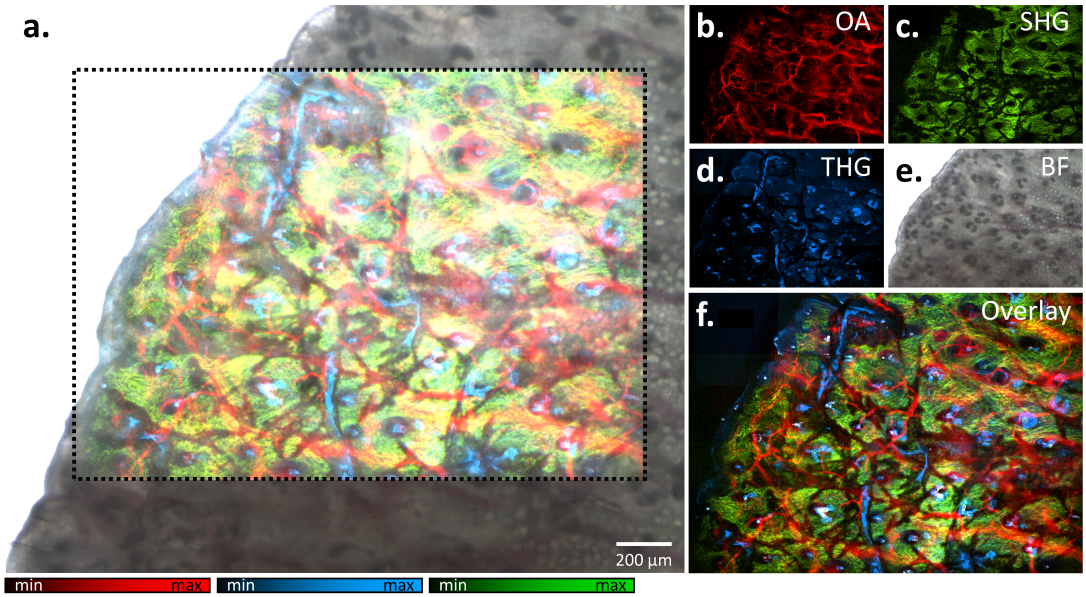

Figure 5.3: Multi-modal microscopy of an *in vivo* mouse ear. Imaging of the ear of an anesthetized mouse. **(a)** Multi-modal microscopy images blended on top of the brightfield image; separate depiction of **(b)** OA, **(c)** SHG, **(d)** THG, and **(e)** BF. **(f)** Overlay of multi-modal microscopy images. (Adapted from [103])

Fig. 5.3a shows a multi-modal image of an *in vivo* mouse ear overlayed with the corresponding brightfield image. In here, HyMPSOM reveals the microvasculature of the mouse pinna (OA; see Fig. 5.3h), the extracellular collagen matrix (SHG; see Fig. 5.3i), and the tissue morphology and sebaceous glands (THG; see Fig. 5.3j). Such details can not be extracted from the brightfield image (BF; see Fig. 5.3k) but are clearly visible in the overlay of the multi-modal images (see Fig. 5.3l).
As showcased, HyMPSOM allows to examine the interplay and spatial distribution of various tissue compartments and moieties on the microscale of *in vivo* specimens being typically used in biomedical and translational research. The label-free sensing of e.g. the vasculature, the collagen and elastin network, and lipid accumulations in sebaceous glands or in lipid droplets, enables therefore to perform longitudinal studies without the need of administering potentially harmful contrast agents. However, specific labels delivered to the specimens can be sensed alongside the label-free information in a complementary manner.

5.2.3 Histopathological tissue slices *ex situ*

The high-resolution and adaptable scanning procedure allow HyMPSOM to investigate *ex situ* histopathological tissue slices of excised specimens. The investigated tissue slices were cut to a thickness between 10 and 50 µm being standard for histopathology.

Further, HyMPSOM was able to image tissue slices in different conditions such as freshly cut, cryo-frozen, or embedded in paraffin or paraformaldehyde (PFA).

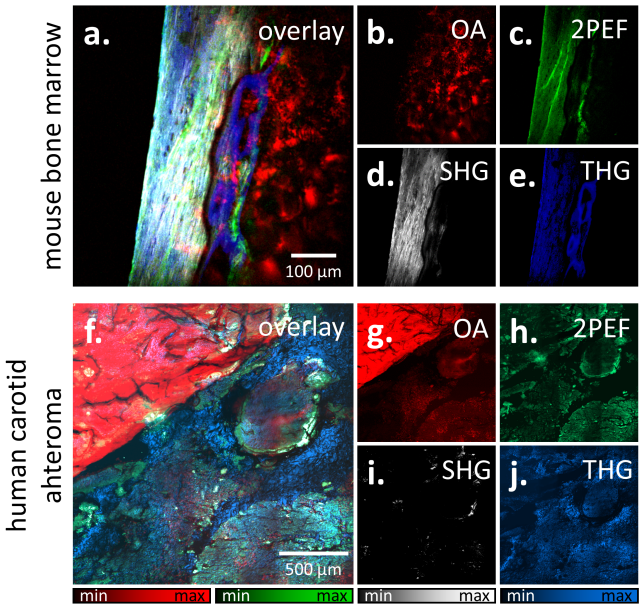

Figure 5.4: Multi-modal microscopy of histopathological tissue slices. **(a-e)** Label-free imaging of a thinned bone marrow of a mouse upper leg. (a) Overlayed multi-modal microscopy images; separate depiction of (b) OA, (c) 2PEF, (d) SHG, and (e) THG. **(f-j)** Label-free imaging of an unstained human carotid atheroma slice. (f) Overlayed multi-modal microscopy images; separate depiction of (g) OA, (h) 2PEF, (i) SHG, and (j) THG.

Fig. 5.4 depicts exemplary microscopy images of unlabeled histopathological samples acquired by HyMPSOM. Fig. 5.4a-e shows the multi-modal microscopy image obtained from a thinned and paraffin-embedded bone marrow of a mouse upper leg. The overlay in Fig. 5.4a reveals the marrow vasculature (OA; see Fig. 5.4b), the marrow itself (2PEF; see Fig. 5.4c), the compact bone (SHG; see Fig. 5.4d), and the niche-like interface between bone and marrow (THG; see Fig. 5.4e). Fig. 5.4f-j shows a multi-modal image obtained from an embedded and unstained human carotid atheroma slice as part of the project elaborated in Section 5.3.5. The overlay depicted in Fig. 5.4f reveals incorporated blood residues and hemorrhages (OA; see Fig. 5.4g), foam cells (2PEF; see Fig. 5.4h), remnants of the collagen network (SHG; see Fig. 5.4i), and the overall tissue morphology as well as lipid embeddings (THG; see Fig. 5.4j).
The shown exemplary imaging results of histopathological specimens illustrate that HyMPSOM can be applied on tissue slices being processed according to standard protocols used in clinical research. Since HyMPSOM can investigate such specimens in a label-free manner, it was therefore able to study the microstructure of the above mentioned moieties with a spatial precision not achievable with staining approaches.

5.3 Key imaging projects of HyMPSOM

This chapter concerns the involvement and application of HyMPSOM in several imaging projects in its standard way of operation as described in detail in Section 4. The shown projects are selected to outline the versatile applicability of HyMPSOM and focus on the contribution of HyMPSOM and its achieved results relevant for the associated imaging projects. Thus, information of the projects which constitute a marginal importance for the use of HyMPSOM, such as measurements performed alongside, by others, or prior to HyMPSOM assessments, are only outlined.
The herein presented imaging projects exploited the multi-modal contrast for extracting congruent details of the respective sample. Depending on the aim of the project, the modalities either complemented one another by revealing different information or validated one another by sensing shared content. In combination with the sub-cellular resolution achieved at imaging depths up to ∼500 µm, these two ways of utilizing the multi-modal imaging capability were applied on specimens ranging from single-cells up to small model organisms. The high-speed and simultaneous imaging enabled in here measurements of dynamic processes as well as longitudinal studies.

5.3.1 Superparamagnetic Ferritin for multi-modal imaging

This imaging project focused on the development of a novel genetically-controlled multi-modal contrast agent and molecular actuator based on variants of the iron-carrier protein ferritin[86].

Introduction

On the one hand, the use of nanomaterials as molecular sensors and actuators is in general of high interest for biological and biomedical research as they can be specifically designed regarding their physical properties. However, such pre-designed materials can be modified by the addressed biological organisms upon uptake or incorporation. On the other hand, genetic control over molecular sensors and actuators is favored as it can be used for determining and interacting with specific cell populations being relevant for the condition and functioning of tissues. In this regard, previous studies have explored the potential use of overexpressing the metallo-protein ferritin for MRI and OA studies [105–108]. Ferritin offers an increased T_2-contrast in MR-imaging due to the antiferromagnetic iron core and relatively high OA signals due to strong optical absorption in the visible spectrum. It further enables cell manipulation via magnetic hyperthermia or magneto-mechanical transduction [109–111]. However, the required

[86] This project was headed by Dr. Christoph Massner and Prof. Dr. Gil Westmeyer, who developed and characterized the genetic encoding of ferritin and prepared the cultured cell specimen. Results are published in [104].

high relaxivity for MRI contrast is limited by the weakly magnetized ferrihydrite core [106, 107, 112–115] and the OA contrast is restricted by the cytosolic distribution of ferritin.
Although full genetic approaches for generating such sensors and actuators in cells are preferred for molecular imaging, synthetic nanomaterials offer superior properties required for the aimed application. Hence, semi-genetic techniques [116–119], in which a genetically-controlled component fuses with an administered exogenous synthetic nanomaterial, enable both high molecular addressability to e.g. agglomerations in lysosomes, and desired physical properties like e.g. substituting the ferryhydrite core with different metal cores such as magnetite due to a higher magnetization [120, 121]. Further, condensed aggregates of ferritin molecules in lysosomes measuring ∼0.1-1 µm could potentially generate significant THG contrast due to its photophysical properties of altering the local refractive index [66, 122, 123] and are best suited for OA contrast due to high local concentrations of light absorbing molecules. Finally, we developed a semi-genetic technique to entrap a superparamagnetic ferritin variant hFTH-Mag and a native ferrihydrite ferritin variant eFTH+L in lysosomes via Tim-2 overexpression for multi-modal and multiscale imaging by means of MRI, OA, and THG, and actuation via magnetic or photonic processes [104].

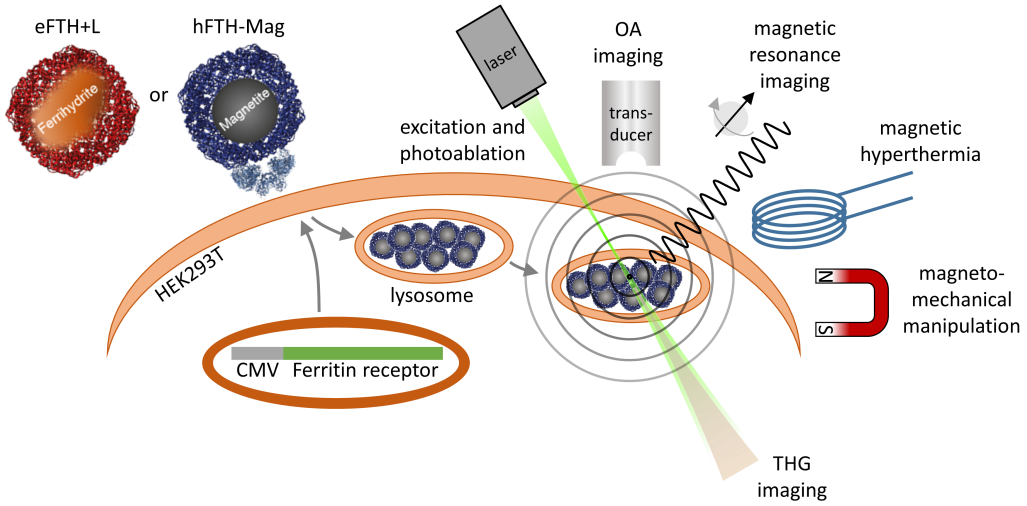

Figure 5.5: Principle of genetically-controlled and lysosomal entrapment of ferritin variants for multi-modal imaging and interaction. (Adapted from [104]).

Materials and Methods

The recombinant human heavy-chain ferritin variant (hFTH) and the native equine heavy-chain and light-chain ferritin (eFTH+L) were expressed in *E. coli* cells (BL21 (D3)), extracted, and purified according to [124, 125]. Next, ferrous iron was added for synthesizing hFTH-Mag based on [126], which was subsequently purified by size exclusion chromatography and investigated biophysically and biochemically by native polyacrylamide gel electrophoresis, dynamic light scattering, Raman microspectroscopy, vibrating magnetometry, and transmission electron microscopy.
For final imaging experiments in HyMPSOM, HEK cells (K293T, ATCC: CRL-11268) were genetically modified in the pcDNA3 site with inserted ferritin receptor Tim-2 gene. Tim-2 mediates uptake and lysosomal trafficking of heavy chain ferritin added to the cells supernatant. Consecutive OA and THG imaging of genetically-modified HEK cells was performed with HyMPSOM using an averaging of 100 and pulse energies of 18.5 nJ (OA) and 1.1 nJ (THG), respectively (see Section 4). Next, the OA-laser pulse energy was increased ∼15.4 fold to 285 nJ for photoablation and rastered across a smaller area with 100 pulses per position. Subsequent to the photoablation scan, the sample was imaged again with OA and THG using the imaging pulse energies as before. Affine transformation was applied for co-registering the images before and after ablation to compensate for slight movements of the cells between measurements.

Results

The trafficking of ferritin molecules to the lysosomes induced by Tim-2 was confirmed via co-localizing fluorescent microscopy based on labeling the lysosomes (mCherryLT) and conjugating a fluorescent dye (Alexa Fluor 488) to hFTH-Mag or eFTH+L (Data not shown; see [104]). The selective uptake and lysosomal accumulation relevant for OA and THG microscopy of both hFTH and eFTH+L was tested on the expression level of Tim-2 and the presence of an iron core.
Tim-2 positive cells uptaking hFTH-Mag generated detectable OA signals (see Fig. 5.6a) and THG signals (see Fig. 5.6b), whereas no OA signals were seen in the Tim-2 negative cells (see Fig. 5.6c). However, THG signals could be observed also for Tim-2 negative cells (see Fig. 5.6d) due to the cell membrane-water interface thereby constituting the THG baseline of ferritin-empty HEK cells. In comparison, THG signals were significantly enhanced in Tim-2 positive cells resulting from ferritin accumulation in lysosomes, which could be used for thresholding in the depiction to separate THG signals from ferritin and from the cells themselves. Further, the THG enhancement was not visible in Tim-2 positive cells at comparing the addition of hFTH-Mag (see Fig. 5.6e) and the apoferritin (apo-hFTH) counterpart (see Fig. 5.6f) lacking the iron core. Hence, increase of THG signals could be assumed to depend on the metal-protein

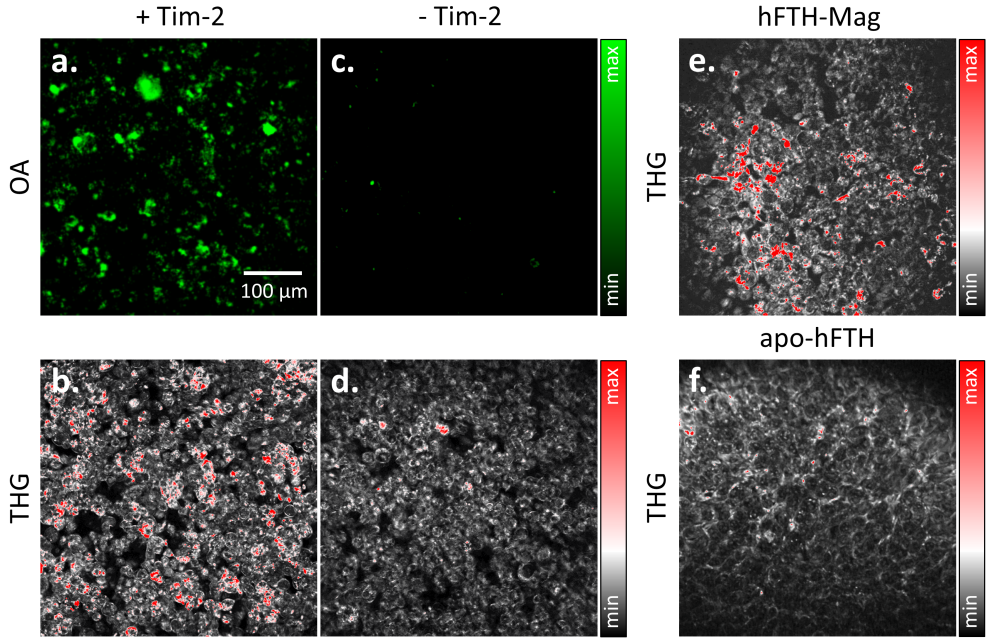

Figure 5.6: Genetically-controlled ferritin uptake and lysosomal trafficking investigated in OA and THG readings using HyMPSOM. Tim-2 overexpressing HEK cells incubated with hFTH-Mag generated strong **(a)** OA and **(b)** THG signals. Tim-2 controls revealed **(c)** negligible OA signals and **(d)** low THG signals arising from just the cell membranes. THG signals were stronger for cells incubated with **(e)** hFTH-Mag compared to **(f)** the apo-hFTH counterpart lacking the iron core. (Adapted from [104])

interface altering the local refractive index required for THG signals. Finally, the combination of Tim-2 overexpression and incubation with ferritin led to its entrapment in lysosomes generating strong OA and THG signals based on its incorporated iron core. Next, specific photoablation of ferritin-positive cells was carried out by illuminating a specific area with 15.4-fold higher pulse energy than for imaging using the OA laser. OA signals (see Fig. 5.7a) seen of hFTH-Mag cells vanished after applying this procedure in re-imaging the identical area (see Fig. 5.7b). The decrease was determined to be ∼70-95% as shown in Fig. 5.7c. THG readings showed similar findings before (see Fig. 5.7d) and after photoablation (see Fig. 5.7e) of the identical sample, each carried out subsequent to the OA scan. The THG image after applying photoablation revealed intact cell morphology of OA negative cells and, thus, confirmed specific interaction with ferritin-positive cells only. The difference image of THG readings (see Fig. 5.7f) showed a signal decrease of 70-95%. Cells being OA negative showed in this procedure a negligible THG signal change below ±5%. Both difference images showed a high spatial congruence (Pearson correlation coefficient (PCC): R = 0.63), thereby confirming the multi-modal contrast of ferritin and the highly cell-specific actuation via photoablation. Analogous findings were observed in applying the identical measurement protocol to cells incubated with eFTH+L. Likewise, OA signals before the ablation (see Fig. 5.8a)

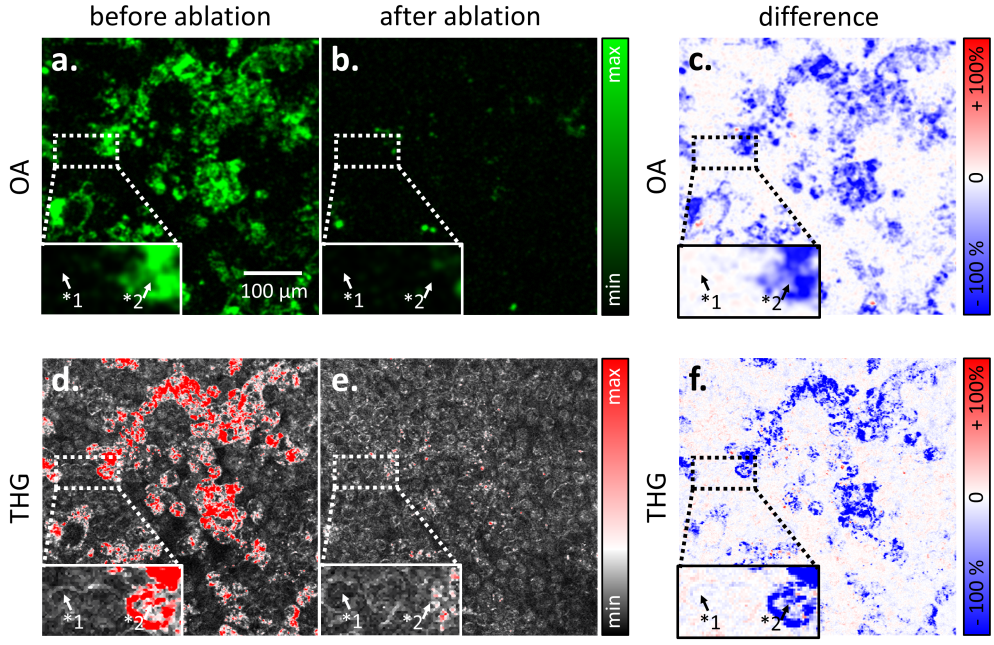

Figure 5.7: Cell-specific photoablation based on lysosomal entrapped hFTH-Mag in Tim-2 positive cells. **(a-b)** Strong OA signals of hFTH-Mag vanished after specific photoablation using ∼15 fold higher laser energy. **(c)** The OA signal decreased by ∼70-95%. **(d-e)** Above-threshold THG signal pattern resembled OA signatures and was eliminated after photoablation. **(f)** THG signal decreased by ∼70-95% and spatially correlated with the OA signal decrease (PCC; R = 0.63), whereas cells generating no OA signals remained constant with a THG change of < 5%. Photoablation was harmless for hFTH-Map negative cells (*1) and specifically ablated hFTH-Map positive cells (*2). (Adapted from [104])

vanished after photoablation (see Fig. 5.8b) by ∼60-85% (see Fig. 5.8c). THG images showed decreased above-threshold signal patterns before (see Fig. 5.8d) compared to after photoablation (see Fig. 5.8e) by ∼50-80% (see Fig. 5.8f). As seen in the THG image after the ablation, OA-negative cells retained their morphology after photoablation and were characterized by a signal change of maximum ±8%. The difference maps showed again a high spatial correlation by determining the PCC of R = 0.34.
In addition to OA and THG characterization, the relevance of both ferritin variants was investigated for MRI techniques. A significantly increased T_2^* contrast was observed for hFTH-Mag compared to eFTH+L. Further, a linear increase of the desired transverse relaxivity was found by increasing Tim-2 concentration inducing entrapment of the ferritin variants to the lysosomes, which was finally estimated to be up to ∼40% of the total lysosomal volume. Finally, a net magnetic moment for cells incubated with hFTH-Mag was revealed high enough to apply magnetic cell sorting, magnetic attraction of cells using an electromagnetic needle, as well as magnetic hyperthermia induced ablation (Data not shown; see [104]).

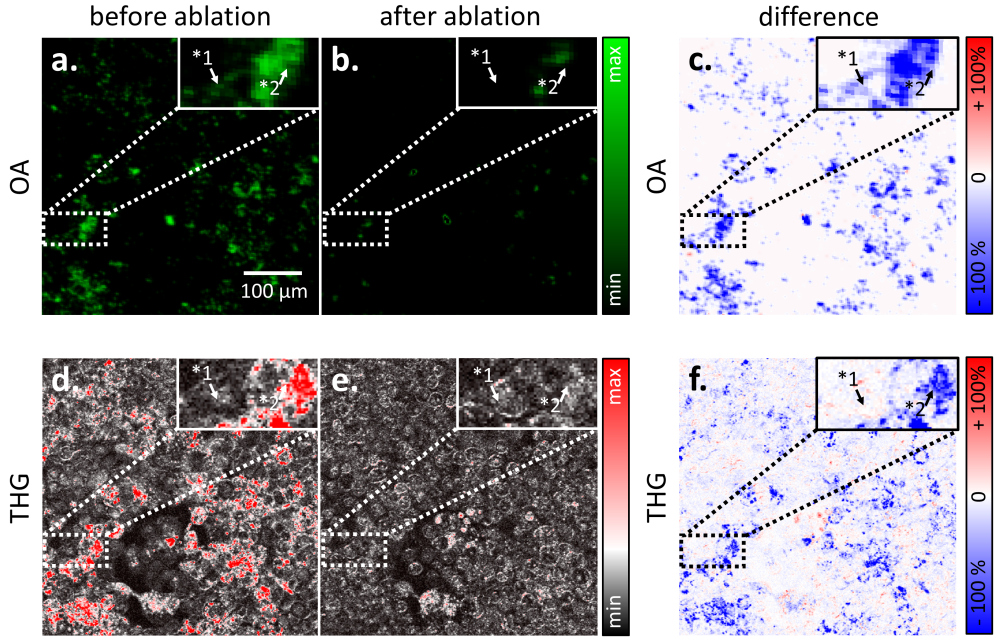

Figure 5.8: Cell-specific photoablation based on lysosomal entrapped eFTH+L in Tim-2 positive cells. (a-b) Strong OA signals of eFTH+L vanished after specific photoablation using ∼15 fold more laser energy. **(c)** The OA signal decreased by ∼60-85%. **(d-e)** Above-threshold THG signal pattern resembled OA signatures and was eliminated after photoablation. **(f)** THG signal decreased by ∼50-80% and spatially correlated with the OA signal decrease (PCC; R = 0.34), whereas cells generating no OA signals remained constant with a THG change of < 8%. Photoablation was harmless for eFTH+L negative cells (*1) and specifically ablated eFTH+L positive cells (*2). (Adapted from [104])

Conclusion

In this project, a genetically controllable multi-modal contrast agent based on the iron-storage protein ferritin was developed for applications of MRI, OA, and THG. The biogenetic development achieved lysosomal entrapment of two variants of ferritin, namely hFTH-Mag and eFTH+L, constituting thereby a novel platform for generating multi-modal contrast by designing its photophysical properties. OA and THG properties of the developed ferritin variants were investigated by the HyMPSOM system. Such local accumulations of strong photoabsorbing molecules in a dense protein-agglomeration led to significant OA and THG contrast. Further, the multi-modal techniques integrated in HyMPSOM in combination with the underlying semi-genetic approach allowed to not only read OA and THG signals of sub-cellular compartments, i.e. lysosomes, but also to interact with individual levels via cell-specific photoablation.
This project outlines how HyMPSOM complements macroscopic techniques like MRI, especially for multi-modal contrast agents such as the herein presented ferritin platforms. It further emphasizes the capabilities of HyMPSOM to study novel genetic

developments for multi-modal contrast mechanisms on the sub-cellular level with high sensitivity and specificity. Such new insights achieved by combining several imaging modalities across the size scale are therefore not only of high interest for optimizing and characterizing genetic markers but can also be exploited in the future to design genetically-controlled theranostic applications.

5.3.2 Multi-modal imaging of bioconjugated Fullerenes

This project concerned the multi-modal imaging of the fullerene C_{70}, which was bioconjugated to the protein lysozyme. The yielded C_{70}@lysozyme construct was designed to enter cells via endocytosis and accumulate in lysosomes not only allowing for OA and THG microscopy but also constituting a potential theranostic platform for photodynamic therapy[87].

Introduction

The soccerball-shaped fullerene molecules own high interest in biomedical research as they potentially serve as a novel theranostic platform for cancer diagnosis and therapy [128–133]. This is mainly due to their high efficiency as sensitizers in photodynamic therapy because they exhibit high photostability, allow for generation of radical oxygen species (ROS) via several physical excitation mechanisms [134–137], and present intrinsic multi-modal imaging contrast [138–141]. These properties are gained by their peculiar molecular structure as an allotrope of carbon shaped into a hollow sphere. On the one hand, the high local density of carbon atoms enables strong optical absorption with negligible quantum yield and, thus, strong OA signals. On the other hand, the hollow core of the sphere presents a significant alteration of the refractive index, which subsequently leads to a strong THG signal. Even though fullerenes such as the herein investigated C_{70} are characterized by the desired intrinsic multi-modal contrast, their application to living organisms is so far still prevented by their low water solubility and low biocompatibility, the dependency of their physical properties and cell toxicity on the environmental conditions (e.g. pH), as well as their dominant tendency to aggregate [142]. The latter is of central importance, as aggregations reduce the intended ROS production by minimizing the area of the reactive surface [143,144]. To overcome these limitations of employing fullerenes for photodynamic therapies *in vivo*, biocompatible host molecules such as proteins and peptides can be conjugated [145–149]. We therefore aimed for synthesizing a C_{70} fullerene bioconjugated to lysozyme (C_{70}@lysozyme) to form a non-covalent supramolecular complex. We chose C_{70} because of its high pho-

[87] This project was headed by Dr. Matteo Giosia, Dr. Alice Solda, and Prof. Calvaresi, who developed and characterized the bioconjugated C_{70}@lysozyme complex, investigated the photodynamic properties, and carried out *in vitro* studies prior to HyMPSOM imaging. During writing this thesis, the results are in revision [127].

todynamic activity compared to alternative fullerene variants such as C_{60} [150–152] as well as high optical absorption at the applied optoacoustic excitation wavelength, and lysozyme because of its high biocompatibility and intracellular trafficking to the endoplasmatic reticulum and lysosomes [153, 154]. Such a local accumulation of monodispersed C_{70}@lysozyme allowed for OA and THG readings during their endocytotic uptake in HeLa cells as well as their multi-modal localization in lysosomes.

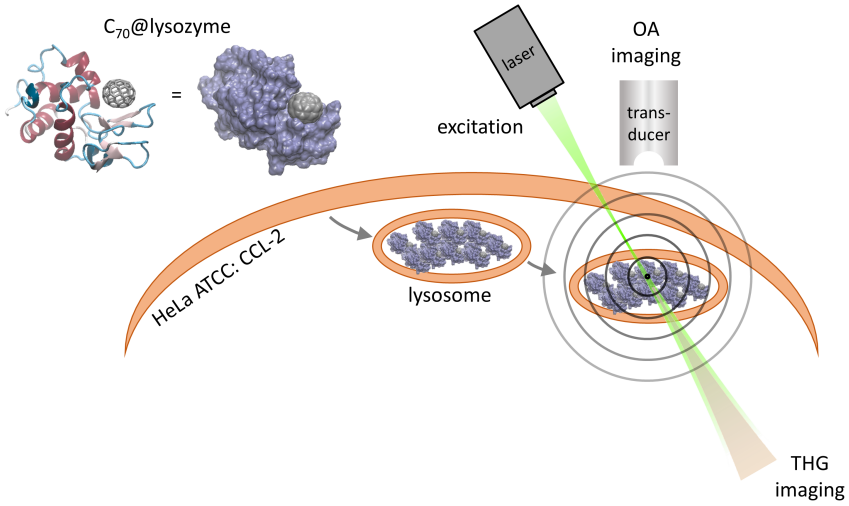

Figure 5.9: Principle of lysosomal uptake of the of C_{70}@lysozyme. The C_{70}@lysozyme bioconjugate accumulated in lysosomes due to endocytosis and allowed for multi-modal imaging. (Adapted from [127])

Materials and Methods

C_{70}@lysozyme was synthesized by suspending C_{70} powder in 1 mL of a 1 mM lysozyme solution in ultrapure water (stoichiometric excess of C_{70} was 2:1). The suspension was sonicated for 60 min on ice (UP200St, Hielscher Ultrasonic Technology, Germany) leading to a dark brown mixture. The mixture was further centrifuged at 10.600 g for 10 min and the supernatant was collected. The yielded aqueous C_{70}@lysozyme suspension was characterized regarding its optical absorption and the stoichiometry via an optical spectrometer (Cary 60 UV-Vis, Agilent, USA), its conformational state changes by a NMR spectrometer (VANCE^{TM}III HD, Bruker, USA), its dispersion state via an AFM microscope (Multimode VIII, Bruker), and its generated singlet oxygen by spectrofluorimetry (FLS920, Edinburgh instruments Ltd., UK). Next, the ROS generation of HeLa cells upon C_{70}@lysozyme uptake was determined by an Amplex^{TM} Red H_2O_2 assay. For that, 1 mL of a phosphate-buffered saline (PBS) solution of 50 mM at pH 7.4 was mixed with 10 µL of Ampex Red 50 mM (in DMSO) and 10 µL of 0.4 mg/mL HRP at pH 7.4 (in 50 mM PBS). The prepared Ampex mixture was added to 90 µL of C_{70}@lysozyme in 50 mM PBS immediately after its irradiation for 1 h with visible light and measured with a photoradiometer (LP 471 RAD, DeltaOhm,

Italy) after 30 min incubation at room temperature. Further, the cytotoxicity and photodynamic activity of C_{70}@lysozyme was investigated *in vitro* in HeLa cells (see Fig. 5.9). The cells were incubated with different concentrations of C_{70}@lysozyme for 3 h in dark condition and washed. Half of the plated cells were illuminated with white light for 10 min and their cell viability was compared to control plates kept in darkness after 24 h by a Vybrant MTT assay.
For final optoacoustic and multi-photon microscopy on HyMPSOM, we first characterized the multi-modal contrast of C_{70}@lysozyme. We let a droplet of C_{70}@lysozyme dry on a glass bottom petri dish and imaged the droplet boundary with OA and THG readings. Next, we incubated HeLa cells (ATCC: CCL-2) with C_{70}@lysozyme while controlling for the environmental condition of the cells using the stage top incubator as described in Section 4.2.3 at 80% humidity, 37 °C, and 20% oxygen during imaging. We monitored the endocytotic uptake of C_{70}@lysozyme over 3 h and finally applied high-resolution multi-modal imaging of an analogously prepared and fixed cell dish with addition of a fluorescent label for lysosomes (LysoTracker$^{(TM)}$ Deep Red, Thermo Fisher Scientific).

Results

The optical characterization indicated typical absorption bands at ∼280 nm of the lysozyme and a broad absorption across the entire visible spectrum of C_{70}. Further, a stoichiometry of 1:1 between C_{70} and lysozyme was found (Data not shown; see [127]). 2D-^{1}H-^{15}N NMR spectroscopy revealed high superposition of coupled H and N atoms of free lysozyme and the C_{70}@lysozyme bioconjugate (Data not shown; see [127]). Hence, lysozyme was found to have a specific binding pocket which hosts the nm-size C_{70} without affecting the protein folding, as confirmed by the NMR spectra. AFM investigations of C_{70}@lysozyme showed mostly a monomolecular dispersion of dimensions of $\sim 3.0 \cdot 3.0 \cdot 4.5$ nm^3 with small presence of dimeric and trimeric structures (Data not shown; see [127]). Besides that, the ability of C_{70}@lysozyme to generate singlet oxygen ($^{1}O_2$) in water was tested in comparison to Rose Bengal as a standard reference. The singlet oxygen phosphorescence at ∼1270 nm upon excitation at $\lambda_{ex} = 514$ nm demonstrated a quantum yield of $\Phi = 0.6$. In contrast to Rose Bengal, C_{70}@lysozyme also produced significant amount of $^{1}O_2$ in water over the entire visible spectrum, probably due to the spatial confinement of C_{70} in the binding pocket reinforcing the $^{1}O_2$ generation (Data not shown; see [127]). Further, C_{70}@lysozyme was investigated towards its *in vitro* cytotoxicity and phototoxicity in HeLa cells. Up to concentrations of ∼5 µM, C_{70}@lysozyme only reduced cell viability upon radiation with light (Mortality at 1 µM: ∼25% for radiated cells and ∼8% for non-radiated cells; data not shown; see [127]). For exploiting the contrast of C_{70}@lysozyme for HyMPSOM, we first imaged the pure C_{70}@lysozyme on a glass cover slide using THG and OA.

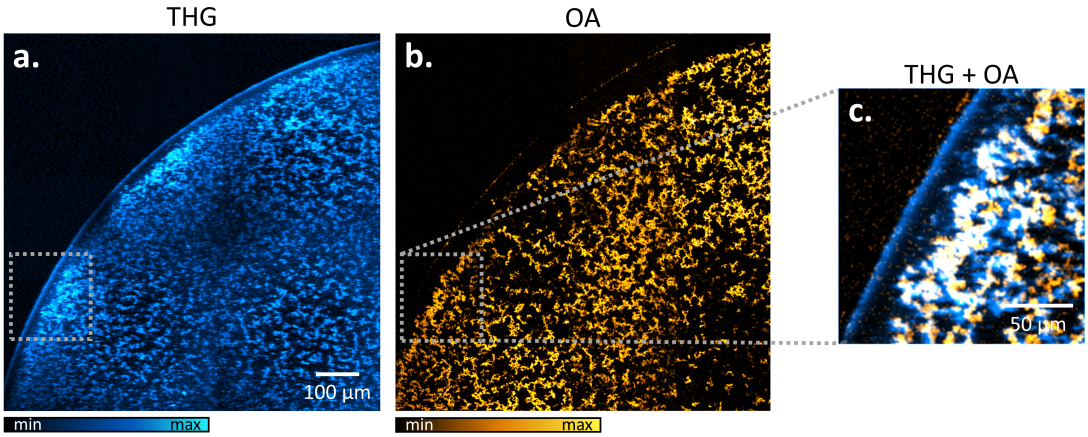

Figure 5.10: Multi-modal contrast of pure C_{70}@lysozyme by imaging the edge of a dried droplet on a glass cover slide. Obtained **(a)** THG and **(b)** OA images indicated strong contrast in a distinct spatial pattern. **(a)** Overlayed zoom-in revealed high congruence between OA and THG readings. (Adapted from [127])

Fig. 5.10a shows the THG image and Fig. 5.10b the OA image obtained at the edge of a dried droplet of C_{70}@lysozyme. For both modalities, C_{70}@lysozyme generated strong signals with a distinct spatial pattern. The latter might be due to the drying process. The overlayed zoom-in of THG and OA shown in Fig. 5.10c revealed a high congruence between those modality further validating the dual-modal contrast of C_{70}@lysozyme. Next, we studied the uptake of C_{70}@lysozyme in HeLa cells.

Fig. 5.11a-c shows OA images at exemplary timepoints of HeLa cells incubated with C_{70}@lysozyme. At the time just before addition of C_{70}@lysozyme to the cell dishes (see Fig. 5.11a), no OA signal was observed. At 60 min (see Fig. 5.11b) and 210 min (see Fig. 5.11c) after C_{70}@lysozyme addition, point-like OA signals spatially smaller than the respective imaging resolutions were detected. Brightfield observations before (see Fig. 5.11d) and after (see Fig. 5.11e) the entire imaging duration confirmed intact and unharmed HeLa cells. Fig. 5.11f plots the time-courses of the point-like signals analyzed by particle tracking algorithms. Whereas the number of detected point-like signals significantly increased ∼10 fold after an incubation time of ∼60 min, their mean OA amplitudes were approximately consistent over time. As the detected OA signals appeared highly localized in defined compartments smaller than the imaging resolution with a consistent OA signal amplitude, we hypothesized their accumulations into lysosomes via endocytosis. To test this, we imaged HeLa cells after 300 min incubation with C_{70}@lysozyme and fluorescent labeled lysosomes.

Fig. 5.12 shows the HyMPSOM images acquired for three exemplary cells. Whereas THG and OA signals were generated herein by the C_{70}@lysozyme, 2PEF signals were based on the fluorescent label of the lysosomes. For all three cells, the THG, OA, and 2PEF signal patterns resembled one another (see Fig. 5.12a, e, and i). Spatial co-

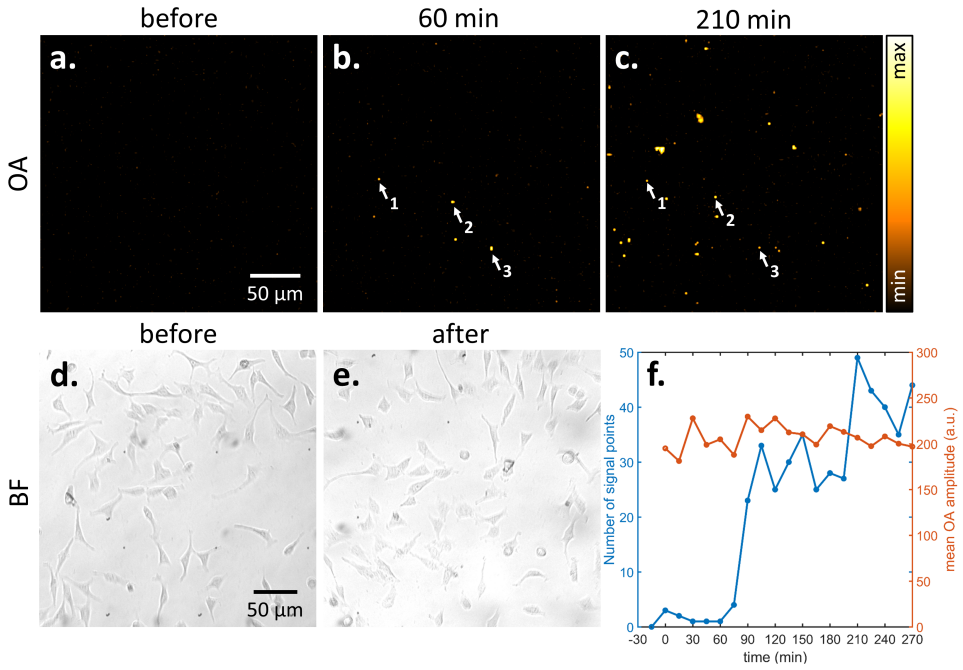

Figure 5.11: C_{70}@lysozyme uptake and lysosomal accumulation investigated in OA readings using HyMPSOM at stage-top incubation of HeLa cells. Imaging at **(a)** 0 min after addition of C_{70}@lysozyme showed no detectable OA signal. Images at **(b)** 90 min and **(c)** 240 min after addition contained consistent point like OA signals (see arrows). BF investigation **(d)** before and **(e)** after 270 min incubation revealed unharmed and intact HeLa cells. **(f)** Analysis of point-like signals over time showed uptake of C_{70}@lysozyme after ~60 min of incubation with consistent signal amplitudes. (Adapted from [127])

localization analysis led to a Pearson-Correlation-Coefficient (PCC) between OA and THG of R ≈ 0.58, between OA and 2PEF of R ≈ 0.33, and between THG and 2PEF of R ≈ 0.32 averaged over the shown three FOV, each covering an individual cell. The non-vanishing and positive PCC values confirmed the majority of C_{70}@lysozyme being accumulated in lysosomes.

Conclusion

In here, we fused the fullerene molecule C_{70} with the protein lysozyme to form highly biocompatible C_{70}@lysozyme bioconjugates. On the one hand, the conjugation to lysozyme diminished the disadvantages of pure fullerenes such as water insolubility, tendency for aggregation, and high cell toxicity, and, on the other hand, reinforced the intrinsic physical properties of fullerenes towards multi-modal imaging contrast and ROS production for photodynamic therapy. The synthesized C_{70}@lysozyme was characterized to appear monodispers with optical properties ideal for OA and THG readings, to be stimulatable with light illumination for significant ROS production, and to accumulate in lysosomes via endocytotic pathways. Finally, C_{70}@lysozyme constitutes

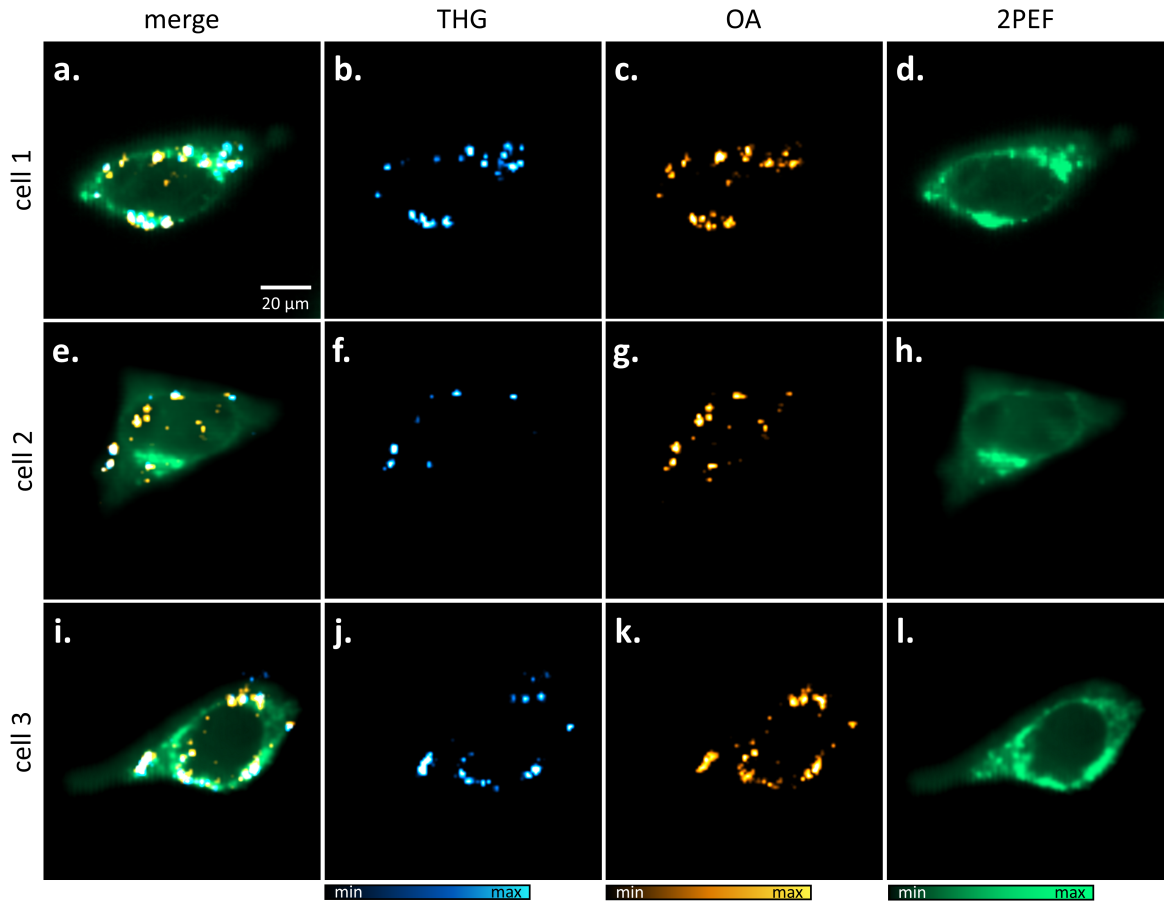

Figure 5.12: Co-localization of C_{70}@lysozyme in lysosomes by multi-modal microscopy applying THG, OA, and 2PEF readings on HeLa cells incubated with C_{70}@lysozyme and fluorescent lysotracker. **(a)** Overlay of recorded multi-modal microscopy images for cell 1 show congruent signal patterns. Separate depiction of the modalities for **(b)** THG, **(c)** OA, and **(d)** 2PEF. Analogous depiction for **(e-h)** cell 2 and **(i-l)** cell 3 validate findings. (Adapted from [127])

a novel approach for combining a synthetic contrast label (i.e. C_{70} fullerene) with a biocompatible host-molecule (i.e. lysozyme protein) to generate an innovative theranostic platform for both multi-modal diagnostic imaging and therapeutic purposes. Besides C_{70} as the synthetic contrast label for OA and THG, other fullerenes like C_{60} or alternative carbon nanomaterials such as nanotubes could potentially present similar or beneficial properties. Thus, compiling a library of biocompatible nanomaterials conjugated to proteins could constitute a novel multi-modal interface, which could be specifically designed for dedicated theranostic settings regarding both imaging and actuation on the cellular level.

For this project, HyMPSOM was utilized to explore C_{70}@lysozyme towards its endocytotic uptake in HeLa cells. HyMPSOM allowed for multi-modal readings in combination with high sensitivity and the ability to maintain the condition for single-cells

in vitro. By that, a precise investigation of C_{70}@lysozyme accumulations in lysosomes was achieved, which constitute extremely small signals in both amplitude and spatial extent. HyMPSOM therefore facilitates the verification of hypothetical assumptions about sub-cellular uptake, dynamic, and trafficking of newly designed bioconjugated carbon nanomaterials.

5.3.3 Calcium sensing by imaging CaSPA

In this project, a novel calcium sensor was developed for optoacoustic sensing (CaSPA), a synthetic metallochromic molecule altering its photophysical properties specifically at the presence of calcium ions[88].

Introduction

Sensing calcium in biological tissue is an essential aim as it constitutes an important second messenger at controlling and triggering e.g. the contraction of heart and skeletal muscles, or secretory processes in immune, neuroendocrine, and neuronal cells [156]. Determination of spatial and temporal distributions of Ca^{2+} ions on size scales ranging from single-cells up to whole organs of living animals is therefore of highest interest. Although optoacoustics allows in this regard the desired deep, fast, and high-resolution imaging across all size scales, neuronal activity is so far only measured indirectly via monitoring hemodynamics, which encodes neurovascular coupling by correlating neuronal activity to vasodilation [157]. Direct measurements of Ca^{2+}-ion dynamics by OA are so far prevented by the lack of appropriate molecular sensors. Such sensors should fulfill certain criteria for a proper application: First, the sensor should be designed best for OA measurements by possessing a high absorption coefficient in combination with a low quantum yield; Second, the sensor should be highly specific for targeting Ca^{2+}-ions over competing divalent metal ions (e.g. Mg^{2+} or Zn^{2+}); and Third, the sensor should enter the cells of interest via highly efficient transmembrane processes [158–160]. For fluorescence imaging techniques such sensors are available, e.g. Oregon Green BAPTA-1, where the presence of Ca^{2+}-ions alters the chromophores quantum yield [161]. Besides quantum-yield changer, metallochromic dyes such as Arsenazo III and Chlorophosphonazo III respond to Ca^{2+}-ions by varying their optical absorbance. Thus, these dyes were tested in OA imaging [162, 163], but were found to exhibit low specificity for calcium [164] and high cell toxicity. Next to Ca^{2+}-ions, OA sensors for Cu^{2+}-ions were reported [165], however ion-binding was in there not reversible.
We developed therefore a cell-permeable and Ca^{2+}-specific sensor for OA imaging (CaSPA). For that, we replaced the chromophore of a metallochromic molecule ex-

[88] This project was headed by Dr. Sheryl Roberts and Prof. Dr. Gil Westmeyer, who developed, synthesized, and characterized the CaSPA molecule complex and prepared the cell samples. The outcome of this project is published in [155].

ecuting photoinduced charge transfer, such as fura-2 [166, 167], by a semi-cyanine chromophore to induce a shift in the absorption characteristics to higher wavelengths preferred for OA.

Materials and Methods

The herein developed CaSPA-550 chromophore was synthesized by condensation reaction of 3-ethyl-1,1,2-trimethyl-1*H*-benzo[*e*]indol-3-ium iodide and 1,2-bis-(2-aminophenoxy)-ethane-*N*, *N*, *N*′, *N*′-tetraacetate. The yielded purple crystals were demethylated by $NaOH_{aq}$, dried under high vacuum, and saponificated regarding the methyl-ester-group with tetrabutylammonium hydroxide. Final esterification with DIPEA and AM bromide in acetonitrile with subsequent purification led to purple crystals of CaSPA-550-AM. Latter constituted the CaSPA-550 variant optimized for *in vivo* measurements. The optical and optoacoustic properties of CaSPA-550 were investigated regarding its absorption spectrum and quantum yield as a function of the Ca^{2+}-ion concentration and of the pH value resembling intracellular conditions. The sensor was further investigated theoretically by quantum chemical calculations as well as practically in NMR- and mass-spectroscopy, and liquid chromatography. The binding selectivity and specificity for Ca^{2+} ions was determined by ratiometric binding measurements.

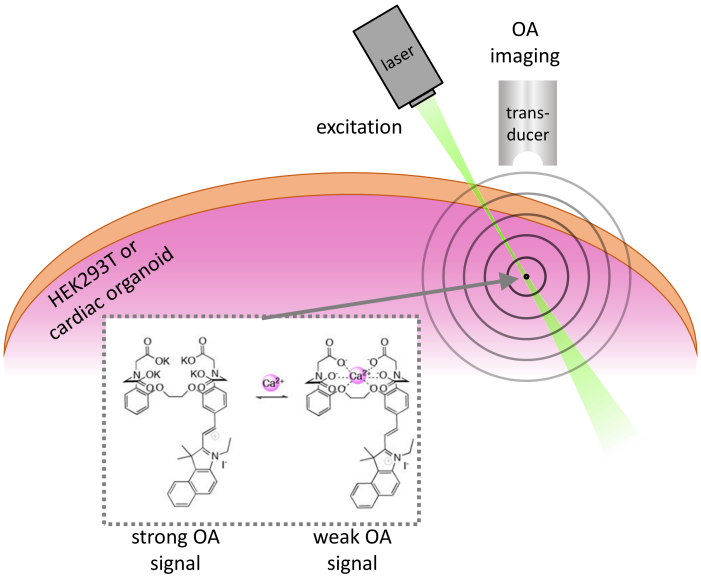

Figure 5.13: Principle of cell-permeable calcium sensor for optoacoustic imaging. The cytosolic located CaSPA-550 changed its absorption and, thus, OA signal upon binding Ca^{2+}-ions. (Adapted from [155])

Finally, HEK cells were incubated with CaSPA-550-AM for investigations using HyMPSOM (see Fig. 5.13). The cells were further stimulated with a calcium-specific ionophore (Br-A23187) to induce a Ca^{2+}-flux. In addition to that, a cardiac organoid was cultured constituting a 3D tissue via mimicking the beating function of a heart triggered

by intrinsic Ca^{2+}-transients. The organoid was loaded with CaSPA-550-AM and imaged by HyMPSOM by an image framerate of ∼1 Hz using OA and in a stationary 3D fashion using 2PEF. CaSPA-550-AM was further injected into zebrafish larva and investigated in an optoacoustic mesoscope and a fluorescence imaging system.

Results

The developed CaSPA-550 showed strong optical absorption at 550 nm of 77.745 $M^{-1}cm^{-1}$, which decreased linearly to ∼50% upon Ca^{2+} concentrations of 39 µM (Data not shown; see [155]). The absorbance remained nearly unchanged at varying the pH. CaSPA-550 further possessed a low quantum yield below 10%, which was almost independent of the local Ca^{2+} concentration as desired. Similar results of ∼50% signal reduction were found in an optoacoustic spectrometer (Data not shown; see [155]). The dissociation constant K_D was obtained optoacoustically at 3.9 µM and optically at 4.0 µM (both with 95% confidence interval). CaSPA-550 was found to be highly selective for Ca^{2+} over Mg^{2+}, Zn^{2+}, and Cu^{2+}, as such competing metal ions does not induce changes in optical absorption. CaSPA-550-AM showed similar characteristics with slightly modified photophysical properties (peak absorption at ∼590 nm with 116.500 $M^{-1}cm^{-1}$; Data not shown; see [155]).
HEK cells incubated with CaSPA-550-AM and stimulated with the calcium-specific ionophore Br-A23187 were imaged in HyMPSOM. Fig. 5.14a shows a large scan of several HEK cells before stimulation. In Fig. 5.14b-d showing zoom-in ROIs just (b) before, (c) 120 s after, and (d) 240 s after ionophore addition (10 µM of Br-A23187), the OA signal significantly decreased over time. The corresponding signal difference maps referenced to the first time-point depicted in Fig. 5.14e-g indicated a signal decrease of ∼50% at the third time-point of 360 s. Fig. 5.14i represents the maximum signal change along the entire imaged duration of the experiments, which clearly shows three cells decreasing in signal by ∼50%. The time-course of the OA signal averaged over the three sensed cells and the associated signal deviation is presented in Fig. 5.14i. During the first 120 s in the vehicle control (i.e. 0.5% DMSO), the OA signal remained almost constant followed by an asymptotic decrease upon stimulation.
Fig. 5.15a depicts a co-registered overlay of 2PEF and an OA maximum amplitude projection of the imaged cardiac organoid incubated with CaSPA-550-AM. Whereas the 2PEF image constitutes the 2D projection of a 3D recording capturing the entire organoid, the OA imaging plane was placed at the most upper layer of the organoid. The organoid was further imaged with a framerate of ∼1 Hz using the OA readout[89]. Fig. 5.15b-d show exemplary time-points at (b) 4 s, (c) 9 s, and (d) 17 s during imaging. The OA signal in here changed both in amplitude and spatial pattern over time. The associated signal difference maps (see Fig. 5.15e-g) revealed a time-dependent

[89] At the time of conducting this experiment, simultaneous reading of OA and 2PEF was not yet available.

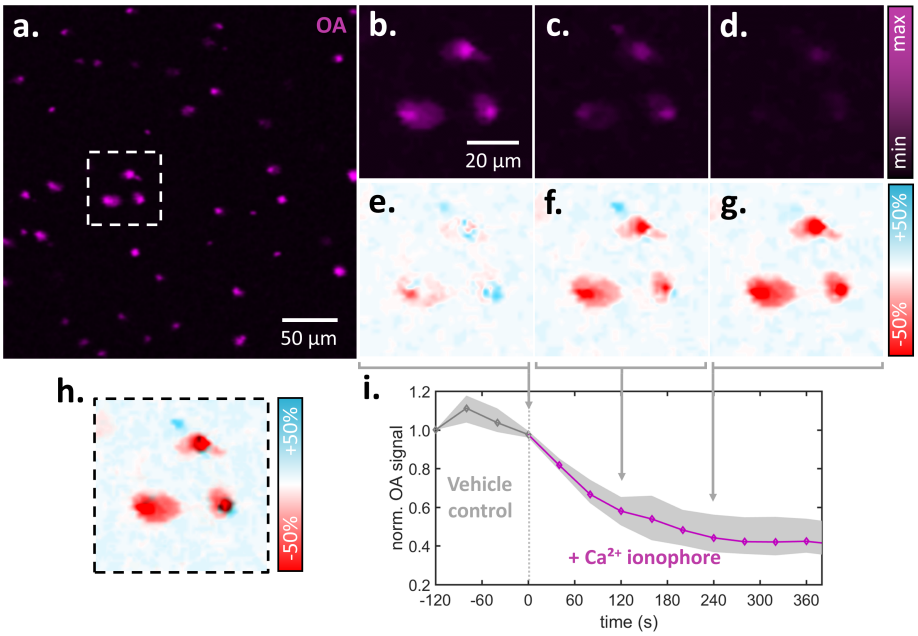

Figure 5.14: Imaging of CaSPA responses in HEK cells upon Ca^{2+} stimulation. **(a)** OA imaging of HEK cells incubated with CaSPA-550-AM. **(b-d)** Zoom-ins showing three HEK cells exemplary for time-points (b) before and (c) 120 s or (d) 240 s after the addition of the Ca^{2+} ionophore. **(e-g)** Corresponding difference maps of (b-d) reveal a signal drop of ∼50%. **(h)** Maximum signal change after complete response. **(i)** Normalized OA signal average (line) and deviation (gray area) over the three cells during the experiment. (Adapted from [155])

maximum amplitude change of up to ±10%. Fig. 5.15h depicts the maximum signal change over the entire measurement duration. The normalized OA signal trajectory shown in Fig. 5.15i averaged over the outlined oval area in Fig. 5.15a indicated time-varying OA signal fluctuations ranging over ±10%. Although the extracted time-course was not validated by simultaneous fluorescence reading, the sensed signal fluctuations resembled findings of analogously performed fluorescence imaging extracting beating frequencies of ∼0.04 Hz (see supplementary information of [155]).
Moreover, the developed CaSPA-550 and CaSPA-550-AM were investigated for applications in zebrafish larvae for optoacoustic mesoscopy and fluorescence imaging. After intraventricular injection, the compound was found to spread over the entire brain (see Fig. 5.2). After addition of ethanol (EtOH, 1% in water) as a neurostimulant, signal fluctuations as well as an overall signal decay was observed for both optoacoustic and fluorescence readings. This effect was also observable upon addition of the potent neurostimulant pentylenetetrazole (PTZ, 5 mM in fish water) inducing strong Ca^{2+} flux in zebrafish brains[90](Data not shown; see [155]).

[90] During this project, the OA sensitivity of HyMPSOM was found to be too poor for performing analogous microscopic imaging.

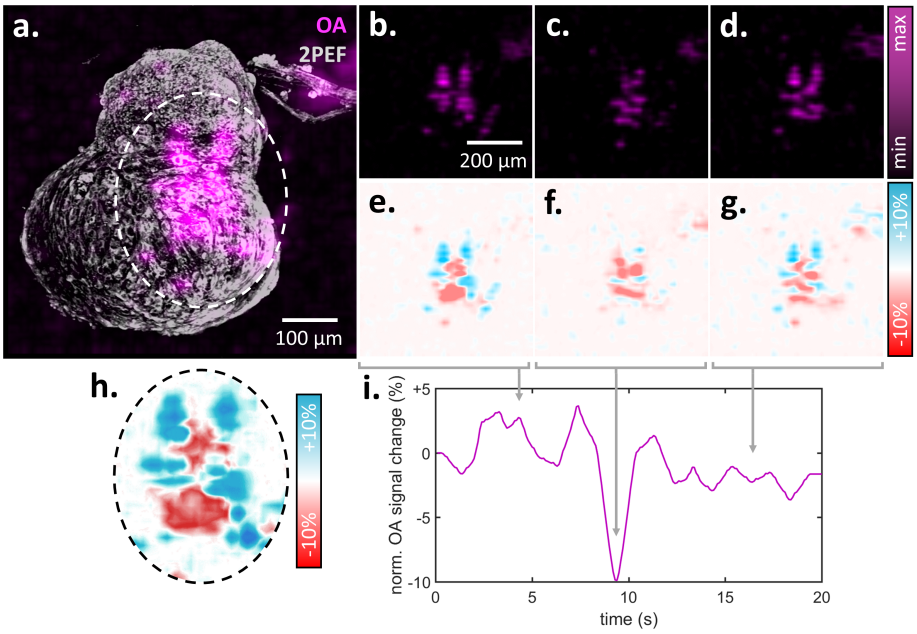

Figure 5.15: Imaging of the CaSPA signature in a beating cardiac organoid. (a) Overlay of 2PEF and OA imaging of the cardiac organoid incubated with CaSPA-550-AM. **(b-d)** Exemplary time-points of the cardiac organoid at (b) 4 s, (c) 9 s, and (d) 17 s reveal time-dependent signal changes. **(e-g)** Corresponding difference maps of (b-d) indicate signal fluctuations of up to ±10%. **(h)** Maximum signal change over the entire time of the measurement. **(i)** Normalized OA signal average over the outlined oval marked in (a). (Adapted from [155])

Conclusion

In here, we developed and characterized a novel metallochromic Ca^{2+}-sensor for optoacoustic imaging. We refined the existing chromophore fura-2 by incorporating a semicyanine chromophore. The thereby yielded CaSPA-550 constitutes the first synthetic sensor allowing to specifically monitor Ca^{2+}-concentrations by optoacoustic detection in living cells, organoids, and zebrafish brains *in vivo*. CaSPA-550 detection using HyMPSOM enabled in this regard to measure both external stimulations by the addition of Ca^{2+}-ionophores as well as intrinsic Ca^{2+}-signaling such as the trigger signal for the cardiac organoid.
This project emphasizes the unique imaging capabilities of HyMPSOM for fast, multimodal, and sensitive measurements. HyMPSOM helps in this regard to study the behavior and photophysical properties of a novel synthetic contrast agent for optoacoustic imaging techniques in general. By allowing imaging of both single-cells as well as organoids, HyMPSOM constitutes a powerful tool in the design and characterization of such novel agents.

5.3.4 Label-free imaging of wound healing sequences

In this imaging project, HyMPSOM was utilized to monitor the entire wound healing process in mouse ears *in vivo* by conducting a longitudinal study. The multi-modal and label-free detection of the key tissue constituents allowed HyMPSOM to collect detailed information and mutual interaction along the process of tissue regeneration. In here, the simultaneous application of all modalities in combination with high acquisition scanning speed enabled to observe large FOVs and, thus, to investigate even distant tissue responses. Finally, the high fidelity allowed to apply advanced analysis algorithms to explore the individual as well as mutual responses of the tissue constituents[91].

Introduction

Skin constitutes the largest organ of vertebrates and acts as a protection barrier against external pathogens, as a preservation of the hydration level of the body, and as a sensor of the environment [169–171]. The composition of skin, with a total thickness between 0.5 and 2 mm, takes shape of a multilayered tissue organization subdivided into the epidermis, the dermis, and the hypodermis[92]. The epidermis contains proliferating basal and differentiated keratinocytes composed into a stratified squamous epithelium and realizes by that the primary barrier to the outside. The dermis, which is separated from the epidermis by the basement membrane, consists of the connective tissue (extracellular matrix: collagen and elastin, fibroblasts, adipocytes), and adapts to the external stress and strain. The hypodermis connects the two above mentioned layers to the underlying muscles, bones, and blood vessels and is mainly built up of connective tissue. [169–171]
As skin is essential for the health condition of the covered organism, skin perforations like wounds constitute a severe danger as they allow environmental pathogens to invade the body. Hence, quick and faultless wound healing is crucial to recover the skin integrity. The skin response to inflicted wounds typically follows a complex and sequential process divided into four essential phases [29,169–176]: Within the first phase, i.e. hemostatis, blood thickens and clots in order to seal the wound and prevent excessive blood loss. During the second phase, i.e. inflammation, macrophages and white blood cells absorb bacteria and debris in the wound via phagocytosis. Simultaneously, the extracellular collagen matrix gets degraded in the close proximity of the wound by enzymes to facilitate migration of epithelial cells. The third phase, i.e. proliferation, starts after complete covering of the wound with re-epithelium and repairs the

[91] This project was performed in cooperation with Dr. Dominik Jüstel and Christoph Dehner, who developed the advanced image analysis methods. During writing of this thesis, this project was in preparation for submission [168].
[92] The hypodermis does not constitute an actual skin layer but is typically mentioned in this context.

inflicted skin defects. Meanwhile, new vasculature is built by angiogenesis, the connective tissue is reformed by collagen and elastin depositioning, and new skin is generated by granulation tissue formation and epithelialization. This phase is further characterized by skin contraction. The final phase, i.e. remodeling, refines the newly built tissue to standard conditions by rearrangement of the connective tissue, intramolecular crosslinking, and reorganization of the vasculature [169]. Depending on the wound size, depth, and location, the final phase can potentially evolve into scar formation via alignment of collagen bundles to the wound tension line, and under abnormal wound healing conditions to clinical cases such as chronic wounds or pathological scarring (e.g. keloid or hypertrophic scars) [169, 172, 175]. Such clinical cases of chronic wounds are e.g. diabetic ulcers or pressure ulcers, two major complications of diabetes mellitus, or acute cutaneous burns, both of which could force severe medical treatments. The entire wound healing process can, depending on size, kind, and location of the wound, last between weeks and months, and requires continuous monitoring to assess the healing progress as well as to deduce correct treatment. [169–177]

Hence, it is of highest importance to unravel the entire wound healing process in detail to predict the prospective progress, the outcome, and potential complications [169, 175, 177, 178]. In this regard, most of the central components involved in tissue healing are characterized by functional units on the microscale like collagen fibrils, keratinocytes, microvessels, and, thus, microscopic investigations are most promising to understand their complex interactions. Besides visual examinations, which is still the main way of wound investigations in clinical practice in form of epiluminescence-based dermoscopy, histological analyses of wound tissue slices are performed regularly for precise analysis. However, tissue extraction via biopsies is invasive and affect the healing process itself as it constitute an additional infliction to the wound site. In contrast, non-invasive optical imaging techniques allow to assess the entire wound tissue without additional harm. It has been demonstrated that microscopy techniques like laser Doppler imaging, multi-photon microscopy, Raman microscopy, tissue spectral imaging, optoacoustic microscopy, and optical coherence tomography enable mapping of the vasculature network based on the optical absorption of hemoglobin or scattering properties of moving blood cells, of the extracellular collagen matrix by reading intrinsic fluorescence or optical harmonic generation, and of the metabolic state by spectral analysis of the molecular composition. [29, 169, 171, 174–176, 178–183]

Although the above mentioned approaches were each shown to investigate certain key components involved in the wound healing process, their individual and isolated application limits a comprehensive examination by disregarding mutual interactions and influences of the constituents. We therefore opted for studying the wound healing process in the well-established mouse ear model for wound healing [173–175, 179, 184–187] using the simultaneous multi-modal and label-free imaging capabilities of HyMPSOM. By combined SHG detection of collagen, 2PEF detection of tissue autofluorescence

(mainly by elastin and hair follicles), THG detection of keratinocytes and sebaceous glands, and OA detection of the microvasculature, HyMPSOM allowed to image all key components of the wound healing process with high spatial resolution.

Materials and Methods

The wound healing process was studied using three athymic nude Hsd foxn1 mice and the wounds were inflicted by punching the ear with a 200 µm sterile needle with a trimmed bevel in order to stamp out a piece of tissue[93]. The mice were imaged consecutively up to 68 days after infliction of the wound according to typical settings performed in analogous studies. During measurements, the mice were anesthetized with ∼2% isofluorane and placed onto the dedicated mouse holder (see Section 5.2.2, Fig. 4.6 and Appendices: Photographs of the optical setup). The imaging was carried out using the hybrid-scanning scheme as explained in Section 4.2.5 covering a FOV of $\sim 2.5 \cdot 3$ mm^2 located at the outside edge of the pinna. Furthermore, all modalities were recorded simultaneously as described in Section 4.2.3 and Section 4.2.4, and were complemented with brightfield microscopy images of the identical FOV.
The recorded data of OA, 2PEF, SHG, and THG images were processed as explained in Section 3.4 and co-registered to each corresponding BF image. The high precision data and large scanned area allowed to apply spatio-temporal analysis techniques to explore the tissue response as a function of time and of distance to the wound. To ensure comparability and spatial equality, the sets of images of each mouse were co-registered within themselves along the time course. The OA images were analyzed to monitor changes in the microvasculature. For that purpose, OA images were first processed with an anisotropic diffusion filter in 10 iterations to reduce image noise. Next, tubularity filters were applied on the entire images as well as on moving windows to generate binary masks, which were finally merged to receive a segmented vasculature map. These maps were subsequently analyzed in terms of different local features. On the one hand, the median vessel thickness was determined by measuring the local vessel thickness using a central circle analysis. On the other hand, the morphology of the vasculature tree was analyzed by determining the fractality, which quantifies the hierarchical complexity of the network in its ability to fill an area with its branches. For that, the box counting dimension (i.e. Minkowski-Bouligand dimension) $dim_{box}(V)$ of the vasculature network V was measured, which is defined by:

$$dim_{box}(V) = \lim_{n \to \infty} \frac{\log N(1/n)}{\log n}, \tag{5.1}$$

[93] The inflicted hole was smaller than the typically used ear punches to mark mice being ∼1 mm diameter.

where $N(1/n)$ is the number of boxes of side length $(1/n)$ needed to cover the vessel network V. Numerically, this quantity was locally approximated in patches of $128 \cdot 128$ µm^2. The box counting dimension of a network is a dimension in the sense that it gives a scaling law for the area occupied by the set $N(1/n) \sim n^{dim_{box}(V)}$. For a set V that is a line or a surface, the box counting dimension agrees with the classic integer dimension and equals one and two, respectively. As dense vessel networks fill an area quite efficiently, a box counting dimension of ∼2 is expected, which has been reported for mouse ears at 1.75 [188]. On the other hand, the median vessel thickness was determined by measuring the local vessel thickness using a central circle analysis. The SHG images mapping the extracellular collagen matrix were analyzed to reveal the skin contracture induced by the connective tissue. In here, the SHG images were normalized within itself to compensate for inter-image fluctuations and were analyzed towards the median value of local signal intensity. Further, the extracted median intensities were normalized across the analyzed region to yield a local collagen density. Spatio-temporal analysis maps of OA and SHG signals were further normalized to the before-image to depict relative changes. The 2PEF images were utilized to monitor the wound size and boundary condition. For that, the 2PEF images were normalized to itself, the wound was outlined using a tracing tool with a tolerance of 5% in legacy mode, and the traced area as characterized by its area, perimeter, and circularity. The above mentioned spatio-temporal maps of each mouse as well as their average were projected along the spatial or temporal dimensions using their maximum intensity. The averaged curves were subsequently fitted by Gaussian functions. More precisely, we used the model:

$$m(s) = a \cdot e^{-\frac{(s-b)^2}{2 \cdot c^2}} + d \cdot s + f \tag{5.2}$$

for the spatial responses using s as the spatial distance to the wound center (the spatial collagen responses were fitted by a sum of two Gaussian functions with a linear slope of $d \neq 0$; all other fits had a static offset with $d = 0$), and the model:

$$m(t) = a \cdot e^{-\frac{(t-b)^2}{2 \cdot c^2}} + f \cdot (g - e^{-(t-h)}) \tag{5.3}$$

for the temporal responses using t to denote the time after wound infliction.

Results

Fig. 5.16 depicts the recorded HyMPSOM images acquired at 9 time points along the entire wound healing process exemplary for one mouse. The hybrid microscopy images[94] (see Fig. 5.16a-i.1) implied the complexity of the tissue response to the inflicted 200 µm wound and revealed manifold insights into the underlying healing phase, which were concealed in the corresponding brightfield microscopy images (see Fig. 5.16a-i.2) or photographs (see Fig. 5.16a-i.3). First, the wound boundary appeared rough at 1 h after the wound infliction and became smoothed and homogenized at day 4 and 7. As expected, the skin closed the inflicted wound within 14 days. Furthermore, the newly generated tissue did not contain any collagen, vasculature, or sebaceous glands before wound closure. Second, the collagen matrix surrounding the wound initially seemed weakened until day 4, which demonstrated the loss of connective tissue to allow cell migration, and then strengthened and densed after day 7, which was associated with skin contraction to accelerate wound closure. The collagen matrix between the wound and the ear boundary further appeared attenuated until day 21. Third, the microvasculature network showed fragments of former vessels immediately after the wound infliction, which got degraded until day 4. Additionally, an overall increased appearance of the vasculature throughout the FOV could be seen, which also included reorganization of the existing vasculature. At day 14, a strong neovascularization of coiled microvessels could be observed at the former wound region, which became normalized till day 36. Fourth, the freshly built tissue did neither contain sebaceous glands until wound closure nor the patch-like surface structure of the stratum corneum, which therefore suggested a faster healing of the dermis than the epidermis. Finally, all revealed skin constituents appeared recovered and normal at day 68, at which the former wound location was hardly recognizable. The wound healing process in here could therefore be assumed successful and complication-free.
These findings were more clearly visualized in depicting the modalities separately as shown in Fig. 5.17[95]. Fig. 5.17a-i.1 depict the microvasculature imaged by OA with vessels ranging from ∼200 µm diameter to microcapillaries of ∼10 µm. Fig. 5.17a-i.2 show the extracellular collagen matrix imaged with SHG organized in skin patches and structured around hair follicles. Fig. 5.17a-i.3 plot the 2PEF readings[96] of the tissue autofluorescence, mainly of elastin and hair follicles. The highlighted zoom-ins reveal strong neovascularization on the microscale induced after closure of the wound (see Fig. 5.17j.1), enhanced collagen density indicating skin contraction to accelerate

[94] The bright local signals in Fig. 5.16a.1 and Fig. 5.16i.1 originated from debris on top of the ear.
[95] Due to the inconsistent THG readings induced by its intrinsic high dependency on the position of the focal plane, only OA, SHG, and 2PEF are depicted here.
[96] The areal-shaped intensity variations in the 2PEF images resulted from a malfunction of the corresponding PMT.

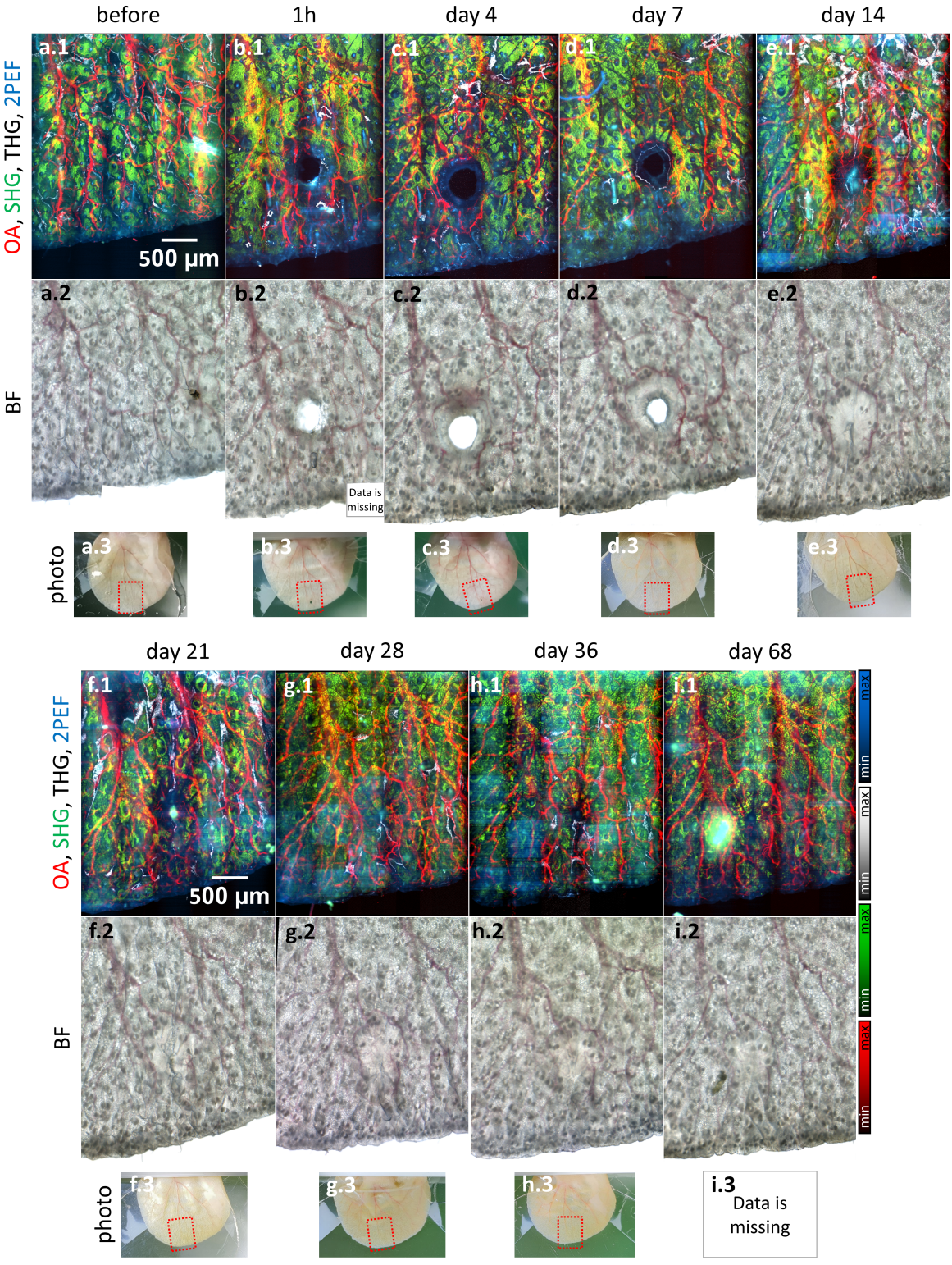

Figure 5.16: Longitudinal imaging of the wound healing process in *in vivo* mouse ears by label-free multi-modal microscopy using HyMPSOM. **(a.1)** Multi-modal image of the mouse ear before wound infliction and corresponding **(a.2)** brightfield microscopy image as well as **(a.3)** photograph of the ear. Analogous depiction of the ear at **(b.1-3)** 1 h, **(c.1-3)** 4 days, **(d.1-3)** 7 days, **(e.1-3)** 14 days, **(f.1-3)** 21 days, **(g.1-3)** 28 days, **(h.1-3)** 36 days, and **(i.1-3)** 68 days after wound infliction. (Adapted from [168])

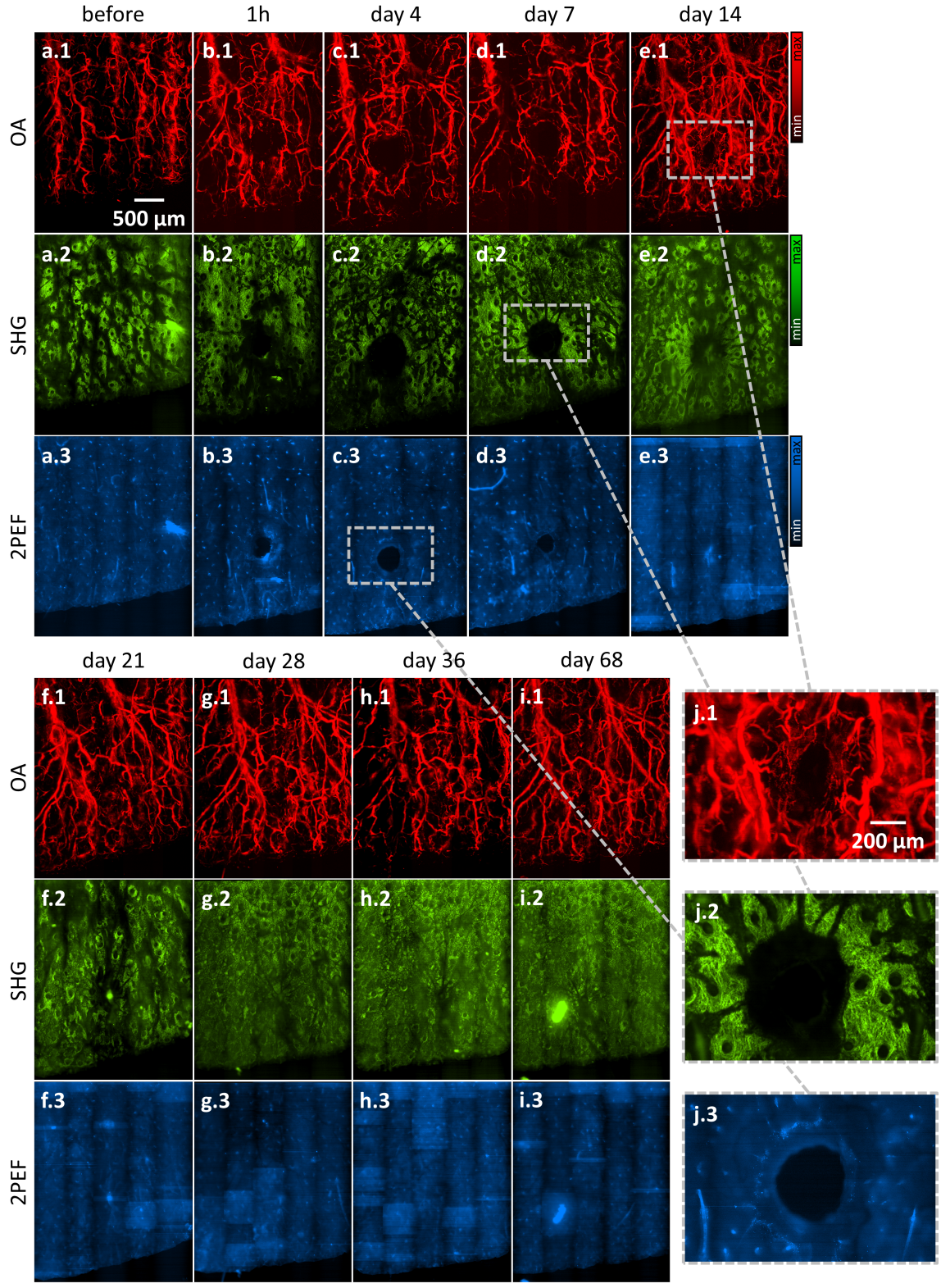

Figure 5.17: Separate depiction of microscopy modalities of the wound healing imaging. **(a.1)** OA, **(a.2)** SHG, and **(a.3)** 2PEF images before wound infliction. Analogous depiction at **(b.1-3)** 1 h, **(c.1-3)** 4 days, **(d.1-3)** 7 days, **(e.1-3)** 14 days, **(f.1-3)** 21 days, **(g.1-3)** 28 days, **(h.1-3)** 36 days, and **(i.1-3)** 68 days after wound infliction. **(j.1-3)** Highlighted zoom-ins showing angiogenesis, collagen enrichment, and wound boundary smoothing, respectively. (Adapted from [168])

wound closure (see Fig. 5.17j.2), and smoothing of the wound boundary line before wound closure (see Fig. 5.17j.3).
Furthermore, the high precision of the data allowed for quantitative assessment of the wound healing process (see Fig. 5.18). As shown in Fig. 5.18a, the wound sizes first increased, which might indicate cleaning of the wound boundary, and then decreased during wound closure. Fig. 5.18b plots the shape the inflicted wounds, which were first found to have an arbitrary contour and then a more circular form[97]. Fig. 5.18c reveals the roughness of the wound boundary line, which was the smoothest at day 4. Fig. 5.18d depicts the spatio-temporally dependent homogeneity of the vasculature network in form of a fractality score normalized to the before-image. The unnormalized fractality was found at 1.71, which locally reached up to 1.83 during neovascularization, and thereby agreed with previous findings. Whereas values below ∼0.8 constituted the actual hole of the tissue, an increased fractality could be observed between day 4 and day 14 at a distance of ∼300-400 µm to the wound. As the fractality was mainly affected by newly generated microvasculature, which typically possesses a coiled structure, this analysis revealed the neovascularization on the microscale. Fig. 5.18e shows the spatio-temporally dependent median vessel thickness normalized analogously to the before-image. In here, a strong increase of the vessel size was found after day 7 at a distance of ∼400-500 µm. Because the vessel thickness is linked to the vasculature throughput, this analysis suggested an increased blood supply and, thus, an increased proliferation at distant locations. Fig. 5.18f is the median collagen density normalized within each image. Although a strong inter-image variation prevented detailed conclusions, the collagen density could be observed unbalanced between 1 h and 14 days after wound infliction. Initially, a decreased collagen density could be seen up to a distance of ∼450 µm to the wound and might be interpreted as loosening of the collagen bundles to soften the skin. After day 7, an increased collagen density at a distance of ∼350 µm might represent skin contraction induced by strengthening of the connective tissue. Furthermore, at the time point of wound closure at day 14, the most inner ∼200 µm lacked collagen, which was compensated for at later timepoints. For a detailed quantitative analysis, the maximum intensities of the spatio-temporal maps were projected along the spatial as well as the temporal dimension to quantitatively investigate the properties of the responses as hallmarks for the wound healing process. Fig. 5.18g depicts the spatial response of the vasculature fractality plotted for each mouse individually (gray lines; Mouse 1-3), as the data-average over the three mice (cyan line; $\mathrm{Avg}_{\mathrm{mice}}$), and as the response-average (orange line; $\mathrm{Avg}_{\mathrm{response}}$) including the associated standard deviation (orange shade), which was further fitted with a Gaussian curve (black line). Fig. 5.18h and i show analogous depiction of the spatial response of the vessel thicknesses and the collagen density. Inter-mouse variations could be disregarded, since the two ways of merging the data resembled each other, thereby

[97] A circularity of 1.0 constitutes a perfect circle.

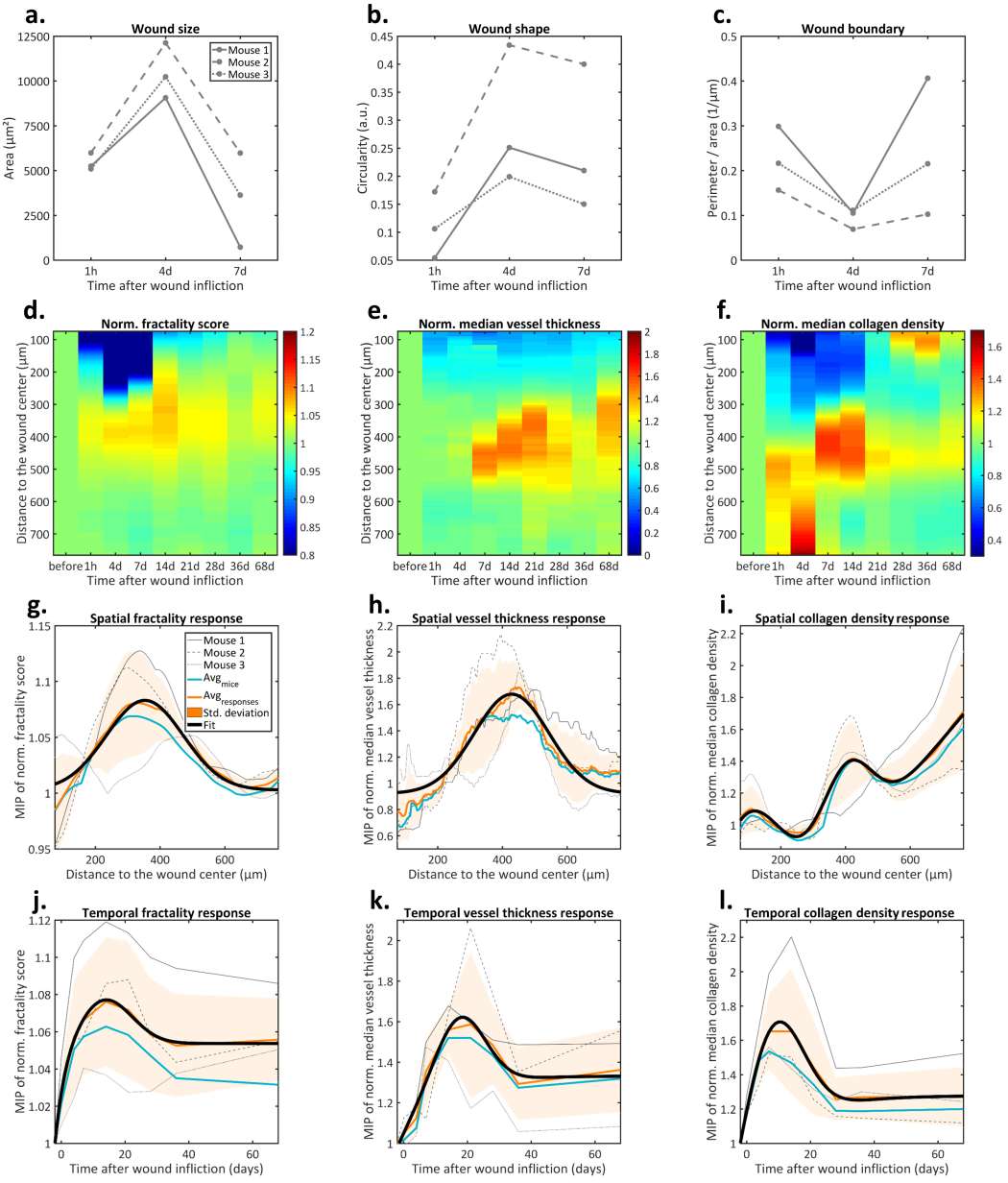

Figure 5.18: Spatio-temporal assessment of the wound healing process via averaging the analysis of OA, 2PEF, and SHG images of three mice. Spatial characterization of the wound towards **(a)** the wound size, **(b)** the wound shape, and **(c)** the wound boundary. Spatio-temporal maps depicting relative changes of **(d)** the fractality and **(e)** the vessel thickness of the microvasculature as well as **(f)** the local collagen density compared to the image recorded before wound infliction. Maximum intensity projections (MIP) along the spatial dimension of **(g)** the norm. fractality score, **(h)** the norm. median vessel thickness, and **(i)** norm. median collagen density. **(j-l)** Analogous analysis along the temporal dimension. (Adapted from [168])

confirming the data consistency. All curves representing the individual or averaged responses of the analyzed hallmark followed a similar Gaussian-shaped profile, which therefore allowed for further quantitative analysis using Equation 5.2. Fig. 5.18j-l illustrate likewise the temporal responses by projecting the spatio-temporal maps along the temporal dimension. Like the spatial responses, all curves of an analyzed hallmark were characterized by a similar curve, which consisted of a Gaussian-shaped peak in the beginning followed by a transition to a long-lasting plateau phase. The applied fitting models were therefore a linear combination of a Gaussian curve and an exponential function using Equation 5.3.

Hallmark	Dimension	Peak	FWHM	Transition	R^2
Fractality	Space	353 µm	280.4 µm	/	0.966
	Time	13.66 days	19.86 days	9.8 days	0.996
Vessel Thickness	Space	428.9 µm	271.7 µm	/	0.916
	Time	17.57 days	18.52 days	9.1 days	0.969
Collagen density	Space	80.0 µm 402.1 µm	186.8 µm 290.9 µm	/	0.995
	Time	8.08 days	21.41 days	7.1 days	0.992

Table 3: Quantitative assessment of analyzed wound healing hallmarks.

Tab. 3 summarizes the results by fitting the averaged responses of the vasculature fractality, the vessel thickness, and the collagen density along the spatial or temporal dimension. On the one hand, the spatial fractality responses was found at a distance of ∼350 µm to the wound center and stretched over ∼280 µm; the spatial vessel thickness responses peaked at ∼430 µm to the wound and extended over ∼270 µm; and the spatial collagen density indicated two peaks at ∼80 µm and at ∼400 µm spreading over ∼185 µm and ∼290 µm, respectively. In combination, the fractality response occurred closer to the wound than the vessel thickness response, whereas the collagen density lied spatially in between. On the other hand, the initial temporal fractality response peaked at ∼13.5 days and lasted for ∼20 days, which transited to a plateau phase after 9.8 days. The temporal vessel thickness response was centered at ∼17.5 days with a duration of ∼18.5 days and a transition time point at 9.1 days. The temporal collagen response showed a peak at ∼8.0 days with a duration of ∼21.5 days and a transit at ∼7.1 days. Combining these findings, a response of the collagen density, which is linked to tissue contracture, was observed the earliest followed by a response of the vasculature fractality, which can be associated with neovascularization, finalized by a response of the vessel thickness, which belongs to the blood supply.

Conclusion

In conclusion, the label-free and simultaneous multi-modal imaging capabilities of HyMPSOM allowed to monitor the entire process of wound healing with high precision across a large FOV. We conducted a longitudinal study by imaging the ear pinna of three mice, which were punctured to inflict a wound. The yielded data reveals a complex interplay of the key tissue constituents involved in wound healing like the microvasculature or the extracellular matrix of connective tissue. The spatially co-registered images further enabled the application of spatio-temporal analysis techniques to assess and monitor the tissue response quantitatively. HyMPSOM allowed for precise characterization of the wound size, shape, and boundary. The achieved wound characterization is in high consistency with the well-established wound healing process model, which involves sequential phases of wound sealing, cleaning, and smoothing. In comparison to previous studies, HyMPSOM extracts more comprehensive information and, thus, facilitates more accurate delineation of the wound characteristics. The high precision images acquired by HyMPSOM across a large FOV surrounding the wound site further enabled the application of spatio-temporal analysis techniques to monitor and assess the tissue response quantitatively. By that, we achieved new insights into remote effects, which therefore outline the mechanism of tissue repair and formation. We found distinct tissue responses at late time points after wound infliction and at locations distant to the former wound site, which are so far unnoticed by previous works due to limited FOVs, poor spatial resolutions, or prevention of longitudinal studies because of using contrast agents. Since such responses as well as their temporal sequence and spatial interplay are crucial for a precise assessment, an accurate prediction of the healing progress, and adaption of suitable treatments, investigating the wound healing process by HyMPSOM constitutes a highly promising approach to unravel the process' complexity. Finally, because HyMPSOM extracted the information of the targeted tissue components across the identical FOV and at identical time points, we found the investigated key tissue components reacting to wound infliction in distinct and interconnected spatio-temporal patterns. By assigning them to the underlying wound healing phases, we were able to determine the spatial interplay and temporal sequence of the tissue responses. By that, HyMPSOM facilitates to precisely outline various hallmarks of the healing process and overcomes by that previous studies only targeting one component.
HyMPSOM yields a wealth of information about the wound healing process on the microscale not accessible before, which showcases its huge potential to examine microscopic skin responses. However, monitoring additional aspects can enlarge the insights and understanding. Tracking the sebaceous glands, analyzing the microvasculature blood flow-maps, and imaging immune cells such as macrophages could complete the monitoring as they constitute other keyplayers in the wound healing process. Whereas

the former two were prevented in here by the insufficient data quality, the latter would require cell-specific and herein unintended labeling, due to which the idea was refrained. Further, a more comprehensive understanding of the wound healing process could be achieved by enlarging the number of mice to discriminate effects among different specimen as well as different wound locations.
Conclusively, the above mentioned information is accessible exclusively by HyMPSOM due to its unique features of applying simultaneous and label-free multi-modal microscopy across a large FOV. In this regard, HyMPSOM overcomes previous studies as it monitors the wound healing process more comprehensively and with higher precision. The herein suggested spatio-temporal assessment of the tissue response to inflicted wounds could therefore not only uncover the underlying healing phases in an unmet accuracy but also allow for future comparisons of different types of wounds as well as possible treatment strategies.

5.3.5 Hybrid microscopy of human carotid atheroma

In this project, histopathological slices of human carotid atheroma samples were investigated in a label-free and multi-modal manner using HyMPSOM[98]. HyMPSOM enabled in this project new insights into the microstructural composition of biological moieties relevant for the underlying disease atherosclerosis and demonstrated a novel approach for studying histopathological samples.

Introduction

Atherosclerosis is a multifactorial disease affecting arterial walls and constitutes a major culprit for ischemic heart diseases and strokes. The latter are two of the most frequent causes of death worldwide [192] as they can induce thrombosis and cerebral ischemia. Atherosclerosis is mostly causing a chronic atheromatous plaque being formed in the sub-endothelial layer (i.e. intima) of carotid arteries. The formation and progression of atheromatous plaques is assumed to result from multiple biomechanical, inflammatory, genetic, and environmental factors. Atheroma tissues are typically inhomogenous and complex regarding their structural and biological composition consisting of inflammatory and smooth muscle cells, incorporated lipids and red blood cells, calcium deposits, and remnants of the connective tissue (i.e. collagen and elastin) [193–195]. Based on their structural characteristics, atheromatous plaques are usually divided into different topological regions being the cap, the shoulders, and the necrotic core. The properties of these regions reflect the pathological condition of the disease and

[98] This project was conducted in equal contribution with Dr. Angelos Karlas, who handled the sample preparation and medical interpretation of the findings. The results were published in [189] and [190] and were reflected towards cardiovascular applications of optoacoustics in [191].

allow for classification along the disease progression into severity levels of early, intermediate, and advanced stages [196]. *W.l.o.g.*, the continuously decreasing tissue integrity and development of serious pathological features (e.g. intraplaque hemorrhages) finally ends in advanced and complicated plaques. Such precarious plaques could potentially rupture, circulate in the vasculature network, and eventually induce vasculature blockages [197–199]. The vulnerability of plaques in this regard is assumed to be enhanced by a large necrotic core (incorporations of lipids, fibrin, blood embeddings, and macrophages), a thinned cap (degraded connective tissue and smooth muscle cells), inflammation, as well as neovascularization. Further, the rupture is thought to occur mostly near the shoulder regions triggered by ulcerations [200–203]. The process of the plaque rupture itself is assumed to be induced mechanically by degraded and disorganized collagen networks [204, 205] as well as embeddings of blood residues [203]. Studying atheromatous plaques on the microscale could therefore facilitate new insights into the condition and composition of the above mentioned spatial regions and, thus, allow for a more precise understanding of the disease progression. Combining the findings to macroscopic techniques applied to humans *in vivo*, in the best case based on identical contrast, could subsequently link microscopic features to macroscopic observations and thereby facilitate novel therapeutic approaches. In this regard, microscopic investigations are typically performed on excised specimens using histopathology techniques based on staining or labeling of several cellular and molecular features [206–210]. Whereas staining or labeling is possible to be applied to excised tissues as well as to some extent murine animal models [211–218], they are not available for *in vivo* human applications and, hence, prevent the desired direct link of investigation techniques. To overcome this limitation, we proposed the application of label-free and multi-modal microscopy performed on HyMPSOM to study unstained/unlabeled excised human carotid atheroma specimens. The variety of label-free modalities in a highly spatially co-registered system should enable the extraction of congruent information on the microscale.

Materials and Methods

Patients diagnosed with advanced carotid artery stenosis underwent carotid thrombendarterectomy for acquiring human atheromatous plaque samples. The excised plaque tissue was further segmented into 3-4 mm blocks, fixed in formalin overnight, and embedded in paraffin. The specimens were further cut into ∼10 µm thick cross sections and were placed onto 170 µm glass slides for imaging. The tissue slice imaged in HyMPSOM remained unstained and was first imaged in brightfield mode (Aperia CS2, Leica) as well as by a coarse sample-scanning optoacoustic scan across a $10 \cdot 10$ mm^2 FOV covering the entire specimen with large step sizes of 100 µm (see Section 4.2.5). Next, several ROIs were selected for high-resolution multi-modal microscopy applying

label-free OA, 2PEF, SHG, THG, and BF across an area of $630 \cdot 630\ \mu m^2$. For cross-validation and comparison, three adjacent slices of the identical sample where stained with Hematoxylin & Eosin (H&E) for cellularity, Picro-Sirius Red (PSR) for collagen, and Orcein for elastin. The yielded images of stained tissue slices (Aperio CS2, Leica) presented thereby standard histopathological examination. Finally, the images of stained tissue specimens were compared to the multi-modal images of HyMPSOM.

Results

The excised, unstained, fixed, and sliced atheromatous plaque was first assessed coarsely.

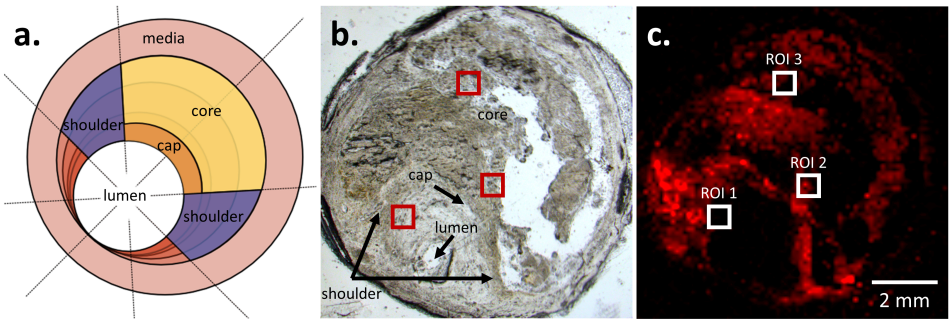

Figure 5.19: Coarse assessment and ROI selection of a human carotid atheroma specimen. **(a)** Schematic subdivision of an atheromatous plaque slice. **(b)** Widefield brightfield image of an unstained human carotid atheroma cross-section and identification of spatial regions like the lumen, cap, shoulders, and necrotic core. **(c)** Coarse optoacoustic scan of the identical tissue sample being co-registered to the brightfield observation in (b). ROI selection for high-resolution multi-modal imaging is indicated by the red and white boxes. (Adapted from [189])

The topological features were used for subdividing the atheroma according to Fig. 5.19a. The shown scheme assigns structural regions of the cross-section to the lumen, lumen, cap, shoulders, and necrotic core. The media constitutes the most inner layer of the arterial wall. Fig. 5.19b presents a widefield BF image of an unstained human carotid atheroma cross-section. The BF image allowed to partition the sample into the above-mentioned structural regions. Fig. 5.19c shows a coarse OA scan of the identical unstained tissue specimen. The spatial pattern obtained in the coarse OA scan resembled the yellow-brownish pattern seen in Fig. 5.19b and, thus, was assumed to emanate from embedded blood residues in the tissue. The coarse assessment of the excised tissue slice allowed also to get first insights into the global morphology of the tissue as well as a rough estimation of the degree of severity of the disease by determining the narrowing of the lumen, the stage of tissue degradation, the size of the necrotic core, and the overall incorporation of blood residues, and thereby could lead to an estimation of the risk of plaque rupture. Next, the coarse assessment enabled to select specific ROIs for applying high-resolution multi-modal microscopy. The selected

ROIs were placed in specific plaque compartments close to the lumen in the shoulder region (ROI 1), centered at the cap (ROI 2), and in the necrotic core (ROI 3) as indicated by the red and white boxes in Fig. 5.19b and c.

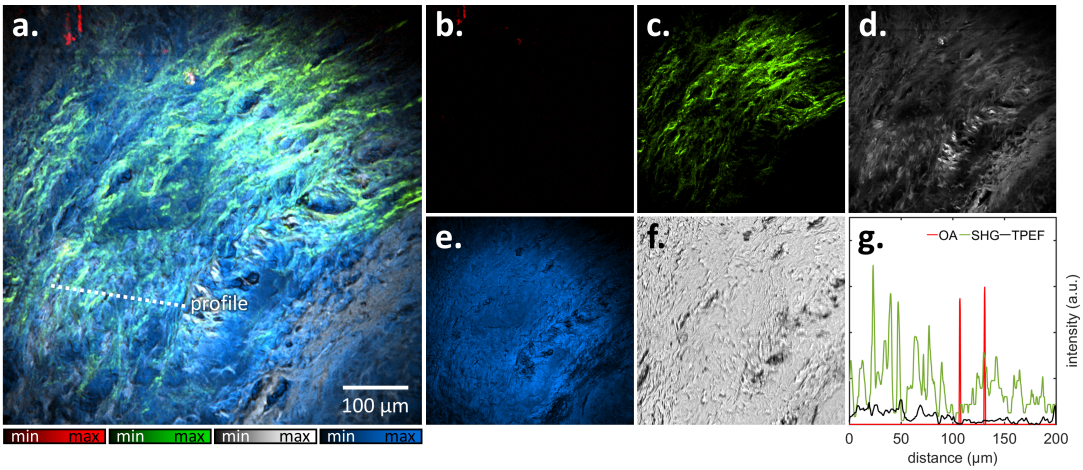

Figure 5.20: Multi-modal microscopy of an unstained human carotid atheroma slice at the shoulder region. (a) Merged depiction of OA, SHG, THG, and 2PEF indicated an unharmed connective tissue, an inclusions- and fissure-free morphology, and nearly no embedded blood residues. Separate depiction of **(b)** OA, **(c)** SHG, **(d)** 2PEF, **(e)** THG, and **(f)** BF. **(g)** Profiles of OA, SHG, and 2PEF along the dashed line in (a) revealed an undisturbed band of collagen with two isolated RBCs. (Adapted from [189])

Fig. 5.20 shows the multi-modal microscopy image obtained at ROI 1 located within the shoulder region close to the former lumen. The overlay of the multi-modal examinations (see Fig. 5.20a) as well as separate depictions (see Fig. 5.20b-f) of the modalities OA, SHG, 2PEF, THG, and BF, revealed a connective tissue network of unfractured fibrillar collagen and elastin ribbons. Further, no blood embeddings or other inclusions of more than tens of micrometer were visible. The profiles of moieties sensed by OA, SHG, and 2PEF along the dashed line shown in (a) are plotted in Fig. 5.20g. They confirmed no congruence of blood embeddings and connective tissue in this ROI but revealed a collagen band of minimum 200 µm width containing individual collagen fibers of 2-10 µm diameter.
The multi-modal microscopy image of ROI 2 being at the cap region is depicted in Fig. 5.21. As before, Fig. 5.21a shows the merged overlay and Fig. 5.21b-f the depictions of the modalities separately. ROI 2 exhibited a spatial pattern of embedded blood residues coarsely alternating with components of the connective tissue. Further, the tissue morphology was characterized by slight disturbances, fissures, and inclusions of maximum 100 µm size. The profile analysis (see Fig. 5.21g) along the dashed line in (a) indicated a widening of intact collagen bands to form gaps of 80–100 µm in which blood residues were incorporated.

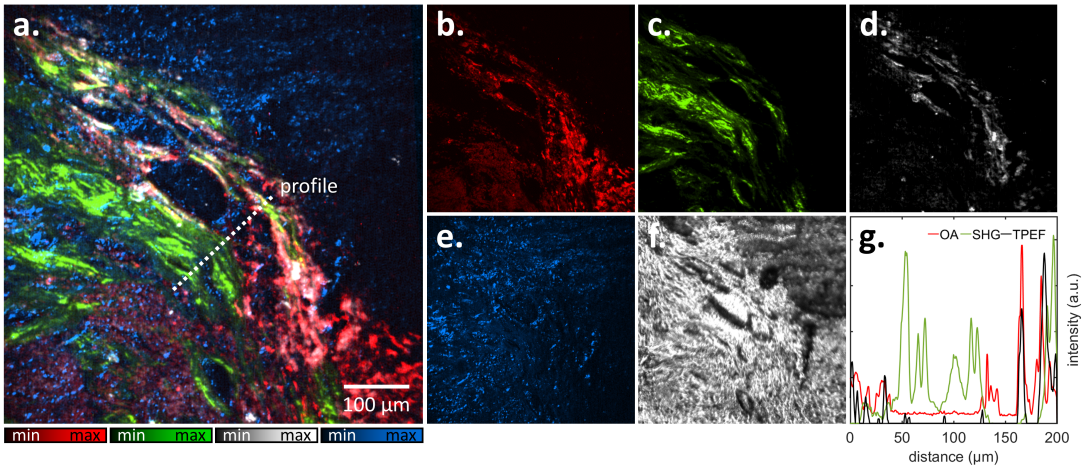

Figure 5.21: Multi-modal microscopy of an unstained human carotid atheroma slice at the cap region. **(a)** Merged depiction of OA, SHG, THG, and 2PEF presented a coarse interleaving pattern of blood residues and bands of connective tissue. Separate depiction of **(b)** OA, **(c)** SHG, **(d)** 2PEF, **(e)** THG, and **(f)** BF. **(g)** Profiles of OA, SHG, and 2PEF along the dashed line in (a) confirmed a coarse interruption of collagen bands by blood embeddings. (Adapted from [189])

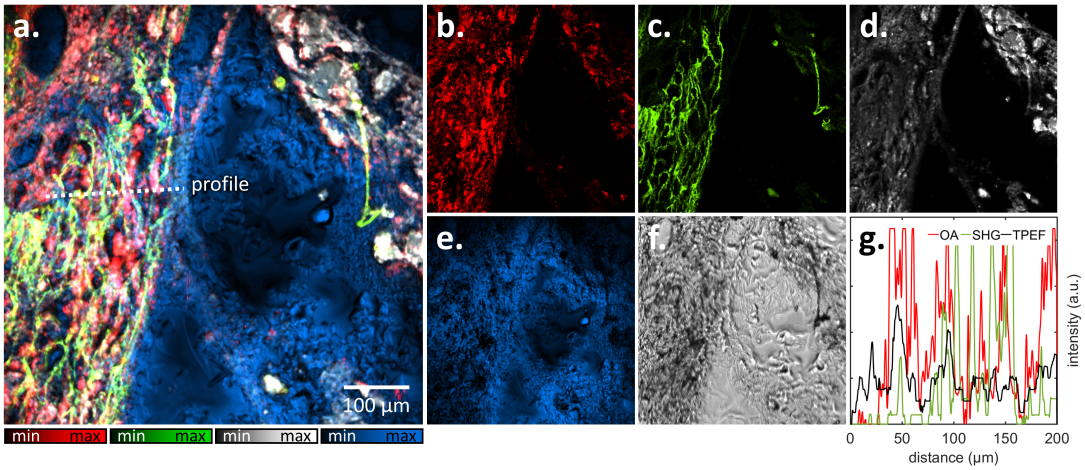

Figure 5.22: Multi-modal microscopy of an unstained human carotid atheroma slice at the necrotic core. **(a)** Merged depiction of OA, SHG, THG, and 2PEF indicated a fine interleaving of collagen fibers with blood residues. Separate depiction of **(b)** OA, **(c)** SHG, **(d)** 2PEF, **(e)** THG, and **(f)** BF. **(g)** Profiles of OA, SHG, and 2PEF along the dashed line in (a) showed a fine intertwined structure of single collagen fibers and blood embeddings. (Adapted from [189])

Fig. 5.22 depicts analogously the multi-modal image of ROI 3 placed in the necrotic core. The overlay in Fig. 5.22a and the individual modalities shown in Fig. 5.22b-f illustrated a fine interleaving of clustered blood embeddings with isolated and split collagen fibrils. Furthermore, the tissue appeared strongly degraded with circular structures with no OA signal, which might constitute low-density lipoproteins and foam

cells[99] being typically found in the lipid core. Such findings were also observable in the profile analysis shown in Fig. 5.22g along the line in (a). The obtained interleaving occurred on a spatial scale of ∼8-15 µm, which was significantly finer than the one seen in ROI 2. However the individual diameters of the collagen fibrils remained unchanged compared to the other regions ROI 1 and ROI 2 and, thus, could be assumed as unharmed but isolated to individual strands due to incorporated blood residues.

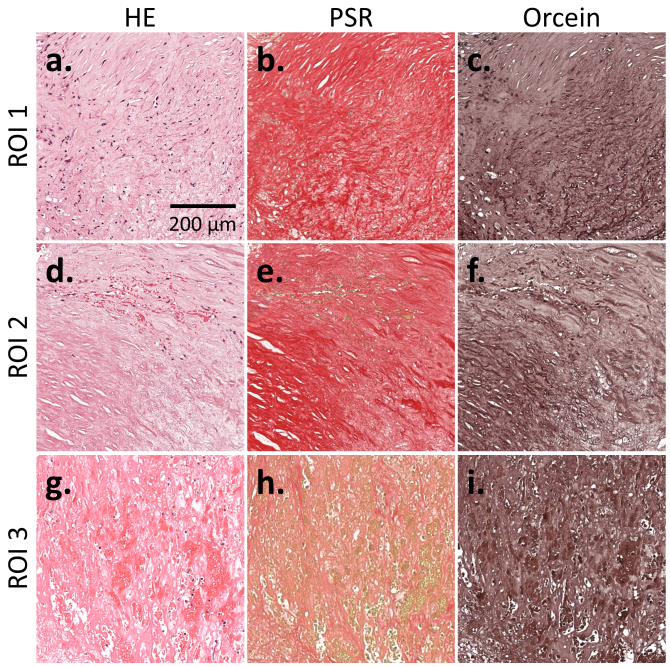

Figure 5.23: Histopathological images of human carotid atheromas based on staining of regions approximately at the same positions as the ones imaged with HyMPSOM. ROI 1 imaged using **(a)** HE staining of cell nuclei (blue), cytoplasm (pink) and RBCs (dark red); **(b)**PSR staining of collagen; and **(c)** Orcein staining of elastin. Analogous depiction of **(d-f)** ROI 2 and **(g-i)** ROI 3. (Adapted from [189])

Next, slices of the identical specimen adjacent to the unstained one imaged with HyMPSOM were stained and imaged by standard histopathological procedures. Fig. 5.22 depicts the yielded images for ROIs approximating the same locations as imaged with HyMPSOM at the shoulder (ROI 1; (a-c)), the cap (ROI 2; (d-f)), and the necrotic core (ROI 3; (g-i)) by applying H&E staining (first column) for cell nuclei, cytoplasm, and RBCs, PSR staining (second column) for collagen, and Orcein staining (third column) for elastin. The shoulder region was characterized by sparsely embedded isolated RBCs (see Fig. 5.22a) as well as unharmed and strong collagen and elastin networks (see Fig. 5.22b and c). The cap region revealed larger blood incorporation (see Fig. 5.22d) and intermediately widened connective tissue (see Fig. 5.22e and f). The necrotic core

[99] Both low-density lipoproteins (LDL) and foam cells have been shown to generate 2PEF and THG signals [219].

exhibited widely spread blood embeddings in coagulated aggregates (see Fig. 5.22g) as well as a fine subdivided and disturbed connective tissue (see Fig. 5.22h and i). This histopathological assessment of the identical specimen confirmed the findings obtained by HyMPSOM imaging visualizing the individual tissue components in the three selected regions. However, as each staining required its own tissue slice, no co-registered overlay was possible and, thus, prevented analysis of mutual interactions on the microscale.

Conclusion

In this project, we investigated possible applications of HyMPSOM for histopathological assessments of human tissue slices. We studied herein a human carotid atheroma, the formation, progression, and possible rupture of which is severe for the underlying disease of atherosclerosis. For that, tissue specimens acquired from a patient were investigated using both label-free HyMPSOM and staining-based histopathological microscopy. We could show that label-free multi-modal microscopy was able to extract similar information content as the staining reference method regarding the microscopic condition of embedded blood residues, the connective tissue of collagen and elastin, and the overall tissue morphology including possible fissures in specific regions outlined from their topological characteristics. These tissue parameters are crucial to not only assess the severity of the underlying disease but also to predict future occurrences like relapses. Whereas staining-based microscopy requires for each tissue component of interest one tissue slice, label-free imaging carried out with HyMPSOM was able to extract the information of the identical unstained tissue slice. On the one hand, this reduced the number of procedural steps and their associated costs. On the other hand, the extracted information was precisely co-registered as it was obtained from the identical sample. This allowed HyMPSOM to study the fine microscopical interaction among the components. In this regard, we could show a mutual interaction between the connective tissue and blood incorporations. As the latter defines the structural integrity of the arterial walls and thereby determines the vulnerability, our data suggests that blood embeddings in the form of intraplaque hemorrhages, inclusions of RBCs, or formation of neovessels have a critical impact on the outcome of the disease. Such new insights could represent a novel approach for targeted therapy. Especially studies comparing patients of different degrees of severity could reveal the sequence of microstructural tissue degradation. In other words, such studies could target the unaddressed question, whether the connective tissue is disrupted first, allowing blood to invade, or vice versa. Further, microscopic investigation of human carotid atheroma could be linked to *in vivo* intravascular catheter-based imaging and *in vivo* macroscopic imaging techniques. As HyMPSOM extracts the herein explored information using label-free imaging modalities, such modalities could potentially be also applied

to humans. Hence, observations carried out on the microscale using HyMPSOM could be straightforwardly transferred to macroscopic examinations based on the identical imaging modality. Generating thereby a portfolio of interconnected multi-system findings could potentially constitute a novel approach for avoiding surgical examinations for diagnosing and staging patients with atherosclerosis.
Within this project, HyMPSOM was able to extract biomedical information in a complete label-free manner. The data shows that HyMPSOM competes with standard performed histopathological assessments and surpasses them in obtaining the interplay of a variety of tissue components on the microscale. This project demonstrates how multi-modal microscopy could potentially become a powerful tool for medicine regarding diagnosis and therapy.

5.4 Technical extensions of HyMPSOM

The following chapters provide an overview of technical extensions of HyMPSOM beyond its standard way of operation (see Section 4) as used for carrying out the key imaging projects presented previously. In this regard, the versatile design, control, and data acquisition of the HyMPSOM framework allowed to explore alternative possibilities of performing optoacoustic microscopy or optoacoustic sensing on the microscale.

5.4.1 Frequency-domain optoacoustic microscopy

In this project, a novel approach for operating optoacoustic microscopy in the frequency domain was elaborated. In comparison to time-domain optoacoustic microscopy based on laser excitation pulses, the herein developed frequency-domain approach utilized frequency-modulated CW lasers and achieved comparable imaging performances[100].

Introduction

The majority of optoacoustic imaging devices operate in the time domain and are based on laser excitation pulses ranging from 100 ps - 100 ns [26, 221, 222]. As explored in Section 3.3, such short laser pulses generate optoacoustic signals in the form of broadband ultrasound waves which are subsequently detected by a time-dependent acquisition [223, 224]. Although the time domain constitutes the standard way of implementing optoacoustics, it requires expensive and complex laser technologies, which are limited in their wavelength availability as well as simultaneous multiwavelength delivery. Furthermore, recording the data time-dependently necessitates elaborate acquisition procedures and leads to large datasets (see Section 4.2.4). In analogy to

[100] This project was conducted in equal contribution with Dr. Stephan Kellnberger, Dr. Dominik Soliman, and Dr. George Tserevelakis, who conceived the underlying approach for FDOM. The results of this project are published in [220] and elaborated in detail in [23].

a huge variety of imaging technologies, which initially have been developed in the time domain and then transferred to the frequency domain [215, 225, 226], a similar approach for optoacoustics could overcome the above mentioned restrictions. Contrarily to time-domain optoacoustic microscopy (TDOM), frequency-domain optoacoustic microscopy (FDOM) is based on exciting the specimen with intensity-modulated continuous wave (CW) lasers with time-independent signal detection. FDOM facilitates thereby higher excitation rates than TDOM and frequency-encoded multiwavelength examination using cost-effective CW lasers, which are available throughout the electromagnetic spectrum. While first attempts of FDOM showed its feasibility of sensing oxygenation in vasculature [227], they operated at a single modulation frequency and, thus, did not capture all spatial frequencies of the specimen [228]. Furthermore, chirp modulation was also considered for multiwavelength FDOM implementation, but was based on recording time-of-flight values by cross-correlating the excitation and detection waves in the time domain [229–233]. Although these first approaches for realizing FDOM proofed the basic principle, they did not achieve high fidelity as required for constituting a sophisticated microscopy modality.
In here, we developed a novel FDOM technique by exciting the sample with CW lasers modulated at multiple discrete frequencies and by detecting optoacoustic signals via time-independent homodyne demodulation to acquire their amplitude and phase. We applied FDOM using modulation frequencies ranging from 5 to 50 MHz to characterize the relationship between modulation frequencies and image quality as well as SNR. Further, our FDOM approach enabled simultaneous spectral examination by loading multiple wavelengths on distinct modulation frequencies, sensing of microcirculatory blood flow *in vivo* by reading Doppler-signals, and integration into the HyMPSOM imaging system for multi-modal microscopy.

Materials and methods

FDOM constitutes an additional sub-system integrated into HyMPSOM, the general design of which is described in Section 4.2.3 and shown in Appendices: Photographs of the optical setup.
Fig. 5.24a schematically depicts the FDOM sub-system excluding all other beam paths of HyMPSOM. The excitations for FDOM were achieved by two CW diode lasers (A350, Omicron-Laserage, Rodgau, Germany) emitting at 488 nm and 808 nm, which were intensity-modulated by two function generators (DG5252, Rigol, Beijing, China) following a sinusoidal waveform of 5-50 MHz frequency. Whereas the free-space emitted beam of the 488 nm-laser was spatially filtered by a pinhole, the 808 nm-laser is fiber-coupled and does not allow for spatial filtering due to its low power. The beam path of the 808 nm-laser was first merged with the path of the multi-photon laser using a dichroic mirror (DMSP1000, Thorlabs), and subsequently combined with

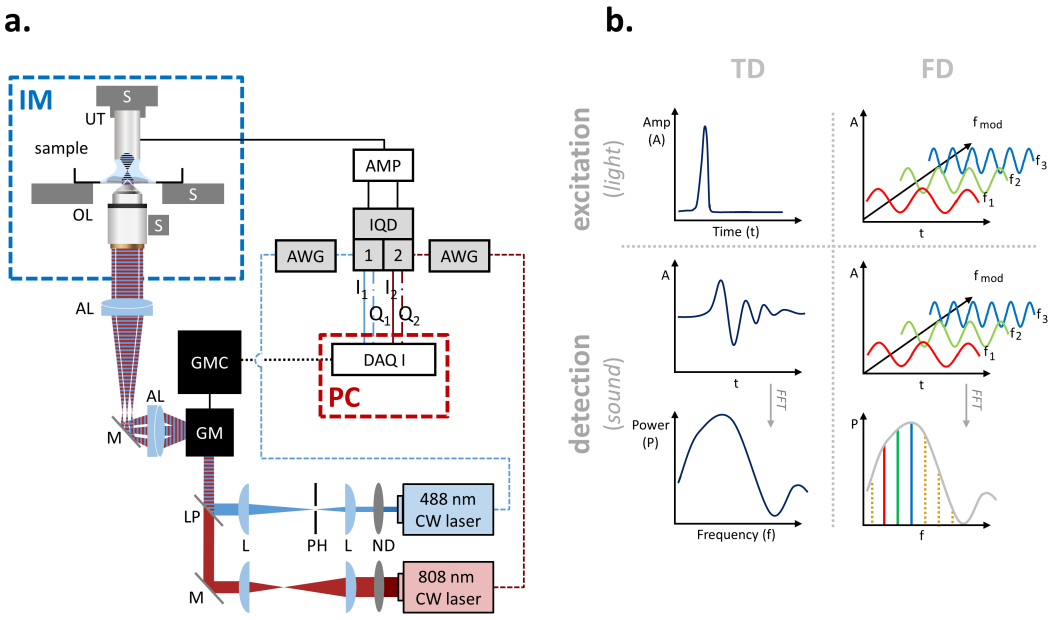

Figure 5.24: Schematic depiction of the FDOM sub-system of HyMPSOM. (a) The FDOM system was based on raster-scanning two optically focused laser excitations at 488 nm and 808 nm across a sample placed in an inverted microscope using galvanometric mirrors. The lasers were frequency-modulated by two separate function generators, which also served as the local oscillator signals for two IQ-demodulators ('1' and '2') reading the OA signals after amplification. Abbreviations: AL: achromatic doublet lens; AMP: low noise amplifier; AWG: arbitrary waveform function generator; DAQ: data acquisition card; GM: galvanometric mirror scanner; GMC: GM controller; IM: inverted microscope; IQD: IQ-demodulator; L: plan-convex lens; M: dielectric mirror; ND: neutral density filter; OL: microscope objective lens; PH: pinhole; S: high-precision motorized stage; UT: ultrasound transducer. **(b)** Representative comparison of the principle of time-domain (TD) optoacoustic microscopy using laser pulses and frequency-domain (FD) optoacoustic microscopy using sinusoidal modulated laser excitation. (Adapted from [220])

the 488 nm-laser beam path using another dichroic mirror (DMLP650, Thorlabs). By that, the two integrated CW lasers for FDOM were co-aligned to the existing lasers in HyMPSOM and followed the identical path over the scanning unit of galvanometric mirrors (see Section 4.2 and Fig. 4.1). The recorded optoacoustic signals were demodulated in a dual homodyne-based IQ-demodulator device (AD8333, Analog Devices, Norwood, MA, USA; RF frequency range, DC to 50 MHz), which was also fed by a local oscillator signal provided from the function generators as a reference signal. The thereby yielded in-phase components I and quadrature component Q were recorded by the 16-bit data acquisition card (i.e. DAQ2 in Section 4.2.4), low-pass filtered by 90 kHz, and converted to amplitude $A = \sqrt{I^2 + Q^2}$ and phase $\Phi = tan^{-1}\left(Q/I\right)$ values. Single-frequency imaging was performed using laser-scanning and image-averaging as described in Section 2.4.3 of $300 \cdot 300$ pixels in ~0.6 s leading to a pixel dwell time of

∼4.2 µs, which was adjusted to the output filter of the demodulation. Multi-frequency imaging was carried out by sequentially repeating this procedure at distinct modulation frequencies. Simultaneous multi-wavelength imaging was enabled by loading the two wavelength onto different frequencies and by using two separate IQ demodulators. Fig. 5.24b schematically illustrates the operation principle of time-domain (TD) and frequency-domain (FD) optoacoustic microscopy. Whereas in TDOM, an ultra-short laser pulse generates a broadband ultrasound wave, FDOM excited the sample with a sinusoidal modulated laser intensity and, thus, generated analogously modulated ultrasound waves carrying only the excitation frequency[101]. The recorded data was arranged for a frequency-space-representation (FSR) in a 3D matrix of $S(x, y, f)$, with x and y being the spatial coordinates and f being a vector containing amplitude and phase of the used modulation frequency. For 2D reconstruction, each data set $S(x, y, f_n)$ recorded at frequency i was projected onto a 2D map $R_{f_i}(x, y)$ whereas the entire FDOM image represented their summation as $R_{all} = (x, y, \sum_{i=1}^{n} f)$. For 3D rendering, a time-space-representation (TSR) was obtained as $S(x, y, f) = \mathcal{F}^{-1}\Big(S(x, y, t)\Big)$, in which t contained the time-dependent signal being the inverse Fourier transform of the FDOM signals.
The FDOM system was first characterized by imaging black sutures and was compared to analogously performed imaging using TDOM as described in Section 4.2.2. Next, FDOM was applied for studying zebrafish larvae and mice *in vivo*. For Doppler-flow measurements, the transducer was tilted to an angle of ∼55° and read out by the built-in spectrum analyzer capability of a high-frequency lock-in amplifier (UFHLI, Zurich Instruments, Zurich, Switzerland). The micro-Doppler (µDoppler) signals were calibrated using a suspension of carbon-nano-particles of 2-12 µm size (∼20%$^{\text{vol.}}$) mixed with sodium polytungstate (Sigma-Aldrich, Germany) to prevent sedimentation and TWEEN^{TM} 20 (Sigma-Aldrich) to prevent aggregation. The suspension was flushed by a syringe pump (540060, TSE systems, Germany) through a microfluidic flow chamber (01-0175-0138-02, microfluidic ChipShop, Germany) of 200 µm thickness and 1 mm width covered with a 140 µm lid of the chip material TOPAS$^{(\text{TM})}$.

Results

First, we investigated the image formation of the developed FDOM system by imaging two intertwined sutures of 50 µm diameter.
Fig. 5.25a shows the yielded images as FSR performed at modulation frequencies ranging from 10 to 40 MHz. The single-color images demonstrated that each modulation frequency was associated with capturing a distinct pattern of spatial frequencies of the specimen. The superimposing of all separately-performed single-frequency scans is shown as a multi-color image (see Fig. 5.25b) and a corresponding gray-scale depiction

[101] For dynamic samples such as in-flow specimens like particles and cells, the detected frequencies in FDOM were shifted to lower or higher frequencies due to the Doppler effect, depending on the flow direction.

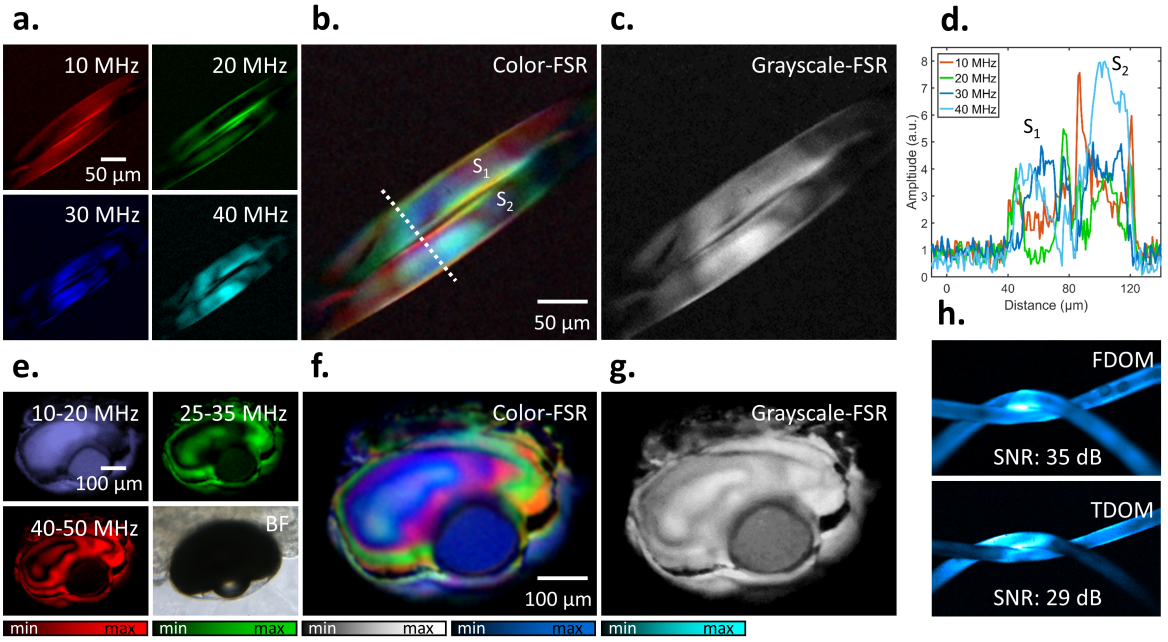

Figure 5.25: Characterization of the FDOM system by imaging a suture phantom and an zebrafish eye *ex vivo* in a single-wavelength approach. **(a)** Singe-frequency scans of two intertwined 50 µm sutures exhibited distinct spatial patterns. Superimposing the individual images as **(b)** the color-frequency-space-representation (FSR) and **(c)** the grayscale-FSR showcased complementary signal patterns. **(d)** Signal profiles along the dashed line in (b) comparing contrast revealed by the applied modulation frequencies. **(e)** *Ex vivo* zebrafish larva eye imaged in frequency bands in frequency steps of 5 MHz and exemplary brightfield image of a zebrafish eye showed analogous signal patterns. **(f)** The color-FSR illustrated the contribution of each frequency band and **(g)** the grayscale-FSR validated homogeneous imaging at summation of all frequencies. **(h)** SNR comparison between TDOM and FDOM carried out with similar experimental conditions. (Adapted from [220])

(see Fig. 5.25c). In here, complementary signal patterns could be observed that, thus, led to a significantly higher representation quality of the sutures than the individual single-frequency scans. Fig. 5.25d plots the signal profiles of the individual frequency scans along the dashed line indicated in the multi-color image and revealed how the different representations of the two sutures depend on the modulation frequency. Further, we analogously measured the eye of a 5 dpf zebrafish larva. Fig. 5.25e shows images reconstructed by combining the data captured at modulation frequencies of 10, 15, and 20 MHz, of 25, 30, and 35 MHz, and of 40, 45, and 50 MHz, respectively. Similarly to the suture experiment, the image of each frequency band was associated with specific spatial frequency pattern, whereas the multi-color (see Fig. 5.25f) as well as the gray-scale superposition (see Fig. 5.25g) yielded a high-fidelity depiction of the entire eye. Both, the suture and the zebrafish eye investigation rendered the need of scanning specimens with FDOM at multiple modulation frequencies to capture all contained

spatial frequencies properly. Based on this, we compared the achieved SNR between FDOM and TDOM by imaging intertwined sutures of 40 µm diameter as depicted in Fig. 5.25h. The FDOM scan was carried out with the 488 nm laser sequentially modulated from 10 to 50 MHz with a fluence of ∼100 W·cm^{-2} at the sample position. The TDOM image was performed as described in Section 4.2.2 with ∼10 nJ/pulse at the sample position. Both measurements utilized the identical transducer and alignment setting, and were set to the identical acquisition time. We obtained herein a SNR of ∼35 dB for FDOM and ∼29 dB for TDOM. The SNR difference of TDOM being ∼6 dB lower than the one from FDOM at the applied measurement settings matched the theoretical estimation as described in detail in [220].

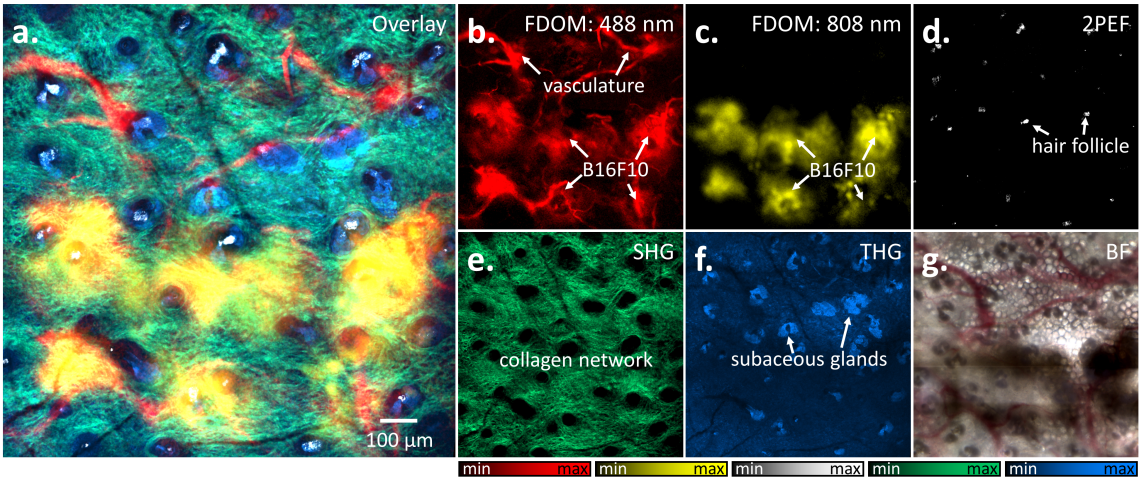

Figure 5.26: Dual-wavelength FDOM and MPM microscopy of an mouse ear *in vivo* in which B16F10 melanoma cells were injected. **(a)** Overlay of the performed modalities. FDOM at **(b)** 488 nm shows vasculature and melanoma cells and at **(c)** only melanoma cells. **(d)** 2PEF reveals hair follicles, **(e)** SHG shows the extracellular collagen network, and **(f)** THG senses tissue morphology and sebaceous glands. **(g)** Co-registered bright-field validates these findings. (Adapted from [220])

Next, we opted for applying simultaneous dual-wavelength FDOM imaging along with the multi-photon modalities integrated in HyMPSOM (see Section 4.2.1) to *in vivo* mouse ears in which we injected B16F10 murine metastatic melanoma cells. For that, the 488 nm and the 808 nm laser were loaded on different modulation frequencies, which then sequentially imaged the specimen with frequencies from 10 to 50 Mhz in 5 MHz steps[102]. Whereas the signals of the B16F10 cells were expected to appear at both examination wavelengths due to the flat absorption spectrum of the contained melanin [234] (see Section 2.3.3), the signals of the vasculature was expected to show up only at

[102]In the first scan, the 488 nm laser was modulated at 10 MHz and the 808 nm laser at 50 MHz. During the following imaging, the modulation of the 488 nm laser was stepwise increased and of the 808 nm laser decreased by 5 MHz. During this sequence, it was ensured that at no image both lasers were modulated with the same frequency simultaneously.

488 nm due to weak absorption of hemoglobin in the near-infrared range. Fig. 5.26a-g show a co-registered and stitched overlay of the acquired dual-wavelength FDOM at (b) 488 nm and at (c) 808 nm, (d) 2PEF, (e) SHG, and (f) THG images across a FOV of 1200 · 1220 µm^2. SHG and THG were performed according to Section 4.2.1. The overlay demonstrated highly compatible contrast among the modalities by revealing the microvasculature (488-nm-FDOM), the injected melanoma cells (488-nm- and 808-nm-FDOM), hair follicles (2PEF), the collagen network (SHG), and sebaceous glands and keratinocytes (THG) of the mouse ear. Fig. 5.26g shows the associated brightfield examination of the identical FOV and validated the findings.

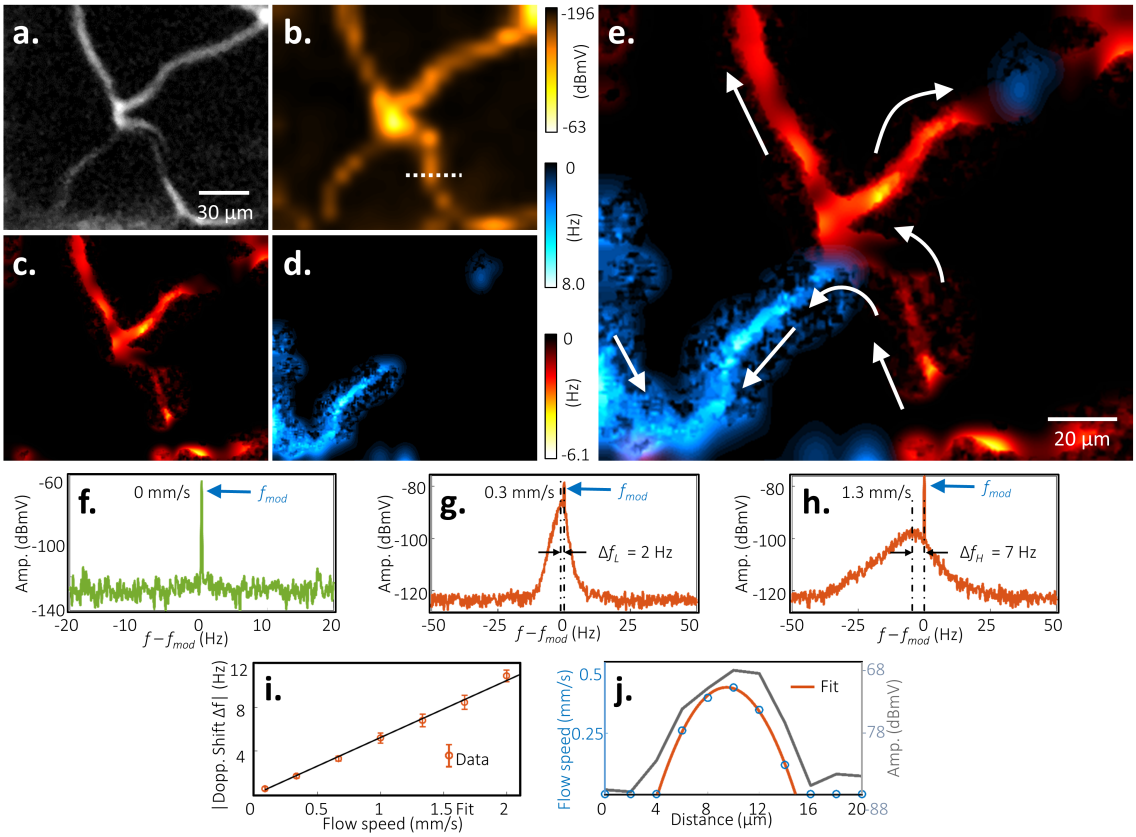

Figure 5.27: Optoacoustic microcirculatory blood flow imaging via µDoppler-FDOM. **(a)** Multi-frequency image of mouse ear *in vivo* microvasculature. **(b)** µDoppler-FDOM image recorded at 42 MHz is congruent to the high-fidelity image (a). Separated **(c)** negative and **(d)** positive µDoppler-maps blended on the high-fidelity image (a). **(e)** Merged negative and positive µDoppler-maps enable to following blood flow directions as indicated by white arrows. Calibration of the µDoppler-signals using carbon particles flowing through a microfluidic chip at **(f)** 0 mm/s; **(g)** 0.3 mm/s, and **(h)** 1.3 mm/s. **(i)** Linear dependence of the detected µDoppler-shifts to the applied flow speed. **(j)** Analysis of the flow profile in the vasculature along the dashed line in (b). The parabolic fit indicates a maximum flow speed of 0.44 mm/s. (Adapted from [220])

Lastly, we aimed for recording flow-maps by detecting µDoppler-effects as described previously. We investigated the microvascular flow of an *in vivo* mouse ear. Fig. 5.27a shows a high-fidelity image of a FOV of 160 · 160 µm^2 recorded at 488 nm using mul-

tiple modulation frequencies analogously to Fig. 5.26b. Subsequently, we performed µDoppler imaging at 42 MHz modulation across the identical FOV. The image reconstructed from the peak amplitude of the µDoppler data (see Fig. 5.27b) matched the high-resolution multi-frequency image and, thus, validated the association between detected Doppler shifts and the vasculature. Color-coding the detected µDoppler shifts in red (lower frequencies; RBC movement away from the transducer) and blue (higher frequencies; RBC movement towards the transducer) and subsequent blending onto the high-fidelity image, as shown in Fig. 5.27c and d, demonstrated the direction sensitivity of µDoppler-FDOM. In Fig. 5.27e, the combined red and blue shift-images enabled thus precise outlining the vasculature structure. Next, we calibrated the µDoppler-FDOM recordings by flushing carbon particles through a microfluidic channel at flow speeds between 0.1 and 2 mm/s and interrogating their FDOM signals analogously using the 488 nm laser at 15 MHz modulation. The calibration measurements were performed by integrating ∼8 s of signal acquisition. As shown in Fig. 5.27f-h, the sensed frequency spectra at flow speeds of 0, 0.3, and 1.3 mm/s contained a central peak corresponding to signals generated by non-moving objects. At flow speeds of 0.3 and 1.3 mm/s, µDoppler shifts of Δf_H= 2 Hz and 7 Hz, respectively, along with spectral broadening could be observed. The latter could be explained by the finite size of the transducer, averaging µDoppler shifts, and by particles flowing at different speeds due to the laminar Poiseuille flow profile inside the channel of the chip. Subsequent characterization of flow speeds up to 2 mm/s revealed a linear dependence of the detected Doppler shifts (R^2=0.996) as plotted in Fig. 5.27h and revealed an actual Doppler angle of 58 ±1° of the transducer (see [220] for the mathematical approach). Finally, the µDoppler-FDOM calibration was used to analyze the cross-sectional flow profile across the vessel indicated by the dashed line in Fig. 5.27b. The parabolic curve across the vessel plotted in Fig. 5.27h revealed a maximum flow speed of ∼0.44 mm/s matching typical flow values of microcapillaries.

Conclusion

In this project, we showcased the first FDOM system entirely working in the frequency domain that achieves high-fidelity image quality and sensitivity comparable to TDOM approaches. The developed system is based on cost-effective CW lasers exciting the specimens with a sinusoidal modulation causing optoacoustic signals with identical frequency modulation. The latter are then acquired in a time-independent fashion using signal demodulation. We explored the underlying image formation principle of FDOM and found that each modulation frequency is associated with a distinct pattern of detected spatial information. Hence, the merge of images obtained at multiple modulation frequencies is essential for acquiring high-fidelity microscopy images. With this approach, we achieved imaging speeds and SNRs approximating the ones typically yielded from TDOM. Furthermore, the frequency-domain operation allowed us to

encode excitation wavelength with distinct modulation frequencies, which facilitated simultaneous multiwavelength examination of biological tissue *in vivo*. Further, the FDOM system was combined with the multi-photon modalities equipped in HyMPSOM. Finally, reading time-independent signals at discrete frequencies allowed us to explore Doppler signals for investigating microcirculatory blood flow. For improving the imaging capabilities of the FDOM system, additional laser sources could be integrated for covering other spectral bands of interest for multiwavelength investigation and could be operated simultaneously at separable modulation frequencies. The maximum amount of applicable excitations would only be limited by the maximum permitted exposure (MPE) values for biological tissues. Moreover, the laser excitation source could potentially be modulated with a non-sinusoidal waveform to simultaneously excite several frequencies of optoacoustic signals. Lastly, even more cost-effective excitation sources such as modulatable laser diodes could replace the current CW lasers, which would further decrease the cost, complexity, and size of the system.
FDOM constitutes another sub-system integrated into HyMPSOM. The presented study took advantage of the versatile applicability of HyMPSOM to read optoacoustic signals in microfluidic flow systems, apply multi-photon microscopy, and compare FDOM to the standardly performed TDOM. HyMPSOM therefore allows for elaborating on an entirely novel approach of performing optoacoustic microscopy and achieves conclusive evaluation of the findings. Furthermore, the development of the FDOM subsystem paves the integration of laser diodes for a similar operation mode as explained in detail in Section 5.4.2.

5.4.2 High-speed and frequency-comb optoacoustic microscopy

In this project, laser diodes were investigated towards their applicability for optical-resolution optoacoustic microscopy. The diodes were controlled by a self-designed diode driver, which allowed to perform high-speed optoacoustic microscopy by means of alternating laser excitation (ALEX) and frequency-comb approaches (FComb) for multiwavelength imaging[103].

Introduction

As mentioned previously, time-domain optoacoustic microscopy is typically performed using excitation lasers emitting pulses in the range 100 ps - 100 ns with pulse energies of tens to hundreds of nanojoules per pulse and repetition rates of up to 1 MHz [26, 221, 222]. Suitable laser sources for such pulsed excitation in optoacoustic imaging are mostly based on diode-pumped solid state lasers (DPSS) in combination with dye-units

[103]This project was conducted in equal contribution with Antonios Stylogiannis. In here, Mr. Stylogiannis developed the diode control unit as well as the FComb data analysis. The diode-control was developed before integration into HyMPSOM [222] and the results were in preparation for submission during writing of this thesis [235].

or optical-parametric-oscillators for wavelength tuning [236, 237]. However, these laser technologies are expensive, bulky, as well as complex and, thus, facilitate neither a miniaturization of the entire imaging system nor a cost-effective and straightforward implementation of multiwavelength optoacoustic microscopy (see Section 5.4.1). To overcome these issues, light-emitting diodes (LEDs) have been considered to provide the requested optical excitation [222, 237–242]. Despite their advantages being of small size, low cost, broad wavelength availability, robustness, high power, and high repetition rates, they emit rather long pulses of up to 0.5 µs generated by an emitting area of up to $1 \cdot 1$ mm^2. Hence, LEDs are suitable for macroscopic optoacoustics [237, 240] but do not allow for diffraction-limited focusing as required for OR-OAM. Furthermore, pulsed laser diodes (PLDs) were shown to provide better optical properties for optoacoustic microscopy with shorter pulses and smaller emitting areas [237, 243]. However, PLDs featuring the required performance for optoacoustic signal excitation are typically only available in the near infrared range [237, 244], which thereby limits their application. In contrast to LEDs and PLDs, continuous wave laser diodes (CWLD) are associated with small-sized emitting areas, beam profiles enabling good optical focusing, and a broad wavelength availability from the ultra-violet to the near infrared spectral range [222, 237]. However, the so far achieved low pulse energies in combination with a low repetition rate necessitated heavy averaging and long acquisition times [222, 244–246]. To overcome these issues, a self-designed electrical circuit was developed [222] for overdriving CWLDs by providing ultra-short current pulses. Such overdriven diodes could potentially exceed their nominal characteristics and, thus, could provide optical pulses of high energy, low duration, and good focusability [222].
To test this assumption, we integrated three CWLDs into the HyMPSOM system, each equipped with a custom-built control circuit. We further investigated two operational principles, namely alternating laser excitation (ALEX) and frequency-comb (FComb) signal detection. Regarding the former, ALEX was based on subsequently firing the three diodes upon a trigger signal one after the other. The generated ALEX-signals of the three diodes were separated in the time domain based on a trigger delay among the diodes. Regarding the latter, FComb triggered the diodes in bursts of pulses running at a burst-frequencies distinct for the equipped diodes. The signals were then separated in the frequency domain. Advantages of such frequency-domain signal acquisition and simultaneous multiwavelength examination of specimens is in analogy to frequency-domain optoacoustic microscopy (FDOM) using modulated continuous wave lasers (see Section 5.4.1). However, as the diodes would still operate in a pulsed mode, the SNR was expected significantly higher than the FDOM counterpart of using sinusoidal-modulated CW laser sources. Whereas FDOM data is recorded as time-independent signals and projected in a frequency-space-representation (FSR), FComb acquisition finally would lead to time-dependent signals resembling the recordings of single-pulse optoacoustic microscopy (see Section 3.3 and Section 5.4.1).

Materials and Methods

The integration of three CWLDs for optoacoustic microscopy operating in ALEX- or FComb-mode led to another sub-system of HyMPSOM, the general design of which is described in Section 4.2.3 and shown in Appendices: Photographs of the optical setup.

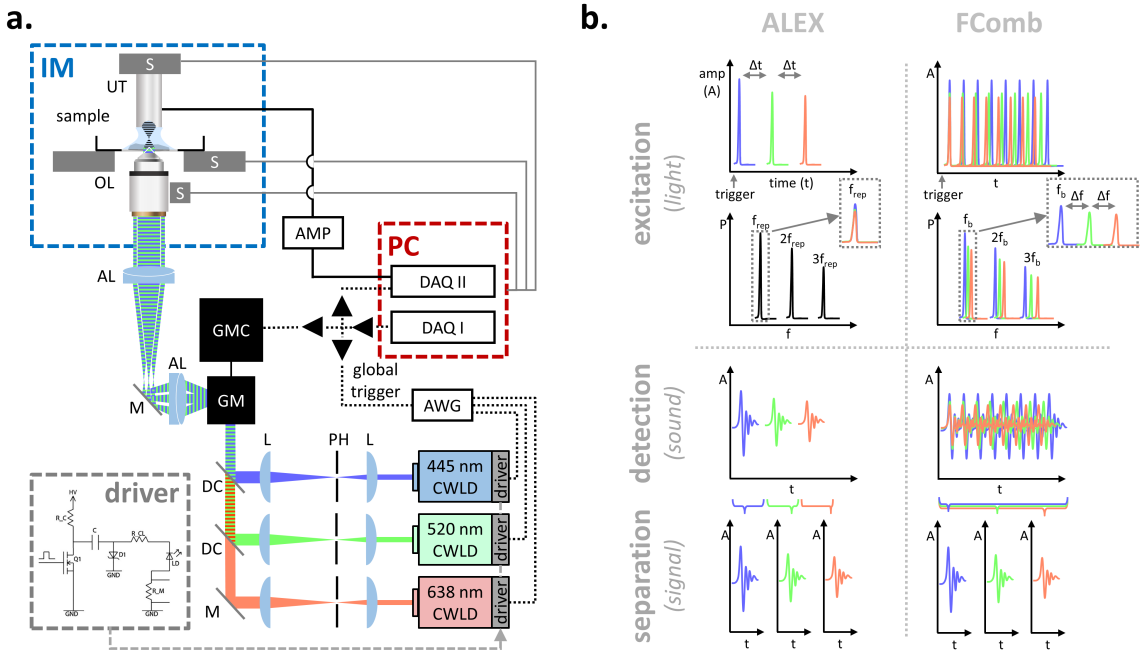

Figure 5.28: Schematic depiction of the CWLD sub-system of HyMPSOM for high-speed ALEX and FComb optoacoustic microscopy. **(a)** The system equips three CWLDs, each of which was controlled by a self-designed electrical circuit driver and received ultrashort trigger signals provided by arbitrary function generators. Abbreviations: AL: achromatic doublet lens; AMP: low noise amplifier; AWG: arbitrary waveform function generator; CWLD: continuous wave laser diode; DAQ: data acquisition card; GM: galvanometric mirror scanner; GMC: GM controller; IM: inverted microscope; L: plan-convex lens; M: dielectric mirror; OL: microscope objective lens; PH: pinhole; S: high-precision motorized stage; UT: ultrasound transducer. **(b)** Principle of using the CWLD for alternating laser excitation (ALEX) or Frequency-Comb (FComb) optoacoustic microscopy. (Driver inset adapted from [222])

As shown in Fig. 5.28a, three CWLDs were integrated into HyMPSOM, each of which following the identical electrical as well as optical settings. All CWLDs were driven by a self-designed electrical circuit (see inset in Fig. 5.28a) as comprehensively described in [222]. In short, the capacitor C was first charged at ~300 V connected to the $R_C - C - D_1$ circuit, and then discharged over the laser diode upon receiving an ultrashort trigger signal on the MOSFET Q_1. R_{CL} served in here to limit the current, which was controlled through the applied high voltage. The rise and fall time of the achieved current pulse was determined by the turn-on speed of MOSFET Q_1 and the time constant of the $R_{CL} - C - LD - Q_1$, respectively. This driver finally achieved

current pulses shorter than ∼10 ns of up to ∼50-60 A at repetition rates surpassing ∼500 kHz. Such drivers were finally controlling each a CWLD module (PD-01236, 6W, 445 nm; PD-01289, 1W, 520 nm; PD-01229, 700 mW, 638 nm, Lasertack, Germany) being hold by a kinematic platform (KM100B, Thorlabs) for beam adjustment. The emitted beam of each diode was guided through a telescopic arrangement of plan-convex lenses equipped with a 50 µm high-power pinhole for collimation, beam cleaning, and size adjustment for the subsequently following scanning unit of HyMPSOM (see Section 4.2). The merging of the beams was achieved by longpass dichroic mirrors (DMLP490R and DMLP550R, Thorlabs) before encountering the galvo mirrors (see Fig. 5.28a). All three diodes were charged by a high-voltage generator to ∼300 V (EA-3050B, EA, Germany) and cooled by a heat sink combined with an attached fan. The temperature was monitored by a self-programmed Arduino platform and always kept below 60 °C. The trigger-TTL-signals for the CWLDs were provided by two electrically synchronized high-speed arbitrary waveform function generators (AWG) (33622A, Keysight Technologies, USA), which themselves receive the global trigger signal as explained in detail in Section 4.2.4. Using two AWGs being triggered by the global trigger signal for data acquisition but operate independently, allowed to carry out multiwavelength optoacoustic microscopy based on two approaches, namely ALEX and FComb as schematically illustrated in Fig. 5.28b. ALEX led to firing all diodes sequentially one after another upon each global trigger signal. The delay between the three timepoints of the actual laser pulses was set to Δt = 200 ns. The frequency-power-spectrum of the optical excitation contained the underlying global trigger signal repetition rate f_{rep} as well as higher harmonic occurrences. Due to f_{rep} ∼ 100-200 kHz, the data was acquired exclusively at f_{rep} and contained time-shifted OA signals corresponding to the excitation of the three CWLDs. Based on the applied Δt in their time-point of emission, the OA signals could then be separated from each other by time-windowing. FComb drove the CWLDs in bursts of 100 trigger signals upon receiving a global trigger signal (i.e. 1 kHz) at a burst repetition rate of $f_{b+n\cdot\Delta f}$, in which f_b was set to 1 MHz, Δf to 4 kHz, and n is 0, 1, or 2 for the respective diodes. By that, every 1 ms the CWLDs sent out 100 pulses at 1000 kHz for the 445 nm diode, at 1004 kHz for the 520 nm diode, and at 1008 kHz for the 638 nm diode. Hence, the frequency-power-spectrum contained three frequency combs, in which their respective peak locations deviate at increasing frequency harmonics. Upon each global trigger signal, a time-window was acquired that captured the entire bursts of OA signals, which were then separated in the frequency domain based on their distinct burst repetition rate.

For appropriate comparison between ALEX and FComb, the measurement time and averaging was set equally. Whereas ALEX measurements were performed at a global trigger signal repetition rate of 100 kHz and an averaging of 500, FComb measurements used a global trigger signal repetition rate of 1 kHz, a burst averaging of 5, and 100 pulses per burst. This led for both approaches to a pixel dwell time of 5 ms with 500 pulses being used for imaging[104].

Results

Since the attempt to overdrive CWLDs in a pulsed mode is beyond their intended way of operation, we first characterized the performance of the CWLDs for both the ALEX and the FComb approach. As each CWLD driver powered the diodes with ultra-short electrical pulses, electrical cross-talk among the diodes could not be excluded. For that, all CWLDs were operating simultaneously during the following characterization according to the operation principle (i.e. ALEX or FComb) as schematically shown in Fig. 5.28b.
Fig. 5.29a-c depicts the optical pulses of the three CWLDs triggered using the ALEX approach with a trigger-delay among the diodes of Δt=200 ns. The optical pulses were recorded with an averaging of 10^4 using the ultra-fast metal-semiconductor-metal photodetector (G4176-03, Hamamatsu; response time: 30 ps) as described in Section 4.2.3. The trigger signal of 16 ns provided by the arbitrary function generators led to optical pulses of 7.89 ns (blue; R^2=0.97), 9.43 ns (green; R^2=0.92), and 9.50 ns (red; R^2=0.94). Furthermore, no after-pulse caused by electric coupling or cross-triggering was observed. The pulse energies as shown in Fig. 5.29d-f further fluctuated with a standard deviation of 2.3% (blue), 3.1% (green), and 3.2% (red). The pulse energies slightly increased over the first ∼100 pulses (see e.g. Fig. 5.29d-f), which might be due to reaching a steady-state operation temperature. The achieved pulse energies at the sample position were characterized by an optical powermeter (S175C and PM100D, Thorlabs) to be 26 nJ/pulse, 18 nJ/pulse, and 11 nJ/pulse at 100 kHz and 300 V high-voltage supply for the blue, green, and red CWLD, respectively. The actual emitted wavelength depicted in Fig. 5.29g-i of the three CWLDs was determined by an optical spectrometer (QWave, rgb photonics) to 440.9 nm at a line width of 1.87 nm (blue; R^2=0.99), 513.5 nm at a line width of 4.00 nm (green; R^2=0.98), and 635.6 nm at a line width of 1.92 nm (red; R^2=0.98), respectively. Analogous characterization using the FComb approach was in very good agreement and exhibited deviations below ∼5% with respect to the above mentioned values.

[104] ALEX employed averaging of 500 signals separately recorded for each pixel; FComb recorded 5 bursts of 100 pulses for each pixel, averaged the bursts first, and applied then frequency-comb analysis. The averaging of 5 bursts was required to ensure proper signal-pixel-assignment and to reduce uptake of electrical coupling noise.

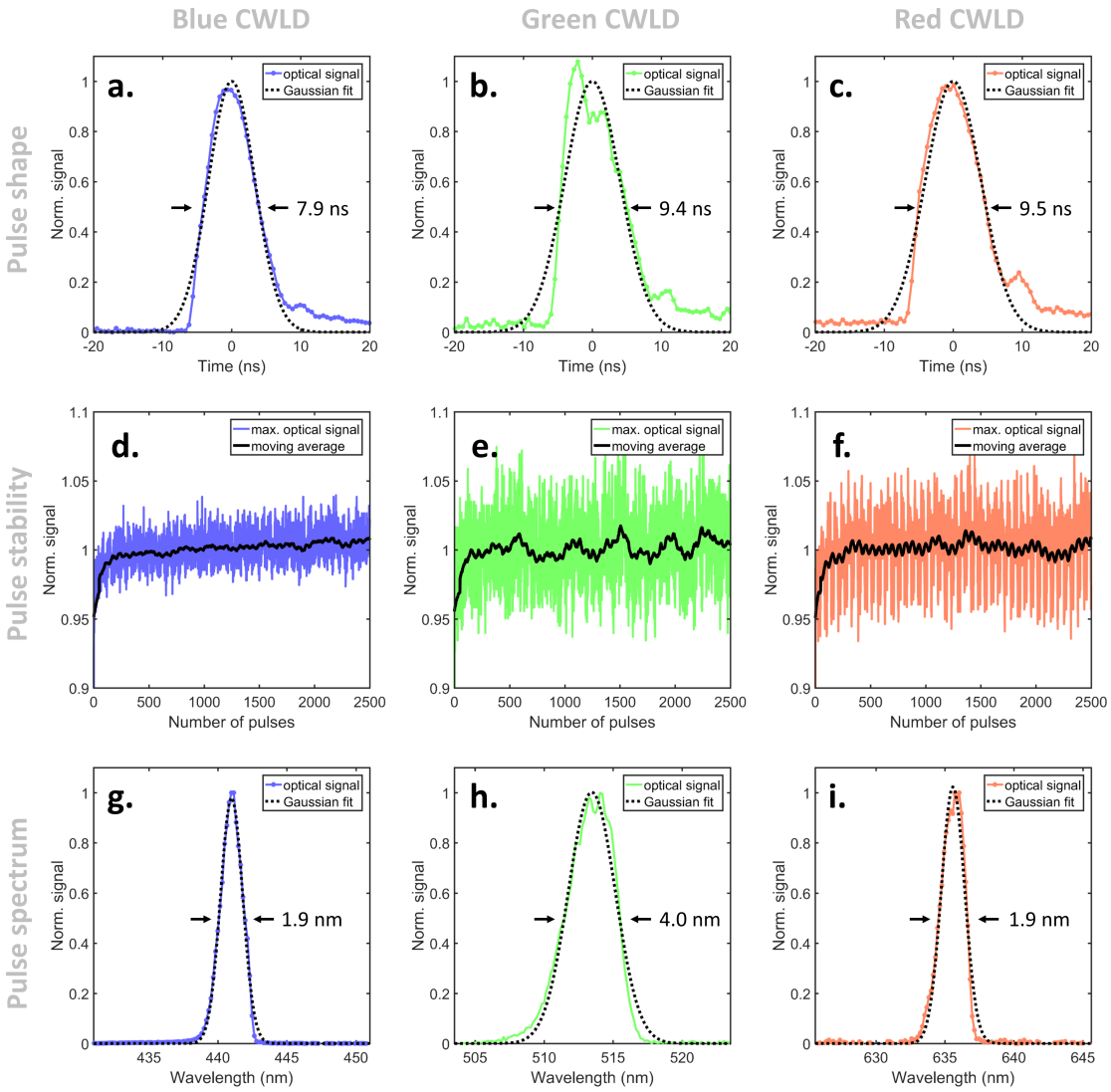

Figure 5.29: Optical characterization of the overdriven CWLD for ALEX and FComb optoacoustic microscopy performed at 100 kHz repetition rate, 16 ns electric trigger signals, and 300 V high-voltage supply. **(a-c)** Optical pulse shapes of the (a) blue, (b) green, and (c) red CWLD. **(d-f)** Pulse energy stability of the (d) blue, (e) green, and (f) red CWLD. **(d-f)** Emitted wavelength of the (d) blue, (e) green, and (f) red CWLD.

Next, we tested the imaging capabilities using a reference phantom of two intertwined black sutures of 18 µm and 30 µm diameter shown in Fig. 5.30. After beam collimation and co-alignment of the laser focii, the sutures were imaged with a 10x 0.45 NA objective by means of the ALEX approach (see Fig. 5.30e-g) and the FComb approach (see Fig. 5.30h-n), both carried out with all three CWLDs simultaneously and their signals separated as described previously. In both operation modes, the sutures were homogeneously revealed by all three CWLDs. The achieved image SNRs were 15.9 dB,

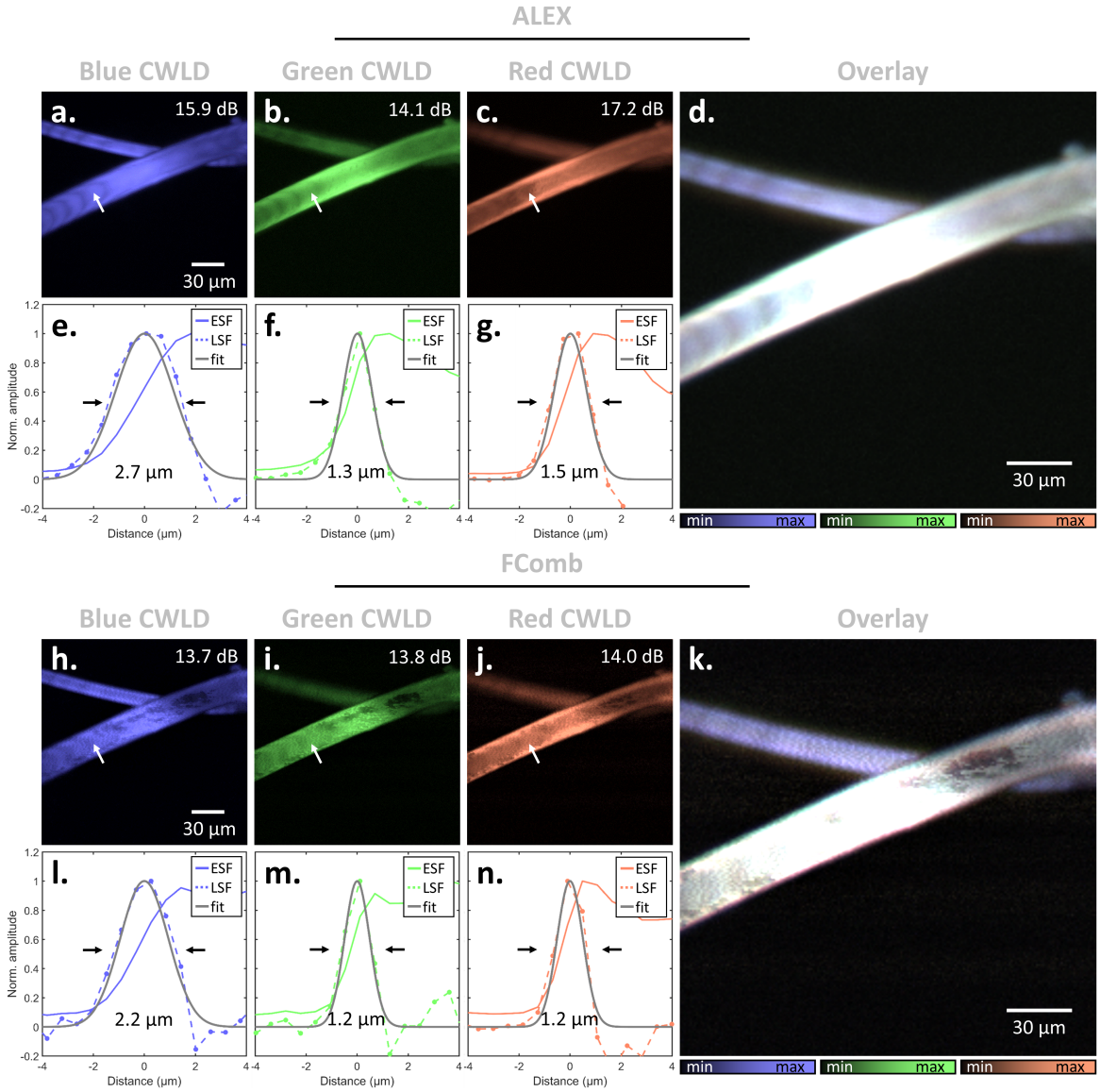

Figure 5.30: Characterization of the imaging performance of overdriven CWLDs for ALEX and FComb optoacoustic microscopy using two intertwined sutures of 18 µm and 30 µm diameter. **(a-c)** Separate depiction of simultaneously recorded images in ALEX mode of the (a) blue, (b) green, and (c) red CWLD, and their (d) overlay. **(e-g)** Achieved resolutions determined by extracting the respective edge-spread-functions (ESF) along the arrows indicated in (a-c) and Gaussian fitting the corresponding line-spread-functions (LSF). **(h-n)** Analogous depictions and analysis of the FComb measurement of the identical sample.

14.1 dB, and 17.2 dB for ALEX (see Fig. 5.30a-c) and 13.7 dB, 13.8 dB, and 14.0 dB for FComb (see Fig. 5.30h-j), respectively for the blue, green, and red CWLD. The lower SNR yielded for FComb might be due to capturing electric noise and non-linearities in generating optoacoustic signals at excitation rates of > 1 MHz. The overlays for ALEX (see Fig. 5.30d) and FComb (see Fig. 5.30k) measurements revealed good spatial co-alignment of the CWLD beams. The yielded resolution, as plotted in Fig. 5.30e-g and Fig. 5.30l-n, were determined via Gaussian fitting of the line-spread-function (LSF), which constitutes the first derivative of the edge-spread-function (ESF) over an arbitrary sharp boundary and, thereby, reveals the achieved spatial resolution. The found resolutions were 2.68 µm (blue; R^2=0.95), 1.34 µm (green; R^2=0.89), and 1.50 µm (red; R^2=0.82) for ALEX and 2.22 µm (blue; R^2=0.93), 1.16 µm (green; R^2=0.89), and 1.19 µm (red; R^2=0.88) for FComb, respectively. The higher resolution achieved in FComb could potentially be caused by a 100 times lower scanning speed of the galvo mirrors and, thus, a higher precision of the optical focii positioning.

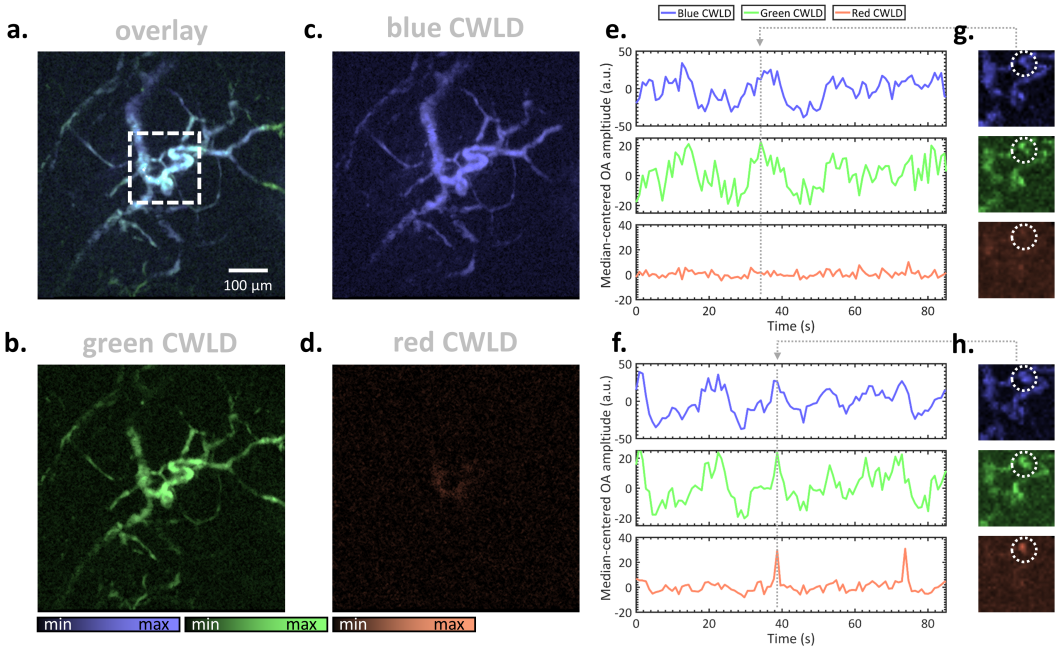

Figure 5.31: ***In vivo*** **multiwavelength microscopy of circulating melanocytes in mouse ears** using overdriven CWLD in ALEX operation mode. **(a-d)** High-resolution images depicted (a) overlaid or (b-d) separately for the respective CWLDs. **(e)** OA signal trajectories averaged across the circle as indicated in the selected **(g)** frames of the ROI marked in (a). **(f-g)** Analogous plots and depiction after tail vein injection of B16F10 melanoma cells.

Finally, we opted for applying simultaneous multiwavelength optoacoustic microscopy of an *in vivo* mouse ear. The mouse was prepared for imaging according to Section 4.2.3 and Section 5.2.2. We further administered $\sim 10^6$ B16F10 murine metastatic melanoma cells via tail vein injection. Whereas the absorption spectrum of hemoglobin coincided

with the wavelengths of the blue and the green CWLDs, which thus could potentially sense blood oxygenation values, it exhibited a negligible absorption for the red CWLD. Hence, the red CWLD was dedicated for revealing B16F10 cells circulating in the vasculature system.
Fig. 5.31 shows ALEX-imaging the mouse ear before and after injection of B16F10 melanocytes to mimic circulating tumor cells. Fig. 5.31a depicts the overlayed images acquired with the three CWLDs before melanocyte injection, which are separately shown in Fig. 5.31c-d. In here, the blue and green CWLDs revealed the microvasculature of the mouse ear in reasonable detail, whereas the red CWLD hardly contained signal in the center of the FOV. Fig. 5.31e plots OA signal trajectories of the vessel marked as a circle in the selected high-speed frames in Fig. 5.31g. The trajectories recorded with the blue and green CWLDs as well as their selected high-speed imaging frames resembled each other indicating similar contrast originating from hemoglobin in flowing RBCs. The trajectory and selected frame of the red CWLD solely contained the background signal. Fig. 5.31f-h analogously illustrate data acquired after tail vein injection of melanocytes. Whereas the blue and green CWLDs again owned similar time-wise trajectories and spatial signal patterns, the red CWLD contained two peaks in the trajectory, which probably originated from a single B16F10 cell passing through the interrogation area as shown in the associated frame[105]. Although the SNR and the reproducability were limited in these proof-of-concept imaging attempts, the data suggested successful discrimination of RBCs and circulating B16F10 melanocytes via simultaneous multiwavelength optoacoustic microscopy.

Conclusion

In conclusion, this project demonstrated the usability of laser diodes for optical-resolution optoacoustic microscopy. We showed that controlling laser diodes, which are designed to emit continuous-wave light, with an ultrashort high-voltage pulse allowed to generate sufficiently short laser pulses for time-domain optoacoustic applications. Furthermore, the custom-designed controlling circuit enabled highly flexible triggering schemes, which we used to conduct simultaneous multiwavelength imaging via alternating laser excitation as well as frequency-comb approaches. The precise optical alignment optimized for diffraction-limited focusing yielded high spatial and temporal resolution. By that, we finally achieved imaging capabilities comparable to standard high-end laser sources regarding *in vivo* discriminating of flowing blood cells and melanocytes; latter are mimicking circulating tumor cells. Conclusively, laser diodes operated in the herein shown way constitute a highly promising alternative excitation sources for optoacoustic imaging by reducing cost and bulkiness and by enlarging the range of acquisition modes. In the future, the former will facilitate the construction of

[105] Analogous findings were obtained by operating the multiwavelength imaging in FComb mode.

portable and small-footprint devices and the latter the addition of more wavelengths without increasing the acquisition time.
In this project, the high flexibility of triggering, data acquisition, and scanning schemes of HyMPSOM were used to explore the feasibility of using laser diodes for optoacoustic microscopy. Furthermore, as HyMPSOM incorporates a variety of excitation sources for optoacoustic signal generation, a direct comparison of the respective imaging performance could be straightforwardly carried out.

5.4.3 All-optical optoacoustic microscopy

This project concerned the integration of an optical ultrasound-sensing method into HyMPSOM for detecting optoacoustic microscopy signals. The herein presented ultrasound-sensor was based on reading a π-phase-shifted fiber Bragg grating (π-FBG) interferometrically and was developed before integration into HyMPSOM[106].

Introduction

The majority of optoacoustic microscopy systems detect the generated ultrasound signals via piezo-electric transducers due to their high sensitivity, commercial availability, ease of use, and excellent resilience (see Section 3.3.3). However, their sizes are typically larger than the specimens or the imaged area A confocal arrangement of the acoustic sensitivity field and the optical focus is thus only achievable by placing the microscope objective and the ultrasound transducer on opposing sides of the sample. As a result, the transducer is located in transmission-mode and the investigated sample needs to be positioned between the microscope objective and the ultrasound transducer, which thereby limit its thickness to a few millimeters [23, 42]. Realization of an epi-mode optoacoustic microscope, i.e. sensing optoacoustic signals in backward-direction on the same side of the sample as the microscope objective, was initially attempted by miniaturizing piezo-electric transducers [251–253]. However, the achieved performance was not sufficient for a widespread use in optoacoustic microscopy due to several reasons: First, the sensitivity depends proportionally to the area of the piezo-electric element and, thus, drops quadratically by downsizing the sensor [42,74]; Second, the frequency bandwidth of the detector is determined by the thickness of the piezo-electric element and, thus, miniaturization restricts the sensed frequencies [74]; Third, piezo-electric transducers are typically characterized by small acceptance angles, i.e. the detectors aperture determining the volume throughout which signals are sensed. The size of the volumetric cone sensed by the transducer is a critical factor, especially for laser-

[106] This project was equally headed by Roman Shnaiderman and Georg Wissmeyer, who developed the optoacoustic sensor head for microscopy based on a π-FBG [247, 248]. The results of this project are published in [249, 250].

scanning optoacoustic microscopes like HyMPSOM detecting signals from positions outside the acoustic focal volume [74].
Although miniaturized piezo-electric ultrasound sensors can be placed in close proximity to the sample in front of the microscope objective to counteract the above mentioned limitations, such a detector position obstructs the illumination path of the microscope objective [251, 252]. Besides positioning a miniaturized piezo-electric transducer between sample and objective, ultrasound-reflecting and light-transmitting prisms are considered and used frequently [187]. Despite enabling epi-mode optoacoustic signal detection, they necessitate long focal distances of both the microscope objective and the ultrasound transducer. Long sound and light paths however lead to loss of high frequencies and poor optical focusing, which subsequently limits the usage of these prisms for high-resolution optoacoustic microscopy, especially in hybrid systems such as HyMPSOM, by impeding other integrated microscopy modalities.
To overcome the above mentioned issues of using piezo-electric transducers for an epi-mode optoacoustic microscope, optical ultrasound detection techniques constitute promising alternatives [74, 254–256]. *W.l.o.g.*, such optical ultrasound detectors operate either refractometrically or interferometrically. The former reads light refraction or deflection altered by refractive index changes, which are induced by mechanical stress in form of incident acoustic waves. The latter detects interference patterns, where the interference condition is altered by acoustic waves acting on the light path, the optical phase, or the optical wavelength [74]. As interference-based approaches consist of two parts, i.e. the sensing and the read-out part [74], the location of optical interference can be placed in an optical fiber. This allows the actual ultrasound sensor to be positioned in the imaging framework freely as required. In this study, we therefore aimed for developing a sensor head based on fiber-interferometry for detecting optoacoustic microscopy signals in epi-mode. We opted for a versatile design to fit on a broad range of standard microscopes as well as to allow other microscopic modalities to be performed alongside through the sensor head. To achieve this, we positioned a fiber exhibiting a π-phase-shifted fiber Bragg grating (π-FBG) in an ellipsoidal acoustic cavity for ultrasound amplification. The entire construct could then sit on top of a standard microscope objective as a compact sensor head.

Materials and methods

The sensor head consisted of a an ellipsoidal acoustic cavity for ultrasound amplification, a metallic sleeve for adaption to the microscope objective, and a fiber-based π-FBG as the actual ultrasound detector. The excitation of OA signals in this project was based on the solid-state laser emitting at 532 nm and 25 kHz as described in Section 4.2.2.

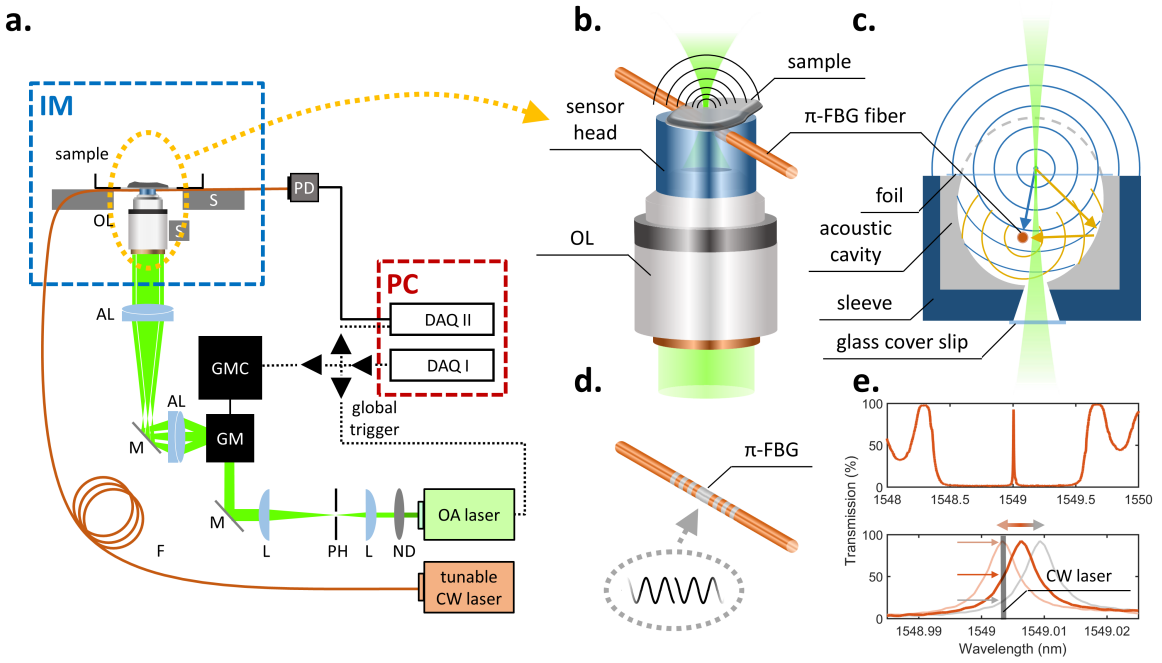

Figure 5.32: Schematic depiction of the all-optical optoacoustic microscope. Sub-system for all-optical optoacoustic microscopy based on interrogating a π-FBG sensor with a CW tunable laser and sensing direct and cavity-amplified indirect optoacoustic signals by a photodiode. Abbreviations: AL: achromatic doublet lens; DAQ: data acquisition card; F: single-mode polarization-maintaining fiber; GM: galvanometric mirror scanner; GMC: GM controller; IM: inverted microscope; L: plan-convex lens; M: dielectric mirror; ND: neutral density filter; OL: microscope objective lens; PH: pinhole; S: high-precision motorized stage. **(b)** Close-up depiction of the manufactured sensor head sitting sitting on top of the equipped objective lens. **(c)** Cross-sectional view of the sensor head showing the path of the direct signal (blue) and indirect signal (orange) after reflection at the inner surface of the ellipsoidal acoustic cavity. **(c)** Schematic depiction of the periodic refractive index pattern of the π-FBG. **(d)** Spectrum of the transmission notch of the π-FBG and exemplary ultrasound-induced spectral shifts of the transmission notch used for OA signal sensing based on transmission changes. (Adapted from [23, 249])

Fig. 5.32a shows the sub-system integrated into HyMPSOM for all-optical optoacoustic microscopy. As depicted in Fig. 5.32a, the π-FBG was interrogated with a tunable continuous wave (CW) laser (INTUN TL1550-B, Thorlabs; 1520–1630 nm, 20 mW) and was guided through an ellipsoidal cavity (see Fig. 5.32b). The cavity, which was manufactured by computerized numerical control (CNC) carved out of stainless steel (acoustic impedance: 47 Mryal; acoustic reflection coefficient: 0.91-1), measured 9.6 mm along a semi-major axis and 8.2 mm along a semi-minor axis. Fig. 5.32c illustrates, that the π-FBG was positioned in the first acoustic focus of the ellipsoid and that the optical focus coincided with the second acoustic focus being 400 µm above the upper rim of the cavity to place the imaging plane deep into the specimen. The cavity was further tilted by 12° with respect to the central axis of the objective to prevent the

π-FBG from obscuring the excitation laser beam path. Since the acoustic cavity had an aperture of ∼7.3 mm in diameter, it allowed for laser-scanning approaches (see Section 2.4.3). The cavity further comprised a lower aperture, which was enclosed during measurements using a circular microscope cover slip of 170 µm thickness to transmit excitation beams through the sensor head into the specimen. The entire cavity was filled with centrifuged ultrasound gel and sealed with a 10 µm thick polyethylene foil on the upper aperture. The π-FBG-holding cavity was then placed on top of a microscope objective (PLN 10X, Olympus, Hamburg, Germany; NA 0.25, WD 10.6 mm) using a custom-designed metal sleeve adapter. The specimen was acoustically coupled to the sealed sensor head either by a drop of deionized water or ultrasound gel. The actual ultrasound sensing area of the π-FBG had an active area of $125 \cdot 300$ µm^2 and is schematically depicted in Fig. 5.32d. The π-FBG itself was produced by UV light engraving a standard single-mode polarization-maintaining fiber (TeraXion, Quebec City, Canada). The thereby yielded grating constituted a periodic alteration of the refractive index of the fiber, i.e. the π-FBG, leading to a transmission bandgap depending on the period of the grating. The grating further included a centered artificial defect (π-shift) to resemble a Fabry-Pérot interferometer, which generated an ultra-narrow transmission notch as depicted in Fig. 5.32e. The spectral position of the transmission notch could be shifted spectrally by acoustic waves encountering the grating and thereby altering the period of the grating. The interrogation laser was for that tuned to the wavelength at which the transmission notch reaches its FWHM in an unperturbed condition (see Fig. 5.32e). Incident OA waves were thereby detected as transmission changes of the interrogation laser by a high-bandwidth photodiode (PDB450C, Thorlabs) and were recorded by the high-speed data acquisition card at 900 MS/s with up to 100 averages as described in Section 4.2.4. The OA signals finally were read upon encountering the π-FBG directly, i.e. direct signal (see Fig. 5.32c; blue), and after being reflected by the acoustic cavity and then focused onto the π-FBG, i.e. indirect signals (see Fig. 5.32c; orange). The signals were further bandpass filtered within a range of 5 to 90 MHz.

Results

First, we characterized the developed π-FBG sensor head using black polystyrene sutures crossing each other.
As plotted in Fig. 5.33a, the raw OA signal contained the direct (highlighted in blue) and indirect signal (highlighted in orange) as anticipated, the latter arriving at later timepoints due to longer travel distances of the acoustic waves. The indirect signal was significantly stronger than the direct signal due to amplification achieved by the acoustic cavity. Time-of-flight difference between the direct and indirect signal confirmed appropriate positioning of the π-FBG and the optical focus into both ellipsoid focii of the cavity. The corresponding frequency content shown in Fig. 5.33b revealed

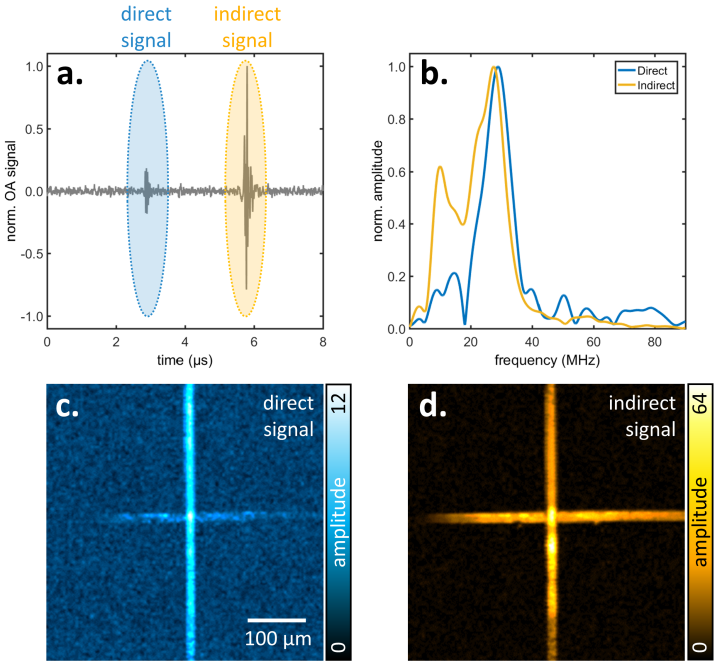

Figure 5.33: Characterization of the π-FBG sensor head by imaging two crossing black sutures. **(a)** Raw OA signal recorded from a black suture contains the direct signal (highlighted in blue) and the indirect signal (highlighted in orange) reflected and amplified by the acoustic cavity. **(b)** Corresponding frequency content of the direct and indirect signals. Maximum amplitude projection onto the xy-plane of the suture scan for **(c)** the direct signal and **(d)** the indirect signal. (Adapted from [249])

influences of the frequency response of the cavity and ultrasound attenuation along the reflection sound path. Whereas both frequency contents peaked at ∼28 MHz, the indirect signal contained stronger low frequencies relative to the normalized maximum than the direct signal. This might be due to a longer travel distance of the indirect signal. Fig. 5.33c and d depict the performed imaging of the two crossing sutures across a FOV of $630 \cdot 630$ µm^2 using the direct and indirect signals for projection, respectively. In here, the SNR of the indirect signal was 5-times higher than of the direct signal. As the sutures were observable across almost the entire scanned area, an acceptance angle of minimum 76.5° could be assumed. The lateral resolution was determined to be 3.7 µm by imaging across the edge of a block of polished silicon-on-isolator (SOI) wafer (Data not shown; see [249]), the axial resolution was theoretically estimated to be ∼37 µm based on the detected bandwidth. Besides that, the noise equivalent pressure was determined to be 88 Pa, the resonance width to be 8 pm at -3 dB, and the Q-factor to be $1.9 \cdot 10^5$.

Next, the usability of the π-FBG sensor head was tested for *in vivo* examinations of mouse tissues. For that, the ear and the abdomen of anesthetized mice were imaged, the latter in a multi-modal setting. Fig. 5.34a shows a stitched image of a total area of $\sim 2 \cdot 2$ mm^2 of a mouse pinna *in vivo*. The image contained well-revealed vascu-

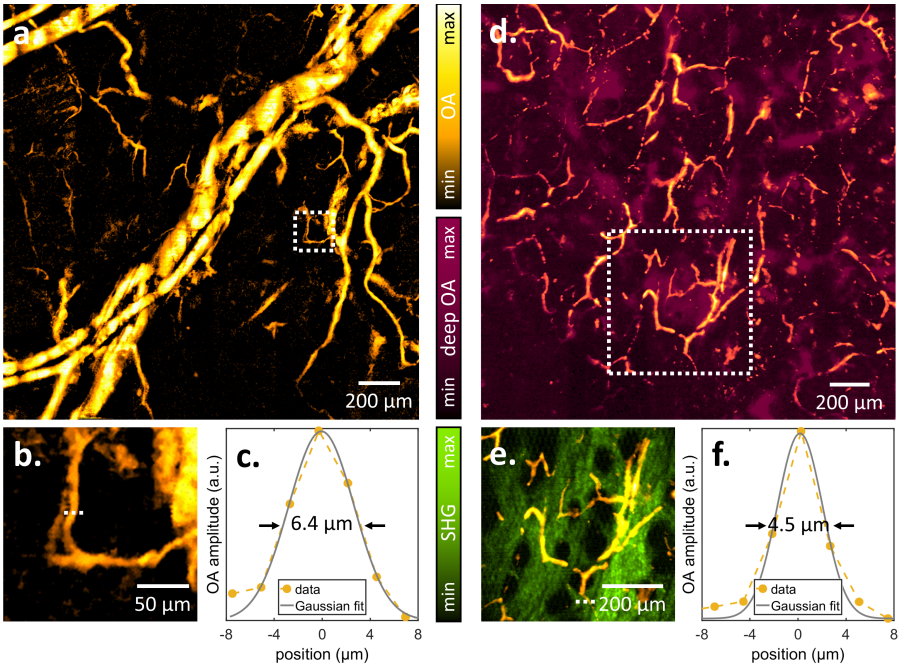

Figure 5.34: Mouse *in vivo* measurements using the π-FBG sensor head of ear and abdomen. **(a)** Stitched OA image of an mouse pinna *in vivo* shows vessels of 6 to 130 µm diameter. **(b)** Zoom-in of the dashed box in (a) reveals microvasculature. **(c)** Fitting a Gaussian curve of the intensity profile along the dashed line in (b). **(d)** Stitched OA image of a mouse lower rear abdomen *in vivo* depicted in two colors for shallow (orange; up to ∼300 µm) and deep (purple; between ∼300-500 µm) vasculature. **(e)** Overlay of OA and SHG image of the area indicated with a dashed box in (d). **(e)** Fitting a Gaussian curve of the intensity profile along the dashed line in (d). (Adapted from [249])

lature with diameters ranging from ∼200 µm down to microcapillaries below 10 µm. Fig. 5.34b depicts an exemplary zoom-in of microvasculature. The intensity profile across a microvessel plotted in Fig. 5.34c indicated vessel diameters as small as 6.4 µm (R^2=0.93). Fig. 5.34d illustrates an analogously performed imaging and stitching across an area of ∼1.8 · 1.8 mm^2 of a mouse lower rear abdomen *in vivo*. The image contained both superficial microvasculature (shown in orange) as well as deep seated bigger vasculature (shown in purple) separated by the arrival time of the acoustic signals. The exemplary zoom-in in Fig. 5.34e shows the superficial vasculature overlayed with SHG imaging (shown in green), acquired as described in Section 4.2.1, performed subsequently through the sensor head. The OA image herein captured microcapillaries entering and exiting the imaging plane. The SHG image revealed a well-defined network of extracellular collagen surrounding hair follicles with an image quality and signal amplitude comparable to measurements carried out without the sensor head (see Section 4.3.1 and Section 5.2.2). Analysis of the microvessels analogously to the ear measurement revealed microcapillaries as small as 4.5 µm (R^2=0.93) (see Fig. 5.34f).

Conclusion

In here, we demonstrated a novel approach for an all-optical optoacoustic microscope for imaging *in vivo* tissues such as mouse ears and abdomen. The proposed system was based on a π-FBG sensor head amplifying optoacoustic signals by an acoustic cavity. The 5-fold amplification of the ellipsoidal shaped cavity was achieved by a bi-focal arrangement of the optically scanned area and the 125 µm diameter π-FBG detector. Further, the CW interrogation of the π-FBG achieved herein a noise equivalent pressure and a Q-factor comparable to highly elaborate approaches of locking the interrogation laser to the optical resonance [253, 257] and, thus, constitutes a novel, promising, and cost-effective approach for optical ultrasound sensing. We showcased that the developed sensor head could be adapted to standard microscope objectives in epi-mode. It allows thereby its usage not only in a almost all microscope systems and in combination with other microscopic modalities, such as SHG, but also for imaging arbitrarily thick samples, which are not accessible for transmission-mode optoacoustic microscopes. However, the performance of the proposed π-FBG sensor head could be further improved by refining the acoustic properties of the π-FBG-containing fiber to match the ones of the medium inside the cavity, by placing the Bragg grating onto thin-clad or polymer fibers, by optimizing the entire sensor head for high-end ultra-long working distance objectives, and by enabling frequency-domain optoacoustic readings. Such improvements would enhance the versatility of the sensor and could potentially enable optical-resolution optoacoustics to become a microscopic modality which can be easily integrated in existing microscope setups.
For this project, HyMPSOM constituted a platform for developing and characterizing innovative approaches for ultrasound detection. Due to the high-flexibility of optoacoustic signal generation, high-speed laser-scanning, and fast acquisition of large datasets, HyMPSOM accomplishes to exploit all features of novel ultrasound sensors. The combination of HyMPSOM with the herein developed all-optical ultrasound detection overcomes typical limitations of piezo-electric transducers and, thus, potentially presents a new way of performing optoacoustic microscopy.

5.4.4 Optoacoustic flow cytometry

This project regarded a proof-of-concept of an optoacoustic flow cytometer. The aim was to read optoacoustic signals referenced to simultaneously recorded light scattering signals of individual cells expressing chromoproteins flowing through a microfluidic channel[107].

[107] This project was performed in cooperation with Dr. André Stiel, who was in charge of cell preparation and protein expression. During writing of this thesis, this project was in preparation for submission [258].

Introduction

High-throughput analysis and online sorting of individual cells constitutes a routine technique well established in a huge variety of scientific fields ranging from basic research up to clinical practice [259–261]. Despite the still standard way of operation using charged droplets of the investigated suspension, microfluidic systems are heavily developed with beneficial properties such as high controllability, ease of use, and precise adaption to the respective flow cytometric experiment [262, 263]. In most cases, the cells under investigation present a fluorescent contrast, either via genetic encoding or exogenous administration, to manifest the information of interest. In this regard, fluorescence-activated cell sorting (FACS) strongly depends on specific and dedicated fluorescent labels as cells typically present only limited information by intrinsic autofluorescent phenotypes [264, 265]. Nevertheless, the molecular composition of cells, which discloses its current condition such as the set of expressed proteins, determines the associated cell with distinct optical phenotype regarding absorption and scattering properties [266, 267]. However, the short optical path-length of individual cells prevent direct measurements of e.g. extensive optical absorption spectra in high-throughput flow techniques. To overcome this limitation, optoacoustic in-flow measurements have been proposed due to their ability of reading optical absorption characteristics at high speed. So far, optoacoustic flow cytometry has been utilized for *in vivo* measurements of circulating tumor cells and administered contrast agents as well as to some extent for *in vitro* characterization of single-cells [268–273]. A critical factor for *in vitro* investigations however is the calibration and normalization of the signals regarding their spatial position in the interrogation area and/or the size of the flowing cells. Mostly, OA flow cytometry techniques record optoacoustic signals along with either fluorescence or ultrasound-backscattering signals to address this problem [274, 275]. In case of the former, fluorescence and optoacoustic signals originate from the identical underlying process of optical absorption and, thus, are not independent and therefore do not represent a valuable strategy for normalization. In case of the latter, ultrasound is associated with much poorer spatial resolution, which thereby impedes proper calibration of the optoacoustic signals. To overcome the current limitations of accurate normalization and calibration of in-flow optoacoustic single-cell measurements, we developed a prototype for detecting optoacoustic and light-scattering signals of individual cells in flow. The combination of optoacoustic and light-scattering signals allowed accurate discrimination and referencing. The light-scattering signal determined herein the overall sensed volume per cell and, thus, could be used for normalizing the optoacoustic signals for cell size and position. It therefore represented a perpendicular methodology to OA readouts, which finally facilitated the discrimination of mixed cell stocks, each expressing an optoacoustically active and distinguishable chromoprotein.

Materials and methods

As schematically depicted in Fig. 5.35a, the herein proposed optoacoustic flow cytometry (OAFC) system utilized the optical excitation of the 532 nm-laser (see Section 4.2.2) focused into a microfluidic chip (01-0175-0138-02, microfluidic ChipShop, Jena, Germany) with a flow channel of 1000 µm width and 100 µm height (see Appendices: Photographs of the optical setup).

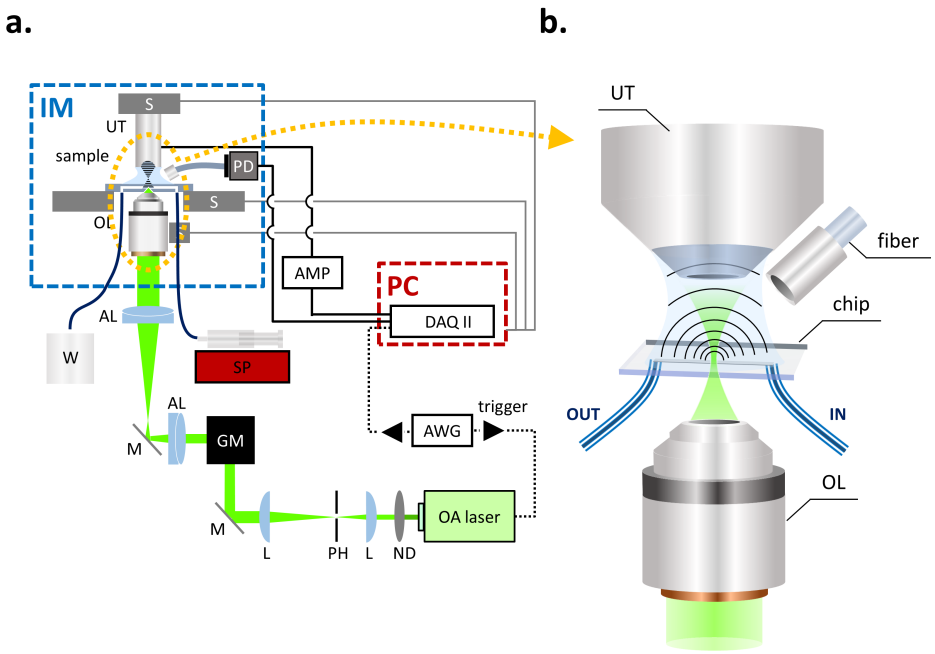

Figure 5.35: Schematic depiction of the OAFC system. (a) The OAFC system is based on focusing a 532 nm laser into a microfluidic channel, which is connected to a syringe pump for controlling the flow of suspensions of particles or cells. OA and LS signals are recording simultaneously. **(b)** Close-up depiction of the microfluidic interrogation area. Abbreviations: AL: achromatic doublet lens; AMP: low noise amplifier; AWG: arbitrary waveform function generator; DAQ: data acquisition card; GM: galvanometric mirror scanner; IM: inverted microscope; L: plan-convex lens; M: dielectric mirror; ND: neutral density filter; OL: microscope objective lens; PH: pinhole; S: high-precision motorized stage; SP: syringe pump; UT: ultrasound transducer; W: waste.

The microfluidic channel was enclosed by a 1 mm thick Cyclo-olefine co-polymer through which the optical excitation was focused and a 140 µm lid facing the sensing detectors. The microfluidic chip was connected to a syringe pump (NE-1000, New Era Pump Systems Inc, USA) in order to push the suspensions with a defined flow speed through the channel. OA signals were sensed in transmission mode by a 50 MHz-transducer (see Section 4.2.2). Light-scattering (LS) signals were detected by a high-speed photodiode equipped with an optical fiber, the tip of which is tilted by 45° with respect to the optical axis (see Fig. 5.35b). Both signals were then projected using their maximum amplitude of dedicated time windows covering the correspond-

ing signals. For characterizing and calibrating the OAFC system, we first recorded flowmetry trajectories of suspensions of 2-12 µm carbon-nano-particles (CNPs) and 10 µm blacked microbeads (µB). In all cases, the suspensions were diluted and replenished with $\sim 1\%^{\text{vol.}}$ TWEEN^{TM} 20 (Sigma-Aldrich, Germany) to reduce the surface tension for preventing agglomeration, and with the appropriate amount of sodium polytungstate (Sigma-Aldrich) for increasing the density of the medium for preventing sedimentation. The required concentration of sodium-polytungstate was determined via calculating the volume fraction of the particles. The prepared suspensions were rested for 1 h to verify proper adjustment of the density.
For cell measurements, coding sequences for mKO (UniProtKB: Q6I7B2) and mCherry (UniProtKB: X5DSL3) were synthesized in a setting optimized for *E. coli* (GeneArt, ThermoFisher) and inserted in pET21a(+) (Novagene) using the NdeI and XhoI (ThermoFisher) sites. Proteins were expressed in BL21 DE3 (New England Biolabs) at 37 °C and 180 rpm. Expression states and cell density were monitored by optical absorption measurements at 600 nm and fluorescence measurements at the respective peak absorption wavelengths of the two proteins. The proteins were finally purified using immobilized metal affinity chromatography (HisTrap HP 5ml, GE Healthcare - Life Sciences) and size exclusion chromatography (HiLoad 26/600 Superdex 75 pg, GE Healthcare - Life Sciences).

Results

In a first step, we investigated the capabilities of the OAFC system regarding the detection of single transits of in-flow absorbers. For that, we flushed a suspension of 10 µm blacked polystyrene beads (µB) at a flow rate of 100 µL/min and recorded OA and LS signals simultaneously.
Fig. 5.36a shows the raw and unprocessed OA signals captured at 50 kHz repetition rate of an individual µB flowing through the interrogation area. Fig. 5.36b shows the simultaneously recorded LS signal of the identical bead. The maximum amplitude projection plotted in Fig. 5.36c and d of the OA and LS signals, respectively, revealed a clear contemporaneous single event. Whereas the OA signal of the transit approximated a Gaussian curve as expected, the LS signal presented a sharp peak occurring at the end of the OA transit curve. This might be due to the LS signal being expected when the bead surface aligns with the optical axis in half the angle of the LS-signal-detecting optical fiber, i.e. ∼22 °, to direct the laser light to the optical fiber. Further, the LS signals were recorded in reverse direction with respect to the flow and, thus, LS signals were expected at the temporal end of the transit. Fig. 5.36e plots the trajectories of simultaneously recorded OA and LS signals over a recordtime of 10 s. Both trajectories were characterized by capturing single transit events above threshold >90% of which appeared in both channels. As depicted in Fig. 5.36f, both auto-correlations of the OA

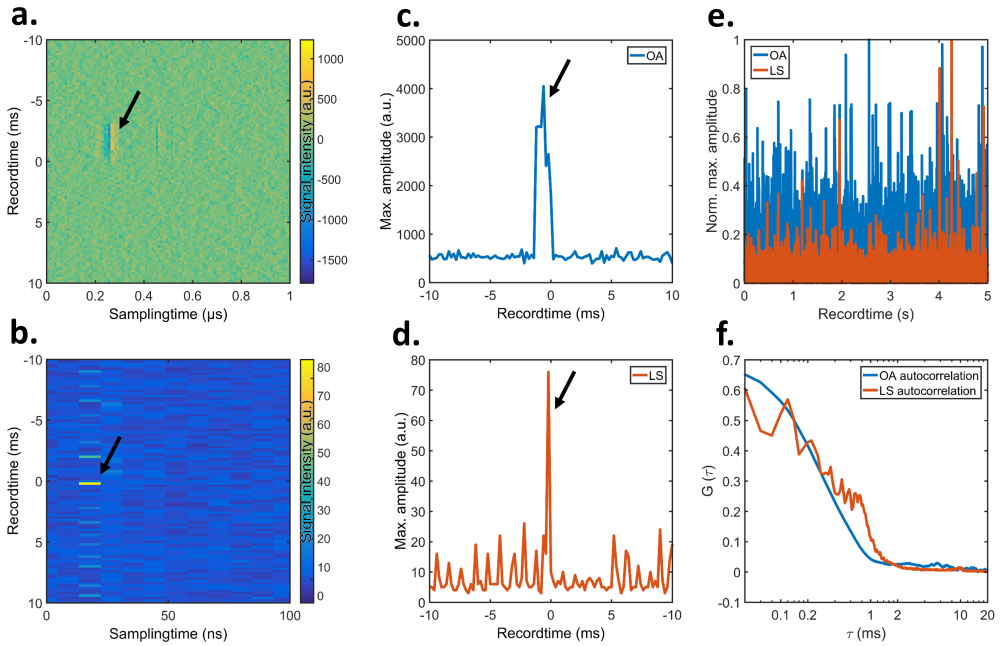

Figure 5.36: Validation of detecting single transit events in OAFC using 10 µm blacked polystyrene beads flowing at 100 µL/min. Raw **(a)** OA and **(b)** LS signals detected from a single bead (indicated by arrows) flowing trough the interrogation area. **(c)** OA and **(d)** LS maximum amplitude projection of the record window shown in (a) and (b). **(e)** Trajectories over the recorded 10 s show transits of individual beads. **(f)** Auto-correlation curves of the OA and LS trajectories in (e) reveal an interrogation time of ∼300 µs.

and LS trajectories exhibited a correlation time of ∼300 µs. Theoretically, a flow rate of 100 µL/min through a channel with a cross-section of 100 · 1000 µm^2 leads to an average flow speed of 16.$\overline{6}$ mm/s and a Reynolds number of ∼3.03. Measuring beads of 10 µm diameter at the center of the microfluidic chip, at which the flow speed is expected to be twice the average flow speed based on a laminar Poiseuille flow profile, this should result in an interrogation time of ∼300 µs, i.e. ∼15 pulses per bead at a repetition rate of 50 kHz and assuming an arbitrarily small optical focus, which matched the experimentally determined correlation time. Based on validating that the OAFC system was able to detect OA and LS signals of single in-flow transits of optical absorbers with diameters of a few micrometers, we next opted for measuring genetically encoded chromophore proteins expressed by identical cell types.

To confirm the sensitivity for detecting single transits, the microfluidic channel was flushed with the respective solvents of the reference samples and the cell suspensions using identical measurement settings regarding flow rate, repetition rate and power of the laser, as well as signal processing. Fig. 5.37a confirms that for water mixed with sodium polytungstate and TWEEN^{TM} 20, which was the solvent for µBs and CNPs, no transit events were recorded. Identical finding held for DPBS, as shown in Fig.

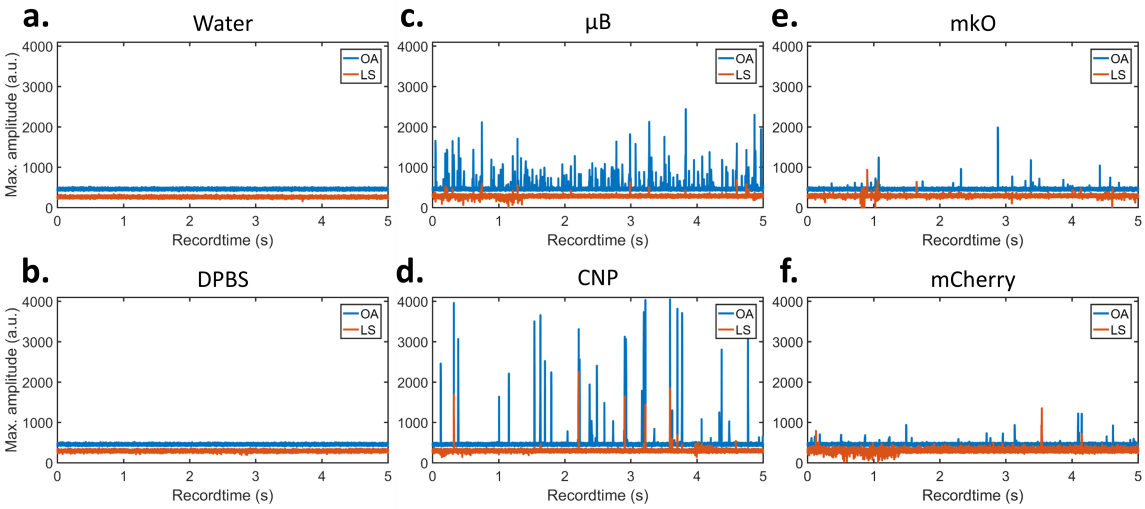

Figure 5.37: Characterization of in-flow signals at 100 µL/min. OA and LS trajectories of **(a)** water as the solvent for µB and CNPs as well as of **(b)** DPBS as the buffer for the cell suspension exhibit no detected transit events over 5 s record time. Water-suspended **(c)** µBs and **(d)** CNPs reveal OA and LS signals of transits of individual particles. OAFC trajectories of *E. coli* expressing **(e)** mKO and **(f)** mCherry in DPBS reveal detectable in-flow signals.

5.37b, being the buffer for the *E. coli* suspensions. In both cases, the background noise level was constant over >5 s recordtime, which enabled signal thresholding for further analysis. The suspensions of µBs (see Fig. 5.37c) and CNPs (see Fig. 5.37d) validated the presence of transit events. In here, the trajectories of the µBs contained a more homogeneous signal amplitude, whereas the ones of the CNPs indicated a large deviation. This could be explained by an assumingly constant particle size of 10 µm for the beads and a size distribution from 2-12 µm for the CNPs. Fig. 5.37e and Fig. 5.37f show the OA and LS trajectories of *E. coli* cells expressing the chromoproteins mKO and mCherry, respectively. Both cell suspensions led to detectable OA and LS signals above threshold.

Finally, we aimed for discriminating cell suspensions of identical cell types based on their respective genetically encoded and expressed chromoprotein. For that, we thresholded both the OA and LS signals, localized single-transit events, fitted Gaussian curves, and assigned the OA peaks to their corresponding LS peaks. The assignment was performed over a window being twice the FWHM of the found OA-peak due to the time-shift between the two signals, as explained previously. Fig. 5.38a and b shows the signal distribution as scatterplots of normalized OA signals against their corresponding normalized LS signals of mKO and mCherry cell suspensions. The inset depicts a signal histogram based on an inclined axis, which also enabled linear discrimination with a separation precision of >92%. Merging the data of separately performed

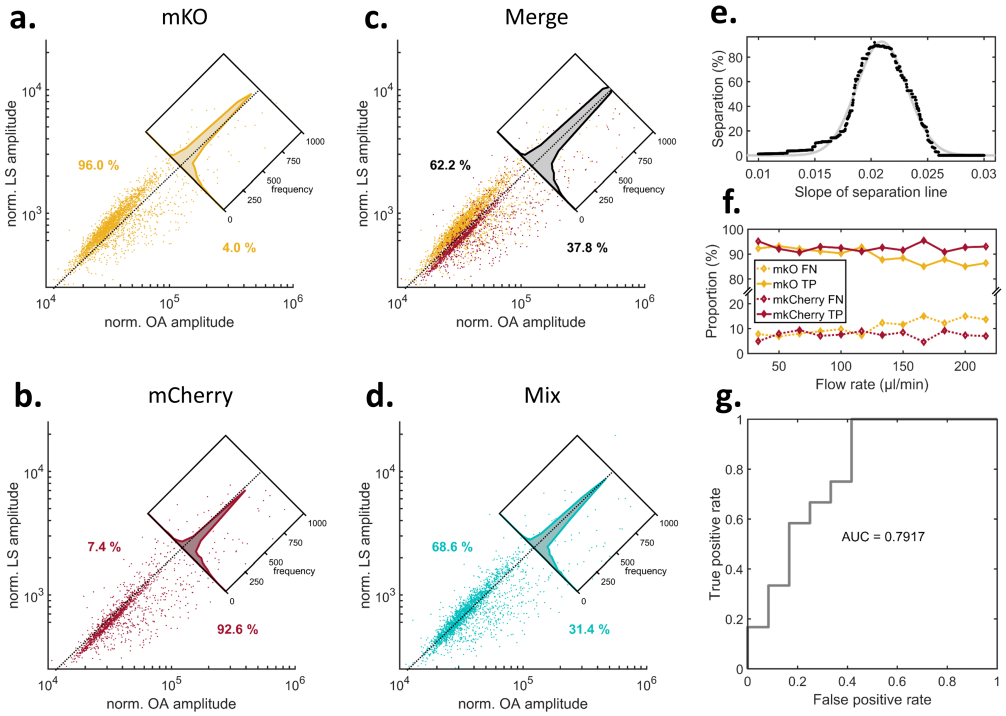

Figure 5.38: Signal distribution of in-flow single transit events of *E. coli* cells expressing optoacoustic labels enabled separation by applying linear discrimination. **(a)** Norm. OA signals against norm. LS signals of *E. coli* cells expressing mKO. Inset depicts separation by linear discrimination of 96.0%. **(b)** Analogous analysis of *E. coli* cells expressing mCherry yields a discrimination of 92.6%. **(c)** Data merge of the separate measurements and **(d)** measurement of cell stock mixture (mixing ratio 1:1) of mKO and mCherry *E. coli* cells yield a linear discrimination of 2:1 indicating cell concentration differences in the stock solutions. **(e)** Varying the slope of the linear discrimination and Gaussian fitting peaked in ∼0.0209 a.u. with an average separation of ∼92.5%. **(f)** Flow speed analysis shows consistent linear discrimination by constant true-positive (TP) and false-negative (FN) assignments of signals. **(g)** ROC analysis reveals an AUC of ∼0.8.

measurements of cell suspensions, each expressing only one chromoprotein, is plotted in Fig. 5.38c. Analogously performed linear discrimination led to a proportion ratio of ∼2:1. Fig. 5.38d plots the signal distribution of measuring a 1:1 mixture of both cell stock suspensions. The linear discrimination in here achieved again a proportion ratio of ∼2:1, which indicated a cell concentration in the mKO stock suspension being twice the one of mCherry. Both, measuring the two cell suspensions separately and then merge their data as well as measuring a 1:1 mixture of the cell suspensions exhibited signal distribution and linear discrimination in very good agreement. Fig. 5.38e shows the dependence of the averaged separation by varying the slope of the linear discrimination. The herein shown Gaussian fit revealed an optimum discrimination of ∼92.5% for all recorded data at an discrimination slope of ∼0.0209 a.u.. As

shown in Fig. 5.38f, the linear discrimination was unaffected by the applied flow rate and consistently achieves separation precisions of >80% true-positives (TP) and <20% false-negatives (FN). The receiver-operator-characteristics (ROC) analysis shown in Fig. 5.38g indicated an area-under-curve of ∼0.8 and, thus, validated the linear discrimination by a true-/false-comparison.

Conclusion

In here, we presented an optoacoustic flowcytomer (OAFC) based on reading optoacoustic and light scattering signals simultaneously. By that, we achieved to detect individual particles and cells in-flow as transit events. The dual-modal data further allowed to reference the acquired optoacoustic signals to their corresponding light scattering signals. By that, we were able to consistently distinguish two cell stock suspensions each expressing a distinct chromoprotein as the optoacoustic label. The underlying reference procedure constitutes an essential difference to other approaches reading e.g. fluorescence signals, as it is based on two independent modalities. This project proofs the concept of an OAFC system for studying specific proteins expressed in cells and could potentially serve as a key research tool in the development of optoacoustic labels in a directed evolution setting as well as an investigation technique for characterizing cells. For the latter, the optoacoustic excitation could be improved by integrating a multiwavelength laser for detecting spectral characteristics of cells. Further, such a multiwavelength excitation could be realized using either high-frequency laser diodes or modulated CW lasers for simultaneous interrogation (see Section 5.4.1 and Section 5.4.2). Lastly, besides a focused optical excitation as used in this proof-of-concept study, a widefield laser illumination could potentially diminish the signal dependence on the position of the object within the interrogation area. As the LS signals in here were necessary for correcting spatial offsets of the flowing objects with respect to the actual optical focus, a widefield reading could overcome this issue by integrating the signals recorded from a larger area.
This non-imaging project showcased how the technical framework of HyMPSOM could be used for exploring novel ideas for reading optoacoustic signals on the microscale in general. Whereas the OAFC did not rely on the imaging capabilities of HyMPSOM, the advanced synchronization and data acquisition methods facilitated in here the required precision for reading small signals of flowing cells.

5.5 Conclusion and Outlook

In conclusion, HyMPSOM facilitates its application for the investigation of biological and biomedical specimens. Based on the technical imaging properties of a sub-cellular spatial resolution, deep imaging, fast and simultaneous data acquisition, and multi-modal imaging contrast in combination with technical flexibility and modular construction allows to perform a huge variety of different imaging projects ranging from single-cells cultured in petri dishes over organoids and small model organisms up to excised human tissue slices. Further, based on the ability of applying HyMPSOM to *in vitro*, *in vivo*, and *ex situ* samples, it therefore constitutes a platform that is able to perform studies across the entire range from basic biological research over translational medicine up to clinical practice.
In this regard, HyMPSOM allows for detailed investigations of innovative multi-modal contrast agents to sense and interact with specimen on the cellular level. The multi-modal contrast enables to comprehensively characterize such contrast agents, which improves both our understanding of their fundamental functionalities as well as to refine their properties. Furthermore, HyMPSOM enables to conduct small animal studies in settings typically used in the field. By that, exploiting the full imaging potential of HyMPSOM gives new insights into biomedical processes, which are not accessible by other imaging techniques. Finally, applying HyMPSOM to clinical relevant tissue samples facilitates to link histopathological findings to living organisms. This is of special importance as most of the imaging modalities of HyMPSOM can potentially be scaled up to macroscopic examinations of humans. HyMPSOM finally bridges by that basic biomedical research with clinical research in a translational fashion.
Extending the standard way of operation with alternative approaches to realize optoacoustic microscopy further broadens the possibilities of exploring the basic nature of multi-modal microscopy. For that, HyMPSOM constitutes a versatile platform for the development of novel approaches to conduct optoacoustic sensing on the microscale. On the one hand, the unique controllability of HyMPSOM allows to investigate novel attempts for performing optoacoustic microscopy based on frequency-domain techniques. As such a transfer of domains is widely spread in all kinds of science and technology, HyMPSOM pioneers in an analogous way for optoacoustic microscopy. On the other hand, HyMPSOM facilitates to trail alternative methods for optoacoustic signal acquisition, which aim to overcome present limitations of widely spread approaches. For that, the extensive range of conducting optoacoustic microscopy eases a direct performance evaluation as well as further development. Finally, the framework of HyMPSOM permits to explore concepts that opt for utilizing the vast potential of microscopic optoacoustic investigations for daily laboratory work. This accompanies the current emergence and advancements of optoacoustic techniques in general and, thus, widens its range of application in future.

6 | Conclusion and Outlook

The work presented in this thesis concerned the development and advancement of a hybrid multi-photon and spectral optical-resolution optoacoustic microscope (HyMPSOM). For that, the thesis first elaborated on the physical background of the equipped modalities in general as light-matter-interaction as well as in detail by presenting the respective theoretical considerations. Next, a precise description of the assembled optical system and its characterization was given. Finally, a selection of relevant projects conducted on HyMPSOM were outlined to showcase its performance to study biological and biomedical specimens as well as to explore novel approaches to perform optoacoustic microscopy. In the following, a conclusive summary (see Section 6.1) and a general outlook (see Section 6.2) is given.

6.1 Conclusive summary

In this chapter, a conclusive summary is provided with respect to the five objectives formulated in Section 1.2.1:

1 Elaborate and equalize the imaging capabilities of the equipped microscopy modalities regarding speed, resolution, and sensitivity

To address the first goal, this thesis gave an in-depth overview of light-matter-interaction phenomena that give rise to contrast mechanisms for photonic microscopy. Based on the fundamental criteria to be fulfilled by microscopy modalities for their merging into a single device of possessing (1) complementary and preferably label-free contrast mechanisms, (2) compatible optical components, and (3) similar imaging properties, multi-photon and optoacoustic modalities were found to be most suitable. The description of the associated physical backgrounds of these imaging modalities as well as their functioning principles illustrated a necessity to improve on the performance of optical-resolution optoacoustic microscopy for enhancing its imaging capabilities to compete with multi-photon microscopy. For that, an innovative approach was developed to correct for the total impulse response (TIR), pushing by that the boundaries of optoacoustic microscopy via increasing the SNR by ∼10 dB and the axial resolution by ∼30%. TIR-correction constitutes in this regard a novel and versatile concept to exploit the maximum potential of optoacoustic microscopy for high-resolution and label-free microscopy in 3D, which lets the technique become significantly more competitive to well-established optical microscopy as well as to the multi-photon modalities implemented in HyMPSOM. Finally, all equipped modalities in HyMPSOM are awarded with equalized imaging capabilities, which pave the way for its application to study biological and biomedical specimens.

2 Achieve complementary multi-modal microscopy in terms of simultaneous and spatially co-registered imaging on the microscale

The second goal was accomplished by developing a highly sophisticated microscopy system regarding both the optical assembly as well as its method of imaging. On the one hand, precisely adapting the optical elements of each modality enabled concurrent imaging application. For that, this thesis explained in detail how HyMPSOM was equipped with specialized optics to allow for spatially and temporally co-registered signal generation. On the other hand, an advanced triggering- and data-acquisition-scheme was devised, which is based on a global trigger signal to synchronize all equipped devices and a streaming-like data recording using temporary buffers to fetch large data sets with high speed.

This allowed to perform truly simultaneous multi-modal microscopy of up to four modalities. The high flexibility of both the optical setup as well as the system control enabled various scanning techniques to be implemented in HyMPSOM. Based on the large amount of utilizable degrees of freedom to translate the optical focii, the investigated specimens, and the equipped detectors in 3D, HyMPSOM was optimized to freely adapt the image scanning mode in terms of resolution, averaging, speed, and field of view to the respective microscopy studies. In conclusion, HyMPSOM was shown to conduct precisely co-registered multi-modal microscopy of specimens ranging from single-cells up to small model organisms.

3 Facilitate and evaluate the development of novel multi-modal contrast agents for multi-modal microscopy

In the scope of the third goal, the unique imaging capabilities of HyMPSOM were shown to enable detailed characterization of innovative contrast agents. In this thesis, three approaches were evaluated to optimize the performance of multi-modal microscopy techniques regarding imaging and manipulation of biological materials on the cellular level. First, the iron-storage protein ferritin was investigated towards its ability of presenting an intrinsic multi-modal contrast and of allowing to interact with individual cells via photothermal ablation. Second, the optoacoustic and optical contrast properties of lysosomal-trafficked fullerenes were examined on the sub-cellular level, thereby constituting a new type of biocompatible synthetic contrast agents. Third, a specialized optoacoustic label for sensing calcium was studied on single-cells and cardiac organoids, which illustrated the ability of ion-sensitive readings in optoacoustic microscopy. In these exploratory projects, HyMPSOM facilitated highly precise *in vitro* characterization of the developed genetic, semi-genetic, or synthetic labels, and gave new insights into their underlying functional principles. In accompany with biophysical and biochemical characterizations performed alongside, HyMPSOM constituted a valuable tool to evaluate and advance the studied contrast agents.

4 Explore the applicability and performance of multi-modal microscopy for biological and biomedical specimens in the scope of translational research

Regarding the fourth goal, HyMPSOM was tested towards its potential to conduct multi-modal microscopy for translational research. This thesis first proofed its applicability to study *in vivo* specimens being standard for biological and biomedical research, such as zebrafish larvae and mouse ears, as well as *ex situ* tissue slices well-established in clinical practice, such as histopathological tis-

sue samples. On the one hand, the achieved high-speed multi-modal and label-free imaging allowed to conduct longitudinal studies on living model organisms. In this regard, HyMPSOM was used to investigate the complex wound healing process and achieved a spatio-temporal assessment of the different healing phases with so far unmet precision. On the other hand, HyMPSOM was utilized to inspect human atheroma tissue slices in a label-free manner. In here, spatially precise co-registered multi-modal observations revealed new insights into the pathological state of the excised tissue and helped to better understand the underlying disease progression on the microscale. In both projects, the possibility of extracting the information of interest in a label-free fashion highlighted the versatile potential of HyMPSOM for translational research. The lacking need of administering a contrast agent not only demonstrated how advanced microscopy could conquer well-established methods used routinely but also establish a basis to develop harmless and non-invasive techniques for human applications.

5 Pioneer on advanced operating principles to conduct optoacoustic microscopy beyond its standard way of execution

For the fifth goal, the framework of HyMPSOM was exploited to test innovative approaches for optoacoustic microscopy techniques. This thesis summarized various projects conducted on HyMPSOM, which aimed to address current limitations of performing optoacoustics on the microscale. First, alternative ways of implementing optoacoustic microscopy were devised by shifting the operational principle to the frequency domain. On the one hand, frequency-modulated continuous-wave lasers were used for optoacoustic signal generation, which allowed to explore the image formation principle in the frequency domain, to encode spectral information by loading several excitation wavelengths onto different frequencies, and extracting microvasculature flow-maps by reading Doppler signals. On the other hand, laser diodes designed for continuous-wave emission, which were modified with a customized control unit, allowed to outperform their specifications by emitting short laser pulses. The thereby achieved high versatility of functioning modes enabled their operation either in the time domain using alternating laser excitation or in the frequency domain using burst excitations for frequency-comb detection, which both made simultaneous and dynamic multiwavelength microscopy possible. Such approaches address various restrictions of standard optoacoustic microscopy by reducing size and cost of the excitation source, by enabling simultaneous multiwavelength imaging, and by increasing imaging speed. Second, this thesis described a novel concept of sensing optoacoustic microscopy signals in an all-optical detection scheme. The shown project concerned a fiber-based sensor to pick up ultrasound waves, which thereby al-

lowed for epi-mode optoacoustic microscopy of thick specimens. The sensor was comprehensively characterized on HyMPSOM and shown to be applicable to *in vivo* samples with detection performances similar to ultrasound transducers standardly used in the field. Third, a proof-of-concept of an optoacoustic flow cytometer was showcased. HyMPSOM was shown to enable discrimination of chromoproteins expressed in cells based on their in-flow detected optoacoustic and light scattering signals. This non-imaging project outlined how the sophisticated framework of HyMPSOM could be used to develop novel techniques of optoacoustic measurements on the microscale. As analogous systems based on e.g. fluorescence detection are well-established tools in biological and biomedical laboratories, such proof-of-concept studies assess the potential of a similar emergence for optoacoustic techniques. In summary, the high flexibility, controllability, and adaptability of HyMPSOM facilitated to explore innovative and alternative approaches of conducting optoacoustics on the microscale.

In conclusion, the development and advancement of multi-photon and optoacoustic modalities in form of the herein devised hybrid microscope HyMPSOM emerged towards a highly powerful tool to exploit the potential of microscopy in biomedical and translational research. By addressing the formulated objectives, this thesis outlined the versatile applicability of HyMPSOM. The multi-modal contrast, either achieved label-free or by reading specifically designed labels, allowed HyMPSOM to conduct profound imaging studies across the scale from single-cells to large tissues yielding a so far unmet wealth of information. The technical extensions further broadened its scope of implementation and showcased alternative and innovative approaches for multi-modal microscopy. Finally, HyMPSOM evolved to a novel high-end microscope setup conquering performance limitations of current microscopy techniques by possessing unique properties of simultaneous multi-modal contrast, high spatial resolution applicable deep in tissue, high imaging speed associated with precisely adaptable scanning operations, and assessment of *in vitro*, *ex situ*, and *in vivo* specimens. Thus, HyMPSOM represents a highly promising platform for advanced microscopic research in future.

6.2 General outlook

HyMPSOM was shown to exceed current limitations of standard microscopy techniques by enabling simultaneous multi-modal contrast on the microscale with high resolution and high speed. By that, HyMPSOM already constitutes a high-end microscope with unique imaging capabilities so far not accessible in the field. However, HyMPSOM could be further improved in several aspects, which are delineated in the following.
Although the in here presented status of the optoacoustic modality of HyMPSOM shows a significant improvement compared to its prior version, several technical im-

provements could further enhance its performance. Currently, the imaging speed is limited by the maximum repetition rate provided by the optoacoustic laser. The integration of other laser sources offering higher repetition rates would accelerate the acquisition and, thus, would allow to investigate either fast dynamic processes like neuronal signaling or to image larger specimens like mouse brains. In this regard, HyMPSOM will be upgraded with a supercontinuum laser source allowing for repetition rates beyond 200 kHz. While the herein developed streaming-like acquisition mode was found to perform well up to ∼100 kHz, higher imaging speed would require to shift the scanning algorithm to faster programming languages such as C or C++. First attempts are already carried out in this regard but necessitate in-depth implementation. Moreover, the optoacoustically covered spectral range could be enlarged to exploit the intrinsic absorption characteristics of biomolecules more comprehensively. For that, the emission spectrum of the previously suggested supercontinuum laser spans up to the near-infrared range, which could enable to read vibrational overtones for label-free sensing of lipids, water, proteins, and carbohydrates. Even further extending the excitation wavelengths for optoacoustic microscopy towards the middle-infrared range could address the fundamental vibrational modes being assigned with absorption coefficients and spectral specificity so unique that even a distinction between different kinds of lipids or proteins is possible. This approach is currently carried out on a system developed alongside HyMPSOM, whereas mutual exchange among the systems help to better understand and improve their functionalities. Finally, the resolution limitation of optoacoustic microscopy could be broken by implementing super-resolution methods taken from fluorescence microscopy. As the signal generation in both modalities is based on an optical excitation, approaches for either spatially confining the excited volume in a stimulated-emission-depletion scheme or time-wise switching the investigated chromophores could be in general transferred to optoacoustic microscopy analogously. Both concepts are currently tested using specialized excitation sources such as the before mentioned supercontinuum laser.
Besides advancing on the optoacoustic microscopy part of HyMPSOM, the multi-photon modalities can be improved to grasp more information of the investigated specimen. As harmonic generation processes intrinsically depend on the orientation of the signal generating constituent, analyzing the signal's polarization could enlarge the extracted information regarding its microscopic organization. Furthermore, detecting the multi-photon excitation fluorescence signals with high-speed photon-counting modules would facilitate to study fluorescence lifetimes, which are in most cases unique for a given chromophore and, thus, could lead to an enhancement of the molecular specificity. In addition to upgrading the signal detection of the multi-photon sub-system, the integration of a tunable femtosecond laser could widen the addressed spectral range. By that, the intrinsic autofluorescence of biomolecules such as DNA or proteins could be targeted to increase the portfolio of imagable constituents. Finally, femtosecond lasers

emitting several tunable excitations could allow for installing additional microscopy modalities based on Raman transitions. Similar to the above suggested shift of optoacoustics towards the infrared spectral range, such modalities would enable molecular specificity based on reading the highly unique spectral fingerprints of biomolecules. Such Raman-based modalities are well established in the field of biomedical research and would optimally complement the existing imaging capabilities of HyMPSOM.
From the optical system's point of view, HyMPSOM could be improved by optimizing the multi-modal excitation, scanning, and detection scheme in general. In this regard, more advanced triggering schemes or shifting the operational mode entirely to the frequency domain would facilitate to read more modalities simultaneously. Whereas the concept of performing optoacoustic microscopy using frequency-domain or frequency-comb methods was showcased in here, similar approaches applied to the multi-photon modalities could simplify their concurrent application. With respect to improving the scanning method, faster laser-scanning units or advancing the optical excitation could overcome current limitations of HyMPSOM. On the one hand, micro-electro-mechanical systems would speed up the pixel scanning rate. On the other hand, the optical excitation could be amended either by integrating bessel-beams for increasing the lateral extent of the excited volume thereby allowing for faster 3D imaging or by applying a multifocal excitation for simultaneously interrogating various focal spots patterned across the specimen. Regarding the current detection scheme allowing already to apply up to four modalities at the same time, novel approaches for signal detection could enable HyMPSOM to be applied to so far unavailable specimens. For that, sensing all modalities in epi-mode, which was conceptualized in this work, and detecting optoacoustic signals without the need of a coupling medium would allow for studying thicker, dry, sensible, and/or fragile samples. As showcased in this work, optoacoustics can in general be detected using all-optical sensors, due to which their potential integration into e.g. the standardly used glass cover slides would ease the system adjustment and its scope of addressable specimens.
Apart from improving HyMPSOM technically, its current imaging capabilities pave the way for performing a huge variety of studies in the field of biological, biomedical, and translational research. As HyMPSOM facilitates measurements on the single-cell level, on small model organisms, and on tissue slices, various research targets could be addressed profoundly by applying HyMPSOM in its current state. Due to its speed, resolution, and multi-modal contrast, the field of studying neuronal dynamics can now be entered. Although HyMPSOM lacks in reading intrinsic neuronal contrast of e.g. the membrane potential, this could be either overcome by sensing potential-induced alterations of the vibrational mode of the lipid bilayer using near-infrared optoacoustics or by administering specified ion-selective contrast agents as exemplary outlined in this work. Furthermore, reading all desired modalities in epi-mode potentially allows to study specific parts of the human body such as the nailfold, which is a typical

assessment in dermatology. Finally, the execution of diverse imaging studies on HyMPSOM would expand its portfolio of novel insights to the microscopic world. As similar modalities exist on larger scales, such as optoacoustic and fluorescence tomography, microscopic findings of HyMPSOM can be linked to macroscopic examinations thereby reciprocally reinforcing the drawn conclusions.
Finally, HyMPSOM exemplary demonstrates how advanced multi-modal microscopy could become a versatile and substantial imaging tool for various scientific fields ranging from basic biological research over translational medicine to clinical practice. Further development towards increasing its usability and applicability as well as its performance in the scope of molecular imaging will render in the future the vast potential and broad range of applications of multi-modal microscopy.

Appendices

The appendices include on the one hand selected photographs of HyMPSOM regarding the optical setup as described in Section 4.2.3, the measurement setting for *in vitro* and *in vivo* specimens as described in Section 5.2 and used in Section 5.3, and the optoacoustic flow cytometry concept as described in Section 5.4.4. On the other hand, the appendices include the developed and utilized MATLAB™ scripts for controlling the HyMPSOM system. First, the script for the simultaneous multi-modal data acquisition and hybrid scanning is shown, which implements Section 4.2.4 and Section 4.2.5. Second, the script for the optoacoustic data processing and TIR correction is provided, which realizes Section 4.4.4. Third, the script used for simulating the optoacoustic TIR is given according to Section 4.4.3.

Photographs of the optical setup

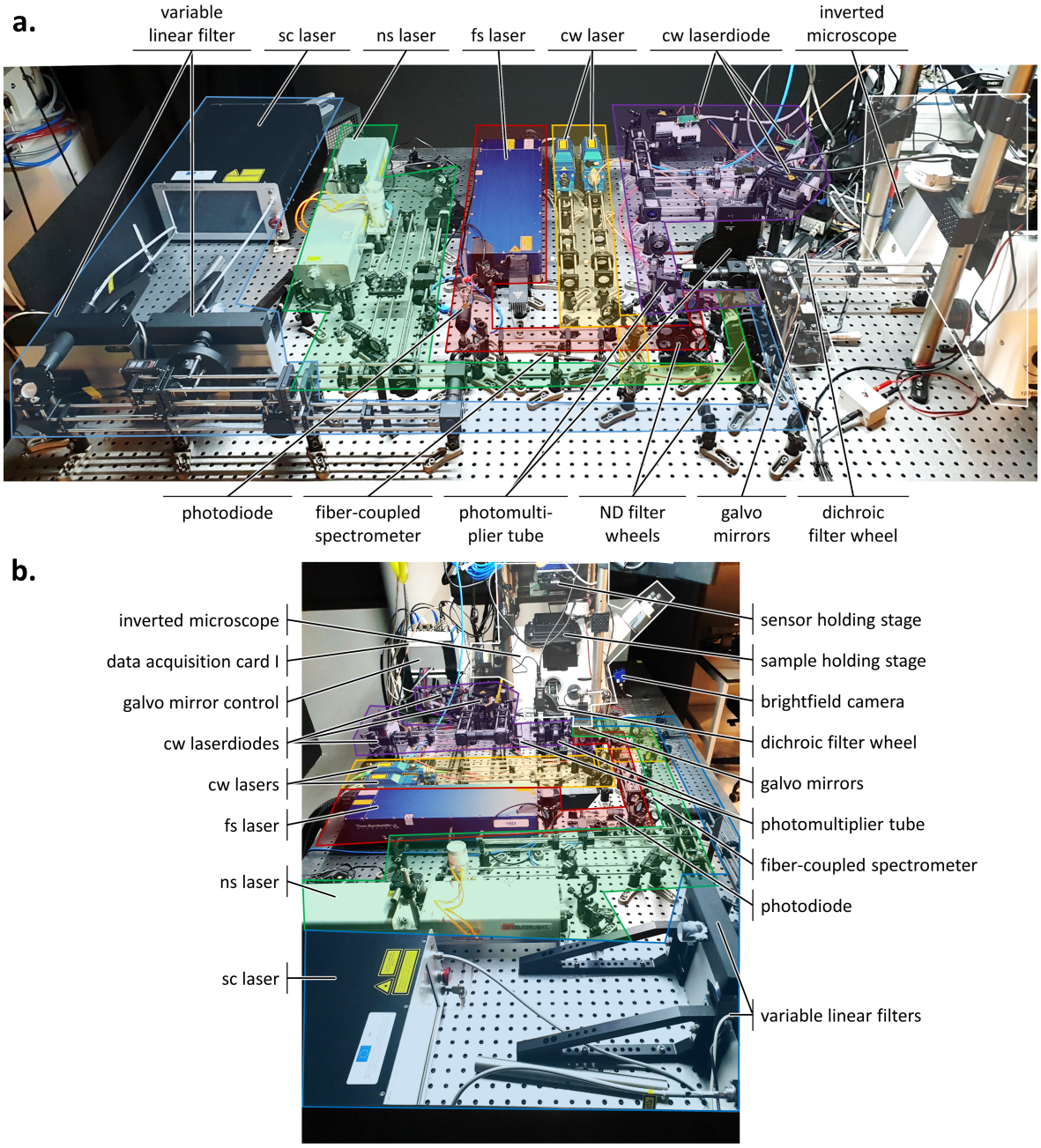

Figure A.1: Optical setup of the HyMPSOM system in **(a)** front and **(b)** side view including six sub-units highlighted in colored shades: white, central scanning unit (see Section 4.2); purple: ALEX or FComb optoacoustic microscopy (see Section 5.4.2); yellow: frequency-domain optoacoustic microscopy (see Section 5.4.1); red: multiphoton microscopy (see Section 4.2.1); green: time-domain optoacoustic microscopy (see Section 4.2.2); blue: spectral optoacoustic microscopy (see Section 4.5). Abbreviations: cw: continuous wave; fs: femtosecond; ND: neutral density; ns: nanosecond; sc: supercontinuum

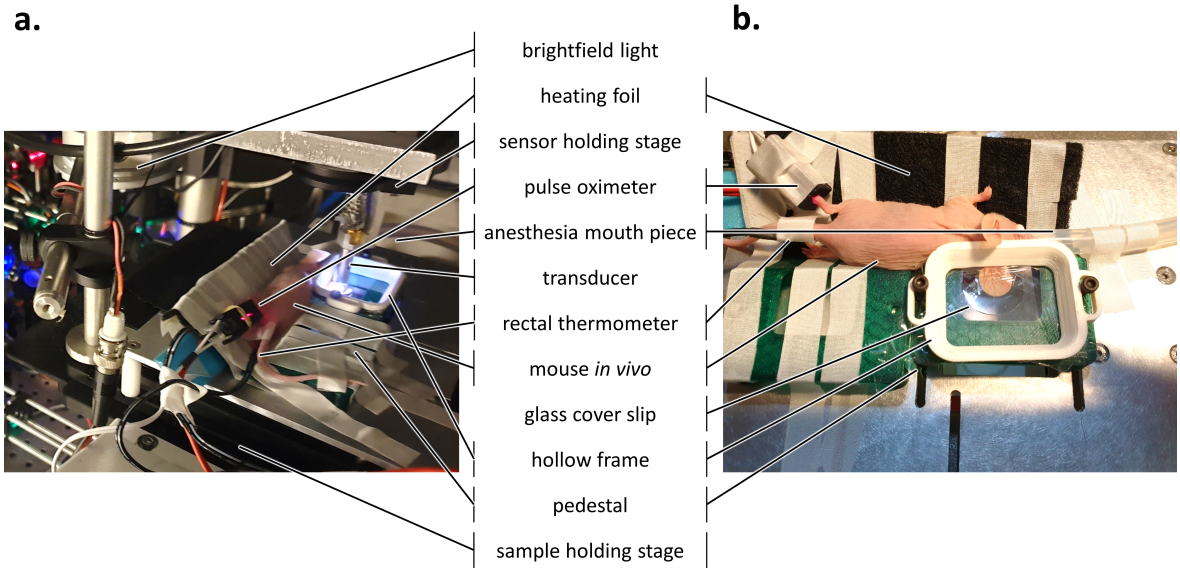

Figure A.2: Arrangement for *in vivo* mouse measurements for controlling and monitoring the physiological conditions of the investigated mouse such as the heart- and breathing rate, blood oxygenation, and body temperature (see Section 4.2.3 and Section 5.2.2). **(a)** Setup during ALEX optoacoustic microscopy (see Section 5.4.2) exemplary for all *in vivo* experiments. **(b)** Close-up of the mouse fixation in the custom-designed holder.

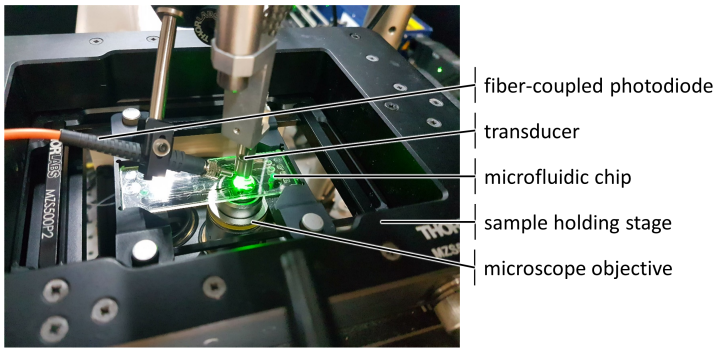

Figure A.3: Arrangement for optoacoustic flow cytometry measurements for detecting in-flow optoacoustic and light-scattering signals of chromoproteins expressed in *E. coli* cells flushed through a microfluidic chip (see Section 5.4.4).

MATLAB™ scripts

Simultaneous multi-modal data acquisition and hybrid scanning

```
% ========================================================================
% INPUT
% ========================================================================
% th:     handle for Thorlabs stages;
% trigf: trigger frequency
% aAvg:  auto averaging
% nF:     number of frames

function [Raw_, S_] = ScanCMRhy_Galvos_AT_MF(th, trigf, aAvg, nF)
global NI_BG        % global parameter for NI background
                    % acquisition of Galvo Feedback

if nargin < 4
    nF =  1;        % [# of Frames]
end

if nargin < 3
    aAvg =  5;      % [# of CMR records per Galvo position] auto-Average
end

if nargin < 2
    trigf =  50e3; % Scanning frequency for active triggering
end

if nargin < 1
   th = aptInit(0,1);
end

% ========================================================================
% SETTINGS
% ========================================================================

    saveOAFlag      = 1;    % save acquired data
    saveMPMFlag     = 1;    % save norm. MPM images

    saveRawOAFlag   = 0;    % save raw OA data
    saveRawMPMFlag  = 0;    % save raw MPM data

    adjustFlag      = 1;    % [1] acquire at 450 MS/s and larger B-Scans
                            % [0] at 900 MS/s
                            % [2] at 112.5 MS/s
                            % [3] at 225 MS/s
                            % [4] at 1800 MS/s
    reconFlag       = 1;    % reconstruct data
```

```
45      rotFlag          = 3;     % rotate Final Image: 0: Stage Scanning;
46                                %                     3: Galvo Scanning
47      BGsubFlag        = 0;     % substract value of 10% of histogram
48      PlotFlag         = 1;     % Plot MPM images
49
50  % Galvo scan parameters
51      resolutionx  = 800;       % [# pixels per line in x] - Th Stage
52      resolutiony  = 200;       % [# pixels per line in y] - Galvos
53      galvoVoltage = 2;         % [V] max. 2.0 (~630 um)
54      peakWidth    = 2;         % [# of CMR records] Half galvo feedback
55                                % peak width for pixel assignment
56      jogx         = resolutionx/resolutiony*0.630;
57                                % [mm] jog step of Th Movement
58      jogy         = 0;         % [mm] jog step of Th Movement
59      jogvel       = jogx/((resolutionx*resolutiony*(aAvg+peakWidth))...
60                       /trigf); % [mm/s] jog velocity of Th Movement
61
62      savePath     = 'M:\Data\';
63      saveName     = 'TD_MM_TestScan';
64
65      a = 1;
66      b = 0;
67
68      aptSetVelocity(th, 1);
69      aptMoveJogX(th, -jogx/2);                % Move Th-X axis out of ROI
70      aptMoveJogY(th, -jogy/2);                % Move Th-X axis out of ROI
71      pause(1)
72
73  % ========================================================================
74  % DAQ1 SETUP
75  % ========================================================================
76
77  % add Parameter to SaveName
78      saveName     = [saveName num2str(resolutionx) 'x'...
79                      num2str(resolutiony) 'res_'...
80                      num2str(10*galvoVoltage) 'GV_'...
81                      num2str(jogx*1000) 'ThX_'...
82                      num2str(round(jogvel*1000)) 'ThXvel_'...
83                      num2str(trigf/1e3) 'kHz_'...
84                      num2str(aAvg) 'Avg_'...
85                      num2str(nF) 'f_'...
86                      num2str(int16(trigf*60/(aAvg*resolutionx^2))) 'fpm'];
87
88  % Galvo Settings
89      maxtrigf = 50e3;                 % [Hz] max. trigger frequency
90      maxscanf = 10;                   % [Hz] max. scanning frequency
91      trigf = trigf*2;                 % correct for digital output
92      aAvg = (aAvg+peakWidth)*2;       % [# of CMR records per Galvo
```

```
93                                      % position] auto-Average enlarged
94                                      % by cutting off movement records
95
96  % Set up NI DAQ Card (galvo waveforms):
97      s = daq.createSession('ni');
98          % NI-session
99      s.addAnalogOutputChannel('Dev1', 0, 'Voltage');
100         % Output 1: X - slow
101     s.addAnalogOutputChannel('Dev1', 1, 'Voltage');
102         % Output 2: Y - fast
103     s.addDigitalChannel('Dev1', 'Port0/Line0', 'OutputOnly');
104         % Output Dig: TTL for Laser
105     s.addDigitalChannel('Dev1', 'Port0/Line1', 'OutputOnly');
106         % Output Dig: TTL for OA Acquisition
107     s.addAnalogInputChannel('Dev1', 0, 'Voltage');
108         % Input 0: Channel A (THG)
109     s.addAnalogInputChannel('Dev1', 1, 'Voltage');
110         % Input 1: CHannel B (SHG, 3PEF)
111     s.addAnalogInputChannel('Dev1', 2, 'Voltage');
112         % Input 2: CHannel C (2PEF)
113
114 % Initialize Galvos, Move to first position
115     s.outputSingleScan([0 0 0 0]);      % set to 0 to all channels
116     s.Rate = trigf;                     % set scanning frequency
117
118 % Create XY-Waveforms for galvos
119     Xwaveform = zeros([resolutionx, resolutiony*aAvg]);
120     Ywaveform = zeros([resolutionx, resolutiony*aAvg]);
121
122 % Create X-waveform (step function - slow axis)
123     Voltage = galvoVoltage;
124
125     Ypos = linspace(Voltage, -Voltage, resolutiony);
126     Yneg = linspace(-Voltage, Voltage, resolutiony);
127     Xpos = linspace(Voltage, -Voltage, resolutionx);
128     Xneg = linspace(-Voltage, Voltage, resolutionx);
129
130 for ii = 1:resolutiony*aAvg
131     for k = 1:resolutionx
132         if jogx == 0;
133         Xwaveform(k,ii) = Xpos(k);
134         else
135         Xwaveform(k,ii) = 0;
136         end
137     end
138 end
139
140 % Create Y-waveform (triangle function - fast axis):
```

```
141 for ii = 1:resolutionx
142     if rem(ii,2) == 0
143         for k = 1:resolutiony
144             Ywaveform(ii,k*aAvg-(aAvg-1):k*aAvg) = Yneg(k);
145         end
146     else
147         for k = 1:resolutiony
148             Ywaveform(ii,k*aAvg-(aAvg-1):k*aAvg) = Ypos(k);
149         end
150     end
151 end
152
153 % Create digital waveform (TTL - laser):
154 dig = ones(size(Xwaveform,1),size(Xwaveform,2));
155 for ii = 1:size(Xwaveform,1);
156     for jj = 1: size(Xwaveform,2)/2;
157     dig(ii,jj*2)=0;
158     end
159 end
160
161 % Safety Check
162 if trigf/2/(aAvg/2*resolutiony^2) > maxscanf;
163     return
164 end
165
166 if trigf/2 > maxtrigf;
167     return
168 end
169
170 % Repeat waveforms according to Number of Frames:
171     Xwaveform = repmat(Xwaveform,[nF,1]);
172     Ywaveform = repmat(Ywaveform,[nF,1]);
173     dig = repmat(dig,[nF,1]);
174
175     Xwaveform = reshape(Xwaveform',[],1);
176     Ywaveform = reshape(Ywaveform',[],1);
177     dig = reshape(dig',[],1);
178
179 % Queue Waveforms
180     s.queueOutputData([Ywaveform Xwaveform dig dig]);
181
182 % ================================================================
183 % DAQ2 SETUP
184 % ================================================================
185
186 % Set CMR parameter
187     boardSN          = 'SPD-02808'; % initialize CSU DAQ
188     aAvg             = aAvg/2;      % compensate for digital output
```

```
189     nRecords        = nF*aAvg*resolutionx*resolutiony;
190                                 % total number of records
191     nofbufrecords   = 4096*2;   % number of buffered records
192                                 % = max size for fetching loop
193     trigMode        = 3;        % trigger Mode:
194                                 % 2: external trigger,
195                                 % 3: level trigger
196     trigLevel       = 1200;     % trigger threshold level
197     trigChannel     = 2;        % trigger channel
198
199 if adjustFlag == 0;
200     fsDiv           = 2;        % sampling skip
201     Fs              = 1800/fsDiv; % Actual sampling frequency
202     nSamples        = 256;      % Number of samples in each record
203     mrinfo          = 2;        % Setting CMR-Mode
204     trigDelay       = 1024;     % trigger delay
205
206 elseif adjustFlag == 1;
207     fsDiv           = 4;        % sampling skip
208     Fs              = 1800/fsDiv; % Actual sampling frequency
209     nSamples        = 256;      % Number of samples in each record
210     mrinfo          = 7;        % Setting CMR-Mode
211     trigDelay       = 1024+256; % trigger delay
212
213 elseif adjustFlag == 2;
214     fsDiv           = 16;       % sampling skip
215     Fs              = 1800/fsDiv; % Actual sampling frequency
216     nSamples        = 512;      % Number of samples in each record
217     mrinfo          = 2;        % Setting CMR-Mode
218     trigDelay       = 256;      % trigger delay
219
220 elseif adjustFlag == 3;
221     fsDiv           = 8;        % sampling skip
222     Fs              = 1800/fsDiv; % Actual sampling frequency
223     nSamples        = 128;      % Number of samples in each record
224     mrinfo          = 2;        % Setting CMR-Mode
225     trigDelay       = 512+128;  % trigger delay
226
227 elseif adjustFlag == 4;
228     fsDiv           = 1;        % sampling skip
229     Fs              = 1800/fsDiv; % Actual sampling frequency
230     nSamples        = 256+128;  % Number of samples in each record
231     mrinfo          = 2;        % Setting CMR-Mode
232     trigDelay       = 4096+1024+256;% trigger delay
233 end
234
235 if fsDiv == 2; % disbale MultiRecordModeDisablePretrigger for 900 MSps
236     mrinfo = 2;
```

```
237 end
238
239 % Set DAQ parameters
240     Setup_PAM(boardSN, fsDiv, trigMode, trigLevel, trigChannel);
241
242 % Set trigger delay
243     spdSetTrigDelay(boardSN, trigDelay);
244
245 % setup acquisition
246     spdSetMultiRecGP(boardSN, nofbufrecords, nSamples, mrinfo);
247
248 % initialize record matrices
249     Raw1 = zeros(int64(nRecords), int64(nSamples), 'int16');    % OAM data
250
251 % ================================================================
252 % DATA ACQUISITION
253 % ================================================================
254
255 if saveOAFlag
256     TotalRecords = 0;
257 % listener for NI-DAQ meanwhile to CMR in Background mode
258     lh = s.addlistener('DataAvailable', @GetNIBG);
259         s.NotifyWhenDataAvailableExceeds =...
260             4e4*(resolutionx/resolutiony);
261
262 % Initialize variables for CMR
263     quitflag            = 0;        % quitflag for CMR
264     lastread_loop       = 0;        % index of last fetched loop
265     lastread_record     = 0;        % index of last fetched record
266     TotalRead           = 0;        % Total number of fetched records
267     max_buffer_used     = 0;        % size of used buffer
268     max_chunk_records   = 2048*4;   % maximum number of records
269                                     % organized as a chunk-unit
270     lastprintedavail    = 0;
271
272 % Rearm the trigger (Start acquisition):
273     spdArmTrig(boardSN,0);          % Rearm CMR
274     spdArmTrig(boardSN,1);
275
276     s.startBackground();            % start Galvo Scan in Background
277     aptSetVelocity(th, jogvel);
278     aptMoveJogX(th, jogx);          % Move Th-X axis
279     aptMoveJogY(th, jogy);          % Move Th-X axis
280
281 while ((quitflag == 0) && (TotalRead < nRecords))
282
283 % Call Board API GetAcquiredRecordsAndLoopCounter to be able to
284 % calculate the number of records ready for readout
```

```
285     [d1, d1, status]=interface_ADQ('GetAcquiredRecordsAndLoopCounter',...
286         boardSN);
287
288 % Calculate the number of records available for readout
289     records     = double(status(3));
290     loops       = double(status(2));
291     real_loops  = double((uint8(loops) - uint8(lastread_loop)));
292     avail       = records - lastread_record;
293     availtmr    = double(real_loops) * double(nofbufrecords);
294     avail       = avail + availtmr;
295
296     if (avail < 0)
297         avail = avail + nofbufrecords;
298     end
299
300 % Store how much of the DRAM buffer that was used this time
301     if (avail > max_buffer_used)
302         max_buffer_used = avail;
303     end
304
305 % Check Readout Overflow
306     if ((avail > 0) || (lastprintedavail ~= 0))
307         lastprintedavail = avail;
308         ovf = interface_ADQ('getstreamoverflow', boardSN);
309         if (ovf == 1)
310             fprintf('ERROR: Readout overflow detected! Aborting.\n');
311             avail = 0;
312             quitflag = 1;
313         end
314     end
315
316 % Check if buffer was overrun
317     if (avail >= nRecords)
318         fprintf('OVERFLOW: Data is overwritten! Aborting.\n');
319         avail = 0;
320         quitflag = 1;
321     end
322
323 % ========================================================================
324 % FETCHING
325 % ========================================================================
326
327 % Enter readout if there are any available records
328     while (avail > 0)
329
330         % Calculate which records to read
331         read_index = lastread_record;
332         lastrecord = read_index + avail - 1;
```

```
333             if (lastrecord > ((nofbufrecords-1)))
334                 lastrecord = nofbufrecords - 1;
335             end
336 
337             avail_limited = lastrecord - read_index + 1;
338 
339             % Available is more than defined max_chunk,
340             % read maximum of max_chunk records
341             if (avail_limited > max_chunk_records)
342                 avail_limited = max_chunk_records;
343             end
344 
345           % Fetch data in chunks of records
346             [sA] = spdGetDataCMR(boardSN, max_chunk_records, read_index,...
347                     avail_limited, nSamples);
348 
349           % build up matrix of all records
350             Raw1(TotalRead+1:TotalRead+size(sA,1), 1:size(sA,2))= sA;  % OAM
351            % Raw2(TotalRead+1:TotalRead+size(sB,1), 1:size(sB,2))= sB; % LS
352 
353           % Decrease the number of available records with the readout amount
354             avail = avail - avail_limited;
355 
356           % Store which record was the last one read
357             lastread_record = lastread_record + avail_limited;
358             TotalRead =  TotalRead + avail_limited;
359 
360             if (lastread_record >= nofbufrecords)
361                 lastread_record = lastread_record - nofbufrecords;
362                 lastread_loop = lastread_loop + 1;
363             end
364         end
365 end
366 
367     stop(s);            % terminate Galvo queue
368     TotalRecords = TotalRecords + TotalRead;
369 
370 % Close multirecord
371     interface_ADQ('multirecordclose', boardSN);
372 
373 % Prepare matrices for processing
374     S = zeros(int64(resolutionx*resolutiony), int64(nSamples), nF, '
            single');
375     MPM_1 = zeros(int64(resolutionx*resolutiony), 1, nF, 'single');
376     MPM_2 = zeros(int64(resolutionx*resolutiony), 1, nF, 'single');
377     MPM_3 = zeros(int64(resolutionx*resolutiony), 1, nF, 'single');
378 
379 % ================================================================
```

```
380 % ASSIGN
381 % ================================================================
382
383 % Assign recorded CMR signals to galvo positions
384 for ff = 1:nF;
385     % Average records for each pixel with cutting off transitions records
386     for ii = 1:(resolutionx*resolutiony)-a;
387         S(ii+a,:,ff)=sum(Raw1((ii+b)*aAvg+peakWidth+((ff-1)*aAvg...
388             *(resolutionx*resolutiony)):(ii+b+1)*aAvg-peakWidth+1+...
389             ((ff-1)*aAvg*(resolutionx*resolutiony)),:),1);
390     end
391 end
392 S = S/(aAvg-peakWidth);
393 end
394
395 % ================================================================
396 % FETCH MPM
397 % ================================================================
398
399 if saveMPMFlag
400   % Generate MPM images
401     NI_BG = NI_BG(end-TotalRead*2:2:end,:);
402
403   % Assign recorded MP signals to galvo position
404     for ff = 1:nF;
405     % Average records for each pixel with cutting off transitions records
406     for ii = 1:(resolutionx*resolutiony)-a;
407         MPM_1(ii+a,:,ff)=sum(NI_BG((ii+b)*aAvg+peakWidth+((ff-1)*...
408             aAvg*(resolutionx*resolutiony)):(ii+b+1)*aAvg-peakWidth+...
409             1+((ff-1)*aAvg*(resolutionx*resolutiony)),1),1);
410         MPM_2(ii+a,:,ff)=sum(NI_BG((ii+b)*aAvg+peakWidth+((ff-1)*...
411             aAvg*(resolutionx*resolutiony)):(ii+b+1)*aAvg-peakWidth+...
412             1+((ff-1)*aAvg*(resolutionx*resolutiony)),2),1);
413         MPM_3(ii+a,:,ff)=sum(NI_BG((ii+b)*aAvg+peakWidth+((ff-1)*...
414             aAvg*(resolutionx*resolutiony)):(ii+b+1)*aAvg-peakWidth+...
415             1+((ff-1)*aAvg*(resolutionx*resolutiony)),3),1);
416     end
417     end
418
419     MPM_1 = MPM_1/(aAvg-peakWidth);
420     MPM_2 = MPM_2/(aAvg-peakWidth);
421     MPM_3 = MPM_3/(aAvg-peakWidth);
422
423     MPM_1 = reshape(MPM_1, resolutiony, resolutionx, nF);
424     MPM_2 = reshape(MPM_2, resolutiony, resolutionx, nF);
425     MPM_3 = reshape(MPM_3, resolutiony, resolutionx, nF);
426
427     MPM_1(:,2:2:end,:)=flipud(MPM_1(:,2:2:end,:));
```

```
428     MPM_2(:,2:2:end,:)=flipud(MPM_2(:,2:2:end,:));
429     MPM_3(:,2:2:end,:)=flipud(MPM_3(:,2:2:end,:));
430
431     MPM_1 = rot90(MPM_1,rotFlag);
432     MPM_2 = rot90(MPM_2,rotFlag);
433     MPM_3 = rot90(MPM_3,rotFlag);
434
435     MPM(:,:,1,ff)=MPM_1(:,:,ff);
436     MPM(:,:,2,ff)=MPM_2(:,:,ff);
437     MPM(:,:,3,ff)=MPM_3(:,:,ff);
438
439     if BGsubFlag
440         val = sort(MPM_1(:),'ascend');
441         MPM_1(:) = MPM_1(:)-val(round(size(val,1)/10));
442
443         val = sort(MPM_2(:),'ascend');
444         MPM_2(:) = MPM_2(:)-val(round(size(val,1)/10));
445
446         val = sort(MPM_3(:),'ascend');
447         MPM_3(:) = MPM_3(:)-val(round(size(val,1)/10));
448
449         MPM_1(MPM_1<0)=0;
450         MPM_2(MPM_2<0)=0;
451         MPM_3(MPM_3<0)=0;
452     end
453
454 % ================================================================
455 % VISUALISATION
456 % ================================================================
457
458     if nF > 1;
459     PlotFlag = 0;
460     end
461
462     for ff = 1:nF;
463     if PlotFlag
464
465         figRes=figure;
466         subplot(1,4,2);
467         imagesc([-galvoVoltage*159 galvoVoltage*159],...
468                 [-jogx*500 jogx*500], MPM(:,:,1,ff)); colorbar;
469         xlabel(gca, 'y (a.u.)', 'FontWeight', 'bold', 'units',...
470                     'normalized', 'FontSize', 12);
471         ylabel(gca, 'x (a.u.)', 'FontWeight', 'bold', 'units',...
472                     'normalized', 'FontSize', 12);
473         axis image
474         set(gcf, 'Position', get(0, 'Screensize'));
475
```

```
476         figure(figRes);
477         subplot(1,4,3);
478         imagesc([-galvoVoltage*159 galvoVoltage*159],...
479                 [-jogx*500 jogx*500], MPM(:,:,2,ff)); colorbar;
480         xlabel(gca, 'y (a.u.)', 'FontWeight', 'bold', 'units',...
481                     'normalized', 'FontSize', 12);
482         ylabel(gca, 'x (a.u.)', 'FontWeight', 'bold', 'units',...
483                     'normalized', 'FontSize', 12);
484         axis image
485         set(gcf, 'Position', get(0, 'Screensize'));
486 
487         figure(figRes);  fprint
488         subplot(1,4,4);
489         imagesc([-galvoVoltage*159 galvoVoltage*159],...
490                 [-jogx*500 jogx*500], MPM(:,:,3,ff)); colorbar;
491         xlabel(gca, 'y (a.u.)', 'FontWeight', 'bold', 'units',...
492                     'normalized', 'FontSize', 12);
493         ylabel(gca, 'x (a.u.)', 'FontWeight', 'bold', 'units',...
494                     'normalized', 'FontSize', 12);
495         axis image
496         set(gcf, 'Position', get(0, 'Screensize'));
497 
498     end
499     MPM(:,:,1,ff)=MPM_1(:,:,ff);
500     MPM(:,:,2,ff)=MPM_2(:,:,ff);
501     MPM(:,:,3,ff)=MPM_3(:,:,ff);
502 
503     MPM_1 = MPM_1./max(max(max(MPM_1)));
504     MPM_2 = MPM_2./max(max(max(MPM_2)));
505     MPM_3 = MPM_3./max(max(max(MPM_3)));
506 
507     end
508 
509 end
510 
511 % ================================================================
512 % SAVING
513 % ================================================================
514 
515     cdat = clock;
516     if cdat(2) < 10
517         cdate = [num2str(cdat(1)) '0' num2str(cdat(2))];
518     else
519         cdate = [num2str(cdat(1)) num2str(cdat(2))];
520     end
521     if cdat(3) < 10
522         cdate = [cdate '0' num2str(cdat(3))];
523     else
```

```
524             cdate = [cdate num2str(cdat(3))];
525         end
526 
527         trigf=trigf/2;
528         savePath = [savePath saveName '\'];
529         mkdir(savePath);
530 
531     if saveOAFlag
532         savePathOA = [savePath 'OA\'];
533         mkdir(savePathOA);
534         saveDat = [savePathOA cdate '_' saveName];
535         savefast(saveDat, 'S', 'trigDelay', 'Fs', ...
536             'resolutionx', 'resolutiony', ...
537             'trigf', 'galvoVoltage', 'aAvg', 'nF', ...
538             'peakWidth', 'jogx', 'jogy', 'jogvel', ...
539             'nSamples', 'nRecords', 'TotalRead');  %'-v7.3'
540     end
541 
542     if saveRawOAFlag
543         savePathOA = [savePath 'OA\'];
544         mkdir(savePathOA);
545         saveDat = [savePathOA cdate '_' saveName '_Raw_OA'];
546         savefast(saveDat, 'Raw1');  %'-v7.3'
547     end
548 
549     if saveRawMPMFlag
550         savePathMPM = [savePath 'MPM\'];
551         mkdir(savePathMPM);
552         saveDat = [savePathMPM cdate '_' saveName '_Raw_MPM'];
553         savefast(saveDat, 'MPM_1', 'MPM_2', 'MPM_3', 'MPM', 'NI_BG');  %'-v7
                .3'
554     end
555 
556 % ================================================================
557 % RECONSTRUCTION OA
558 % ================================================================
559 
560     if reconFlag
561       % Build final image
562         reconFOC_GalvosCMRhy_MF(savePath, saveName, [cdate '_' saveName],...
563                                 savePathOA, figRes, S, Fs, nF, 3);
564     end
565 
566 % ================================================================
567 % RECONSTRUCTION MPM
568 % ================================================================
569 
570     if saveMPMFlag
```

```
571         savePathMPM = [savePath 'MPM\'];
572         mkdir(savePathMPM);
573         for ff = 1:nF
574             imwrite(rot90(MPM_1(:,:,ff),3), [savePathMPM 'r_' cdate...
575                 '_' saveName '_MPM_Ch1_F' num2str(ff) '.png'], 'png');
576             imwrite(rot90(MPM_2(:,:,ff),3), [savePathMPM 'r_' cdate...
577                 '_' saveName '_MPM_Ch2_F' num2str(ff) '.png'], 'png');
578             imwrite(rot90(MPM_3(:,:,ff),3), [savePathMPM 'r_' cdate...
579                 '_' saveName '_MPM_Ch3_F' num2str(ff) '.png'], 'png');
580             imwrite(uint16(1000.*MPM(:,:,1,ff)),[savePath saveName...
581                 '_MM_F' num2str(ff) '.tiff'], 'tiff', 'writemode', 'append');
582             imwrite(uint16(1000.*MPM(:,:,2,ff)),[savePath saveName...
583                 '_MM_F' num2str(ff) '.tiff'], 'tiff', 'writemode', 'append');
584             imwrite(uint16(1000.*MPM(:,:,3,ff)),[savePath saveName...
585                 '_MM_F' num2str(ff) '.tiff'], 'tiff', 'writemode', 'append');
586         end
587     end
588
589     %% ========================================================================
590     % RESET HYBRID SCANNING
591     %% ========================================================================
592
593         aptSetVelocity(th, 1);
594         aptMoveJogX(th, -jogx/2);                   % Move Th-X axis
595         aptMoveJogY(th, -jogy/2);                   % Move Th-Y axis
596
597     %% ========================================================================
598     % OUTPUT
599     %% ========================================================================
600
601     if nargout == 2
602         Raw_ = Raw1;
603         S_ = S;
604     end
605     end
```

Optoacoustic data processing and TIR correction

```
% ========================================================================
% INPUT
% ========================================================================
% SavePath: directory for saving reconstructed data
% saveName: file name for saving reconstructed data
% DataName: file name of acquired data
% DataPath: directory of acquired data
% figRes:   figure-handle for multimodal acquisition
% S:        assigned and averaged data matrix
% Fs:       sampling frequency
% nF:       number of frames
% plotAxis: orientation for visualization

function [R_, H_] = reconFOC_GalvosCMR_MF...
    (SavePath,saveName,DataName, DataPath, figRes, S, Fs, nF, plotAxis)

SFlag = 1;

if nargin < 9
    plotAxis = 3;       % orientation for visualization
end

if nargin < 8
    nF = 1;             % number of frames
end

if nargin < 7
    Fs = 900;           % sampling frequency
end

if nargin < 6
    SFlag = 0;          % assigned and averaged data matrix
end

if nargin < 5
    figRes = figure;% figure-handle for multimodal acquisition
end

if nargin < 4
    DataPath = 'M:\Data\';
end

if nargin < 1
    DataName = 'TD_MM_TestScan';
end

```

```
47 if nargin < 3
48     saveName = DataName;
49 end
50
51 if nargin < 2
52     SavePath = DataPath;
53 end
54
55 SavePathOA = DataPath;
56 ReconExt = '';
57
58 if SFlag == 1;
59         load([DataPath DataName], '-regexp', '^(?!S)\w')
60 elseif SFlag == 0;
61         load([DataPath DataName])
62 end
63
64 % load Data
65 load([DataPath DataName])
66 % define directory for TIR data
67 DataTIRPath = 'M:\Data\';
68 DataTIRName = 'r_TD_MM_TIR';
69
70 % ================================================================
71 % SETTINGS
72 % ================================================================
73
74 resolution = sqrt(size(S,1));
75 first = 1;
76 S(1:resolution^2-first+1,:,:) = S(first:resolution^2,:,:);
77
78 % Reconstruction Flags:
79 rotFlag          = 3;    % rotate Final Image
80 PlotFlag         = 1;    % Plot reconstructed image
81 RawFlag          = 1;    % Plot raw BScan
82 cutFlag          = 0;    % Cut BScan-matrix
83 HilbertFlag      = 1;    % Envelope signal
84 ZStackFlag       = 0;    % Create Z Stack (only with Hilbert)
85
86 CorrectToFFlag  = 1;    % Correct ToF of OA signals
87 CorrectdBFlag   = 0;    % Correct reconstruction bounds according to TIR
88 CorrectTIRFlag  = 0;    % Apply spatial matched filter to raw A-lines
89                         % with corresponding TIR
90
91 FilterFlag      = 1;    % Bandpass filter - 1: asymmetric, 2: symmetric
92 SaveImageFlag   = 1;    % Save projection as image
93
94 R_Format        ='double';      % 'int16' / double
```

```
95
96  f_BP = [5  110]*1e6;      % [MHz] Transducer bandwidth
97
98  if CorrectdBFlag == 1;
99      [XX,YY] = meshgrid(100/resolution:100/resolution:100);
100     f_BP (:,:,1) = interp2(SFdBbound(:,:,1),XX,YY);
101     f_BP (:,:,2) = interp2(SFdBbound(:,:,2),XX,YY);
102 end
103
104 % ================================================================
105 % SETUP RECONSTRUCTION
106 % ================================================================
107
108 Fs = Fs*1e6;
109 defocus = 700;
110 focal_dist = 2850;
111
112 NSamples = size(S,2);
113 NPoints  = size(S,1);
114
115 dt = 1/Fs;
116
117 t = 0:dt:(NSamples-1)*dt;
118 t = t + trigDelay*dt;
                                                        % Add
    trigger delay offset to each entry
119
120 Nx = resolution;
121 Ny = resolution;
122
123 % ================================================================
124 % APPLY FREQUENCY BANDPASS FILTER
125 % ================================================================
126
127 if FilterFlag
128         S = permute(S,[2  1  3]);
129         NRows  = 4000;

              % Number of signals to be filtered simultaneously
130         NIterations = ceil(NPoints/NRows);
131         f = linspace(-Fs/2, Fs/2, length(t)); f = f';
132
133         switch FilterFlag
134             case 1
135                 filtOrder = 6;
136                 filtArray = (exp(-(f/f_BP(2)).^filtOrder)) ...
137                           .* (1-(exp(-(f/f_BP(1)).^filtOrder)));
138                 filtArray = repmat(filtArray, 1, NRows);
```

```
139             case 2
140                 filtOrder = 8;
141                 sig       = 1/2*diff(f_BP)/(log(2)^(1/filtOrder));
142                 filt      = max(exp(-((f-mean(f_BP))/sig).^filtOrder) ,...
143                             exp(-((f+mean(f_BP))/sig).^filtOrder));
144                 filtArray = repmat(filt , 1, NRows);
145         end
146
147         % Take fourier transform of the signals (FFT)
148         for ii = 1:NIterations
149             SS = S(:, (ii-1)*NRows+1:min(ii*NRows, NPoints) ,:);
150             SS = fftshift(fft(ifftshift(SS, 1), [], 1), 1);
151
152             if NIterations == ii
153                 filtArray = filtArray(:, 1:size(SS, 2));
154             end
155
156         % Multiply with f-window and transform back to time domain (iFFT)
157             for ff = 1:nF;
158             SS(:,:,ff) = real(fftshift(ifft(ifftshift(SS(:,:,ff).*...
159                          filtArray , 1), [], 1), 1));
160             end
161             S(:, (ii-1)*NRows+1:min(ii*NRows, NPoints) ,:) = SS;
162
163         end
164
165         S = permute(S,[2 1 3]);
166         clear filtArray SS;
167 end
168
169 if cutFlag
170       S = S(:,61:end-60,:);
171       NSamples = size(S,2);
172 end
173
174 if (RawFlag == 1) && (CorrectTIRFlag == 0);
175     figure;
176     imagesc([], [], S(:,:,1)); colormap gray;
177     [cut1,cut2]=ginput;
178     cut1 = int16(cut1);
179 else
180     cut1 =[1,NSamples];
181 end
182
183 % ========================================================================
184 % PROCESS WITHOUT TIR CORRECTION
185 % ========================================================================
186
```

```
187 % Apply Hilbert transform
188     if CorrectTIRFlag == 0;
189         if HilbertFlag
190             S = double(S);
191     for i=1:NPoints
192          S(i,:,:) = abs(hilbert(S(i,:,:)));
193     end
194         end
195
196 % Sort signals
197 R_data  = zeros(Nx, Ny, NSamples, nF, R_Format);
198
199     if exist('ContScan', 'var') == 0
200         for i = 1:Ny
201             if rem(i,2) == 0
202             s = S((i-1)*Nx+1:i*Nx,:,:);
203
204             S((i-1)*Nx+1:i*Nx,:,:) = s(end:-1:1,:,:);
205             end
206         end
207     end
208
209 R_data = reshape(S, Nx, Ny, NSamples, nF);
210
211     if CorrectToFFlag
212         for ii = 1:resolution
213             for jj = 1:resolution
214             dist = sqrt((resolution/2-ii+1)^2+(resolution/2-jj+1)^2);
215             dist=int16(2*((abs((focal_dist+defocus)...
216                 -sqrt((dist*galvoVoltage*315/resolution)^2...
217                 +(focal_dist+defocus)^2)))/1.5e9*Fs));
218             R_data(ii,jj,1:int16(size(R_data,3)-dist),:)...
219                 = R_data(ii,jj,int16(dist+1):end,:);
220             end
221         end
222     end
223
224 %=========================================================
225 % PROCESS WITH TIR CORRECTION
226 %=========================================================
227
228 elseif CorrectTIRFlag == 1;
229     R_data = reshape(S, Nx, Ny, NSamples, nF);
230
231     if CorrectToFFlag
232         for ii = 1:resolution
233             for jj = 1:resolution
234             dist = sqrt((resolution/2-ii+1)^2+(resolution/2-jj+1)^2);
```

```
235             dist=int16(2*((abs((focal_dist+defocus)...
236                 -sqrt((dist*galvoVoltage*315/resolution)^2...
237                 +(focal_dist+defocus)^2)))/1.5e9*Fs));
238             R_data(ii,jj,1:int16(size(R_data,3)-dist),:)...
239                 = R_data(ii,jj,int16(dist+1):end,:);
240             end
241         end
242     end
243
244   % load corresponding TIR data
245     load([DataTIRPath DataTIRName])
246   % Interpolate TIR matrix to data matrix dimensions
247     [XX,YY,ZZ] = meshgrid(1:(size(R,1)-1)/(resolution-1):size(R,1),...
248                   1:(size(R,1)-1)/(resolution-1):size(R,2), 1:1:size(R,3));
249     R_TIR = interp3(R,XX,YY,ZZ);
250   % Interpolate data matrix to TIR matrix sampling
251     [XX,YY,ZZ] = meshgrid(1:1:size(R_data,1), 1:1:size(R_data,2),...
252                   900e6/Fs:900e6/Fs:size(R_data,3));
253     R_data_inter = interp3(R_data,XX,YY,ZZ);
254
255   % Apply matched filter by correlate TIR with Data A-lines
256     for ff = 1:nF;
257         for ii = 1:resolution;
258             for jj =1:resolution;
259                 R_TIR(ii,jj,:)       = R_TIR(ii,jj,:)...
260                                      - mean(R_TIR(ii,jj,:));
261                 R_data(ii,jj,:,ff)   = R_data(ii,jj,:,ff)...
262                                      - mean(R_data(ii,jj,:,ff));
263             R_corr_data(ii,jj,:,ff) = xcorr((R_TIR(ii,jj,:)...
264                                      ./max(max(R_TIR(ii,jj,:)))),...
265                                      squeeze(R_data(ii,jj,:,ff)));
266             end
267         end
268     end
269
270   % Remove neg. correlation values
271     R_corr_data(R_corr_data<=0)=0;
272
273     if RawFlag
274     figure;
275     S = reshape(R_corr_data, size(R_corr_data,1)*size(R_corr_data,2),...
276         size(R_corr_data,3), size(R_corr_data,4));
277     imagesc([], [], S(:,:,1)); colormap gray;
278     [cut1,cut2]=ginput;
279     cut1 = int16(cut1);
280     end
281
282   % Apply Hilbert transform
```

```
283     if HilbertFlag
284         S = double(S);
285 
286         for i=1:NPoints
287          S(i,:,:) = abs(hilbert(S(i,:,:)));
288         end
289     end
290         if exist('ContScan', 'var') == 0
291         for i = 1:Ny
292             if rem(i,2) == 0
293             s = S((i-1)*Nx+1:i*Nx,:,:);
294 
295             S((i-1)*Nx+1:i*Nx,:,:) = s(end:-1:1,:,:);
296             end
297         end
298         end
299 
300     R_data = reshape(S, Nx, Ny, size(S,2), nF);
301 end
302 
303 % ================================================================
304 % GENERATE MAXIMUM AMPLITUDE PROJECTIONS
305 % ================================================================
306 
307 for ff = 1:nF;
308     for c = 1:size(cut1)-1;
309 
310     H(:,:,c,ff) = double(squeeze(max(R_data(:,:,cut1(c):cut1(c+1),ff),...
311                   [], plotAxis)))-double(squeeze(min(R_data...
312                   (:,:,cut1(c):cut1(c+1),ff), [], plotAxis)));
313 
314 if plotAxis ~= 3
315     H = H';
316 end
317 
318 % ================================================================
319 % VISUALIZATION
320 % ================================================================
321 
322 if nF > 1;
323     PlotFlag = 0;
324 end
325 
326 if PlotFlag
327     if plotAxis == 3
328         figure(figRes);
329         subplot(1,4,1);
330         imagesc([-galvoVoltage galvoVoltage], ...
```

```
                [-galvoVoltage galvoVoltage], ...
                 rot90(H(:,:,c,ff),rotFlag));
        colorbar('southoutside');
        axis image

    elseif plotAxis == 2
        figure; imagesc([-resolution/2 resolution/2], [], H'); colorbar;

        ylabel(gca, 'z (um)', 'FontWeight', 'bold', 'units',...
                'normalized', 'FontSize', 12);
        xlabel(gca, 'x (um)', 'FontWeight', 'bold', 'units',...
                'normalized', 'FontSize', 12);
    else
        figure; imagesc([-resolution/2 resolution/2], [], H'); colorbar;

        ylabel(gca, 'z (um)', 'FontWeight', 'bold', 'units',...
                'normalized', 'FontSize', 12);
        xlabel(gca, 'x (um)', 'FontWeight', 'bold', 'units',...
                'normalized', 'FontSize', 12);
    end

    set(gca, 'units', 'normalized', 'FontSize', 12);
end

% ==========================================================
% SAVING
% ==========================================================

if SaveImageFlag

    Hr(:,:,c,ff) = rot90(H(:,:,c,ff),rotFlag);
    save([SavePathOA 'r_' DataName ReconExt], 'R_data', 'f_BP', 'H');
    imwrite((Hr(:,:,c,ff)/max(max(max(Hr(:,:,c,:))))),...
            [SavePathOA 'rn_' DataName ReconExt '_OA_F' ...
             num2str(ff) '_' num2str(c) '.png'], 'png');
    imwrite(uint16(Hr(:,:,c,ff)), [SavePathOA 'r_' DataName ReconExt...
            '_OA_F' num2str(ff) '.tiff'], 'tiff', 'writemode', 'append');
    imwrite(uint16(Hr(:,:,c,ff)), [SavePath saveName '_MM_F' ...
            num2str(ff) '.tiff'], 'tiff', 'writemode', 'append');
end
end
end

if ZStackFlag
DataPath = [DataPath 'ZStack\'];
mkdir(DataPath);
for ff = 1:nF
zstack(R_data(:,:,:,ff), 3, [DataPath 'Frame_' num2str(ff) '\']);
```

```
379 end
380 end
381
382 if nargout
383     R_ = R_data;
384     H_ = H;
385 end
386
387 end
```

Simulation of Total Impulse Response

```
% ==========================================================================
% SETTINGS
% ==========================================================================
addpath(genpath(pwd));

ZStackFlag   = 0;              % Create Z Stack
GPUFlag      = 1;              % use GPU; 0: no GPU;  1: gpuArray-single;
                               %          2: gsingle; 3: GPUsingle
SaveFlag     = 1;              % save simualtion results
PlotFlag     = 0;              % Plot Raw signals
PlotSimlive  = 1;              % Plot live simulation
RecordMovie  = 0;              % Record Simulation movie

Datapath     = 'M:\Data\';
Dataname     = 'TIR_Simulation';

% Simulation Grid
Gridz        = 14e-3;          % [m] z grid size
Gridx        = 6e-3;           % [m] x grid size
Gridy        = 6e-3;           % [m] y grid size
SoS_med      = 1500;           % [m/s] speed of sound of coupling medium
dens_med     = 1000;           % [kg/m^3] density of coupling medium
max_time     = 5e-6;           % [s] simulation time
max_freq     = 100e6;          % [Hz] max simulation frequency
CFL          = 0.3;            % CFL = c*dt/dx;
                               % ratio of spatial and temporal sampling

% Transducer
focus_dist   = 2.85e-3;        % [m] focal length of transducer
aper_size    = 3e-3;           % [m] aperture of transducer
actel_size   = 3e-3;           % [m] size of active element
lens_thick   = 2.6e-3;         % [m] thickness of focusing lens
lens_thick2  = 4e-3;           % [m] lens thickness including inclination
lens_rim     = 0.5e-3;         % [m] rim-thickness of lens
lens_curv    = 1.1e-3;         % [m] radius of concave curvature
lens_depth   = 0.5e-3;         % [m] depth of concave curvature in lens
max_defocus  = 2000e-6;        % [m] max defocus
min_defocus  = -2000e-6;       % [m] min defocus
step_defocus= 10;              % [#] number of defocusing steps
SoS_trans    = 5200;           % [m/s] speed of sound of transducer lens
dens_trans   = 2500;           % [kg/m^3] density of transducer lens

% Source % Offsets
step_lat     = 20;             % [#] spatial offset steps
source_rad   = 1e-6;           % [m] source radius
lat_off      = 2000e-6;        % [m] max lateral offset
```

```
source_pres = 10;           % [Pa] source magnitude
if lat_off > Gridx/2
    lat_off = Gridx/2;
end

% Set parameters to k-Wave
defocus     = (min_defocus:abs(max_defocus-min_defocus)/...
              (step_defocus-1):max_defocus);
time_step   = (SoS_med/(2*max_freq))*CFL/SoS_trans;
                                % [s] simulation time step
dx = SoS_med/(2*max_freq);      % [m] grid point spacing in x
dy = SoS_med/(2*max_freq);      % [m] grid point spacing in y
dz = SoS_med/(2*max_freq);      % [m] grid point spacing in z
Nz = Gridz/dx+1;                    % [#] number of grid points x
Ny = Gridy/dy+1;                    % [#] number of grid points y
Nx = Gridx/dz+1;                    % [#] number of grid points z
kgrid = kWaveGrid(Nz, dx, Nx, dz, Ny, dy);% prepare simulation Grid
sensor.mask = zeros(Nz,Nx,Ny);      % prepare sensor mask
stept = 0;

% Create focusing lens (speed of sound and density)
lensthick_points = round(lens_thick/dz);  % [#] thickness focusing lens
lens_rim_points = lens_rim/dx;            % [#] rim-thickness of lens
lens_radius = round(lens_curv/dz);        % [#] focal length transducer
arc_angle = (2*asin(aper_size/(2*lens_curv)))/2; % [rad] 1/2*curvature
lens_mask = makeCircle(Nx, Nz, Nx/2,...
 (lens_thick2+lens_curv/2)/dz, lens_radius, arc_angle);% create curve

for ll = round(Nx/2-aper_size/(2*dx)):round(Nx/2);
   if ll+round(lens_thick/dz)-round(Nx/2-aper_size/(2*dx))<lens_thick2/dz
 lens_mask(ll,ll+1+round(lens_thick/dz)-round(Nx/2-aper_size/(2*dx)))=1;
    else
        if lens_mask(ll,:)==0;
    lens_mask(ll,1+lens_thick2/dz)=1;
        end
   end
end

for kk = 1+lens_thick2/dz:size(lens_mask,2)
    for ll = 1:size(lens_mask,1)
    if  lens_mask(ll,kk)==1;
        lens_mask(ll,lens_thick2/dz)=1;
        lens_mask(ll,1+lens_thick2/dz:size(lens_mask,2))=0;
    end
    end
end

lens_mask = lens_mask + flipud(lens_mask);  % double the arc
```

```
lens_mask = rot90(lens_mask,3);                % rotate line to axial orient

[s_zz,s_xx] = find(lens_mask);                 % enlarge lens in z direction

for zz = 1:size(s_xx,1)
    for xx = 1:s_zz(zz)
        lens_mask(xx,s_xx(zz)) = 1;
    end
end

for xx = 1:(size(lens_mask,2)+1)/2;
    for yy = 1:(size(lens_mask,2)+1)/2;
        try
            lens_mask_3D((size(lens_mask,2)-1)/2+xx,...
                (size(lens_mask,2)-1)/2+yy,:) ...
                = lens_mask(:,(size(lens_mask,2)-1)/2+...
                round(sqrt((xx)^2+(yy)^2)));
        end
    end
end

lens_mask_3D = max(lens_mask_3D,rot90(lens_mask_3D,2));
lens_mask_3D = max(lens_mask_3D,rot90(lens_mask_3D,1));

for zz = 1:size(lens_mask_3D,3);
    for yy = 1:size(lens_mask_3D,2);
        for xx = 1:size(lens_mask_3D,1)
            if lens_mask_3D(xx,yy,zz) == 1;
                medium.sound_speed(zz,xx,yy) = SoS_trans;
                medium.density(zz,xx,yy) = dens_trans;
            else
                medium.sound_speed(zz,xx,yy) = SoS_med;
                medium.density(zz,xx,yy) = dens_med;
            end
        end
    end
end

for def = 1:size(defocus,2);
defocus_points = round(defocus(def)/dz);  % [#] z defocus of transducer
lat_off_points = round(lat_off/dz);       % [#] max lateral offset

step = round(lat_off_points/(step_lat-1));% [#] size of offset step
actel_points = round(actel_size/dx/2);    % [#] size of active element
sensor.mask(round(Nz/2-lens_thick2/dz-focus_dist/dz),...
    round(Nx/2-actel_points:Nx/2+actel_points),...
    round(Ny/2-actel_points:Ny/2+actel_points)) = 1;

```

```
% Create pressure source
if source_rad < dx;
    source_rad = dx;
end
source_rad_points = source_rad/dx;
source_print = zeros(Nz,Nx, Ny);

% ================================================================
% SIMULATION
% ================================================================

kgrid.t_array = 0:time_step:max_time;
clear sensor_output_hil
for aa = 1:step_lat;

   Savepath = [Datapath Dataname '_defocus_' int2str(defocus(def)*1e6)...
        '_FOV_' int2str(2*lat_off*1e6)];
    if ( ~exist([Savepath '\' Dataname '_defocus_'...
            int2str(defocus(def)*1e6) '_FOV_' int2str(2*lat_off*1e6)...
            '_lat_' int2str(aa) '.mat'],'file'))

    stept = stept+1;
        fprintf('Step: %d of %d | Lateral: %d um | Axial: %d um \n',...
            stept, step_lat*step_defocus, step*(aa-1)*dx*1e6,...
            defocus_points*dz*1e6);

% place a disc-shaped source near the focus of the detector
        source.p0 = source_pres*makeBall(Nz, Nx, Ny,...
           Nz/2+defocus_points, Nx/2+step*(aa-1), size(lens_mask,2)/2,...
            source_rad_points)*2;
        source_print = source_print+source.p0;

% run the first simulation

if GPUFlag == 1;
sensor_data1 = kspaceFirstOrder3D(kgrid, medium, source, sensor,...
    'PlotSim', logical(PlotSimlive), 'RecordMovie',...
    logical(RecordMovie), 'DataCast', 'gpuArray-single');
elseif GPUFlag == 2;
sensor_data1 = kspaceFirstOrder3D(kgrid, medium, source, sensor,...
    'PlotSim', logical(PlotSimlive), 'RecordMovie',...
    logical(RecordMovie), 'DataCast', 'gsingle');
elseif GPUFlag == 3;
sensor_data1 = kspaceFirstOrder3D(kgrid, medium, source, sensor,...
    'PlotSim', logical(PlotSimlive), 'RecordMovie',...
    logical(RecordMovie), 'DataCast', 'GPUsingle');
else
sensor_data1 = kspaceFirstOrder3D(kgrid, medium, source, sensor,...
```

```
    'PlotSim', logical(PlotSimlive), 'RecordMovie',...
    logical(RecordMovie), 'DataCast', 'single');
end

sensor_output(aa,:) = sum(gather(sensor_data1),1)/sum(sensor.mask(:));
sensor_output_hil(aa,:) = abs(hilbert(sensor_output(aa,:)));

if SaveFlag
   Savepath = [Datapath Dataname '_defocus_' int2str(defocus(def)*1e6)...
        '_FOV_' int2str(2*lat_off*1e6)];
    if aa == 1;
        mkdir(Savepath);
    end
    save([Savepath '\' Dataname '_defocus_' int2str(defocus(def)*1e6)...
        '_FOV_' int2str(2*lat_off*1e6) '_lat_' int2str(aa)]);
end
        else
            disp('homma scho... ');
            load([Savepath '\' Dataname '_defocus_'...
                int2str(defocus(def)*1e6) '_FOV_'...
                int2str(2*lat_off*1e6) '_lat_' int2str(aa)]);
            disp([Savepath '\' Dataname '_defocus_'...
                int2str(defocus(def)*1e6) '_FOV_'...
                int2str(2*lat_off*1e6) '_lat_' int2str(aa)]);
            disp(['defocus size ' num2str( size(defocus))]);
        end

end

% ==========================================================================
% TIR
% ==========================================================================

trigdel = round((defocus(def)+focus_dist)/SoS_med/time_step);
sensor_output_hil = sensor_output_hil(:,trigdel:end);
TIR = single(zeros(size(sensor_output_hil,1),...
    size(sensor_output_hil,1), size(sensor_output_hil,2)));
TIR_rot = single(zeros((size(sensor_output_hil,1)*2)-1,...
    (size(sensor_output_hil,1)*2)-1,size(sensor_output_hil,2)));

for xx = 1:size(sensor_output_hil,1);
    for yy = 1:size(sensor_output_hil,1);
        try
          TIR(xx,yy,:) = sensor_output_hil(round(sqrt((xx)^2+(yy)^2)),:);
        end
    end
end
```

```
for zz = 1:size(TIR,3);
TIR_rot(1:size(TIR,1),1:size(TIR,2),zz)...
    = rot90(TIR(:,:,zz),2);
TIR_rot(size(TIR,1):2*size(TIR,1)-1,size(TIR,1):2*size(TIR,1)-1,zz)...
    = TIR(:,:,zz);
TIR_rot(1:size(TIR,1),size(TIR,1):2*size(TIR,1)-1,zz)...
    = flipud(TIR(:,:,zz));
TIR_rot(size(TIR,1):2*size(TIR,1)-1,1:size(TIR,2),zz)...
    = fliplr(TIR(:,:,zz));
end

if GPUFlag ~= 0;
    TIR_rot = gather(TIR_rot);
    sensor_output = gather(sensor_output);
    sensor_output_hil = gather(sensor_output_hil);
end

%% ======================================================================
% VISUALIZATION
%% ======================================================================

if ZStackFlag
TIR_rot = TIR_rot./max(max(max(TIR_rot)));
SavepathStack = [Savepath '\Stack\'];
mkdir(SavepathStack);
zstack(TIR_rot, 3, SavepathStack);
end

axisx = (-((Gridx-dx)/2):dx:((Gridx-dx)/2))*1e3;
axisz = (-((Gridz-dz)/2):dz:((Gridz-dz)/2))*1e3;
axis2 = 0:step*dx:lat_off-step*dx;
axis3 = -lat_off+step*dx:step*dx:lat_off-step*dx;
time = (defocus(def)+focus_dist)/SoS_med:time_step:max_time+time_step;

if PlotFlag
figure;
subplot(2,2,1);
plot(time,sensor_output(:,trigdel:end)');
    title 'raw OA signal';
    xlabel 'time (us)';
    ylabel 'amplitude (a.u.)';
subplot(2,2,2);
plot(time,sensor_output_hil')
    title 'Hilbert trans. OA signal';
    xlabel 'time (us)';
    ylabel 'amplitude (a.u.)';
subplot(2,2,3);
imagesc(time, axis2*1e3,sensor_output); colormap gray; c = colorbar;
```

```
287     title 'raw OA signal';
288     xlabel 'time (us)';
289     ylabel 'spatial offset (mm)';
290 subplot(2,2,4);
291 imagesc(axis3*1e3,axis3*1e3,squeeze(max(permute(TIR_rot, [3,1,2]))));
292     colormap hot; c = colorbar;
293     title 'MAP';
294     xlabel 'spatial offset (mm)';
295     ylabel 'spatial offset (mm)';
296
297 figure;
298 subplot(2,2,1);
299 imagesc(axisx, axisz, sensor.mask); colormap cool; c = colorbar;
300     grid on;
301     title 'Sensor';
302     xlabel 'lateral (mm)';
303     ylabel 'axial (mm)';
304 subplot(2,2,2);
305 imagesc(axisx, axisz, medium.density); colormap cool; c = colorbar;
306     grid on;
307     title 'Density';
308     xlabel 'lateral (mm)';
309     ylabel 'axial (mm)';
310 subplot(2,2,3);
311 imagesc(axisx, axisz, medium.sound_speed); colormap cool; c = colorbar;
312     grid on;
313     title 'Speed of Sound';
314     xlabel 'lateral (mm)';
315     ylabel 'axial (mm)';
316 subplot(2,2,4);
317 imagesc(axisx, axisz, source_print);
318     colormap cool; c = colorbar;
319     grid on;
320     title 'Initial pressure';
321     xlabel 'lateral (mm)';
322     ylabel 'axial (mm)';
323 end
324
325 %% ========================================================================
326 % SAVING
327 %% ========================================================================
328
329 if SaveFlag
330 save([Savepath '\' Dataname '_defocus_' int2str(defocus(def)*1e6)...
331     '_FOV_'  int2str(2*lat_off*1e6)]);
332 end
333 clear sensor_output_hil
334 end
```

Attachments

The attachments contain first a section dedicated to acknowledge all people helping me in conducting this thesis. Second, a list of reprint permissions of published material regarding is provided. Third and finally, an overview of all publications is given including first and co-authored articles as well as conference proceedings both published or in preparation.

Acknowledgments

Conducting this Ph.D. was an exciting and life-changing experience, which would never have been remotely possible without the decisive input and unrelenting support of many different people. The following lines face the difficult task of condensing and phrasing my sincere gratitude to those whose professional and private contribution pushed me to bring the best out of my research.

First and foremost, I would like to express my deepest thankfulness to my Ph.D. advisor Prof. Dr. Vasilis Ntziachristos for giving me the opportunity to work in the fascinating field of multi-modal microscopy for biomedical research. With his enthusiastic and visionary mindset, he inspired me to think outside the box and encouraged me to challenge myself in performing at my best. I feel greatly honored to have worked in the captivating atmosphere he established by gathering excellent people around him, essentially forming an outstanding scientific workplace. I also highly appreciate his excessive support by sending me to international conferences, by elating me to freely develop and realize my own ideas, by promoting the hybrid microscope in both its funding as well as awareness in the field, and by mentoring me in close collaboration. I gratefully acknowledge the chance he granted me to be part of such an breathtaking journey.
Next, I would like to deeply thank Prof. Dr. Gil Westmeyer for the exciting and fruitful cooperation projects as well as for his valuable input and support regarding the overall execution of my thesis. His inquisitive and motivating manner inspired my intention and dedication for excelling my predefined goals.
Furthermore, I am very thankful to Dr. Simon Jacob, whose expertise in advanced microscopy for neuroimaging brought me to shed light on my research from other perspectives and, thus, enlarged my field of view of microscopy in general as well as ascertain my future vision.
Finally, I would like to thank my thesis committee, Prof. Dr. Vasilis Ntziachristos, Prof. Dr. Gil Westmeyer, and Dr. Simon Jacob, for participating in fertile discussions, for guiding my research on the organizational side, and for promoting my scientific career.

While conducting my Ph.D., I was honored to meet and interact with a variety of outstanding people, who not only I deeply enjoyed to work with but who emerged to true friends.
My special thanks go to Dr. Dominik Soliman, with whom I worked on the hybrid microscope during the first half of my Ph.D. and who quickly emerged to an excellent associate both on the scientific as well as on the friendship level. He not only was a true OCD companion (see [23]), but we shared a passion for multi-modal microscopy, duty cycles of 100%, profound and verbose conversations about glue drying in seconds, appropriately placed '+++', and naturally given abilities to express science in romanic languages. I am exceedingly grateful for the outstanding time we shared in and outside the lab.

I would like to express my thanks to Dr. Murad Omar, who was leading the microscopy group during the starting phase of my Ph.D. and who introduced me into the field of optoacoustic imaging. Besides helpful discussions and memorable conference attendances, we also shared a brilliant time outside work. He taught me basic optoacoustic concepts the same manner as how requests for high-impact papers should be replied. I will always remember with a smile on my face how we scientifically determined our heads' circumferences or enjoyed in-depth discussions during business lunches.
Further, some special thanks go to Dr. Juan Aguirre Bueno. Despite being a convivial office mate, I thank him for many lessons on optoacoustic methodologies, close support and constant availability at upcoming hurdles during my Ph.D., unremitting supply chain with Gazpacho, motivational influence to aim for getting rid of the appellation 'candidate', to understand the statistical evaluation for choosing appropriate means of transportation, as well as for his education in polite etiquette and its associated hand gestures.
Another thank you goes to Dr. Miguel Pleitez, with whom I already shared the lab in our joint days back in Frankfurt. Since my Master's study he educated me in spectroscopy and optoacoustics, in the behavioral characteristics of free radicals, in how to select correctly scientific equipment as armrests, in the importance of grinding degree and that even roasted plants should bloom, and when to call a *project - good!*
In addition, I would like to acknowledge Dr. Alice Soldá, who joined the microscopy team in the second half of my Ph.D.. On the one hand, her expertise and know-how led to various projects perfectly exploiting my labor on hybrid microscopy as well as to many briefings improving my knowledge of cellular processes. On the other hand, her Italian solicitude and joyfulness resulted in a tidier laser lab, in debates about denying exocrine glands, and in culinary yet sometimes enduringly-sung-of revelations like pasta alla carbonara and panettone.
I am glad to have met Dr. Ara Ghazaryan, with whom I shared many moments on the multi-photon subsystem of the hybrid microscope and who always tinkered a custom-made solution out of his box of tricks when encountering a problem, or as he would fleet-footed say: shmoblems. He improved not only my understanding on advanced microscopy but also my working life as a Ph.D. with his cheerful and attentive character.
Moreover, I would like to thank Dr. Andriy Chmyrov, we took over the lead of the microscopy team. His in-depth knowledge and expertise in optical microscopy helped me to improve both the optical system as well as my understanding of microscopy principles.
Even though we never directly shared time together in the lab, I would like to say thank you to Dr. Stephan Kellnberger and Dr. George Tserevelakis, two alumni of the hybrid microscope, comrades of frequency-domain optoacoustics, and always happy-to-meet people when attending conferences.
Further thanks go to Dr. Dimitris Gorpas and Maximilian Koch. Their work on fluorescent techniques not only allowed to exchange knowledge and optical equipment but also caused me to amend the hybrid microscope for being more robust towards external interfering sources.

Additionally, I am much obliged for my project-specific collaboration partners, with whom I shared a fantastic and inspiring time in the lab: Antonios Stylogiannis for the initially frustrating but finally fruitful implementation of ALEX and FComb optoacoustic microscopy, Roman Shnaiderman and Georg Wissmeyer for the exhaustive yet entertaining realization of all-optical optoacoustic microscopy, Dr. Christoph Massner for exploiting multi-modal contrast to study ferritins, Dr. Sheryl Roberts for reading calcium signals on the cellular level, Dr. Angelos Karlas for applying the hybrid microscope to achieve new insights into atherosclerosis, Dr. Dominik Jüstel and Christoph Dehner for applying computational magic to extract information out of wound healing images, Jacob Wierzbowksi for manufacturing gold nanolayers, and Dr. André Stiel for incessantly supported me in executing optoacoustic flow cytometry measurements. Moreover, for exciting discussions, lively exchange of ideas, and funny moments, I would like to thank Andrei Berezhnoi, Ludwig Prade, Francesca Gasparin, Yuanhui Huang, Dr. Paul Vetschera, Dr. Johannes Rebling, Dr. Xosé Luis Dean-Ben, Ben McLarney, Ivana Ivankovic, Kanuj Mishra, Ivan Olefir, Avihai Ron, Kaushik Basak Chowdhury, Jan Kukacka, Felix Sigmund, Jeffrey Truong, Dr. Dmitry Bozhko, Dr. Josefine Reber, Dr. Niclas Bézière, Dr. Juan Pablo Fuenzalida Werner, Dr. Hailong He, Dr. Lucas Ríobo, Dr. Xiaopeng Ma, Dr. Mikhail Mazurenka, Dr. Nasire Uluc, Dr. Christian Zakian, Dr. Ina Weidenfeld, Prof. George Sergiadis, and Prof. Dr. Daniel Razansky.
I am further deeply indebted to Dr. Dominik Soliman and Dr. Juan Aguirre Bueno, who reviewed the entire thesis and whose valuable comments and corrections greatly improved it, but also to Dr. Alice Soldá, Antonios Stylogiannis, Dr. Christoph Massner, Roman Shnaiderman, Dr. George Tserevelakis, Dr. Andreas Hillmair, and Dr. Robert Wilson, who revised specific chapters.
I would like to express my sincere thankfulness to Sarah Glasl, Uwe Klemm, Pia Anzenhofer, and Florian Jurgileit for their assistance with *in vivo* mouse measurements, and Dr. Anja Stelz for her help with zebrafish experiments. Besides their excellent work in sample preparation and monitoring, we had a great and joyful time in the lab.
Furthermore, I would like to express my gratitude to Dr. Andreas Hillmair, Susanne Stern, Dr. Katharina Schaar, Lidia Seidl, Dr. Chapin Rodriguez, Prof. Karl-Hans Englmeier, Dr. Roland Boha, Silvia Weinzierl, Dr. Doris Bengel, Dr. Julia Niefecker, Dr. Nike Tsalas, Dr. Manfred Türke, Ines Baumgartner, Dr. Robert Wilson, and Martina Riedl, whose constant and patient support, advice, and assistance helped me to handle organizational issues, animal experiments, purchasing orders, conference and symposium attendances, manuscript writing and finalization, and IT problems. Without their contribution and engagement, the work for this thesis would not have been possible.
In addition to that, I would like to thank Desislava Zlatanova, Dr. Katrin Offe, Bettina Kratzer, and Raphaela Blum for their prompt and competent guidance in all matters concerning the Ph.D. program 'Medical Life Science and Technology'. In this context, many thanks are further addressed to my fellow students for interesting and amusing time during lectures, lab courses, retreats, as well as get-togethers outside the Ph.D. program.

Finally, for the unconditional support and incessant help, I am endlessly grateful to my family. Only the indispensable encouragement of my parents and my sister created the basis that allowed me to freely evolve and orient myself in the scientific world. From the beginning sparks of my curiosity in science in high school up to the final days of my doctorate, I had the pleasure of experiencing an unreservedly and trustful backing paired with a highly motivational entourage. It was essentially this group of people, who brought meaning and purpose to my work and endeavor.

Published material and reprint permissions

The majority of the shown results in this thesis has been published in different articles and conferences proceedings or are parts of publications in preparation, in submission, or in revision during the time of writing this thesis.

- The results and figures presented in Section 4.4 were in revision at *Nature Communication* during the submission of the thesis [78].
- In Section 5.2.2, Fig. 5.2 and Fig. 5.3 are adapted from [103] (©2019, Society of Photo-Optical Instrumentation Engineers (SPIE)).
- In Section 5.3.1, results and Fig. 5.6, Fig. 5.7, and Fig. 5.8 are adapted from [104] (©2018, WILEY-VCH).
- The results and figures presented in Section 5.3.2 were in revision at *ACS Nano* during the submission of the thesis [127].
- In Section 5.3.3, results and Fig. 5.14 and Fig. 5.15 are adapted from [155] (©2018, American Chemical Society).
- In Section 5.3.5, results and Fig. 5.19, Fig. 5.20, Fig. 5.21, Fig. 5.22, and Fig. 5.23 are adapted from [189] (©2016, Elsevier) and [190] (©2017, Society of Photo-Optical Instrumentation Engineers (SPIE)).
- In Section 5.4.1, results and Fig. 5.24, Fig. 5.25, Fig. 5.26, and Fig. 5.27 are adapted from [220] (Creative Commons Attribution 4.0 International License).
- The results and figures presented in Section 5.4.2 were in preparation for publication during the submission of the thesis [235].
- In Section 5.4.3, results and Fig. 5.14 and Fig. 5.15 are adapted from [249] (©2017, Optical Society of America) and [250] (©2018, Society of Photo-Optical Instrumentation Engineers (SPIE)).
- The results and figures presented in Section 5.4.4 were in preparation for publication during the submission of the thesis [258].

Permissions to reproduce both text and images are granted through the author rights in copyright transfer agreements for the above mentioned publications and have been obtained in written electronic form by the editorial boards.

List of publications

First author publications

1. **M. Seeger***, A. Karlas*, D. Soliman, J. Pelisek and V. Ntziachristos, "Multimodal optoacoustic and multi-photon microscopy of human carotid atheroma," *Photoacoustics*, vol. 4, no. 3, pp. 102-111, 2016.

2. S. Kellnberger*, D. Soliman*, G. J. Tserevelakis*, **M. Seeger***, H. Yang, A. Karlas, L. Prade, M. Omar, and V. Ntziachristos, "Optoacoustic microscopy at multiple discrete frequencies," *Light: Science and Applications*, vol. 7, no. 1, pp. 109-120, 2018.

In preparation, submission, or revision

3. **M. Seeger**, D. Soliman, J. Aguirre, G. Diot, J. Wierzbowski, and V. Ntziachristos, "Pushing the boundaries of optoacoustic microscopy by Total Impulse Response characterization," in revision at *Nature Communications*.

4. **M. Seeger**, C. Dehner, D. Jüstel, and V. Ntziachristos, "Spatio-temporal assessment of wound healing sequences enabled by label-free multimodal microscopy," in preparation.

5. **M. Seeger***, A. Stylogiannis*, and V. Ntziachristos, "Simultaneous multiwavelength optoacoustic microscopy by high-speed laser diodes," in preparation.

6. **M. Seeger**, A. C. Stiel, and V. Ntziachristos, "Optoacoustic flow-cytometry of genetically encoded chromoproteins," in preparation.

Co-author publications

7. S. Roberts, **M. Seeger**, Y. Jiang, A. Mishra, F. Sigmund, A. Stelzl, A. Lauri, P. Symvoulidis, H. Rolbieski, M. Preller, X. L. Deán-Ben, D. Razansky, T. Orschmann, S. C. Desbordes, P. Vetschera, T. Bach, V. Ntziachristos, and G. G. Westmeyer, "Calcium Sensor for Photoacoustic Imaging," *Journal of the American Chemical Society*, vol. 140, pp. 2718-2721, 2017.

8. R. Shnaiderman*, G. G. Wissmeyer*, **M. Seeger**, D. Soliman, H. Estrada, D. Razansky, A. Rosenthal, and V. Ntziachristos, "Fiber interferometer for hybrid optical and optoacoustic intravital microscopy," *Optica*, vol. 4, no. 10, p. 1180-1187, 2017.

9. C. Massner, F. Sigmund, S. Pettinger, **M. Seeger**, C. Hartmann, N. P. Ivleva, R. Niessner, H. Fuchs, M. H. de Angelis, A. Stelzl, N. L. Koonakampully, H. Rolbieski, U. Wiedwald, M. Spasova, W. Wurst, V. Ntziachristos, M. Winklhofer,

* Equal contribution

and G. G. Westmeyer, "Genetically Controlled Lysosomal Entrapment of Superparamagnetic Ferritin for Multimodal and Multiscale Imaging and Actuation with Low Tissue Attenuation," *Advanced Functional Materials*, vol. 28, no. 19, p. 1706793, 2018.

10. P. S. P. Poh*, V. Schmauss*, J. A. McGovern, D. Schmaus2, M. P. Chhaya, P. Foehr, **M. Seeger**, V. Ntziachristos, D. W. Hutmacher, M. van Griensven, J.-T. Schantz, and E. R. Balmayor, "Non-linear optical microscopy and histological analysis of collagen, elastin and lysyl oxidase expression in breast capsular contracture," *European Journal of Medical Research*, vol. 23, pp. 30-41, 2018.

11. A. Karlas, N.-A. Fasoula, K. Paul-Yuan, J. Reber, M. Kallmayer, D. Bozhko, **M. Seeger**, H.-H. Eckstein, M. Wildgruber, and V. Ntziachristos, "Cardiovascular Optoacoustics: From Mice to Men - A Review," *Photoacoustics*, vol. 14, pp. 19-30, 2019.

In preparation, submission, or revision

12. M. D. Giosia*, A. Soldà*, **M. Seeger**, A. Cantelli, F. Arnesano, M. Nardella, V. Mangini, F. Valle, M. Montalti, F. Zerbetto, S. Rapino, V. Ntziachristos, and M. Calvaresi, "C70@lysozyme: A Label-free Phototheranostic Platform for Photoacoustic/Third Harmonic Generation Imaging and Photodynamic Therapy," in revision at *ACS Nano*.

13. J. Aguirre, C. Schönmann, B. Hindelang, **M. Seeger**, A. Berezhnoi, I. Weidenfeld, U. Darsow, A. C. Stiel, C. Posch, and V. Ntziachristos, "Non-invasive characterization of tumor depth in melanoma at single-cell resolution," in preparation.

14. M. A. Pleitez, A. A. Khan, A. Soldà, A. Chmyrov, J. Reber, F. Gasparin, **M. Seeger**, B. Schätz, S. Herzig, M. Scheideler, and V. Ntziachristos, "Label-free metabolic monitoring of living cells by mid-infrared optoacoustic microscopy," in revision at *Nature Biotechnology*.

Conference proceedings

15. **M. Seeger**, A. Karlas, D. Soliman, J. Pelisek, and V. Ntziachristos, "Hybrid microscopy of human carotid atheroma by means of optical-resolution optoacoustic and non-linear optical microscopy," in *Photons Plus Ultrasound: Imaging and Sensing 2017*, vol. 10064, p. 1006455, 2017.

16. R. Shnaiderman*, G. G. Wissmeyer*, H. Estrada, **M. Seeger**, and V. Ntziachristos, "Intravital hybrid optical-optoacoustic microscopy based on fiber-Bragg interferometry," in *Progress in Biomedical Optics and Imaging*, vol. 10494, p. 92, 2018.

* Equal contribution

17. **M. Seeger**, G. G. Westmeyer, and V. Ntziachristos, "In-vivo hybrid microscopy of small model organisms," in *Opto-Acoustic Methods and Applications in Biophotonics IV*, vol. 11077, p. 21, 2019.

Preprints

18. M. A. Pleitez, A. A. Khan, J. Reber, A. Chmyrov, **M. Seeger**, M. Scheideler, S. Herzig, and V. Ntziachristos, "Mid-infrared optoacoustic microscopy with label-free chemical contrast in living cells and tissues," *bioRxiv*, p. 270082, 2018.

References

[1] E. O. Wilson, *Consilience: The Unity of Knowledge*, vol. 18. Alfred A. Knopf, sep 1999.

[2] M. Herrera, D. C. Roberts, and N. Gulbahce, "Mapping the evolution of scientific fields," *PLoS ONE*, vol. 5, no. 5, pp. 3–8, 2010.

[3] H. Frauenfelder, P. G. Wolynes, and R. H. Austin, "Biological Physics," *Reviews of Modern Physics*, vol. 71, pp. S419–S430, mar 1999.

[4] T. G. Van Leeuwen and R. Tijssen, "Interdisciplinary dynamics of modern science: analysis of cross-disciplinary citation flows," *Research Evaluation*, vol. 9, pp. 183–187, dec 2000.

[5] P. O'Shea, "Future medicine shaped by an interdisciplinary new biology," *The Lancet*, vol. 379, pp. 1544–1550, apr 2012.

[6] A. R. Kherlopian, T. Song, Q. Duan, M. A. Neimark, M. J. Po, J. K. Gohagan, and A. F. Laine, "A review of imaging techniques for systems biology.," *BMC systems biology*, vol. 2, p. 74, jan 2008.

[7] J. F. Allemand and P. Desbiolles, *Physics and Biology*, vol. 11. WORLD SCIENTIFIC, dec 2014.

[8] N. Walliman, *Research Methods: The Basics*. Routledge, nov 2010.

[9] H. Liljenström and U. Svedin, *Micro meso macro: Addressing complex systems couplings*. World Scientific, 2005.

[10] R. Hooke, *Micrographia*. The British Library, 1665.

[11] J. Kuriyan, B. Konforti, and D. Wemmer, *The Molecules of Life*. Garland Science, jul 2012.

[12] L. V. Wang and H.-I. Wu, *Biomedical Optics*. Hoboken, NJ, USA: John Wiley & Sons, Inc., jul 2009.

[13] J. D. Morris and C. K. Payne, "Microscopy and Cell Biology: New Methods and New Questions," *Annual Review of Physical Chemistry*, vol. 70, no. 1, pp. 199–218, 2019.

[14] R. Marshall, "Under the microscope," *Journal of Medical Humanities*, vol. 29, pp. 61–66, sep 2008.

[15] T. Breidenmoser, F. O. Engler, G. Jirikowski, M. Pohl, and D. G. Weiss, "Transformation of scientific knowledge in biology: changes in our understanding of the living cell through microscopic imaging," *Max-Planck-Institut f{ü}r Wissenschaftsgeschichte, Reprint 408*, pp. 1–89, 2010.

[16] B. R. Masters, P. T. C. So, and W. W. Mantulin, "Handbook of Biomedical Nonlinear Optical Microscopy," *Journal of Biomedical Optics*, 2009.

[17] M. Leslie, "Two microscopes are better than one," *Journal of Cell Biology*, vol. 192, no. 1, p. 3, 2011.

[18] N. Pavillon, K. Fujita, and N. Isaac Smith, "Multimodal label-free microscopy," *Journal of Innovative Optical Health Sciences*, vol. 7, no. 05, pp. 1–22, 2014.

[19] R. Mouras, P. Bagnaninchi, A. Downes, and A. Elfick, "Multimodal, label-free nonlinear optical imaging for applications in biology and biomedical science," *Journal of Raman Spectroscopy*, vol. 44, no. 10, pp. 1373–1378, 2013.

[20] D. Evanko, "Label-free microscopy," *Nature Methods*, vol. 7, no. 1, p. 36, 2010.

[21] D. Soliman, G. J. Tserevelakis, M. Omar, and V. Ntziachristos, "Combining microscopy with mesoscopy using optical and optoacoustic label-free modes," *Nature Publishing Group*, pp. 1–9, 2015.

[22] G. J. Tserevelakis, D. Soliman, M. Omar, and V. Ntziachristos, "Hybrid multiphoton and optoacoustic microscope," *Optics Letters*, vol. 39, pp. 1819–1822, apr 2014.

[23] D. Soliman, "Augmented microscopy: Development and application of high-resolution optoacoustic and multimodal imaging techniques for label-free biological observation," *Chair for Biological Imaging*, vol. Ph.D., 2016.

[24] M. K. Beyer, "Lehrbuch der Physikalischen Chemie. 6. Auflage, mit Arbeitsbuch. Von Gerd Wedler und Hans-Joachim Freund.," *Angewandte Chemie*, vol. 125, pp. 3893–3893, apr 2013.

[25] S. Kellnberger, "Thermoacoustic Imaging in time and frequency domain. Theory and experiments," *Chair for Biological Imaging*, vol. Ph.D., p. 188, 2012.

[26] V. Ntziachristos, "Going deeper than microscopy: the optical imaging frontier in biology.," *Nature methods*, vol. 7, pp. 603–14, aug 2010.

[27] L. V. Wang, "Prospects of photoacoustic tomography," *Medical Physics*, vol. 35, p. 5758, nov 2008.

[28] P. K. Johansson, L. Schmüser, and D. G. Castner, "Nonlinear Optical Methods for Characterization of Molecular Structure and Surface Chemistry," *Topics in Catalysis*, vol. 61, pp. 1101–1124, jun 2018.

[29] C. Kuntner-Hannes and Y. Haemisch, *Image Fusion in Preclinical Applications*. Cham: Springer International Publishing, 2019.

[30] C. Ascheron and M. S. Dresselhaus, *The Current Trends of Optics and Photonics*, vol. 129 of *Topics in Applied Physics*. Dordrecht: Springer Netherlands, 2015.

[31] P. Wormell, "Advanced optical imaging theory," *Optics and Lasers in Engineering*, vol. 33, pp. 237–238, mar 2000.

[32] W. Demtröder, *Experimentalphysik 2*. Springer-Lehrbuch, Berlin, Heidelberg: Springer Berlin Heidelberg, 2008.

[33] V. V. Tuchin, *Handbook of Coherent-Domain Optical Methods*, vol. 1-2. New York, NY: Springer New York, 2013.

[34] P. J. Tisch, *Nonlinear Optics*. Elsevier, 2003.

[35] A. Rosencwaig and P. R. Griffiths, "Photoacoustics and Photoacoustic Spectroscopy," *Physics Today*, 2008.

[36] G. M. Hale and M. R. Querry, "Optical Constants of Water in the 200-nm to 200-microm Wavelength Region.," *Applied optics*, vol. 12, pp. 555–63, mar 1973.

[37] S. Prahl, "Tabulated Molar Extinction Coefficient for Hemoglobin in Water."

[38] S. Prahl, "Tabulated Molar Extinction Coefficient for Eumelanin."

[39] S. Prahl, "Tabulated Molar Extinction Coefficient for Fat."

[40] A. Croce and G. Bottiroli, "Autofluorescence spectroscopy and imaging: a tool for biomedical research and diagnosis," *European Journal of Histochemistry*, vol. 58, no. 4, p. 2461, 2014.

[41] L. Shi, L. Lu, G. Harvey, T. Harvey, A. Rodríguez-Contreras, and R. R. Alfano, "Label-Free Fluorescence Spectroscopy for Detecting Key Biomolecules in Brain Tissue from a Mouse Model of Alzheimer's Disease," *Scientific Reports*, vol. 7, no. 1, 2017.

[42] J. Yao and L. V. Wang, "Sensitivity of photoacoustic microscopy," *Photoacoustics*, vol. 2, no. 2, pp. 87–101, 2014.

[43] W. Wallace, L. H. Schaefer, and J. R. Swedlow, "A Workingperson's Guide to Deconvolution in Light Microscopy," *BioTechniques*, vol. 31, pp. 1076–1097, nov 2001.

[44] J. G. Mcnally, T. Karpova, J. Cooper, and J.-A. Conchello, "Three-Dimensional Imaging by Deconvolution Microscopy Three-Dimensional Imaging by Deconvolution Microscopy," *Methods*, vol. 385, no. October 2016, pp. 373–385, 1999.

[45] J. B. Sibarita, "Deconvolution microscopy," *Advances in Biochemical Engineering/Biotechnology*, vol. 95, pp. 201–243, 2005.

[46] P. J. Shaw and D. J. Rawlins, "The point-spread function of a confocal microscope: its measurement and use in deconvolution of 3-D data," *Journal of Microscopy*, vol. 163, pp. 151–165, aug 1991.

[47] A. Majewska, G. Yiu, and R. Yuste, "A custom-made two-photon microscope and deconvolution system," *Pflugers Archiv European Journal of Physiology*, vol. 441, no. 2-3, pp. 398–408, 2000.

[48] A. Periasamy, P. Skoglund, C. Noakes, and R. Keller, "An evaluation of two-photon excitation versus confocal and digital deconvolution fluorescence microscopy imaging in Xenopus morphogenesis," *Microscopy Research and Technique*, vol. 47, pp. 172–181, nov 1999.

[49] A. Govil, D. M. Pallister, and M. D. Morris, "Three-dimensional digital confocal Raman microscopy," *Applied Spectroscopy*, vol. 47, pp. 75–79, jan 1993.

[50] C. W. Freudiger, W. Min, B. G. Saar, S. Lu, G. R. Holtom, C. He, J. C. Tsai, J. X. Kang, and X. S. Xie, "Label-Free Biomedical Imaging with High Sensitivity by Stimulated Raman Scattering Microscopy," *Science*, vol. 1857, no. December, pp. 1857–1861, 2008.

[51] J. Ling, S. D. Weitman, M. A. Miller, R. V. Moore, and A. C. Bovik, "Direct Raman imaging techniques for study of the subcellular distribution of a drug," *Applied Optics*, vol. 41, no. 28, pp. 6006–6017, 2002.

[52] P. Lasch and D. Naumann, "Spatial resolution in infrared microspectroscopic imaging of tissues," *Biochimica et Biophysica Acta - Biomembranes*, vol. 1758, no. 7, pp. 814–829, 2006.

[53] M. J. Nasse, E. C. Mattson, R. Reininger, T. Kubala, S. Janowski, Z. El-Bayyari, and C. J. Hirschmugl, "Multi-beam synchrotron infrared chemical imaging with high spatial resolution: Beamline realization and first reports on image restoration," *Nuclear Instruments and Methods in Physics Research, Section A: Accelerators, Spectrometers, Detectors and Associated Equipment*, vol. 649, no. 1, pp. 172–176, 2011.

[54] G. L. Carr, "Resolution limits for infrared microspectroscopy explored with synchrotron radiation," *Review of Scientific Instruments*, vol. 72, no. 3, pp. 1613–1619, 2001.

[55] Y. Liu, Y. Liang, G. Mu, and X. Zhu, "Deconvolution methods for image deblurring in optical coherence tomography," *Journal of the Optical Society of America A*, vol. 26, p. 72, jan 2009.

[56] P. D. Woolliams, R. A. Ferguson, C. Hart, A. Grimwood, and P. H. Tomlins, "Spatially deconvolved optical coherence tomography," *Applied Optics*, vol. 49, no. 11, pp. 2014–2021, 2010.

[57] J. Ripoll, B. Koberstein-Schwarz, and V. Ntziachristos, "Unleashing Optics and Optoacoustics for Developmental Biology.," *Trends in biotechnology*, vol. 33, pp. 679–91, nov 2015.

[58] C. Lefort, "A review of biomedical multiphoton microscopy and its laser sources," *Journal of Physics D: Applied Physics*, vol. 50, no. 42, 2017.

[59] W. R. Zipfel, R. M. Williams, and W. W. Webb, "Nonlinear magic: multiphoton microscopy in the biosciences.," *Nature biotechnology*, vol. 21, no. 11, pp. 1369–1377, 2003.

[60] E. E. Hoover and J. A. Squier, "Advances in multiphoton microscopy technology," *CPEM Digest (Conference on Precision Electromagnetic Measurements)*, vol. 7, no. February, pp. 64–65, 2014.

[61] M. Oheim, D. J. Michael, M. Geisbauer, D. Madsen, and R. H. Chow, "Principles of two-photon excitation fluorescence microscopy and other nonlinear imaging approaches," 2006.

[62] D. Sandkuijl, A. E. Tuer, D. Tokarz, J. E. Sipe, and V. Barzda, "Numerical second- and third-harmonic generation microscopy," *Journal of the Optical Society of America B*, vol. 30, no. 2, p. 382, 2013.

[63] F. Träger, *Springer Handbook of Lasers and Optics*. New York, NY: Springer New York, 2007.

[64] R. W. Boyd and B. R. Masters, "Nonlinear Optics, Third Edition," *Journal of Biomedical Optics*, vol. 14, no. 2, p. 029902, 2009.

[65] G. J. Tserevelakis, "Nonlinear Optical Procedures for the Diagnostics and Processing of Biological Samples By Using Ultra-Short Laser Pulses," p. 187, 2013.

[66] B. Weigelin, G.-J. Bakker, and P. Friedl, "Third harmonic generation microscopy of cells and tissue organization.," *Journal of cell science*, vol. c, pp. 245–255, jan 2016.

[67] Y. Wang, O. Y. H. Tai, C. H. Wang, and A. K. Y. Jen, "One-, two-, and three-photon absorption Induced fluorescence of a novel chromophore in chloroform solution," *Journal of Chemical Physics*, vol. 121, no. 16, pp. 7901–7907, 2004.

[68] P. Cronstrand, *Quantum Chemical Calculations of Nonlinear Optical Absorption*. 2004.

[69] W. Liu, Y. Zhou, M. Wang, L. Li, E. Vienneau, R. Chen, J. Luo, C. Xu, Q. Zhou, L. V. Wang, and J. Yao, "Correcting the limited view in optical-resolution photoacoustic microscopy," *Journal of Biophotonics*, no. November, 2017.

[70] X. L. Deán-Ben and D. Razansky, "On the link between the speckle free nature of optoacoustics and visibility of structures in limited-view tomography," *Photoacoustics*, vol. 4, no. 4, pp. 133–140, 2016.

[71] J. Yao and L. V. Wang, "Photoacoustic microscopy," *Laser & Photonics Reviews*, vol. 7, pp. 758–778, sep 2012.

[72] F. Gao, X. Feng, R. Zhang, S. Liu, R. Ding, R. Kishor, and Y. Zheng, "Single laser pulse generates dual photoacoustic signals for differential contrast photoacoustic imaging," *Scientific Reports*, vol. 7, no. 1, pp. 1–12, 2017.

[73] L. V. Wang, *Photoacoustic Imaging and Spectroscopy*, vol. 144 of *Optical Science and Engineering*. CRC Press, mar 2009.

[74] G. Wissmeyer, M. A. Pleitez, A. Rosenthal, and V. Ntziachristos, "Looking at sound: optoacoustics with all-optical ultrasound detection," *Light: Science and Applications*, vol. 7, no. 1, 2018.

[75] Q. Sheng, K. Wang, J. Xia, L. Zhu, L. V. Wang, and M. A. Anastasio, "Photoacoustic computed tomography without accurate ultrasonic transducer responses," in *SPIE BiOS* (A. A. Oraevsky and L. V. Wang, eds.), vol. 34, pp. 1–6, mar 2015.

[76] Y. Lou, A. Oraevsky, and M. A. Anastasio, "Application of signal detection theory to assess optoacoustic imaging systems," vol. 9708, pp. 1–9, mar 2016.

[77] M. A. A. Caballero, A. Rosenthal, A. Buehler, D. Razansky, and V. Ntziachristos, "Optoacoustic determination of spatio-temporal responses of ultrasound sensors," *IEEE Transactions on Ultrasonics, Ferroelectrics, and Frequency Control*, vol. 60, no. 6, pp. 1234–1244, 2013.

[78] M. Seeger, D. Soliman, J. Aguirre, G. Diot, J. Wierzbowski, and V. Ntziachristos, "Pushing the boundaries of optoacoustic microscopy by Total Impulse Response characterization," *in revision at Nature Communications*.

[79] G. Ludwig and K. Brendel, "Calibration of Hydrophones Based on Reciprocity and Time Delay Spectrometry," *IEEE Transactions on Ultrasonics, Ferroelectrics, and Frequency Control*, vol. 35, no. 2, pp. 168–174, 1988.

[80] R. A. Smith and D. R. Bacon, "A multiple-frequency hydrophone calibration technique," *The Journal of the Acoustical Society of America*, vol. 87, no. 5, pp. 2231–2243, 1990.

[81] A. Rosenthal, V. Ntziachristos, and D. Razansky, "Optoacoustic methods for frequency calibration of ultrasonic sensors," *IEEE Transactions on Ultrasonics, Ferroelectrics, and Frequency Control*, vol. 58, pp. 316–326, feb 2011.

[82] C. Zhang, K. Maslov, J. Yao, and L. V. Wang, "In vivo photoacoustic microscopy with 7.6-μm axial resolution using a commercial 125-MHz ultrasonic transducer," *Journal of biomedical optics*, vol. 11, no. 17, pp. 1–6, 2012.

[83] C. Zhang, K. Maslov, S. Hu, R. Chen, Q. Zhou, K. K. Shung, and L. V. Wang, "Reflection-mode submicron-resolution in vivo photoacoustic microscopy," *Journal of Biomedical Optics*, vol. 17, no. 2, p. 020501, 2012.

[84] R. C. Gonzalez and R. E. Woods, "Digital Image Processing," 2002.

[85] N. Chaudhari and B. Pawar, "Microscope Image Processing: An Overview," *International Journal of Computer Applications*, vol. 124, no. 12, pp. 23–28, 2015.

[86] C. Kervrann, C. O. Sanchez Sorzano, S. T. Acton, J.-C. Olivo-Marin, and M. Unser, "A Guided Tour of Selected Image Processing and Analysis Methods for Fluorescence and Electron Microscopy," *IEEE Journal of Selected Topics in Signal Processing*, vol. 10, pp. 6–30, feb 2016.

[87] C. Baroux and V. Schubert, "Technical Review: Microscopy and Image Processing Tools to Analyze Plant Chromatin: Practical Considerations," vol. 1675 of *Methods in Molecular Biology*, pp. 537–589, New York, NY: Springer New York, 2018.

[88] D. Cohen-Or, O. Sorkine, R. Gal, T. Leyvand, and Y.-Q. Xu, "Color harmonization," in *ACM SIGGRAPH 2006 Papers on - SIGGRAPH '06*, vol. 1, (New York, New York, USA), p. 624, ACM Press, 2006.

[89] L. Zhou and C. D. Hansen, "A Survey of Colormaps in Visualization," *IEEE Transactions on Visualization and Computer Graphics*, vol. 22, pp. 2051–2069, aug 2016.

[90] S. Silva, B. Sousa Santos, and J. Madeira, "Using color in visualization: A survey," *Computers and Graphics (Pergamon)*, vol. 35, no. 2, pp. 320–333, 2011.

[91] C. Healey, "Choosing effective colours for data visualization," in *Proceedings of Seventh Annual IEEE Visualization '96*, pp. 263–270,, ACM, 2002.

[92] J. Tan, J. Echevarria, and Y. Gingold, "Palette-based image decomposition, harmonization, and color transfer," *arXiv*, vol. 1, apr 2018.

[93] Y.-S. Chang, "CIE Chromaticity Diagram," 2011.

[94] S. Psilodimitrakopoulos, I. Amat-Roldan, P. Loza-Alvarez, and D. Artigas, "Effect of molecular organization on the image histograms of polarization SHG microscopy," *Biomedical Optics Express*, vol. 3, no. 10, p. 2681, 2012.

[95] P. B. Johnson and R. W. Christy, "Optical constants of the noble metals," *Physical Review B*, vol. 6, pp. 4370–4379, dec 1972.

[96] P. B. Johnson and R. W. Christy, "Optical constants of transition metals: Ti, V, Cr, Mn, Fe, Co, Ni, and Pd," *Physical Review B*, vol. 9, pp. 5056–5070, jun 1974.

[97] B. E. Treeby, B. T. Cox, and J. Jaros, "k-Wave: A MATLAB toolbox for the time domain simulation of acoustic wave fields," vol. 1, p. 75, 2012.

[98] J. A. Jensen and P. Gori, "Spatial filters for focusing ultrasound images," *Proceedings of the IEEE Ultrasonics Symposium*, vol. 2, pp. 1507–1511, 2001.

[99] A. Hazra, C. S. Fuchs, A. T. Chan, E. L. Giovannucci, and J. Hunter, "Beamforming using spatial matched filtering with annular arrays," *Cancer*, vol. 19, no. 9, pp. 975–980, 2009.

[100] D. Sage and M. Unser, "Teaching Image-Processing Programming in Java," *IEEE Signal Processing Magazine*, vol. 20, no. 6, pp. 43–52, 2003.

[101] M. A. Pleitez, A. A. Khan, A. Soldà, A. Chmyrov, J. Reber, F. Gasparin, M. Seeger, B. Schätz, S. Herzig, M. Scheideler, and V. Ntziachristos, "Label-free metabolic monitoring of living cells by mid-infrared optoacoustic microscopy," *in revision at Nature Biotechnology*, pp. 1–21.

[102] M. A. Pleitez, A. A. Khan, J. Reber, A. Chmyrov, M. Seeger, M. Scheideler, S. Herzig, and V. Ntziachristos, "Mid-infrared optoacoustic microscopy with label-free chemical contrast in living cells and tissues," *bioRxiv*, p. 270082, feb 2018.

[103] M. Seeger, G. G. Westmeyer, and V. Ntziachristos, "In-vivo hybrid microscopy of small model organisms," in *Opto-Acoustic Methods and Applications in Biophotonics IV* (V. Ntziachristos and R. Zemp, eds.), no. July, p. 21, SPIE, jul 2019.

[104] C. Massner, F. Sigmund, S. Pettinger, M. Seeger, C. Hartmann, N. P. Ivleva, R. Niessner, H. Fuchs, M. H. de Angelis, A. Stelzl, N. L. Koonakampully, H. Rolbieski, U. Wiedwald, M. Spasova, W. Wurst, V. Ntziachristos, M. Winklhofer, and G. G. Westmeyer, "Genetically Controlled Lysosomal Entrapment of Superparamagnetic Ferritin for Multimodal and Multiscale Imaging and Actuation with Low Tissue Attenuation," *Advanced Functional Materials*, vol. 28, p. 1706793, may 2018.

[105] G. Genove, U. DeMarco, H. Xu, W. F. Goins, and E. T. Ahrens, "A new transgene reporter for in vivo magnetic resonance imaging," *Nature Medicine*, vol. 11, pp. 450–454, apr 2005.

[106] Y. Gossuin, P. Gillis, A. Hocq, Q. L. Vuong, and A. Roch, "Magnetic resonance relaxation properties of superparamagnetic particles," *Wiley Interdisciplinary Reviews: Nanomedicine and Nanobiotechnology*, vol. 1, pp. 299–310, may 2009.

[107] B. Iordanova, T. K. Hitchens, C. S. Robison, and E. T. Ahrens, "Engineered Mitochondrial Ferritin as a Magnetic Resonance Imaging Reporter in Mouse Olfactory Epithelium," *PLoS ONE*, vol. 8, p. e72720, aug 2013.

[108] J. Stritzker, L. Kirscher, M. Scadeng, N. C. Deliolanis, S. Morscher, P. Symvoulidis, K. Schaefer, Q. Zhang, L. Buckel, M. Hess, U. Donat, W. G. Bradley, V. Ntziachristos, and A. A. Szalay, "Vaccinia virus-mediated melanin production allows MR and optoacoustic deep tissue imaging and laser-induced thermotherapy of cancer.," *Proceedings of the National Academy of Sciences of the United States of America*, vol. 110, pp. 3316–20, feb 2013.

[109] S. A. Stanley, J. E. Gagner, S. Damanpour, M. Yoshida, J. S. Dordick, and J. M. Friedman, "Radio-Wave Heating of Iron Oxide Nanoparticles Can Regulate Plasma Glucose in Mice," *Science*, vol. 336, pp. 604–608, may 2012.

[110] S. A. Stanley, J. Sauer, R. S. Kane, J. S. Dordick, and J. M. Friedman, "Remote regulation of glucose homeostasis in mice using genetically encoded nanoparticles," *Nature Medicine*, vol. 21, pp. 92–98, jan 2015.

[111] S. A. Stanley, L. Kelly, K. N. Latcha, S. F. Schmidt, X. Yu, A. R. Nectow, J. Sauer, J. P. Dyke, J. S. Dordick, and J. M. Friedman, "Bidirectional electromagnetic control of the hypothalamus regulates feeding and metabolism," *Nature*, vol. 531, pp. 647–650, mar 2016.

[112] B. Iordanova, C. S. Robison, and E. T. Ahrens, "Design and characterization of a chimeric ferritin with enhanced iron loading and transverse NMR relaxation rate," *JBIC Journal of Biological Inorganic Chemistry*, vol. 15, pp. 957–965, aug 2010.

[113] Y. Matsumoto, R. Chen, P. Anikeeva, and A. Jasanoff, "Engineering intracellular biomineralization and biosensing by a magnetic protein," *Nature Communications*, vol. 6, p. 8721, dec 2015.

[114] S. M. Pereira, D. Moss, S. R. Williams, P. Murray, A. Taylor, S. M. Pereira, D. Moss, S. R. Williams, P. Murray, and A. Taylor, "Overexpression of the MRI Reporter Genes Ferritin and Transferrin Receptor Affect Iron Homeostasis and Produce Limited Contrast in Mesenchymal Stem Cells," *International Journal of Molecular Sciences*, vol. 16, pp. 15481–15496, jul 2015.

[115] S. M. Pereira, A. Herrmann, D. Moss, H. Poptani, S. R. Williams, P. Murray, and A. Taylor, "Evaluating the effectiveness of transferrin receptor-1 (TfR1) as a magnetic resonance reporter gene," *Contrast Media and Molecular Imaging*, vol. 11, pp. 236–244, may 2016.

[116] H. Huang, S. Delikanli, H. Zeng, D. M. Ferkey, and A. Pralle, "Remote control of ion channels and neurons through magnetic-field heating of nanoparticles," *Nature Nanotechnology*, vol. 5, pp. 602–606, aug 2010.

[117] R. J. Mannix, S. Kumar, F. Cassiola, M. Montoya-Zavala, E. Feinstein, M. Prentiss, and D. E. Ingber, "Nanomagnetic actuation of receptor-mediated signal transduction," *Nature Nanotechnology*, vol. 3, pp. 36–40, jan 2008.

[118] B. B. Bartelle, C. A. Berríos-Otero, J. J. Rodriguez, A. E. Friedland, O. Aristizábal, and D. H. Turnbull, "Novel genetic approach for in vivo vascular imaging in mice," *Circulation Research*, vol. 110, pp. 938–947, mar 2012.

[119] P. S. Patrick, T. B. Rodrigues, M. I. Kettunen, S. K. Lyons, A. A. Neves, and K. M. Brindle, "Development of Timd2 as a reporter gene for MRI," *Magnetic Resonance in Medicine*, vol. 75, pp. 1697–1707, apr 2016.

[120] J. W. M. Bulte, T. Douglas, S. Mann, R. B. Frankel, B. M. Moskowitz, R. A. Brooks, C. D. Baumgarner, J. Vymazal, M.-P. Strub, and J. A. Frank, "Magnetoferritin: Characterization of a novel superparamagnetic MR contrast agent," *Journal of Magnetic Resonance Imaging*, vol. 4, pp. 497–505, may 1994.

[121] F. C. Meldrum, B. R. Heywood, and S. Mann, "Magnetoferritin: in vitro synthesis of a novel magnetic protein.," *Science (New York, N.Y.)*, vol. 257, pp. 522–3, jul 1992.

[122] H. Xu and D. Ren, "Lysosomal Physiology," *Annual Review of Physiology*, vol. 77, pp. 57–80, feb 2015.

[123] A. S. Chen-Plotkin, T. L. Unger, M. D. Gallagher, E. Bill, L. K. Kwong, L. Volpicelli-Daley, J. I. Busch, S. Akle, M. Grossman, V. Van Deerlin, J. Q. Trojanowski, and V. M.-Y. Lee, "TMEM106B, the Risk Gene for Frontotemporal Dementia, Is Regulated by the microRNA-132/212 Cluster and Affects Progranulin Pathways," *Journal of Neuroscience*, vol. 32, pp. 11213–11227, aug 2012.

[124] C. Cao, L. Tian, Q. Liu, W. Liu, G. Chen, and Y. Pan, "Magnetic characterization of noninteracting, randomly oriented, nanometer-scale ferrimagnetic particles," *Journal of Geophysical Research: Solid Earth*, vol. 115, p. B07103, jul 2010.

[125] P. Rucker, F. M. Torti, and S. V. Torti, "Recombinant ferritin: modulation of subunit stoichiometry in bacterial expression systems," *Protein Engineering Design and Selection*, vol. 10, pp. 967–973, aug 2002.

[126] K. Fan, C. Cao, Y. Pan, D. Lu, D. Yang, J. Feng, L. Song, M. Liang, and X. Yan, "Magnetoferritin nanoparticles for targeting and visualizing tumour tissues," *Nature Nanotechnology*, vol. 7, pp. 459–464, jul 2012.

[127] M. D. Giosia, A. Soldà, M. Seeger, A. Cantelli, F. Arnesano, M. Nardella, V. Mangini, F. Valle, M. Montalti, F. Zerbetto, S. Rapino, V. Ntziachristos, and M. Calvaresi, "Development of a C70-Based Phototheranostic Platform via Protein Incorporation," *in revision at ACS Nano*.

[128] S. Bosi, T. Da Ros, G. Spalluto, and M. Prato, "Fullerene derivatives: An attractive tool for biological applications," 2003.

[129] R. Partha and J. L. Conyers, "Biomedical applications of functionalized fullerene-based nanomaterials.," *International journal of nanomedicine*, 2009.

[130] A. Dellinger, Z. Zhou, J. Connor, A. Madhankumar, S. Pamujula, C. M. Sayes, and C. L. Kepley, "Application of fullerenes in nanomedicine: an update," *Nanomedicine*, vol. 8, pp. 1191–1208, jul 2013.

[131] E. Castro, A. H. Garcia, G. Zavala, and L. Echegoyen, "Fullerenes in biology and medicine," *Journal of Materials Chemistry B*, vol. 5, no. 32, pp. 6523–6535, 2017.

[132] E. Nakamura and H. Isobe, "Functionalized Fullerenes in Water. The First 10 Years of Their Chemistry, Biology, and Nanoscience," *Accounts of Chemical Research*, 2003.

[133] S. Goodarzi, T. Da Ros, J. Conde, F. Sefat, and M. Mozafari, "Fullerene: biomedical engineers get to revisit an old friend," *Materials Today*, vol. 20, pp. 460–480, oct 2017.

[134] P. Mroz, G. P. Tegos, H. Gali, T. Wharton, T. Sarna, and M. R. Hamblin, "Photodynamic therapy with fullerenes," *Photochemical & Photobiological Sciences*, vol. 6, no. 11, p. 1139, 2007.

[135] Z. Markovic and V. Trajkovic, "Biomedical potential of the reactive oxygen species generation and quenching by fullerenes (C60)," 2008.

[136] S. K. Sharma, L. Y. Chiang, and M. R. Hamblin, "Photodynamic therapy with fullerenes in vivo : reality or a dream?," *Nanomedicine*, vol. 6, pp. 1813–1825, dec 2011.

[137] P. Mroz, G. P. Tegos, H. Gali, T. Wharton, T. Sarna, and M. R. Hamblin, "Fullerenes as Photosensitizers in Photodynamic Therapy," in *Carbon Materials: Chemistry and Physics*, pp. 79–106, 2008.

[138] V. Krishna, A. Singh, P. Sharma, N. Iwakuma, Q. Wang, Q. Zhang, J. Knapik, H. Jiang, S. R. Grobmyer, B. Koopman, and B. Moudgil, "Polyhydroxy fullerenes for non-invasive cancer imaging and therapy," *Small*, 2010.

[139] Z. Chen, L. Ma, Y. Liu, and C. Chen, "Applications of Functionalized Fullerenes in Tumor Theranostics," *Theranostics*, vol. 2, no. 3, pp. 238–250, 2012.

[140] F. Z. Henari, S. MacNamara, O. Stevenson, J. Callaghan, D. Weldon, and W. J. Blau, "Low power nonlinear optical response of C60 and C70 fullerene solutions," *Advanced Materials*, 1993.

[141] A. Mateo-Alonso, K. Iliopoulos, S. Couris, and M. Prato, "Efficient modulation of the third order nonlinear optical properties of fullerene derivatives," *Journal of the American Chemical Society*, 2008.

[142] S. R. Chae, A. R. Badireddy, J. Farner Budarz, S. Lin, Y. Xiao, M. Therezien, and M. R. Wiesner, "Heterogeneities in fullerene nanoparticle aggregates affecting reactivity, bioactivity, and transport," *ACS Nano*, 2010.

[143] E. M. Hotze, J. Labille, P. Alvarez, and M. R. Wiesner, "Mechanisms of photochemistry and reactive oxygen production by fullerene suspensions in water," *Environmental Science and Technology*, 2008.

[144] D. M. Guldi and M. Prato, "Excited-state properties of C60 fullerene derivatives," *Accounts of Chemical Research*, 2000.

[145] M. Di Giosia, P. H. Bomans, A. Bottoni, A. Cantelli, G. Falini, P. Franchi, G. Guarracino, H. Friedrich, M. Lucarini, F. Paolucci, S. Rapino, N. A. Sommerdijk, A. Soldà, F. Valle, F. Zerbetto, and M. Calvaresi, "Proteins as supramolecular hosts for C60: A true solution of C60 in water," *Nanoscale*, 2018.

[146] M. Di Giosia, F. Nicolini, L. Ferrazzano, A. Soldà, F. Valle, A. Cantelli, T. D. Marforio, A. Bottoni, F. Zerbetto, M. Montalti, S. Rapino, A. Tolomelli, and M. Calvaresi, "Stable and Biocompatible Monodispersion of C 60 in Water by Peptides," *Bioconjugate Chemistry*, 2019.

[147] A. Soldà, A. Cantelli, M. Di Giosia, M. Montalti, F. Zerbetto, S. Rapino, and M. Calvaresi, "C60@lysozyme: A new photosensitizing agent for photodynamic therapy," *Journal of Materials Chemistry B*, 2017.

[148] M. di Giosia, F. Valle, A. Cantelli, A. Bottoni, F. Zerbetto, and M. Calvaresi, "C60 bioconjugation with proteins: Towards a palette of carriers for all pH ranges," *Materials*, 2018.

[149] M. Calvaresi, F. Arnesano, S. Bonacchi, A. Bottoni, V. Calò, S. Conte, G. Falini, S. Fermani, M. Losacco, M. Montalti, G. Natile, L. Prodi, F. Sparla, and F. Zerbetto, "C60@Lysozyme: Direct observation by nuclear magnetic resonance of a 1:1 fullerene protein adduct," *ACS Nano*, 2014.

[150] Q. Liu, M. Guan, L. Xu, C. Shu, C. Jin, J. Zheng, X. Fang, Y. Yang, and C. Wang, "Structural effect and mechanism of C 70 -carboxyfullerenes as efficient sensitizers against cancer cells," *Small*, 2012.

[151] Y. Doi, A. Ikeda, M. Akiyama, M. Nagano, T. Shigematsu, T. Ogawa, T. Takeya, and T. Nagasaki, "Intracellular uptake and photodynamic activity of water-soluble [60]- and [70]fullerenes incorporated in liposomes," *Chemistry - A European Journal*, 2008.

[152] A. Ikeda, Y. Doi, M. Hashizume, J. I. Kikuchi, and T. Konishi, "An extremely effective DNA photocleavage utilizing functionalized liposomes with a fullerene-enriched lipid bilayer," *Journal of the American Chemical Society*, 2007.

[153] D. Callerio-Babudieri, "Lysozyme granules and lysosome structures in cell sulture," *Nature*, 1966.

[154] T. Kooistra, A. M. Duursma, J. M. Bouma, and M. Gruber, "Effect of size and charge on endocytosis of lysozyme derivatives by sinusoidal rat liver cells in vivo," *Biochimica et Biophysica Acta - General Subjects*, 1980.

[155] S. Roberts, M. Seeger, Y. Jiang, A. Mishra, F. Sigmund, A. Stelzl, A. Lauri, P. Symvoulidis, H. Rolbieski, M. Preller, X. L. Deán-Ben, D. Razansky, T. Orschmann, S. C. Desbordes, P. Vetschera, T. Bach, V. Ntziachristos, and G. G. Westmeyer, "Calcium Sensor for Photoacoustic Imaging," *Journal of the American Chemical Society*, vol. 140, pp. 2718–2721, feb 2018.

[156] M. J. Berridge, M. D. Bootman, and H. L. Roderick, "Calcium signalling: Dynamics, homeostasis and remodelling," jul 2003.

[157] S. Gottschalk, T. Felix Fehm, X. Luís Deán-Ben, and D. Razansky, "Noninvasive real-time visualization of multiple cerebral hemodynamic parameters in whole mouse brains using five-dimensional optoacoustic tomography," *Journal of Cerebral Blood Flow and Metabolism*, vol. 35, pp. 531–535, mar 2015.

[158] Y. Li-Smerin, E. S. Levitan, and J. W. Johnson, "Free intracellular Mg2+ concentration and inhibition of NMDA responses in cultured rat neurons," *Journal of Physiology*, vol. 533, pp. 729–743, jun 2001.

[159] B. I. Kalappa, C. T. Anderson, J. M. Goldberg, S. J. Lippard, and T. Tzounopoulos, "AMPA receptor inhibition by synaptically released zinc," *Proceedings of the National Academy of Sciences*, vol. 112, p. 201512296, dec 2015.

[160] S. Li, G. Chen, Y. Zhang, Z. Guo, Z. Liu, J. Xu, X. Li, and L. Lin, "Identification and characterization of colorectal cancer using Raman spectroscopy and feature selection techniques.," *Optics express*, vol. 22, pp. 25895–908, oct 2014.

[161] C. D. Wilms and J. Eilers, "Photo-physical properties of Ca2+-indicator dyes suitable for two-photon fluorescence-lifetime recordings," *Journal of Microscopy*, vol. 225, pp. 209–213, mar 2007.

[162] N. Dana, R. A. Fowler, A. Allen, J. Zoldan, L. Suggs, and S. Emelianov, "In vitro photoacoustic sensing of calcium dynamics with arsenazo III," *Laser Physics Letters*, vol. 13, p. 075603, jul 2016.

[163] E. J. Cooley, P. Kruizinga, D. W. Branch, and S. Emelianov, "Evaluation of arsenazo III as a contrast agent for photoacoustic detection of micromolar calcium transients," in *Reporters, Markers, Dyes, Nanoparticles, and Molecular Probes*

for Biomedical Applications II (S. Achilefu and R. Raghavachari, eds.), vol. 7576, p. 75761J, International Society for Optics and Photonics, feb 2010.

[164] A. C. H. Durham and J. M. Walton, "A survey of the available colorimetric indicators for Ca2+ and Mg2+ ions in biological experiments," *Cell Calcium*, vol. 4, pp. 47–55, feb 1983.

[165] H. Li, P. Zhang, L. P. Smaga, R. A. Hoffman, and J. Chan, "Photoacoustic Probes for Ratiometric Imaging of Copper(II)," *Journal of the American Chemical Society*, vol. 137, pp. 15628–15631, dec 2015.

[166] G. Grynkiewicz, M. Poenie, and R. Y. Tsien, "A new generation of Ca2+ indicators with greatly improved fluorescence properties," *Journal of Biological Chemistry*, vol. 260, pp. 3440–3450, mar 1985.

[167] M. Oheim, M. van 't Hoff, A. Feltz, A. Zamaleeva, J.-M. Mallet, and M. Collot, "New red-fluorescent calcium indicators for optogenetics, photoactivation and multi-color imaging," *Biochimica et Biophysica Acta (BBA) - Molecular Cell Research*, vol. 1843, pp. 2284–2306, oct 2014.

[168] M. Seeger, C. Dehner, D. Jüstel, and V. Ntziachristos, "Spatio-temporal assessment of wound healing sequences enabled by label-free multimodal microscopy," *in preparation*.

[169] G. Deka, S.-W. Chu, and F.-J. Kao, "Skin Wound Healing Revealed by Multimodal Optical Microscopies," in *Microscopy and Analysis*, p. 16, InTech, sep 2016.

[170] P. Martin, "Wound Healing–Aiming for Perfect Skin Regeneration," *Science*, vol. 276, no. 5309, pp. 75–81, 1997.

[171] A. H. Zhou, "A Survey of Optical Imaging Techniques for Assessing Wound Healing," *International Journal of Intelligent Control and Systems*, vol. 17, no. 3, pp. 79–85, 2012.

[172] J. S. Boateng, K. H. Matthews, H. N. Stevens, and G. M. Eccleston, "Wound Healing Dressings and Drug Delivery Systems: A Review," *Journal of Pharmaceutical Sciences*, vol. 97, pp. 2892–2923, aug 2008.

[173] a. D. Metcalfe and M. W. J. Ferguson, "Harnessing wound healing and regeneration for tissue engineering.," *Biochemical Society transactions*, vol. 33, pp. 413–417, 2005.

[174] S. Yousefi, J. Qin, S. Dziennis, and R. K. Wang, "Assessment of microcirculation dynamics during cutaneous wound healing phases using optical microangiography in vivo," *Journal of Biomedical Optics*, vol. 19, no. 7, p. 076015, 2014.

[175] Y. Jung, S. Dziennis, Z. Zhi, R. Reif, Y. Zheng, and R. K. Wang, "Tracking Dynamic Microvascular Changes during Healing after Complete Biopsy Punch on the Mouse Pinna Using Optical Microangiography," *PLoS ONE*, vol. 8, no. 2, 2013.

[176] B. Lange-Asschenfeldt, A. Alborova, D. Krüger-Corcoran, A. Patzelt, H. Richter, W. Sterry, A. Kramer, E. Stockfleth, and J. Lademann, "Effects of a topically applied wound ointment on epidermal wound healing studied by in vivo fluorescence laser scanning microscopy analysis," *Journal of Biomedical Optics*, vol. 14, no. 5, p. 054001, 2009.

[177] D. W. Paul, P. Ghassemi, J. C. Ramella-Roman, N. J. Prindeze, L. T. Moffatt, A. Alkhalil, and J. W. Shupp, "Noninvasive imaging technologies for cutaneous wound assessment: A review," *Wound Repair and Regeneration*, vol. 23, no. 2, pp. 149–162, 2015.

[178] A. T. Yeh, B. Kao, W. G. Jung, Z. Chen, J. S. Nelson, and B. J. Tromberg, "Imaging wound healing using optical coherence tomography and multiphoton microscopy in an in vitro skin-equivalent tissue model," *Journal of Biomedical Optics*, vol. 9, no. 2, p. 248, 2004.

[179] Gangaraju Vamsi K. Lin Haifan, "Label-free optical imaging of lymphatic vessels within tissue beds in vivo," *Nat Rev Mol Cell Biol.*, vol. 10 (2), no. 1, pp. 116–125, 2009.

[180] R. Cicchi, D. Kapsokalyvas, V. De Giorgi, V. Maio, A. Van Wiechen, D. Massi, T. Lotti, and F. S. Pavone, "Scoring of collagen organization in healthy and diseased human dermis by multiphoton microscopy," *Journal of Biophotonics*, vol. 3, no. 1-2, pp. 34–43, 2010.

[181] S. Bancelin, C. Aimé, I. Gusachenko, L. Kowalczuk, G. Latour, T. Coradin, and M. C. Schanne-Klein, "Determination of collagen fibril size via absolute measurements of second-harmonic generation signals," *Nature Communications*, vol. 5, pp. 1–8, 2014.

[182] A. Zoumi, A. T. Yeh, and B. J. Tromberg, "Imaging cells and extracellular matrix in vivo by using second-harmonic generation and two-photon excited fluorescence.," *Proceedings of the National Academy of Sciences of the United States of America*, vol. 99, no. 17, pp. 11014–11019, 2002.

[183] X. Zhu, Y. Tang, J. Chen, S. Xiong, S. Zhuo, and J. Chen, "Monitoring wound healing of elastic cartilage using multiphoton microscopy," *Osteoarthritis and Cartilage*, vol. 21, no. 11, pp. 1799–1806, 2013.

[184] J. H. Barker, D. Kjolseth, M. Kim, J. M. Frank, I. Bondar, E. Uhl, M. Kamler, K. Messmer, G. R. Tobin, and L. J. Weiner, "The hairless mouse ear: an in vivo model for studying wound neovascularization," *Wound Repair and Regeneration*, vol. 2, pp. 138–143, apr 1994.

[185] A. L. Sander, D. Henrich, C. M. Muth, I. Marzi, J. H. Barker, and J. M. Frank, "In vivo effect of hyperbaric oxygen on wound angiogenesis and epithelialization," *Wound Repair and Regeneration*, vol. 17, pp. 179–184, mar 2009.

[186] E. Heber-Katz, "The regenerating mouse ear," *seminars in CELL & DEV ELOPMENTAL BI OLOGY*, vol. 10, 1999.

[187] S. Hu, K. Maslov, and L. V. Wang, "In vivo functional chronic imaging of a small animal model using optical-resolution photoacoustic microscopy," *Medical Physics*, vol. 36, no. 6, p. 2320, 2009.

[188] R. Reif, J. Qin, L. An, Z. Zhi, S. Dziennis, and R. Wang, "Quantifying Optical Microangiography Images Obtained from a Spectral Domain Optical Coherence Tomography System," *International Journal of Biomedical Imaging*, vol. 2012, pp. 1–11, 2012.

[189] M. Seeger, A. Karlas, D. Soliman, J. Pelisek, and V. Ntziachristos, "Multimodal optoacoustic and multiphoton microscopy of human carotid atheroma," *Photoacoustics*, vol. 4, pp. 102–111, sep 2016.

[190] M. Seeger, A. Karlas, D. Soliman, J. Pelisek, and V. Ntziachristos, "Hybrid microscopy of human carotid atheroma by means of optical-resolution optoacoustic and non-linear optical microscopy," in *Photons Plus Ultrasound: Imaging and Sensing 2017* (A. A. Oraevsky and L. V. Wang, eds.), vol. 10064, p. 1006455, mar 2017.

[191] A. Karlas, N.-A. Fasoula, K. Paul-Yuan, J. Reber, M. Kallmayer, D. Bozhko, M. Seeger, H.-H. Eckstein, M. Wildgruber, and V. Ntziachristos, "Cardiovascular optoacoustics: From mice to men – A review," *Photoacoustics*, vol. 14, pp. 19–30, jun 2019.

[192] WHO, "The top 10 causes of death," 2011.

[193] W. Insull, "The Pathology of Atherosclerosis: Plaque Development and Plaque Responses to Medical Treatment," *American Journal of Medicine*, vol. 122, pp. S3–S14, jan 2009.

[194] B. C. Dickson and A. I. Gotlieb, "Towards understanding acute destabilization of vulnerable atherosclerotic plaques," *Cardiovascular Pathology*, vol. 12, pp. 237–248, jan 2003.

[195] R. B. Singh, S. A. Mengi, Y. J. Xu, A. S. Arneja, and N. S. Dhalla, "Pathogenesis of atherosclerosis: A multifactorial process," *Experimental and Clinical Cardiology*, vol. 7, pp. 40–53, jan 2002.

[196] R. Virmani, A. P. Burke, E. Ladich, and F. D. Kolodgie, "Pathology of carotid artery atherosclerotic disease," *Pathology*, pp. 1–10, 2007.

[197] D. Gutstein, "Pathophysiology and clinical significance of atherosclerotic plaque rupture," *Cardiovascular Research*, vol. 41, pp. 323–333, feb 1999.

[198] H. C. Stary, A. B. Chandler, R. E. Dinsmore, V. Fuster, S. Glagov, W. Insull, M. E. Rosenfeld, C. J. Schwartz, W. D. Wagner, and R. W. Wissler, "A Definition of Advanced Types of Atherosclerotic Lesions and a Histological Classification of Atherosclerosis," *Circulation*, vol. 92, pp. 1355–1374, sep 1995.

[199] J. M. Mann and M. J. Davies, "Vulnerable plaque. Relation of characteristics to degree of stenosis in human coronary arteries.," *Circulation*, vol. 94, pp. 928–31, sep 1996.

[200] E. Falk, P. K. Shah, and V. Fuster, "Coronary Plaque Disruption," *Circulation*, vol. 92, pp. 657–671, aug 1995.

[201] P. RICHARDSON, "INFLUENCE OF PLAQUE CONFIGURATION AND STRESS DISTRIBUTION ON FISSURING OF CORONARY ATHEROSCLEROTIC PLAQUES," *The Lancet*, vol. 334, pp. 941–944, oct 1989.

[202] G. Pasterkamp, A. H. Schoneveld, A. C. van der Wal, D. J. Hijnen, W. J. van Wolveren, S. Plomp, H. L. Teepen, and C. Borst, "Inflammation of the atherosclerotic cap and shoulder of the plaque is a common and locally observed feature in unruptured plaques of femoral and coronary arteries.," *Arteriosclerosis, thrombosis, and vascular biology*, vol. 19, pp. 54–58, jan 1999.

[203] D. A. Chistiakov, A. N. Orekhov, and Y. V. Bobryshev, "Contribution of neovascularization and intraplaque haemorrhage to atherosclerotic plaque progression and instability," *Acta Physiologica*, vol. 213, pp. 539–553, mar 2015.

[204] S. K. Nadkarni, B. E. Bouma, J. de Boer, and G. J. Tearney, "Evaluation of collagen in atherosclerotic plaques: the use of two coherent laser-based imaging methods," *Lasers in Medical Science*, vol. 24, pp. 439–445, may 2009.

[205] J. O. Deguchi, E. Aikawa, P. Libby, J. R. Vachon, M. Inada, S. M. Krane, P. Whittaker, and M. Aikawa, "Matrix metalloproteinase-13/collagenase-3 deletion promotes collagen accumulation and organization in mouse atherosclerotic plaques," *Circulation*, vol. 112, pp. 2708–2715, oct 2005.

[206] K.-R. Purushothaman, M. Purushothaman, P. Muntner, P. a. Lento, W. N. O'Connor, S. K. Sharma, V. Fuster, and P. R. Moreno, "Inflammation, neovascularization and intra-plaque hemorrhage are associated with increased reparative collagen content: implication for plaque progression in diabetic atherosclerosis.," *Vascular medicine (London, England)*, vol. 16, no. 2, pp. 103–8, 2011.

[207] J. F. Bentzon, F. Otsuka, R. Virmani, and E. Falk, "Mechanisms of Plaque Formation and Rupture," *Circulation Research*, vol. 114, no. 12, pp. 1852–1866, 2014.

[208] R. Virmani, "Atherosclerotic Plaque Progression and Vulnerability to Rupture: Angiogenesis as a Source of Intraplaque Hemorrhage," *Arteriosclerosis, Thrombosis, and Vascular Biology*, vol. 25, no. 10, pp. 2054–2061, 2005.

[209] J. Milei, J. C. Parodi, M. Ferreira, A. Barrone, D. R. Grana, and L. Matturri, "Atherosclerotic plaque rupture and intraplaque hemorrhage do not correlate with symptoms in carotid artery stenosis," *Journal of Vascular Surgery*, vol. 38, no. 6, pp. 1241–1247, 2003.

[210] R. Virmani, F. D. Kolodgie, A. P. Burke, A. Farb, and S. M. Schwartz, "Lessons From Sudden Coronary Death," *Arteriosclerosis & Thrombosis*, pp. 1262–1275, 2000.

[211] M. Van Zandvoort, W. Engels, K. Douma, L. Beckers, M. Oude Egbrink, M. Daemen, and D. W. Slaaf, "Two-Photon Microscopy for Imaging of the (Atherosclerotic) Vascular Wall: A Proof of Concept Study," *Journal of Vascular Research*, vol. 41, no. 1, pp. 54–63, 2004.

[212] S. Massberg, K. Brand, S. Gruner, S. Page, E. Muller, I. Muller, W. Bergmeier, T. Richter, M. Lorenz, I. Konrad, B. Nieswandt, and M. Gawaz, "A critical role of platelet adhesion in the initiation of atherosclerotic lesion formation," *J. Exp. Med.*, vol. 196, no. 7, pp. 887–896, 2002.

[213] S. Massberg, M. Gawaz, S. Gruner, V. Schulte, I. Konrad, D. Zohlnhofer, U. Heinzmann, and B. Nieswandt, "A Crucial Role of Glycoprotein VI for Platelet Recruitment to the Injured Arterial Wall In Vivo," *Journal of Experimental Medicine*, vol. 197, no. 1, pp. 41–49, 2002.

[214] W. Yu, J. C. Braz, A. M. Dutton, P. Prusakov, and M. Rekhter, "In vivo imaging of atherosclerotic plaques in apolipoprotein E deficient mice using nonlinear microscopy.," *Journal of biomedical optics*, vol. 12, p. 054008, jan 2007.

[215] H. Yoo, J. W. Kim, M. Shishkov, E. Namati, T. Morse, R. Shubochkin, J. R. McCarthy, V. Ntziachristos, B. E. Bouma, F. A. Jaffer, and G. J. Tearney, "Intra-arterial catheter for simultaneous microstructural and molecular imaging in vivo.," *Nature medicine*, vol. 17, no. 12, pp. 1680–4, 2011.

[216] F. A. Jaffer, M. A. Calfon, A. Rosenthal, G. Mallas, R. N. Razansky, A. Mauskapf, R. Weissleder, P. Libby, and V. Ntziachristos, "Two-dimensional intravascular near-infrared fluorescence molecular imaging of inflammation in atherosclerosis and stent-induced vascular injury.," *Journal of the American College of Cardiology*, vol. 57, pp. 2516–26, jun 2011.

[217] M. A. Calfon, C. Vinegoni, V. Ntziachristos, and F. A. Jaffer, "Intravascular near-infrared fluorescence molecular imaging of atherosclerosis: toward coronary arterial visualization of biologically high-risk plaques.," *Journal of biomedical optics*, vol. 15, p. 011107, jan 2010.

[218] C. Vinegoni, I. Botnaru, E. Aikawa, M. a. Calfon, Y. Iwamoto, E. J. Folco, V. Ntziachristos, R. Weissleder, P. Libby, and F. A. Jaffer, "Indocyanine Green Enables Near-Infrared Fluorescence Imaging of Lipid-Rich, Inflamed Atherosclerotic Plaques," *Science Translational Medicine*, vol. 3, pp. 84ra45–84ra45, may 2011.

[219] T. T. Le, I. M. Langohr, M. J. Locker, M. Sturek, and J.-X. Cheng, "Label-free molecular imaging of atherosclerotic lesions using multimodal nonlinear optical microscopy," *Biomedical microdevices*, vol. 12, no. 5, pp. 1–20, 2009.

[220] S. Kellnberger, D. Soliman, G. J. Tserevelakis, M. Seeger, H. Yang, A. Karlas, L. Prade, M. Omar, and V. Ntziachristos, "Optoacoustic microscopy at multiple discrete frequencies," *Light: Science & Applications*, vol. 7, p. 109, dec 2018.

[221] M. Xu and L. V. Wang, "Photoacoustic imaging in biomedicine," *Review of Scientific Instruments*, vol. 77, p. 041101, apr 2006.

[222] A. Stylogiannis, L. Prade, A. Buehler, J. Aguirre, G. Sergiadis, and V. Ntziachristos, "Continuous wave laser diodes enable fast optoacoustic imaging," *Photoacoustics*, vol. 9, pp. 31–38, 2018.

[223] A. A. Oraevsky, R. O. Esenaliev, S. L. Jacques, and F. K. Tittel, "Laser-based optoacoustic imaging in biological tissues," in *Laser-Tissue Interaction V; and Ultraviolet Radiation Hazards*, p. 16, SPIE, aug 2017.

[224] A. Taruttis and V. Ntziachristos, "Advances in real-time multispectral optoacoustic imaging and its applications," *Nature Photonics*, vol. 9, pp. 219–227, apr 2015.

[225] M. Choma, M. Sarunic, C. Yang, and J. Izatt, "Sensitivity advantage of swept source and Fourier domain optical coherence tomography.," *Optics express*, vol. 11, pp. 2183–9, sep 2003.

[226] R. Leitgeb, C. Hitzenberger, and A. Fercher, "Performance of fourier domain vs time domain optical coherence tomography," *Optics Express*, vol. 11, p. 889, apr 2010.

[227] S. s. S. Choi, A. Mandelis, X. Guo, B. Lashkari, S. Kellnberger, and V. Ntziachristos, "Wavelength-Modulated Differential Photoacoustic Spectroscopy (WM-DPAS) for noninvasive early cancer detection and tissue hypoxia monitoring," *Journal of Biophotonics*, vol. 9, pp. 388–395, apr 2016.

[228] G. Langer, B. Buchegger, J. Jacak, T. A. Klar, and T. Berer, "Frequency domain photoacoustic and fluorescence microscopy," *Biomedical Optics Express*, vol. 7, p. 2692, jul 2016.

[229] S. Kellnberger, N. C. Deliolanis, D. Queirós, G. Sergiadis, and V. Ntziachristos, "In vivo frequency domain optoacoustic tomography.," *Optics letters*, vol. 37, pp. 3423–5, aug 2012.

[230] B. Lashkari, S. s. S. Sean Choi, M. E. Khosroshahi, E. Dovlo, and A. Mandelis, "Simultaneous dual-wavelength photoacoustic radar imaging using waveform engineering with mismatched frequency modulated excitation," *Optics Letters*, vol. 40, p. 1145, apr 2015.

[231] S. Telenkov, A. Mandelis, B. Lashkari, and M. Forcht, "Frequency-domain photothermoacoustics: Alternative imaging modality of biological tissues," *Journal of Applied Physics*, vol. 105, p. 102029, may 2009.

[232] Y. Fan, A. Mandelis, G. Spirou, and I. Alex Vitkin, "Development of a laser photothermoacoustic frequency-swept system for subsurface imaging: Theory and experiment," *The Journal of the Acoustical Society of America*, vol. 116, pp. 3523–3533, dec 2004.

[233] S. s. S. Choi, B. Lashkari, E. Dovlo, and A. Mandelis, "Wavelength-modulated differential photoacoustic radar imager (WM-DPARI): accurate monitoring of absolute hemoglobin oxygen saturation," *Biomedical Optics Express*, vol. 7, p. 2586, jul 2016.

[234] M. Omar, M. Schwarz, D. Soliman, P. Symvoulidis, and V. Ntziachristos, "Pushing the Optical Imaging Limits of Cancer with Multi-Frequency-Band Raster-Scan Optoacoustic Mesoscopy (RSOM)," *Neoplasia*, vol. 17, pp. 208–214, feb 2015.

[235] M. Seeger, A. Stylogiannis, and V. Ntziachristos, "Simultaneous multiwavelength optoacoustic microscopy by high-speed laser diodes," *in preparation*.

[236] M. Schwarz, A. Buehler, J. Aguirre, and V. Ntziachristos, "Three-dimensional multispectral optoacoustic mesoscopy reveals melanin and blood oxygenation in human skin in vivo," *Journal of Biophotonics*, vol. 9, pp. 55–60, jan 2016.

[237] H. Zhong, T. Duan, H. Lan, M. Zhou, and F. Gao, "Review of Low-Cost Photoacoustic Sensing and Imaging Based on Laser Diode and Light-Emitting Diode," *Sensors*, vol. 18, p. 2264, jul 2018.

[238] T. Agano, N. Sato, H. Nakatsuka, K. Kitagawa, T. Hanaoka, K. Morisono, and Y. Shigeta, "Comparative experiments of photoacoustic system using laser light source and LED array light source," in *Photons Plus Ultrasound: Imaging and Sensing 2015* (A. A. Oraevsky and L. V. Wang, eds.), vol. 9323, p. 93233X, International Society for Optics and Photonics, mar 2015.

[239] X. Dai, H. Yang, and H. Jiang, "In vivo photoacoustic imaging of vasculature with a low-cost miniature light emitting diode excitation," *Optics Letters*, vol. 42, p. 1456, apr 2017.

[240] T. J. Allen and P. C. Beard, "High power visible light emitting diodes as pulsed excitation sources for biomedical photoacoustics," *Biomedical Optics Express*, vol. 7, p. 1260, apr 2016.

[241] P. K. Upputuri and M. Pramanik, "Performance characterization of low-cost, high-speed, portable pulsed laser diode photoacoustic tomography (PLD-PAT) system," *Biomedical Optics Express*, vol. 6, p. 4118, oct 2015.

[242] R. G. Kolkman, W. Steenbergen, and T. G. Van Leeuwen, "In vivo photoacoustic imaging of blood vessels with a pulsed laser diode," *Lasers in Medical Science*, vol. 21, pp. 134–139, sep 2006.

[243] L. Zeng, G. Liu, D. Yang, and X. Ji, "Portable optical-resolution photoacoustic microscopy with a pulsed laser diode excitation," *Applied Physics Letters*, vol. 102, p. 053704, feb 2013.

[244] T. Wang, S. Nandy, H. S. Salehi, P. D. Kumavor, and Q. Zhu, "A low-cost photoacoustic microscopy system with a laser diode excitation," *Biomedical Optics Express*, vol. 5, p. 3053, sep 2014.

[245] L. Zeng, Z. Piao, S. Huang, W. Jia, and Z. Chen, "Label-free optical-resolution photoacoustic microscopy of superficial microvasculature using a compact visible laser diode excitation," *Optics Express*, vol. 23, p. 31026, nov 2015.

[246] P.-H. Wang and M.-L. Li, "DVD pickup head based optical resolution photoacoustic microscopy," in *Photons Plus Ultrasound: Imaging and Sensing 2012*, vol. 8223, p. 82232V, 2012.

[247] G. Wissmeyer, R. Shnaiderman, D. Soliman, and V. Ntziachristos, "Optoacoustic microscopy based on pi-FBG ultrasound sensors," in *Photons Plus Ultrasound: Imaging and Sensing 2017* (A. A. Oraevsky and L. V. Wang, eds.), vol. 10064, p. 1006423, International Society for Optics and Photonics, mar 2017.

[248] G. Wissmeyer, D. Soliman, R. Shnaiderman, A. Rosenthal, and V. Ntziachristos, "All-optical optoacoustic microscope based on wideband pulse interferometry," *Optics Letters*, vol. 41, p. 1953, may 2016.

[249] R. Shnaiderman, G. Wissmeyer, M. Seeger, D. Soliman, H. Estrada, D. Razansky, A. Rosenthal, and V. Ntziachristos, "Fiber interferometer for hybrid optical and optoacoustic intravital microscopy," *Optica*, vol. 4, no. 10, p. 1180, 2017.

[250] R. Shnaiderman, G. Wissmeyer, H. Estrada, M. Seeger, and V. Ntziachristos, "Intravital hybrid optical-optoacoustic microscopy based on fiber-Bragg interferometry," in *Photons Plus Ultrasound: Imaging and Sensing 2018* (A. A. Oraevsky and L. V. Wang, eds.), vol. 10494, p. 92, SPIE, feb 2018.

[251] W. Song, Q. Xu, Y. Zhang, Y. Zhan, W. Zheng, and L. Song, "Fully integrated reflection-mode photoacoustic, two-photon, and second harmonic generation microscopy in vivo," *Scientific Reports*, vol. 6, pp. 1–8, oct 2016.

[252] W. Song, W. Zheng, R. Liu, R. Lin, H. Huang, X. Gong, S. Yang, R. Zhang, and L. Song, "Reflection-mode in vivo photoacoustic microscopy with subwavelength lateral resolution.," *Biomedical optics express*, vol. 5, pp. 4235–41, dec 2014.

[253] A. Rosenthal, S. Kellnberger, D. Bozhko, A. Chekkoury, M. Omar, D. Razansky, and V. Ntziachristos, "Sensitive interferometric detection of ultrasound for minimally invasive clinical imaging applications," *Laser and Photonics Reviews*, vol. 8, pp. 450–457, may 2014.

[254] P. Hajireza, W. Shi, K. Bell, R. J. Paproski, and R. J. Zemp, "Non-interferometric photoacoustic remote sensing microscopy," *Light: Science & Applications*, vol. 6, p. e16278, jun 2017.

[255] X. Zhu, Z. Huang, G. Wang, W. Li, D. Zou, and C. Li, "Ultrasonic detection based on polarization-dependent optical reflection," *Optics Letters*, vol. 42, p. 439, feb 2017.

[256] S.-L. Chen, L. J. Guo, and X. Wang, "All-optical photoacoustic microscopy," *Photoacoustics*, vol. 3, pp. 143–150, dec 2015.

[257] A. Rosenthal, D. Razansky, and V. Ntziachristos, "Wideband optical sensing using pulse interferometry," *Optics Express*, vol. 20, p. 19016, aug 2012.

[258] M. Seeger, A. C. Stiel, and V. Ntziachristos, "Optoacoustic flow-cytometry of genetically encoded chromoproteins," *in preparation*.

[259] H. M. Shapiro, *Practical Flow Cytometry*, vol. 139. Wiley, jun 2003.

[260] M. G. Ormerod, "Flow Cytometry," in *Encyclopedia of Molecular Cell Biology and Molecular Medicine*, pp. 589–617, Weinheim, Germany: Wiley-VCH Verlag GmbH & Co. KGaA, sep 2006.

[261] B. Barlogie, M. N. Raber, J. Schumann, T. S. Johnson, B. Drewinko, D. E. Swartzendruber, W. Göhde, M. Andreeff, E. J. Freireich, B. Barlogie, M. N. Raber, J. Schumann, T. S. Johnson, B. Drewinko, D. E. Swartzendruber, W. Göhde, M. Andreeff, E. J. Freireich, B. Barlogie, M. N. Raber, J. Schumann, T. S. Johnson, B. Drewinko, D. E. Swartzendruber, W. Göhde, M. Andreeff, E. J. Freireich, B. Barlogie, M. N. Raber, J. Schumann, T. S. Johnson, B. Drewinko, D. E. Swartzendruber, W. Göhde, M. Andreeff, and E. J. Freireich, "Flow Cytometry in Clinical Cancer Research," *Cancer Research*, vol. 43, pp. 3982–3997, sep 1983.

[262] D. Huh, W. Gu, Y. Kamotani, J. B. Grotberg, and S. Takayama, "Microfluidics for flow cytometric analysis of cells and particles," *Physiological Measurement*, vol. 26, pp. R73–R98, jun 2005.

[263] T. D. Chung and H. C. Kim, "Recent advances in miniaturized microfluidic flow cytometry for clinical use," *ELECTROPHORESIS*, vol. 28, pp. 4511–4520, dec 2007.

[264] J. Krueger, K. Singh, A. O'Neill, C. Jackson, A. Morrison, and P. O'Brien, "Development of a microfluidic device for fluorescence activated cell sorting," *Journal of Micromechanics and Microengineering*, vol. 12, p. 324, jul 2002.

[265] L. A. Herzenberg, D. Parks, B. Sahaf, O. Perez, M. Roederer, and L. A. Herzenberg, "The history and future of the fluorescence activated cell sorter and flow cytometry: a view from Stanford.," *Clinical chemistry*, vol. 48, pp. 1819–27, oct 2002.

[266] T. Blasi, H. Hennig, H. D. Summers, F. J. Theis, J. Cerveira, J. O. Patterson, D. Davies, A. Filby, A. E. Carpenter, and P. Rees, "Label-free cell cycle analysis for high-throughput imaging flow cytometry," *Nature Communications*, vol. 7, p. 10256, apr 2016.

[267] X. Su, S. E. Kirkwood, M. Gupta, L. Marquez-Curtis, Y. Qiu, A. Janowska-Wieczorek, W. Rozmus, and Y. Y. Tsui, "Microscope-based label-free microfluidic cytometry," *Optics Express*, vol. 19, p. 387, jan 2011.

[268] D. A. Nedosekin, M. Sarimollaoglu, E. V. Shashkov, E. I. Galanzha, and V. P. Zharov, "Ultra-fast photoacoustic flow cytometry with a 0.5 MHz pulse repetition rate nanosecond laser.," *Optics express*, vol. 18, pp. 8605–20, apr 2010.

[269] D. A. Nedosekin, T. Fahmi, Z. A. Nima, J. Nolan, C. Cai, M. Sarimollaoglu, E. Dervishi, A. Basnakian, A. S. Biris, and V. P. Zharov, "Photoacoustic in vitro flow cytometry for nanomaterial research," *Photoacoustics*, vol. 6, pp. 16–25, 2017.

[270] E. I. Galanzha and V. P. Zharov, "Photoacoustic flow cytometry," *Methods*, vol. 57, no. 3, pp. 280–296, 2012.

[271] E. V. Shashkov, E. I. Galanzha, and V. P. Zharov, "Photothermal and photoacoustic Raman cytometry in vitro and in vivo.," *Optics express*, vol. 18, no. 7, pp. 6929–6944, 2010.

[272] C. Cai, D. A. Nedosekin, Y. A. Menyaev, M. Sarimollaoglu, M. A. Proskurnin, and V. P. Zharov, "Photoacoustic Flow Cytometry for Single Sickle Cell Detection In Vitro and In Vivo," *Analytical Cellular Pathology*, vol. 2016, pp. 1–11, sep 2016.

[273] P. van den Berg, K. Daoudi, and W. Steenbergen, "Review of photoacoustic flow imaging: its current state and its promises," *Photoacoustics*, vol. 3, pp. 89–99, sep 2015.

[274] D. A. Nedosekin, M. Sarimollaoglu, E. I. Galanzha, R. Sawant, V. P. Torchilin, V. V. Verkhusha, J. Ma, M. H. Frank, A. S. Biris, and V. P. Zharov, "Synergy of photoacoustic and fluorescence flow cytometry of circulating cells with negative and positive contrasts," *Journal of Biophotonics*, vol. 6, pp. 425–434, may 2013.

[275] V. Gnyawali, E. M. Strohm, J. Z. Wang, S. S. Tsai, and M. C. Kolios, "Simultaneous acoustic and photoacoustic microfluidic flow cytometry for label-free analysis," *Scientific Reports*, vol. 9, p. 1585, dec 2019.

Index

π-Fiber Bragg grating, π-FBG, 175

Absorption, 10, 15, 52
  coefficient, 18, 50, 54, 56
  cross section, 47, 49, 50
  multi-photon, 18, 46, 48–50
  single-photon, 17, 49
Acoustic
  attenuation, 57
  focusing, 58, 78
  lens, 58, 78
Airy pattern, *see* Point spread function (PSF)

Beer-Lambert law, 34
Birefringences, 45

Calcium, 135
  sensor of photoacoustics, CaSPA, 135
Cell
  Escherichia coli, *E. coli*, 118, 123, 181
  3T3-L1 adipocytes, 118
  Chinese Hamster Ovary, CHO, 118
  Human cervical cancer, HeLa, 118, 129
  Human Embryonic Kidney, HEK, 118, 123, 135
CIE-XYZ space, 68
Circulating tumor cells, 166
Colormap, 67, 68
  harmonized, 70
Continuous multi-Record, CMR, 83
Continuous multi-record, CMR, 85
Contrast mechanism, 23, 28
  label, 28, 123, 129, 135, 181
  label-free, 28, 140, 151, 158, 166, 175

Data acquisition, 83
Diffraction, 10
Diffraction limit, 31, 56
  Abbe criterion, 32
  Rayleigh criterion, 32
  Sparrow criterion, 32

Effect
  inductive, 17
  mesomeric, 17
  optoacoustic, 20, 52, 56
  photoelectric, 16
  photothermal, 20
  solvatochromatic, 17
Electrical Impulse Response, EIR, *see* Impulse Response
Energy levels, 11, 27, 47
  electronic, 11, 17, 27, 47
  rotational, 11
  vibrational, 11, 14, 27, 47
  virtual, 13
Energy transfer
  Förster resonance (FRET), 22
Excitation, 10
  electronic, 17, 25
  rotational, 19
  vibrational, 14, 18, 25

Ferritin, 123
Field of view, FOV, 36, 96
  hybrid-scanning, 88, 140
  laser-scanning, 36, 51, 74, 88
  sample-scanning, 36, 87
  widefield, 36
Flow
  in vitro, 181
  in vivo, 158, 166
  cytometry, 181
Fluence, 26, 54, 56
Fluorescence, 21, 26, 47, 48
  bleaching, 23
  molecular tomography (FMT), 26
  one-photon excitation, 1PEF, 46–48
  quenching, 22
  three-photon excitation, 3PEF, 26, 46, 48, 77, 92, 94
  two-photon excitation, 2PEF, 26, 46, 48, 77, 92, 94, 129, 135, 140, 151, 158, 175
Fractality, 142
Fullerene, 129

Gamma correction, 64
Global trigger signal, 83, 84
Gold nanolayer, GNL, 101, 103
Grüneisen parameter, 54
Green's function, 54

Harmonic generation, 14, 24, 42
  second, SHG, 14, 43, 44, 77, 92, 94, 140, 151, 158, 175
  third, THG, 14, 43, 45, 77, 92, 94, 123, 129, 140, 151, 158
Heating function, 54
Histogram
  adjustment, 64
  equalization, 65
  normalization, 65
  processing, 65
Histopathology
  Bone marrow, 122
  Human carotid atheroma, 122, 151

Hue-saturation-value model, HSV, 68

Image processing, 62
Imaging
  ex situ, 121, 151
  in vitro, 82, 118, 123, 129, 135
  in vivo, 46, 82, 120, 140, 158, 166, 175
  label-free, 46, 140, 151, 175
  multi-modal, 79, 96, 123, 129, 135, 140, 151, 158, 175
Imaging depth, 34, 57
Imaging speed, 99
Impulse response
  correction, 110
  electrical, EIR, 59, 100, 101, 103, 107, 110
  simulation, 107
  spatial, SIR, 59, 100, 101, 103, 107, 110
  total, TIR, 59, 100, 101, 103, 107, 110

Jablonski diagram, 12

Kernel filter, 66
  despeckling, 66
  Gaussian, 66
  mean, 66
  median, 66

Laser diodes, 166
Light-matter-interaction, 10

Mean free path, MFP, 34
Microfluidic, 181
Microscopy
  brightfield, 82, 140, 151
  confocal, 26
  fluorescence, 26
  multi-modal, 79, 123, 129, 135, 140, 151, 158, 175
  multi-photon, 24, 26, 40, 51, 76, 79, 123, 129, 135, 140, 151, 158, 175
  optical coherence, 24
  optoacoustic, *see* Optoacoustic microscopy
  Raman, 24
  super-resolution, 26, 33
Molecular orbital
  highest occupied (HOMO), 17
  lowest unoccupied (LUMO), 17
Morse potential, 11
Mouse
  in vivo, 82, 120, 140, 158, 166, 175
Multiplicity, 12
  singlet, 12, 17, 21
  triplet, 12, 21

Near-infrared spectroscopy (NIRS), 25
Non-centrosymmetry, 45
Numerical aperture, 32, 56, 75, 96

Optical anisotropy, 45
Optical coherence microscopy (OCM), 24
Optical coherence tomography (OCT), 24
Optical sectioning, 51
Optoacoustic, 19, 25, 52
  frequency content, 57
  Frequency domain, 54, 158
  frequency-dependent attentuation, 57
  mesoscopy, 25
  microscopy, *see* Optoacoustic microscopy, 123, 129, 135, 140, 151
  Time domain, 20, 54, 78
  tomography, 25
Optoacoustic microscopy, 25, 52, 56, 78, 158, 166, 175
  all-optical, 175
  alternating laser excitation, ALEX, 166
  Frequency Comb, FComb, 166
  Frequency-domain, FDOM, 158
  optical-resolution, 78
Organoid, 135
  cardiac, 118, 135

Penetration depth, 34
Phosphorescence, 21
Photoacoustic, *see* Optoacoustic
Photochemistry, 22
Photodynamic therapy, 129, 140
Photoluminescence, 20
Photomultiplier tube, 51, 77
Point source, 61, 101
  surrogate, SOAP, 62, 101, 103
Point spread function, PSF, 31, 33, 57, 58, 67
  deconvolution, 33, 67
  Figure of Merrit, 67
Polarization
  hyperpolarizability, 44
  linear, 41, 42
  non-linear, 41, 42, 44, 45, 49
Principle
  Franck-Condon, 12, 17, 47
  Huygen, 31, 55
  Nyquist-Shannon, 36, 67, 85, 94

Quantum yield, 21, 48

Raman scattering, 24
Reactive oxygen species, ROS, 22, 129
Reflection, 10, 24
Refraction, 10
Refractive index, 24, 41, 45, 46
Resolution, 31, 93

Scanning
    Hybrid, 36, 87
    Laser, 36, 74, 87, 96, 99
    Sample, 36, 87
Scattering, 10
    Compton, 16
    elastic, 10, 13
    inelastic, 10, 13
    Mie, 15
    multi-photon, 14
    Raman, 14, 15, 24
    Rayleigh, 14
    Stokes, 14
Signal-to-noise ratio, SNR, 91
Slowly varying amplitude approximation, 43
Spatial Impulse Response, SIR, *see* Impulse Response
Spatial matched filter, SMF, 110
Spectral fingerprint, 27
Stokes-shift, 21
Stress confinement, 53
Susceptibility, 41–44, 46, 49, 50

Thermal ablation, 123
Thermal confinement, 53, 54
Thermoelastic expansion, 20, 25
Total Impulse Response, TIR, *see* Impulse Response
Transport mean free path, TMFP, 35

Ultrasound transducers, 57, 78

Wound healing, 140

Zebrafish
    in vivo, 82, 120, 158
    casper, 120
    medaka, 120